



**HAL**  
open science

# Detection of travelling electrons in the Quantum Hall effect regime with a singlet-triplet quantum bit detector

Vivien Thiney

► **To cite this version:**

Vivien Thiney. Detection of travelling electrons in the Quantum Hall effect regime with a singlet-triplet quantum bit detector. Mesoscopic Systems and Quantum Hall Effect [cond-mat.mes-hall]. Université Grenoble Alpes, 2017. English. NNT : 2017GREAY069 . tel-01757271

**HAL Id: tel-01757271**

**<https://theses.hal.science/tel-01757271>**

Submitted on 3 Apr 2018

**HAL** is a multi-disciplinary open access archive for the deposit and dissemination of scientific research documents, whether they are published or not. The documents may come from teaching and research institutions in France or abroad, or from public or private research centers.

L'archive ouverte pluridisciplinaire **HAL**, est destinée au dépôt et à la diffusion de documents scientifiques de niveau recherche, publiés ou non, émanant des établissements d'enseignement et de recherche français ou étrangers, des laboratoires publics ou privés.

## THÈSE

Pour obtenir le grade de

**DOCTEUR DE LA COMMUNAUTÉ**  
**UNIVERSITÉ GRENOBLE ALPES**

Spécialité : **NanoPhysique**

Arrêté ministériel : 7 Août 2006

Présentée par

**Vivien THINEY**

Thèse dirigée par **Tristan MEUNIER**

préparée au sein de l'**Institut Néel- CNRS**  
et de l'**École doctorale de Physique de Grenoble**

# Detection of travelling electrons in the Quantum Hall effect regime with a singlet-triplet quantum bit detector

Thèse soutenue publiquement le **16 octobre 2017**,  
devant le jury composé de :

**D.Mailly**

Directeur de recherche, LPN-CNRS, Rapporteur

**F.Portier**

Directeur de recherche, Iramis - CEA, Rapporteur

**P.Degiovanni**

Directeur de recherche, ENS Lyon, Examineur

**W.Guichard**

Professeure, UGA, Président

**Tristan Meunier**

Chargé de recherche Institut Néel - CNRS, Directeur de thèse





---

# Contents

---

<b>Introduction</b>	<b>1</b>
<b>1 Electrons confinement and manipulation</b>	<b>5</b>
1.1 Confinement in a quantum dot	6
1.1.1 Two dimensional electron gas	6
1.1.2 Lateral confinement	7
1.1.3 Constant Interaction model	8
1.2 Charge sensing of a quantum dot	10
1.2.1 Transport measurement	10
1.2.2 QPC detection	11
1.2.3 Charge detection with a QPC	11
1.3 Single quantum dot	13
1.4 Double quantum dot	13
1.5 Two electron spin states in quantum dots	15
1.6 Couplings to the environment	18
1.6.1 Relaxation and dephasing of the spin state	18
1.6.2 Hyperfine interactions	19
1.7 Quantum Hall effect	21
<b>2 Experimental setup</b>	<b>25</b>
2.1 Cryogenics	26
2.1.1 Dilution refrigerator	26
2.1.2 DC and RF connections	27
2.1.2.1 DC connections	28
2.1.2.2 RF connections	29
2.2 DC electronics	31
2.2.1 DC voltages	31
2.2.2 DC measurements	31
2.2.3 Controlling software	32
2.3 RF manipulations and detection	32
2.3.1 RF manipulations	32
2.3.2 RF detection	32
2.4 RF-QPC	34

---

---

2.4.1	RF-QPC: working principle . . . . .	34
2.4.2	Complete RF-QPC setup . . . . .	36
2.4.2.1	Measurement chain . . . . .	36
2.4.2.2	Tank circuit components and its tuning . . . . .	38
2.4.3	Detection bandwidth . . . . .	39
2.4.4	Signal to Noise Ratio and charge sensitivity . . . . .	42
2.4.5	RF carrier power . . . . .	42
2.5	Single shot spin detection . . . . .	43
2.6	Conclusion . . . . .	52
<b>3</b>	<b>Singlet-triplet spin qubit as charge detector</b>	<b>53</b>
3.1	Introduction . . . . .	54
3.2	Charge manipulation with RF gates . . . . .	54
3.2.1	RF stability diagram . . . . .	54
3.2.2	Charge manipulations with the RF gates . . . . .	57
3.3	Preliminary spin measurements . . . . .	59
3.3.1	Pauli spin blockade based spin readout . . . . .	59
3.3.2	Measuring position using the Pauli spin blockade . . . . .	61
3.4	Detuning mapping of the (1,1)-(2,0) spin states . . . . .	63
3.5	Concept of adiabaticity and singlet triplet mixing . . . . .	67
3.5.1	Concept of adiabaticity . . . . .	67
3.5.2	singlet-triplet spin mixing . . . . .	69
3.6	Coherent exchange oscillations . . . . .	71
3.6.1	adiabaticity . . . . .	73
3.6.2	chevron pattern . . . . .	74
3.7	$ S\rangle -  T_0\rangle$ spin qubit as charge detector . . . . .	78
3.8	Detection of travelling electrons into the ECs . . . . .	80
<b>4</b>	<b>Towards single electron detection</b>	<b>85</b>
4.1	Introduction . . . . .	86
4.2	Coherent exchange oscillations in amplitude . . . . .	86
4.2.1	Experimental procedure and results . . . . .	87
4.2.2	Noise origin . . . . .	90
4.2.3	Reduction of the charge noise . . . . .	91
4.3	Estimation of a single electron influence from a DC excitation . . . . .	93
4.3.1	Coherent exchange oscillations in amplitude influenced by the ECs electron density . . . . .	94
4.3.2	Qubit detector exposure time . . . . .	95
4.3.3	Single electron effect on the qubit detector . . . . .	96
4.4	Discussion on the qubit detector sensitivity . . . . .	99
4.4.1	(1,1)-(0,2) charge transition . . . . .	99
4.4.2	Number of ECs . . . . .	101

---

---

4.5	Injection of a single electron into the ECs	104
4.5.1	Single quantum dot	105
4.5.2	Electron injection	106
4.6	Detection of Edge Magneto Plasmon	108
4.6.1	Experimental sequence	109
4.6.2	First detection : mapping of the injection pulse delay	111
4.6.3	Delay dependence	112
4.6.4	Amplitude dependence	113
4.6.5	Magnetic field dependence	115
4.6.6	EMP effect on coherent exchange oscillations in amplitude	116
4.7	Single travelling charge detection	117
4.7.1	Fixed injecting position	117
4.7.2	Sweeping of the injecting position using single shot spin readout acquisition mode	119
4.7.3	Sweeping of the injecting position using signal averaging acquisition mode	121
4.7.4	Conclusion	123
<b>5</b>	<b>Conclusion &amp; perspectives</b>	<b>125</b>
<b>A</b>	<b>Parasitic losses in the tank circuit</b>	<b>127</b>
<b>B</b>	<b>Non adiabatic S(2,0)-S(1,1) transfer</b>	<b>129</b>
<b>C</b>	<b>Exchange energy evolution with the detuning</b>	<b>132</b>
<b>D</b>	<b>French summary</b>	<b>134</b>
	<b>Acknowledgement</b>	<b>149</b>
	<b>Bibliography</b>	<b>159</b>

---



---

# Introduction

---

Once elusive, the perfect control of a single elementary particle is now routinely achieved, opening up a completely new research field dedicated to the observation and understanding of quantum effects. In particular, when cooled-down at cryogenic temperature, newly engineered solid state systems with characteristic size smaller than the electron coherence length can be elaborated. The electron phase properties being hold over the engineered structures, electron quantum interference experiments can be implemented using the wave nature of electrons. Among the pioneering works of this new field called mesoscopic physics, the observation in 1985 of the Aharonov-Bohm oscillations in gold ring [1] stands as a major breakthrough.

Over the years, the constant progress in material science, nanofabrication quality and electronic control participate to the rapid development of the electron quantum optics where optics-like experiments are implemented with electrons. Performing quantum optics experiments with electrons instead of photons holds a twofold interest. First, electrons are fermions and do not follow the same boson statistic as photons. In particular, in correlations experiments radically different phenomenon can be observed. For example, the electron anti-bunching opposed to the photon bunching was experimentally demonstrated [2, 3, 4]. The second advantage is the possibility to interact and control electrons with electric fields since they are charged particles. Such control does not exist for photons.

For experimentalist, the semiconducting heterostructure of Aluminium Gallium Arsenide/ Gallium Arsenide (AlGaAs/GaAs) hosting a bidimensional electron gas (2DEG) approximately 100 nm below the surface is commonly used today as test bed for electron quantum optics. The reason is the quality of the structure with an electron mobility which can be up to  $35 \times 10^6 \text{ cm}^2/\text{Vs}$  [5]. As a consequence, in such structure, a ballistic electron can travel over several micrometers without colliding with any defects, preserving its phase properties. In addition, it is possible to reshape the 2DEG with negatively polarised metallic gates deposited on top of the heterostructure. Combined, these two elements allows the fabrication of the basic components necessary to perform quantum optics experiments with electrons. By positioning two gates face-to-face, it is possible to define a local constriction of the 2DEG called Quantum Point Contact (QPC) [6]. This QPC can be electrically tuned to constrain the electron propagation, when the constriction width is comparable to the Fermi wavelength, conductance plateaus appear [7, 8]. If the QPC conductance is tuned to lie in between two conductance plateaus, it is a tunnel barrier with a tunable transparency, i.e. a beam splitter for electrons. As an extension, two parallel gates can be engineered to deplete the 2DEG to form a 1D channel for guiding ballistic electrons. Ballistic channels can also be obtained in 2DEG systems using the edge channels (ECs) of the Quantum Hall effect (QHE) [9, 10]. These described components have been used to implement the electron counter part of the double slit

---

interference [11] or a Mach-Zehnder interferometers [12, 13, 14, 15]. Such ballistic interferometers are now considered as candidates for quantum information applications [16, 17, 18] where the two states of a quantum bit (qubit) are the presence of an electron in different path of the interferometer. This approach has been demonstrated experimentally with the so called flying qubit [19]. Recently, coherence properties [20, 21, 22] and energy relaxation [23, 24, 25] of flying electrons in EC have been studied. However, these works were performed in DC measurements. From a fundamental point of view, to pursue the electron correlation experiments and have access to the full counting statistic, or for the quantum processing with flying electron, it is necessary to control and detect a single electron.

Recently, different approaches have been employed to implement the on-demand single electron injection in ballistic channels, like the AC driven quantum dot [26], the surface acoustic waves (SAW) [27, 28] or the short Lorentzian voltage pulses [29, 30]. Such single electron sources have already been used to perform a single electron Hanbury Bown-Twiss [31] correlation experiment, or two indistinguishable electrons Hong Ou Mandel correlation experiment [29, 32]. There again, measurements were not single electron detection, but based on the current noise.

The single shot detection of a flying electron has been demonstrated already but with the electron carried with SAW, which is a system rather different than the 1D ballistic channel. Indeed, the transport is implemented by the injection of an electron in a moving quantum dot, a moving trapping potential, and it is caught at the end of the transport in a static quantum dot to freeze the charge for a time long enough to permit its detection with a conventional QPC charge detector. The SAW transport performed in a 0D confining potential drifting at the speed of sound of about  $\sim 3 \text{ km s}^{-1}$  is different than the ballistic channels where the electron is free to propagate in a 1D channel at the Fermi velocity  $\sim 10^5 \text{ m s}^{-1}$ . Besides, even if the electron injection has been optimised recently [33, 34], it is still performed statistically in a train of a few moving quantum dots, so unsuitable for the correlation experiments. One can think about catching such flying electron in a static quantum dot too. However, considering only the drift velocity, a triggering at the picosecond timescale is required to catch a flying electron, which is experimentally inconceivable with conventional electronics.

In the flying electrons experiments with 1D ballistic channels, the single electron detection challenge arises from the short interaction time the electron has with the charge detector. This time is defined by the speed of the particule, the size of its wave packet and the distance over which the charge detector is sensitive. As an example, for an electron moving at the Fermi velocity in an EC, this time does not exceed  $1 - 10 \text{ ps}$ . Up to know, the most sensitive on-chip charge detector in 2DEG [35] requires an interaction time larger than this one by several orders of magnitude, the detection bandwidth being limited to the order of  $10 \text{ MHz}$ . The detection of such single travelling charge is therefore possible only with a charge sensitivity about  $\sim 1 - 3 \cdot 10^{-6} \text{ e Hz}^{-1/2}$ , with a detection bandwidth from  $0.1 - 1 \text{ THz}$  typically. As it stands, single electron sources are available but a detector for single electron detection in a single shot manner is still to be developed.

Recently, quantum systems have been identified as being extremely sensitive to the environment fluctuations, consequently they are well adapted to be used as detector [36]. For instance, they have already been used to detect a single phonon excitation of a nanomechanical system [37]. In AlGaAs/GaAs struc-

tures, double quantum dot charge qubits or a Mach-Zehnder interferometer have been proposed [38] have been proposed for such purpose. In this thesis, we will focus on another type of detector, the singlet-triplet spin qubit.

This spin qubit is a quantum system defined in a double quantum dot by the two electron anti-parallel spin states singlet  $|S\rangle$  and triplet  $|T_0\rangle$ , separated in energy by the exchange energy  $J(\varepsilon)$ . This energy depends on the interdot tunnel coupling and the detuning  $\varepsilon$  between the two quantum dots. The detuning is the difference of chemical potential between the two quantum dots so it is varying with the electrostatic environment. Experimentally, oscillations of the spin state can be induced with an oscillation frequency defined by  $J(\varepsilon)$ . These oscillations, called coherent exchange oscillations, first demonstrated in 2005 [39], are sensitive to the electrostatic environment via  $\varepsilon$  and have already been used as charge detector [40]. The advantage of using these oscillations for charge detection is double: an interaction for a short time and a long-time storage of the acquired information. These advantages arise from the quick manipulation of the spin states permitting a control of  $J$  on short timescale. The spin qubit can therefore be used as an ultra-sensitive large bandwidth charge detector with a tunable charge sensitivity. The information acquired during this interaction time, oscillating time of the spin state, is encoded in the phase of the oscillations, the resulting spin state of the qubit, which can be stored for several hundred microseconds [41]. A time long enough to be readout with a conventional charge detector. Hence, this system appears as a promising candidate to succeed the in flight detection of the flying electron in ballistic channels.

The goal of my PhD was to develop such spin qubit detector for the single shot detection of a flying electron travelling at the Fermi velocity in the ECs of the QHE. This project was initiated by the work of R.Thalineau [42, 43], in which experimental constrains limit the qubit detector sensitivity to the detection of few tens of electrons. Improvements of the experimental setup and sample design should allow us to detect in-flight such single flying electrons. From a single electron source similar to Ref. [26], an electron is injected and propagate in the ECs, on its way, it interacts by capacitive coupling with such spin qubit detector placed nearby the ECs. If during this sub-nanosecond interaction time coherent exchange oscillations are performed, the presence of the flying electron modifying the qubit detector electrostatic environment, it leads to a phase shift of the oscillations measured in a second time with a conventional charge detector.

There are two challenges to succeed in detecting single shot the flying electron. The interaction between the flying electron should induce a  $\pi$  phase shift to perfectly map the presence or not of the electron onto the spin state of the qubit detector. Then, one has to readout the final spin state of the qubit detector in a single shot manner. If both challenges are succeed, a direct correspondence between the detection of the flying electron and the spin qubit detector state is obtained.

The manuscript is organised as follow.

In the first chapter the electron confinement in quantum dots is described. The two electrons spin system in a double quantum dot is then presented. In the last section of this chapter, the QHE is introduced to explain the origin of the ECs.

In the second chapter, the experimental setup is presented with a detailed description of the RF-QPC

---

(Radio Frequency Quantum Point Contact) employed. It is an improved version of the conventional QPC charge detector with a detection bandwidth meeting the requirement for the successful single shot detection of the qubit detector.

In the third chapter, the qubit detector development is described with the presentation of results demonstrating the sensitivity of this singlet-triplet spin qubit detector to the ECs electron density in an operating DC mode.

Finally, in the fourth chapter, the optimisation and use of the qubit detector for the single flying electron detection is presented in a pulsed experiment.

---

---

# Electrons confinement and manipulation

---

## Introduction

In this first chapter, the different basic principle necessary to the understanding of the different manipulations performed in the rest of the manuscript are presented. First, it will be explained how few electrons can be confined and manipulated, starting from the growth of our semiconductor heterostructure to the development of the quantum dot necessary to the manipulation of the electron at the single charge level. Then, the spin states for two electrons confined in a double quantum dot used for the development of the singlet-triplet spin qubit are presented. Finally, the impact of their coupling to the environment are described and the Quantum Hall effect is introduced.

### 1.1 Confinement in a quantum dot

Nowadays, confining a few electrons is a task routinely achieved by different techniques. Since a quantum dot is only a confining potential for trapping electrons, it exists a complete zoology of systems able to do so, such as the single molecules [44], self assembled quantum dots [45], vertical quantum dots [46] or laterally defined quantum dots [47].

To perform our experiment, laterally defined quantum dot in a heterostructure of Aluminium Gallium Arsenide/ Gallium Arsenide (AlGaAs/GaAs) doped with silicon are employed. Such structures benefit from many advantages, like the quality of the material, ensuring a high electron mobility and density, their large tunability and simplicity to use. In such system, the heterostructure hosts a two-dimensional electron gas (2DEG) permitting a confinement along the growth axis. The confinement along the two remaining free axes is realised thanks to negatively polarised metallic gates deposited on top of the heterostructure (cf. Fig. 1.1a).

Perpetually improved nanofabrication processes allow to have more and more dense patterning, which in return increase the number of electrostatically tunable parameters. Nowadays, it is possible to fabricate single [47], double [39], triple [48], quadruple quantum dots [49],... The main limitation being the coupling to the electrons reservoirs, for the exchange of electrons, and the ability of the experimentalist to use wisely the degrees of freedom (i.e. metallic gates) to define the trapping potentials.

#### 1.1.1 Two dimensional electron gas

To understand how it is possible to realise such 3D trapping potential, the first step is the explanation of the origin of the 2DEG permitting the confinement along the growth axis, introducing the advantages of using such heterostructures. The sample used is made of a  $\text{Al}_{0.34}\text{Ga}_{0.66}\text{As}/\text{GaAs}$  heterostructure silicon doped (negative doping) grown by molecular beam epitaxy (MBE) with the 2DEG approximately 100 nm below the surface. The growth is performed by Andreas D. Wieck from Bochum University. The main advantage of using AlGaAs/GaAs heterostructure is the quality of the interface between the two species resulting in samples with a low level of defects  $1 \times 10^{14} \text{ cm}^{-3}$  [50] and high electron mobility  $\mu_e = 1.5 \times 10^6 \text{ cm}^2 \text{ V}^{-1} \text{ s}^{-1}$ . Those levels of defects and mobility can be reached thanks to the low lattice mismatch between the two materials, with a lattice parameter equal to 565.35 pm for GaAs and 565.6 pm for the  $\text{Al}_{0.34}\text{Ga}_{0.66}\text{As}$  [51]. The lattice mismatch of about -0.4% ensures sharp interfaces almost strain

free. The two species having different energy bandgaps, with the conduction energy of the AlGaAs higher than the one of the GaAs substrate, the additional electrons provided by the donors tend to travel toward the substrate layer. This charge displacement induces the appearance of an electric field with the ionised donors which traps the electron at the interface between the two materials. In the end, locally a trapping potential filled with electrons is formed corresponding to the 2DEG sketched in Fig. 1.1b. By adjusting the doping concentration and profile, its electron density can be engineered. In order to maintain the high quality of the 2DEG, a silicon free AlGaAs layer, called the spacer, separates the dopant atoms from the 2DEG. A capping layer of GaAs is protecting the doped layer from the environment, also used as Schottky barrier with the metallic gates deposited on top of the heterostructure, avoiding current to flow down to the 2DEG when the gates are polarised.

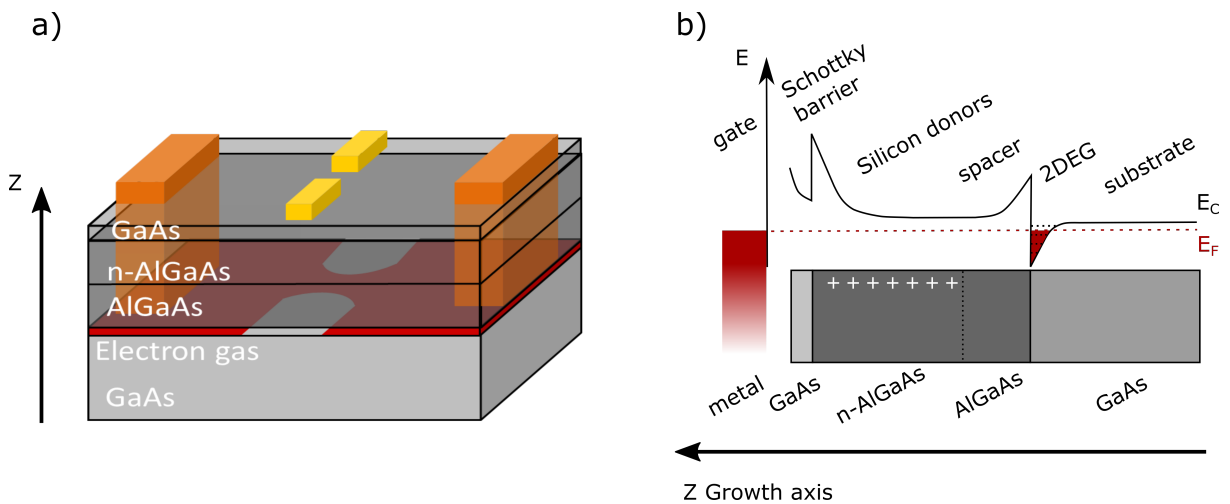


**Figure 1.1** – a) Sketch of the semiconducting heterostructure of  $Al_{0.34}Ga_{0.66}As/GaAs$ . The 2DEG is represented in red, the TiAu metallic gates used to control the electrostatic potential applied on the 2DEG in yellow, and the annealed AuGe alloy forming these Ohmic contacts permitting to measure the current flowing in the 2DEG are sketched in orange. Here the gates are negatively polarised to repel the electron underneath. b) Schematic representation of the heterostructure band gap as a function of the depth for the considered stack of GaAs, silicon doped AlGaAs, AlGaAs and GaAs layers. The 2DEG is the quantum well filled with electrons provided by the silicon donors located at the interface between the GaAs substrate and the AlGaAs layer. The silicon doped AlGaAs is separated from the 2DEG by a 40 nm layer of intrinsic AlGaAs to ensure the high quality of the interface. A 10 nm GaAs capping layer protects the AlGaAs layer from the environment.

### 1.1.2 Lateral confinement

To define a quantum dot, the confinement along the growth axis is not enough, an in plane one is also required. Moreover, the resulting confining potential should be small enough to enter in the quantum regime where the energy are quantised. An order of magnitude illustrating this regime is given by the Fermi wavelength:

$$\lambda_F = \sqrt{\frac{2\pi}{n_e}} \approx 70 \text{ nm} \quad (1.1)$$

With the modern techniques of ebeam lithography it is possible to deposit metallic gates of few nanometers. The Schottky barrier formed at the interface between these gates and the semiconductor heterostructure allows to applied negative voltages large enough to repel the electrons of the 2DEG underneath without inducing a flow of current through the heterostructure. By engineering their position and tuning properly the applied voltages, it is possible to isolate one, two islands of electrons having a size sufficiently reduced to allow this quantisation. This type of structure are the so called laterally defined quantum dot, with a double quantum dot as used in this manuscript sketched in Fig. 1.2.

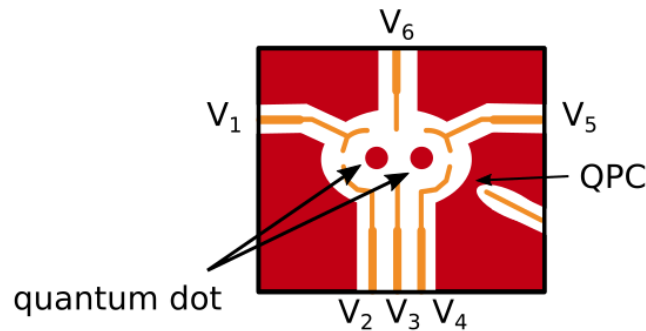


**Figure 1.2** – Top view representation of the sample. The 2DEG is represented in red, and the TiAu metallic gates in yellow. The gates are spatially engineered to define quantum dots in the 2DEG 100 nm below the surface. On the right side, the gate defines the so called quantum point contact (QPC) used as a charge detector.

The laterally defined quantum dot benefit from two main advantages, the first one is the quality of the heterostructure, the second is the use of such gate offering a large potential of tunability.

The advantage of such heterostructure is not the large electron mobility or the possibility to engineer their density, it is the quality of the interface which ensure a low level of defects. This point is particularly interesting for our manipulations because it is likely to define the quantum dots in a defect free area. Therefore, the manipulated electrons are not interacting with impurities in their vicinity, so they can be fully and only controlled by the voltages applied to the gates.

This control by the voltage is the second advantage of this type of system. Indeed, each gate can be used for a specific purpose, decoupling the control of the different parameters. For instance, some gates are dedicated to the control of the coupling to the electron reservoirs, like  $V_{1,5,6}$  in Fig. 1.2, another is used to define the coupling between two quantum dots,  $V_3$ , or to tune the chemical potential of the quantum dots with the so called plunger gates  $V_{2,4}$ .

### 1.1.3 Constant Interaction model

This last point of using only the voltage potential illustrates the fact that an experimentalist manipulates and detects only the electron charge. To understand more in detail their behaviour, the Constant Interaction model (CI model) [47, 52] can be useful. It is a model where the interactions between the different elements related to a quantum dot are modelled thanks to capacitances, as sketched in Fig. 1.3, based

on two assumptions. First, the Coulomb interaction of an electron in a quantum dot and the ones of its environment is parametrised by a single capacitance  $C$ . Second, the single particle energy level spectrum is independent of the number of electrons in the quantum dot.

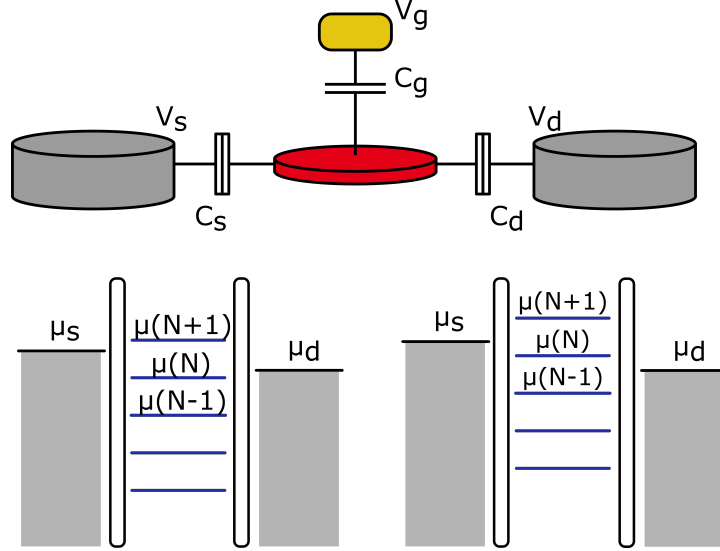


**Figure 1.3** – *a)* Sketch of the capacitive interactions of a quantum dot with its environment. In red, the quantum dot coupled to the source and drain via tunnel barriers, and capacitively coupled to a metallic gate (in yellow) at a potential  $V_g$ . These capacitive interactions are used in turns to parameterise the constant interaction model described in the main text. *b)* Representation of the source, drain and quantum dot chemical potential in the Coulomb blocked regime. In this regime, the chemical potential of the quantum dot is not within the source drain bias voltage window, therefore no electron can tunnel in or out of the quantum dot, and there is no measurable current. *c)* This time the chemical potential is within the bias windows so electrons can hop through the quantum dot.

If we consider a single quantum dot, as represented in Fig. 1.3, coupled to a gate  $g$  and connected to two electron reservoirs (a source and drain), a quantum dot filled with  $N$  electrons has an energy:

$$E(N) = \frac{(-Ne + C_s V_s + C_g V_g + C_d V_d)^2}{2C} + \sum_{n=1}^N E_n \quad (1.2)$$

with  $V_i(C_i)$  the different voltages (capacitances) of the gates and reservoirs, and  $E_n$  the single particle orbital energies of the quantum dot.

To speak about the charge state, it is more relevant to use the chemical potential term which corresponds to the energy required to add the  $N^{\text{th}}$  electron to the quantum dot. Considering  $V_s = V_d = 0$ :

$$\mu(N) = E(N) - E(N-1) = E_c \left(N - \frac{1}{2}\right) + \frac{C_g}{C} V_g + E_N \quad (1.3)$$

where we introduced  $E_C = \frac{e^2}{C}$  the charging energy of the system, and  $E_N$  the cost in orbital energy to add the  $N^{\text{th}}$  electron. Another quantity interesting to the understanding of the charge behaviour is  $\frac{C_g}{C}$  the  $\alpha$ -factor, or gate lever-arm, which corresponds to the conversion from applied voltage to chemical

potential. In some sense, it is like the efficiency of the applied voltages on the chemical potential. To add an electron to the system, the energy to pay corresponds to the charging energy since:

$$\mu(N + 1) - \mu(N) = E_C \quad (1.4)$$

This charging energy illustrates the regular structure of the energy spectrum of a quantum dot which can be observed with the Coulomb diamond or the artificial atom behaviour of these structures for instance [46, 53, 54]. The experimental constraint to the definition of quantum dots is illustrated by this energy. Considering the quantum dot as a disk with a radius about 40 nm, its capacitance  $C = 8\epsilon_0\epsilon_r r$  results in a charging energy of the order of 4 meV equivalent to a temperature about 40 K. To properly manipulate the charge, the only acting parameter should be the applied voltage on the metallic gates. Then, to avoid the perturbations from the thermal excitation, the electron temperature has to be much lower than 40 K.

## 1.2 Charge sensing of a quantum dot

Going toward the few electron regime, and more precisely the single electron manipulation, implies being able to detect the electron population of a quantum dot at the single electron level. Different techniques exist to perform this single charge detection, one is the transport measurement sketched in Fig. 1.3 which does not require any additional element than the quantum dot and two electrons reservoirs but it is limited and we will see why. Instead, a local charge detector sensor called Quantum Point Contact (QPC) is used. The advantages of using this charge detector will be presented such as the single electron detection with it.

### 1.2.1 Transport measurement

The transport measurement consists in probing the current flowing through a quantum dot when its chemical potential is within the source and drain bias window as sketched in Fig. 1.3. While sweeping the chemical potential of the quantum dot, each time it is passing within this bias window, a Coulomb peak appears in the current trace. Each Coulomb peak indicates a transition between two charge states of the quantum dot.

The limitation of such technique are reached while entering in the few-electron regime. Indeed, such detection requires a high coupling to the reservoir to ensure a measurable current. However, to reduce the number of trapped charge, the gates are polarised with voltages more and more negative, to repel them out of it. Increasing this polarisation induces a reduction of the coupling to the electron reservoirs. Therefore, the flowing current is decreasing in the same time than the number of trapped charges. In the end, when there is no flowing current anymore, it is not possible to determine if it is because of the coupling to the reservoir, or the empty quantum dot. Instead of using such transport measurement further developed in [46, 47, 54], a QPC is employed. Being on the side of the quantum dot, as sketched in Fig. 1.2, it is rather independent to its tuning and therefore have a sensitivity independent of the number of trapped charges.

### 1.2.2 QPC detection

A QPC is a charge detector composed by at least two metallic gates (see Figs. 1.2 and 1.4b) inducing a local constriction of the 2DEG forcing the electrons to flow through a local 1D channel [6]. When the constriction width is comparable to the Fermi wavelength, the lateral confinement induces quantised modes of conductance in integer values of  $\frac{2e^2}{h}$ . This quantisation has been measured already in 1988 [7, 8] and is visible in Fig. 1.4a, for the most negative voltages of  $V_{2:3}$ . At the transition between two plateaus, one can notice the high sensitivity of the current to the electrostatic environment, materialised here by the gate voltage. When the QPC is located close to a quantum dot, it is in particular sensitive to its charge state as first measured in a single [55] or coupled quantum dots [56] and shown in Fig 1.4c. In comparison with the transport measurement, the QPC benefits from its non invasive nature. Indeed, since it is on the side of the quantum dot, its tuning is rather independent to the quantum dot one, so does its sensitivity. Then, even when the quantum dot is weakly coupled to the reservoir, the QPC is still sensitive to its charge state so it is possible to discriminate between the low coupling of the quantum dot to the electron reservoir and an empty quantum dot.

### 1.2.3 Charge detection with a QPC

This detector being used all along the experiments presented in this manuscript, it is important to see the detail of its use from the definition of its working position to the analyse of a typical trace recorded with it. The Fig. 1.4b represents a scanning electron micrograph (SEM) of the sample, with the QPC gates labelled  $V_{2:1}$  and  $V_{2:2}$ . Considering  $V_{2:1}$  as grounded, since it is not relevant for the present discussion, and the other gates of the quantum dot at a fixed voltage. A QPC is formed with  $V_{2:2}$  and  $V_{4:6}$  for instance, with a single active gate being  $V_{2:2}$ . When sweeping it while measuring the QPC current results in a typical trace called pinch-off similar to the one of Fig. 1.4a. The first step of current for  $V_{2:2} = -0.3$  V corresponds to the depletion, the electrons under the gate are repelled. The three other steps of current for  $V_{2:2} = -0.6, -0.8$  and  $-0.95$  V are the conductance plateaus previously mentioned.

To be able to detect a change in the electron population of the quantum dot, a tunneling event, the first step is to define the QPC working position. This working position, the  $V_{2:2}$  gate voltage, corresponds to the position where the QPC charge sensitivity is maximal, ideally between two conductance plateaus, where the derivative of the QPC current with respect to the gate voltage is the largest.

Once this position set, the detection of tunneling events can be forced by changing the chemical potential of the quantum dot with a gate voltage like  $V_{4:3}$  in Fig. 1.4c.

In the resulting current trace, two things can be noticed. The first one is the general tendency of the current to decrease while moving toward more negative voltages. Such evolution is due to the capacitive coupling between the QPC current and the swept gate. The gate controlling the chemical potential of the quantum dot, called plunger gate, is also capacitively coupled to the QPC current, with a  $\alpha$ -factor reduced compare to  $V_{2:2}$  but still non zero. Therefore, while sweeping the plunger voltage towards more negative values the confinement in the QPC region increases resulting in this global decrease of current. The second element which is noticeable is the positive step of current like the one for  $V_{4:3} = -0.75$  V. A positive (negative) step like this one corresponds to an abrupt reduction (increase) of the confinement

in the QPC vicinity, an electron leaving (loaded into) the quantum dot.

The only relevant information of this trace being abrupt changes of signal like this one, usually it is the derivative of the current with regard to the gate voltage which is plotted. The objective is to highlight the change of electron population resulting in charge stability diagram like the one of Fig. 1.4d explained in the following.

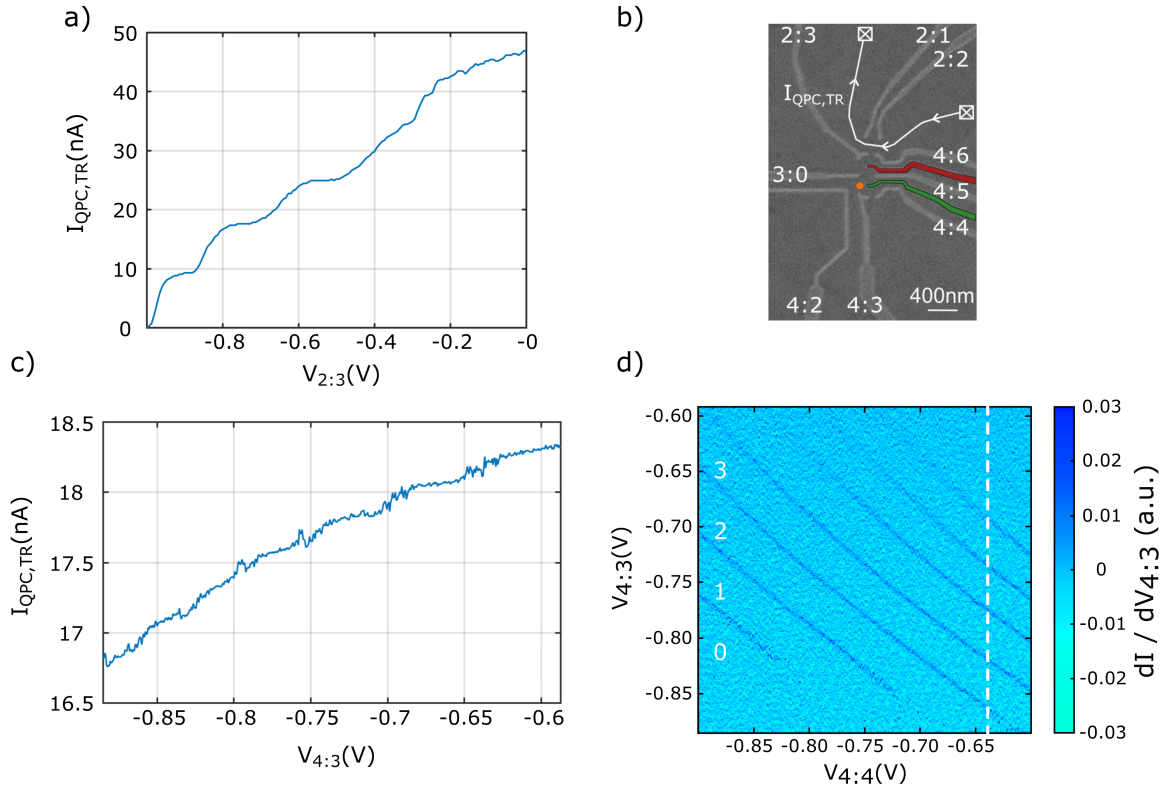


**Figure 1.4** – **a)** QPC current trace of a current pinch using the gates  $V_{2:2}$  and  $V_{2:3}$  showing first the depletion, i.e. the electrons below the gates are repelled, between  $V_{2:2} = 0$  and  $-0.5$  V. We can also see some conductance plateaus. The voltage bias applied between the two ohmic contacts is  $200 \mu\text{V}$ . **b)** Scanning electron micrograph of the right part of the sample with the gates labelled in white. The two coloured gates are RF gates discussed in 2.3.1 and later. The estimated quantum dot location is indicated by the orange dot. **c)** QPC current trace plotted as a function of  $V_{4:3}$ . Regularly spaced current steps are observable (e.g. at  $V_{4:3} = -0.8$  V), indicating the tunnelling of an electron out of the neighbouring quantum dot. This trace has been extracted from the same data set shown in the stability diagram of d) at the position indicated with the white dashed line. **d)** So called stability diagram corresponding to  $dI_{QPC,TR}/dV_{4:3}$ , the numerical derivative of the QPC current with respect to  $V_{4:3}$ . For this map,  $V_{4:3}$  was swept in the range  $-0.6$  to  $-0.9$  V while  $V_{4:4}$  was stepped in the same range. The light grey lines are charge degeneracy lines indicating a change of the number of trapped electron in the quantum dot. This number of charges is labelled in white.

### 1.3 Single quantum dot

To manipulate the charge trapped in the quantum dot, it is more convenient to have a map of its charge configurations, such map is the so called "charge stability diagram". It is obtained by sweeping a quantum dot gate voltage while stepping a second one. Here, the single quantum dot stability diagram is measured by sweeping the coupling to the reservoir with  $V_{4:3}$  and stepping the chemical potential with  $V_{4:4}$ . The aim of controlling these two gates is to induce the electron tunneling with the plunger gate and study the evolution of the coupling to the reservoir with the other one.

The resulting map is the Fig. 1.4d, corresponding to the derivative of the current with respect to the swept gate voltage as explained before. The light grey lines are charge degeneracy lines indicating a change of population of the nearby quantum dot. The sweep direction being toward more negative voltages, electrons are forced to leave the quantum dot explaining this positive change of current.

A map like this one provide different useful information about the quantum dot, one is the confirmation of the sample tuning as single quantum dot. Indeed, the charge degeneracy lines have the same slope, which means the same  $\alpha$ -factor for the entire charge map, so only one quantum dot is formed.

These lines can also be used to determine the quantum dot population. In the bottom left part of the diagram, where the gates are very negative, the area is empty of lines, meaning that no electron leaves the quantum dot, so it is empty. Then, for each crossed line an electron is added in the quantum dot as indicated in the stability diagram with the charge configuration labelled in white. It is therefore the absolute number of electrons trapped in the quantum dot which is deduced.

Finally, the coupling to the reservoir can also be estimated from the shape of these degeneracy lines. In the top part of the diagram, while moving toward less negative voltages of  $V_{4:3}$ , the lines are getting broader before disappearing. In this region, the width of the charge degeneracy line is not anymore defined by the electron temperature, but by the coupling to the electron reservoir. In other words, the coupling is larger than the thermal excitation. The electron temperature is about 100 mK equivalent to 1 GHz, therefore, this coupling to the reservoir is at least of the same order of magnitude.

On the contrary, in the bottom part of the diagram, when  $V_{4:3}$  is very negative, the lines disappear because of a low coupling to the reservoir. The stochasticity of the tunnelling events means that the tunnelling time is of the same order than the detection rate. If the same trace is recorded two times, the position of the change of population varies. For this map, the speed of the measurement was 1.4 ms per point, so the coupling to the electron reservoir is of the same order, estimated to  $\sim$  kHz.

Notice that for a shift of gate voltage about 30 mV, the coupling of the quantum dot to the electron reservoir goes from  $\sim$  GHz to  $\sim$  kHz showing the high range of tunability afforded by this type of system.

### 1.4 Double quantum dot

On the other side of the sample, and for another set of gate voltages, a double quantum dot can be tuned and studied with a similar stability diagram. On that side of the sample the charge detector is not a QPC

---

but a RF-QPC, this specificity will be explained in the next chapter (section 2.4.1). The only difference with a standard QPC is the signal which is a voltage labelled  $V_{RF}$ .

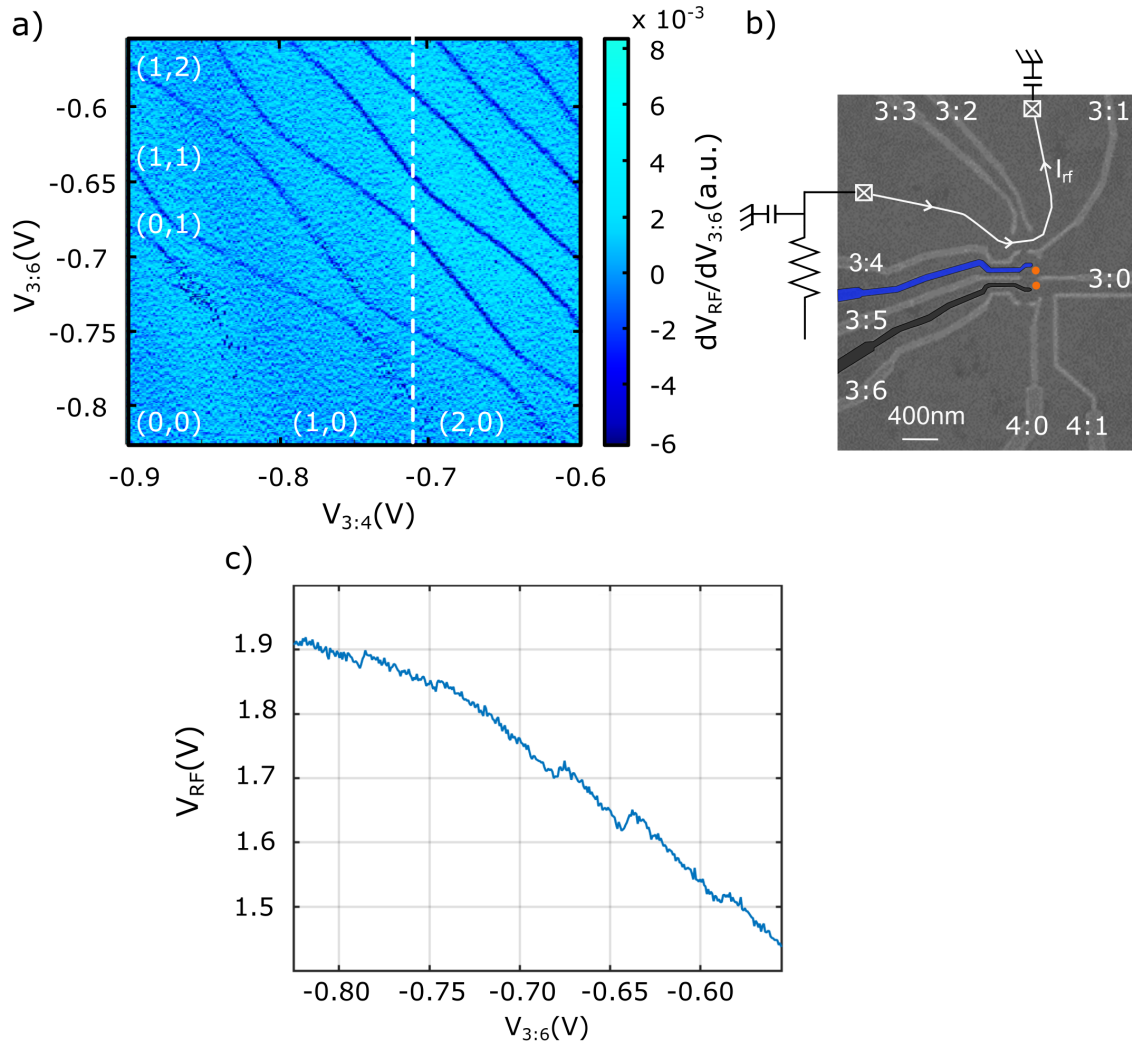


**Figure 1.5** – *a)* Double quantum dot stability diagram in which the derivative of the charge detector signal  $dV_{RF}/dV_{3:6}$  is plotted against  $V_{3:4}$  along the x axis, and  $V_{3:6}$ , along the y axis. The charge states are labelled in white, and the charge degeneracy lines in dark grey. The white dashed line indicates the position on the stability diagram of the curve presented in c). Compared to the single quantum dot case of Fig. 1.4, the opposite sign is only due to the use of a RF-QPC, presented in the section 2.4.1 of the next chapter. *b)* Scanning electron micrograph of the left part of the sample with the gates labelled in white, and the quantum dot the estimated positions represented by orange dots. *c)* Slice along the white dashed line of a) of the non derivated RF-QPC signal  $V_{RF}$ . The difference in voltage step sizes indicates from which quantum dot an electron is tunnelling in or out. For  $V_{3:6} = -0.75$  V the step in  $V_{RF}$  is approximately two times smaller than the one for  $V_{3:6} = -0.675$  V corresponding to the tunnelling of an electron in the quantum dot farthest and closest to the QPC, respectively.

Similarly to the single quantum dot, the stability diagram is obtained by sweeping a gate voltage while stepping another one, here the plunger of each quantum dot  $V_{3:6}$  and  $V_{3:4}$ , see Fig. 1.5. The resulting

map is presented in Fig. 1.5 where this time two sets of lines are visible, forming this characteristic honey comb lattice of a double quantum dot.

The most vertical line depends highly on the  $V_{3;4}$  voltage, so it corresponds to a quantum dot located close to this gate, the upper one (see Fig. 1.5b). The same reasoning is followed for the second set of degeneracy lines, the most horizontal ones, which are highly influenced by  $V_{3;6}$  so they are associated to the lower quantum dot. In the map, the tunneling of an electron between these two quantum dots is indicated by the anti-crossing of these charge degeneracy lines.

The charge states of the quantum dots are usually labelled as  $(n_U, n_L)$  with  $n_U(n_L)$  the number of electron in the upper (lower) quantum dot. Like for the single quantum dot, the bottom left corner is empty of lines which corresponds to the (0,0) charge state, crossing the adjacent vertical line leads to the (1,0) charge occupancy, crossing the horizontal one leads to the (1,1) one as depicted in Fig. 1.5a.

Here also the coupling to the reservoir can be evaluated from this map. For instance, the lines for  $n_U = 1$  and 2 which disappears because of a low coupling. Again, the stochastic events means a coupling to the reservoir about  $\sim$  kHz. Notice that the other quantum dot does not show the same behaviour, demonstrating the possibility to tune the two quantum dots independently and differently. A last comment about the additional coupling of this double quantum dot in comparison to the single one, the interdot tunnel coupling. It is visible by the shape of the anti-crossing of the charge degeneracy lines. The larger the anti-crossing, the larger the interdot tunnel coupling. One can see that it highly depends on the gate voltages configuration. From the bottom left to the top right corner, it is increasing up to a point where the double quantum dot becomes a single one, noticeable by the unique set of  $\alpha$  factor of these lines.

Finally, a word on the charge sensitivity of the RF-QPC for a tunneling event in or out of these quantum dot. Since they are not at the same distance of it, the capacitive coupling, so the charge sensitivity, are not the same. The upper quantum dot being closer, a tunneling event in that quantum dot induces a QPC current variation approximately two times larger than for the same event in the lower quantum dot. It can be seen in Fig. 1.5c by comparing the step of current for  $V_{3;6} = -0.65$  mV or  $V_{3;6} = -0.75$  mV. From the amplitude of the QPC step of current it is therefore possible to associate a tunneling event to a quantum dot.

## 1.5 Two electron spin states in quantum dots

As mentioned in the introduction, the aim of our experiment is to detect a single electron travelling in the edge channels of the Quantum Hall effect. The detection relies on the implementation of coherent oscillations of a two electron spin states in a double quantum dot, which in some conditions can be sensitive to the electrostatic environment. Before coming to the detail of the development of these oscillations, in the Chapter 3, these two electron spin states are introduced. For the single electron spin state in a quantum dot, the reader can refer to the following review [57].

### Two electrons in a single quantum dot

When two electrons are trapped in a quantum dot, they are indistinguishable and described by a wavefunction. Thus, this wavefunction composed by an orbital part and a spin part must be anti-symmetric

---

with respect to the exchange of particles. This point means that, if the orbital part is symmetric, the spin part is anti-symmetric, and vice versa. In a configuration with two orbitals, a ground  $|g\rangle$  and an excited state  $|e\rangle$ , four different spin states are possible with the symmetrical orbital,  $|gg\rangle$ , being the singlet:

$$|S\rangle = \frac{|\uparrow\downarrow\rangle - |\downarrow\uparrow\rangle}{\sqrt{2}} \quad (S = 0) \quad (1.5)$$

the anti-symmetric orbitals  $\frac{|eg\rangle - |ge\rangle}{\sqrt{2}}$  states are the triplet states  $|T\rangle$ :

$$|T_+\rangle = |\uparrow\uparrow\rangle \quad (S = +1) \quad (1.6)$$

$$|T_0\rangle = \frac{|\uparrow\downarrow\rangle + |\downarrow\uparrow\rangle}{\sqrt{2}} \quad (S = 0) \quad (1.7)$$

$$|T_-\rangle = |\downarrow\downarrow\rangle \quad (S = -1) \quad (1.8)$$

At zero magnetic field,  $|S\rangle$  is the ground state and the three triplet states  $|T_{+,-,0}\rangle$  are degenerated in energy. Due to their non zero spin, the states  $|T_+\rangle$  and  $|T_-\rangle$  are linearly dependent on the magnetic field due to the Zeeman effect. The difference in energy between  $|S\rangle$  and  $|T_0\rangle$  corresponds to the orbital energy  $\Delta E$ . This energy arises from the Pauli exclusion principle which avoids the charge configuration with more than two electrons per orbital when the spin degeneracy is considered. Typically this energy is:

$$\Delta E = \frac{\hbar^2}{2m^*} \left( \frac{\pi}{L} \right)^2 \quad (1.9)$$

with  $m^* = 0.067 m_e$  the effective mass of an electron in GaAs,  $L \sim 100$  nm the typical size of a quantum dot, the orbital energy is of the order of  $0.5$  meV  $\approx 5$  K.

### Two electrons in a double quantum dot

This description stands for two electrons confined in a single quantum dot, with a tunnel coupled double quantum dot, the discussion is more complex because different charge configurations are possible. Indeed, by varying the detuning energy  $\varepsilon$ , which is equal to the difference between the two potential minima of the quantum dots, the charge configuration of the double quantum dot can be (2,0), (1,1) or (0,2). Hence, depending on the detuning, the spin states are varying and the energy diagram presented in Fig. 1.6, a sketch of a calculated one, is commonly used to summarise the situation. Another quantity is introduced, the exchange energy  $J(\varepsilon)$ , corresponding to the energy between the spin states  $|S\rangle$  and  $|T_0\rangle$ .

As it can be noticed in the energy diagram, the two charge transitions (0,2)-(1,1) or (1,1)-(2,0) are symmetric. For the present discussion we will focus on the (1,1)-(2,0) one, and we set  $\varepsilon = 0$  at the transition between the two charge configurations. Then, there is three different regimes to present one after the other, first the (2,0) charge state, the transition from (2,0) to (1,1) and finally the (1,1) charge configuration.

When  $\varepsilon \gg 0$ , the double quantum dot is in the (2,0) charge configuration and the situation can be assimilated to the one presented before, with the same spin states and energy splitting, the states are labelled  $S(2,0)$  and  $T_{+,-,0}(2,0)$ . Here the exchange energy can be maximal and equal to the orbital energy  $\Delta E$ .

At the transition between the two charge configurations, close to  $\varepsilon = 0$ , the tunnel coupling  $t_c$  has to be considered such as the change of charge occupancy. The singlet and triplets are progressively replaced by the  $S(1,1)$  and  $T_{+,-,0}(1,1)$ . In the same time, the orbital part of the spin states is also modified, leading to the energy splitting between the  $|S\rangle$  and  $|T_0\rangle$  spin states, the exchange energy  $J(\varepsilon)$ , which is decreasing while  $\varepsilon$  is getting negative, see Fig. 1.6.

Second, the tunnel coupling  $t_c$  induces a hybridisation of the two singlet states leading to the appearance of an anti-crossing also visible in the energy diagram Fig. 1.6. However, the tunneling process being spin conservative, this anti-crossing is not possible between the singlet and the triplet spin states. The triplets spin states being higher in energy, their anti-crossing appears at higher energy too, so for larger detuning value in comparison to the singlet spin states. Hence, locally and for  $\varepsilon \sim 0$ , the lower energy state is  $S(2,0)$  for the singlet  $|S\rangle$  while it is  $T_{+,-,0}(1,1)$  for the triplet  $|T\rangle$ . The Pauli spin blockade based spin readout relies on this difference of preferential charge configuration, explained more precisely in the third chapter section 3.3.1.

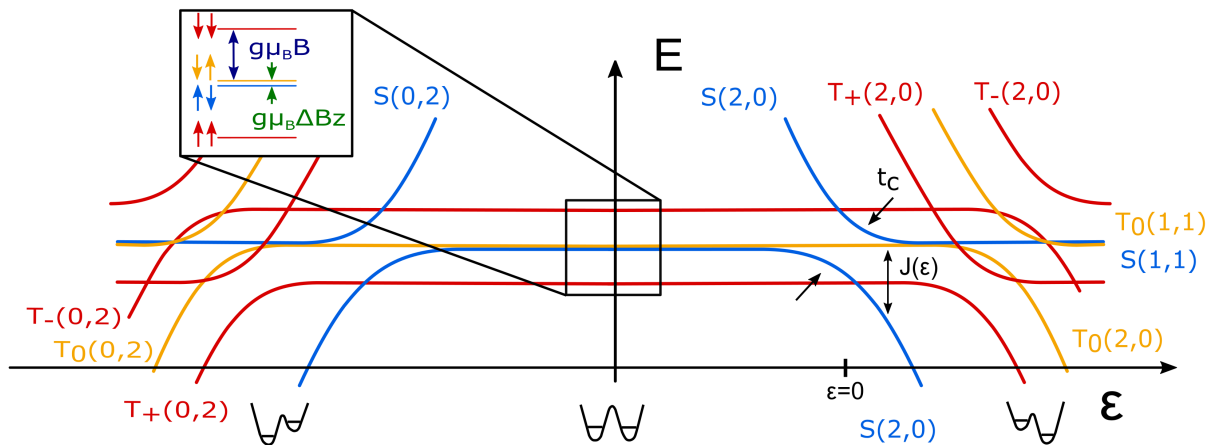


**Figure 1.6** – Energy diagram of the two electron spin states in a double quantum dot as a function of the detuning  $\varepsilon$ . The different characteristic energies of the system are indicated. In particular, the exchange energy  $J(\varepsilon)$  is the energy splitting between  $|S\rangle$  and  $|T_0\rangle$ , and  $t_c$  is the tunnel coupling between the quantum dots. The Zeeman energies are also indicated, the one due to the external magnetic field  $B$  which lifts the energy degeneracy of  $|\uparrow\uparrow\rangle$  and  $|\downarrow\downarrow\rangle$ , and the one arising from the difference of nuclear spin polarisation between the two quantum dots  $\Delta B_z$  lifting the degeneracy between the  $|\downarrow\uparrow\rangle$  and  $|\uparrow\uparrow\rangle$  spin states.

Finally, the last regime is the one deeply in the  $(1,1)$  charge configuration. There, the spin states are not the singlet and triplets anymore but  $|\uparrow\downarrow\rangle$ ,  $|\downarrow\uparrow\rangle$ ,  $|\uparrow\uparrow\rangle$  and  $|\downarrow\downarrow\rangle$  since the two electrons can be regarded as independent. The  $|\uparrow\uparrow\rangle$  and  $|\downarrow\downarrow\rangle$  spin states can be separated in energy from the two other ones by the Zeeman energy  $E_Z = g\mu_B B$ , with  $g$  the Landé g-factor of GaAs equal to  $-0.44$ ,  $\mu_B$  the Bohr magneton and  $B$  the applied magnetic field. In bulk GaAs, the resulting energy splitting is about  $25 \mu\text{eV T}^{-1}$ . One could expect that the two other spin states are degenerated in energy, but they are not. Indeed, the trapped electrons are not isolated from the environment and they are interacting with the nuclear spins of the

heterostructure via the hyperfine interaction developed in the section 1.6.2. The difference in nuclear spin polarisation between the two quantum dots can be regarded as an effective magnetic field labelled  $\Delta B_z$  leading to a Zeeman splitting between  $|\uparrow\downarrow\rangle$  and  $|\downarrow\uparrow\rangle$  which is typically of the order of  $5 \text{ mT} \sim 100 \text{ neV}$ .

The singlet-triplet spin qubit detector for the single electron detection experiment is obtained by the manipulation of the spin state between the two spin basis  $|\uparrow\downarrow\rangle$ ,  $|\downarrow\uparrow\rangle$  and  $|S\rangle$ ,  $|T_0\rangle$  as presented in the third chapter. By displacing the spin state from a spin basis to the other, two type of coherent spin oscillations can be implemented as first demonstrated by Foletti *et al.* [58] in 2009. Among the two, one is of particular interest for our purpose, the coherent exchange oscillations. Demonstrated in 2005 by Petta *et al.* [39] these oscillations have their frequency defined by the exchange energy  $J(\varepsilon)$ , depending on the detuning  $\varepsilon$  which can be modified by the travelling charge to detect.

## 1.6 Couplings to the environment

We just saw that the quantum system is not fully decoupled from the environment. In our system two interactions can be encountered, the spin orbit and the hyperfine interactions. These interactions being mainly uncontrolled they can lead to the loss of the stored information in the qubit by relaxation of the spin state, or dephasing.

The spin orbit interaction is the fact that a moving charge in an electric field experience an internal magnetic field, consequently the spin of the electron is coupled to its momentum. In our experiment, the qubit detector sensitivity is determined by the coherence properties and the fidelity of the spin readout is limited by the spin relaxation [35, 59, 60]. The spin orbit does not affect the coherence in our system. It might have an impact on the spin readout, but the spin relaxation is dominated by the hyperfine interaction. Therefore, this interaction is not relevant in our experiment.

The two concepts of spin relaxation and dephasing are presented in this section. The hyperfine interaction will follow with in particular it influences in the spin dephasing.

### 1.6.1 Relaxation and dephasing of the spin state

To understand these interactions with the environment and how they can lead to the loss of the spin information, the Bloch sphere is commonly used to represent this situation of a two level quantum system modelled as:

$$|\Psi\rangle = \alpha |0\rangle + \beta |1\rangle \quad (1.10)$$

where  $|0\rangle$  corresponds to the ground state and  $|1\rangle$  is the excited one,  $\alpha$  and  $\beta$  are complex numbers satisfying the normalisation criterion  $|\alpha|^2 + |\beta|^2 = 1$ . From this relation, the spin information  $\Psi$  can be regarded as a point of a sphere (Fig. 1.7a), where the pole are the ground and excited state, with:

$$|\Psi\rangle = \cos(\theta/2) |1\rangle + \sin(\theta/2)e^{i\phi} |0\rangle \quad (1.11)$$

The action of the environment can be illustrated by modifications of the location of this point on the

sphere, leading to two phenomenons, the spin relaxation and the dephasing.

The spin relaxation corresponds to the tendency of any spin state to relax toward its ground state, sketched in Fig. 1.7b. This process involves a release of the excess energy to the environment, dissipated toward the phonon bath [61] for electron spin in GaAs. In our system, the main source of relaxation has been identified as the hyperfine interaction [35, 59, 60] which limits the spin relaxation time  $T_1$  to typically  $\sim 30 \mu\text{s}$ . This point will be further explained in the third chapter section 3.3. Experimentally we employ the Pauli spin blockade as spin readout technique which is limited by  $T_1$ . This time being shorter than the standard QPC detection bandwidth  $\sim 10 \text{ kHz}$ , we had to use a RF-QPC having a larger detection bandwidth to be able to perform the single shot spin readout. The RF-QPC is explained in the next chapter section 2.4.

The second process, the spin dephasing is associated to the loss of spin phase information. This process occurs when a same manipulation is performed many times but the experimental conditions are not precisely the same. For instance, if the oscillating frequency of the spin state is not constant in time, by repeating the same experiment many times, the accumulated phase varies and is distributed over the different attempts. In a Bloch sphere it can be seen as staying at the same latitude of the Bloch sphere, there is no exchange of energy, but the phase is distributed over the plane as sketched in Fig. 1.7c. The phase information is lost in a timescale called dephasing time  $T_2^*$ . In our system, depending on the performed manipulation, this process of dephasing can be related to the hyperfine interaction associated to a timescale about  $T_2^* \sim 10 \text{ ns}$ .

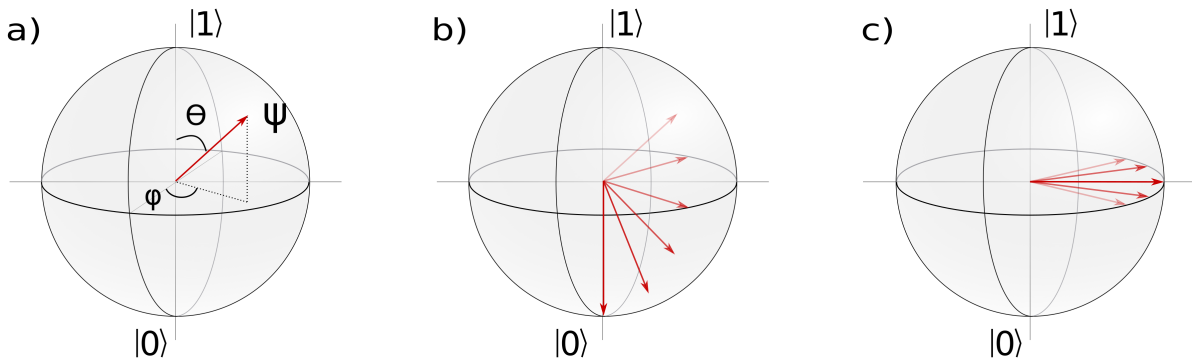


**Figure 1.7** – *a)* Representation of the quantum state  $\Psi$  in a Bloch sphere, with  $|1\rangle$  the excited and  $|0\rangle$  the ground state, with the different angles defines in the expression 1.11. *b)* sketch of the relaxation process, with the initial  $\Psi$  state moving toward the ground state  $|0\rangle$ . *c)* Sketch of the dephasing process, with different speed of rotation leading to this spreading of the spin phase.

## 1.6.2 Hyperfine interactions

The hyperfine interaction corresponds to the interaction between the spin of the manipulated electrons and the one of its host nuclei. In our system, the electrons are embedded in a crystal of Al, Ga and As atoms, all having a non zero spin ( $3/2$ ). Thus, a trapped electron interacts with a large number of nuclei  $N \sim 10^6$ , which following [57] can be described with the Hamiltonian:

$$H_{HF} = \sum_k \vec{S} \vec{I}_k A_k \quad (1.12)$$

where  $\vec{I}_k$  and  $\vec{S}$  are the nuclei and electron spin operator, with  $A_k$  the hyperfine coupling constant between the nuclear and electron spins. In our structure,  $A_k$  depends on the nuclei and the overlapping with the electron wavefunction, but it is typically of the order of  $\sim 90 \mu\text{eV}$  [62].

This situation can be simplified, by treating the ensemble of the nuclear spin as an apparent magnetic field  $\vec{B}_N$ , and the interaction electron nuclear spin can be rewritten as:

$$H_{HF} = g\mu_B \vec{B}_N \vec{S} \quad (1.13)$$

here the Overhauser field is introduced,  $\vec{B}_N = \sum_k \vec{I}_k A_k / g\mu_B$ . For a full polarisation of the nuclear spin, the resulting  $B_N \approx 5 \text{ T}$  [62], independent to the number of nuclei. However, in experimental conditions the spin polarisation fluctuates because of thermal activation. Consequently, the Overhauser field is fluctuating around 0 T with a Gaussian distribution in all three directions with standard deviation  $\sigma = B_N / \sqrt{N}$ . Considering this diffusion process, the actual polarisation is about  $\Delta B_{nuc} \approx 5 \text{ mT}$ , already measured in different systems and all in the same range of 1 – 10 mT [59, 63, 64], with fluctuations in a timescale of the order of  $\sim 1 \text{ s}$  [65] for the z direction and faster in the transverse direction 10 – 100  $\mu\text{s}$  [60, 66].

This diffusion process is at the origin of the dephasing, and can be understood as follow: under the application of an external magnetic field, the electron spin precesses around the field axis at a Larmor frequency  $\omega_e = \gamma_e B_{ext}$ . If the nuclear field is also taken into account, the resulting magnetic field is  $\vec{B} = \vec{B}_N + \vec{B}_{ext}$ . Then, the frequency of the electron precession is defined by a constant element, the external field  $B_{ext}$ , and  $B_N$  which is fluctuating in time. This fluctuations being rather slow compare to the electron spin manipulation, the effective magnetic field  $B$  is fixed during an experiment but not from one to the other. Hence, by repeating the same spin manipulation, the accumulated phase will not be the same. Averaging over many attempts results in a decay of coherent evolution, to the dephasing process. Considering the Gaussian distribution of the nuclear magnetic fields, the decay has an envelope with a Gaussian shape defined as  $\exp\left(-\left(\frac{t}{T_2^*}\right)^2\right)$  [67], where:

$$T_2^* = \frac{\hbar\sqrt{2}}{g\mu_B\sqrt{\langle(\Delta B_N^z)^2\rangle}} \quad (1.14)$$

The spread of the distribution of nuclear magnetic fields  $\langle(\Delta B_N^z)^2\rangle \propto 1/\sqrt{N}$ , so it depends on the size the quantum dot. Typically,  $\Delta B_N^z \approx 5 \text{ mT}$  so the dephasing time can be evaluated to  $T_2^* \sim 10 \text{ ns}$ .

The nuclear polarisation diffusion being a rather slow process, it can be compensated experimentally, recently, by associating Dynamical Nuclear Polarisation (DNP) [58, 68] and a feedback loop, Bluhm *et al.* succeed to extend  $T_2^*$  by a factor of 10 [41].

## 1.7 Quantum Hall effect

The charge manipulations and electron spin states being presented, a last key element of the experiment has to be introduced, the Quantum Hall effect.

Before coming to the quantum effect, the classical one is briefly review. It is the accumulation of charges at the border of a metallic sample. This phenomenon arises from the curvature of their trajectories as a response to an applied perpendicular magnetic field. The voltage difference between the borders of the sample is  $V_H = R_H \frac{IB}{a} = \frac{IB}{nea}$ , with  $I$  the current flowing in the sample,  $B$  the perpendicular magnetic field,  $n$  the charge carrier density,  $e$  the charge of a carrier and  $a$  the sample thickness.

The Quantum Hall effect can be seen as an extension of the classical Hall effect. In 1980 Von Klitzing *et al.* [9] discovered that in a 2DEG, the conductivity is quantised with the current flowing on the edges of the sample while the bulk is insulating. This effect can be observed by measuring the transverse and longitudinal voltage response to a current  $I$  with an applied magnetic field  $B$  perpendicular to the plan. Performing such measurement exhibit a vanishing longitudinal resistance  $R_{xx} = V_{xx}/I$  for certain value of magnetic field while the Hall conductance is quantised  $\sigma_{xy} = \nu \frac{e^2}{h}$ , with  $\nu$  the filling factor (a dimensionless density). Notice the universality of this quantisation which is independent of the material, the purity of the sample, etc...

To understand and describe this phenomenon, the following approach can be used [69, 70]. Considering a 2DEG with an area  $S = L_x L_y$  in an out of plane magnetic field  $\vec{B}_z$ . The Hamiltonian of an electron in this system is:

$$H = \frac{1}{2m} (\vec{p} + e\vec{A})^2 \quad (1.15)$$

with  $\vec{p}$  the electron momentum,  $e$  the charge of an electron,  $c$  the celerity and  $\vec{A}$  the vector potential. Using the Landau gauge:

$$\vec{A} = \begin{pmatrix} 0 \\ Bx \\ 0 \end{pmatrix} \quad (1.16)$$

and the cyclotron frequency:

$$\omega_c = \frac{eB}{m^*} \quad (1.17)$$

with the free propagation along the  $y$  axis, the Hamiltonian is can be rewritten as:

$$H = \frac{1}{2m} p_x^2 + \frac{1}{2} m \omega_c^2 \left( x + \frac{\hbar k_y}{m \omega_c} \right)^2 \quad (1.18)$$

which is equivalent to a harmonic oscillator, with the energy of the system being:

$$E_N = \hbar \omega_c \left( N + \frac{1}{2} \right), N \in \mathbb{N} \quad (1.19)$$

the levels of the oscillator are the so called Landau levels (LLs). Since the sample has a finite size, their energy should increase on the edges. Furthermore,  $\omega_c$  depends on the magnetic field and so do the LLs. Consequently, depending on the magnetic field, the bulk can be conductive when  $E_N = E_F$ , or

insulating when  $E_N \neq E_F$ . In the last situation, the current is only carried by the LLs crossing the Fermi energy, also called the edge channels, as represented in Fig. 1.8.

A way to understand these edge channels is the following: under the application of a magnetic field, the electrons have a circular motion around it. Hence, in the middle of the sample the electrons can complete this circular motion leading to an insulating behaviour of the bulk. However, on the edges of the sample, at the conducting/insulating interface, such trajectory cannot be completed, and the electrons can be seen as bouncing on the interface resulting in a current flowing only on the edges, in these edge channels. The propagation direction being set by the magnetic field orientation, the ECs are chiral and the backscattering is not possible.

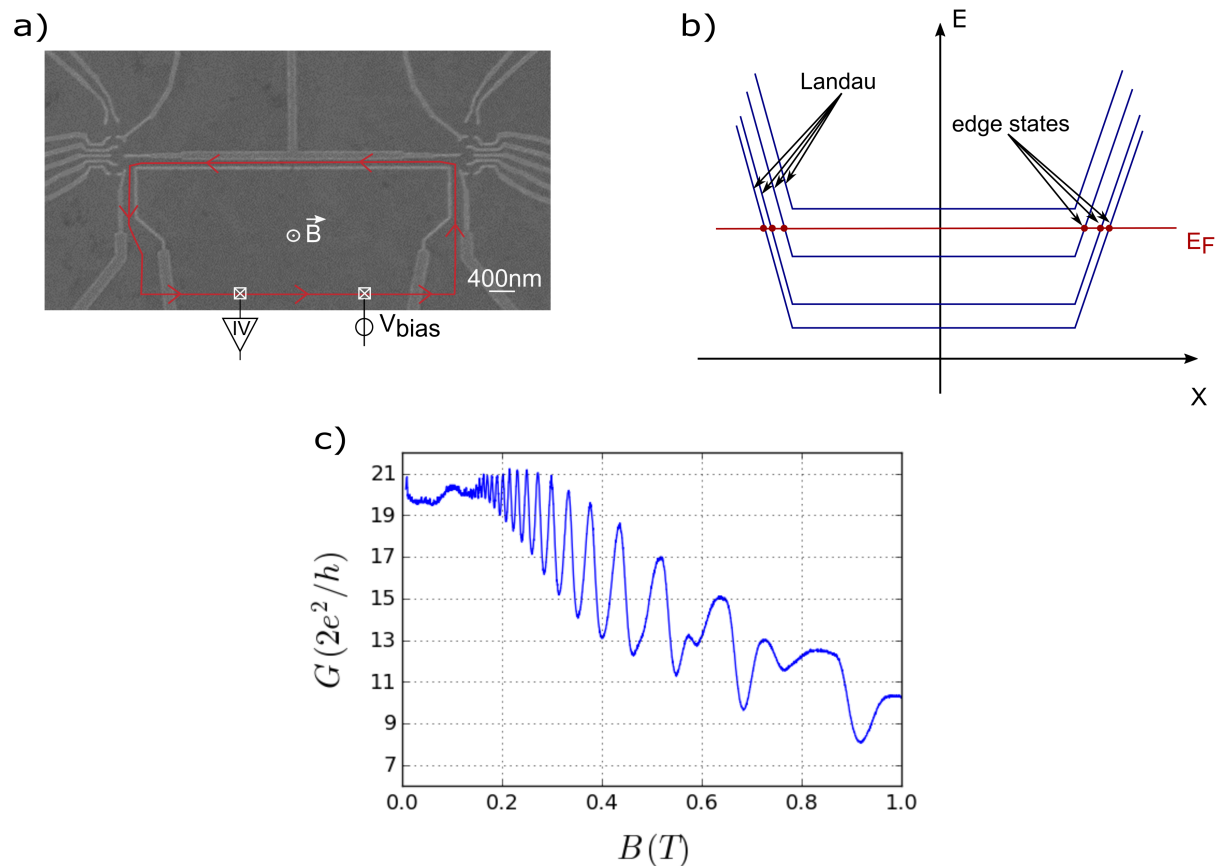


**Figure 1.8** – **a)** Scanning electron micrograph of the sample, with the two ohmic contacts used to record the Shubnikov de Haas oscillations represented by white crossed squares. The current flowing in the sample is recorded from an ohmic contact while a bias of  $100 \mu\text{V}$  is applied to the second one. Meanwhile, the out-of-plane magnetic field  $B$  is swept between 0 and 1 T. In red are sketched the edge channels. **b)** Sketch of the Landau levels where the magnetic field is set such that the bulk of the sample is insulating and the current conduction takes place only where these levels cross the Fermi energy  $E_F$  creating edge channels. **c)** Shubnikov de Haas oscillations of the conductance  $G$  as a function of the magnetic field  $B$ . At low magnetic field the Landau levels are not differentiated. Starting from 0.6 mT the spin splitting of the edge states appears.

A standard characterisation of the Quantum Hall effect consists in recording the current flowing in

the 2DEG from an ohmic contact, a constant DC bias  $V_{\text{bias}}$  being applied to another one, while sweeping the perpendicular magnetic field. Performing this measurement is a way to observe the Shubnikov de Haas oscillations, a way to probe the LLs. The energy separation between these levels being dependent on the magnetic field, by sweeping it, they can be aligned or not with the Fermi energy  $E_F$ . When the bulk is conductive the measured current is minimal, and it is maximal when it is only carried by the ECs. This oscillating behaviour, presented in Fig. 1.8, is periodic in  $1/B$  and is commonly used to determine the electron density  $n_e$  since the spacing between two extrema scale as  $\nu = \frac{n_e h}{eB}$ . From this experiment we extracted the electron density of our sample which is about  $n_e = 1.2 \times 10^{11} \text{ cm}^{-2}$ .

In the experimental trace, two elements can be noticed, the first one being the non vanishing current between two LLs meaning that the energy splitting between two levels is smaller than the thermal excitation. Secondly, starting from  $B = 600 \text{ mT}$  the peaks start to be split in two, coming from the lifting of the spin degeneracy of the ECs.

For our purpose, the magnetic field has to be set such that the current is only carried in the ECs, for a maximum of conductance of Fig. 1.8, and ideally we would like to work at  $\nu = 1$ . However, two constraints prevent us to be in such regime. The first one is the energy splitting between the spin states  $|S\rangle$  and  $|T_0\rangle$  which is decreasing with the magnetic field. Then, to be able to define the singlet-triplet spin qubit, so the qubit detector, the magnetic field has to be limited to approximately  $\sim 1 \text{ T}$  [61]. The second constraint is specific to our experiment and comes from the charge sensitivity of the used RF-QPC which, as developed in the next chapter, was decreasing with the magnetic field. The charge readout being extremely difficult starting from  $B \sim 500 \text{ mT}$ , it limits us to work at  $B = 430 \text{ mT}$  so at  $\nu = 10$ . Therefore, the single travelling electron to detect will not be necessarily in the EC the closest to the qubit detector but in any of them. This distribution will complicate its detection because, the travelling charge interacts with the qubit detector by capacitive coupling which decrease with the distance between them. Thus, depending on its position in the ECs, its influence, impact on the qubit detector will not be the same.



---

## Experimental setup

---

## Introduction

To succeed the challenge of detecting single shot an electron travelling in the ECs of the QHE, different technical constraints should be overcome.

One is to be able to initialise perfectly the electron spin state of the qubit detector. As presented in the previous chapter section 1.5, for two electrons in a double quantum dot, the singlet ground spin state is separated from the excited triplet spin states by an energy of  $500 \mu\text{eV}$  equivalent to a temperature of 5 K. Thus, an operating temperature well below such 5 K, routinely achieved by dilution refrigerators, is necessary. Furthermore, a large number of both DC and RF connections going from room temperature to the sample are necessary to define, control and read out the quantum dot state. However, if these connections are not properly thermally anchored along the different stages of the fridge, a substantial sample overheating might occur.

To be able to perform fully the detection of the travelling electron single shot, the outcome of the spin qubit detector has to be readout single shot too. This means being able to perform single shot an electron spin readout, which is not possible with a standard QPC (c.f. section 1.6 previous chapter). An improved version of it, the RF-QPC, having a larger detection bandwidth is required. This point and the RF setup used for it will be detailed in the last part of this chapter. Before, the home-made dilution refrigerator will be presented, with the methods and electronic setup ensuring the operating temperature and DC manipulations.

## 2.1 Cryogenics

### 2.1.1 Dilution refrigerator

The basic principle of a dilution refrigerator is hereafter briefly reviewed, however, for a more detailed description the reader can refer to [71].

Below 0.87 K, a mixture of  $^3\text{He}/^4\text{He}$ , having a  $^3\text{He}$  concentration  $> 6\%$ , separates into two phases, one rich in  $^3\text{He}$ , another rich in  $^4\text{He}$ . The dilution of  $^3\text{He}$  into  $^4\text{He}$  being an endothermic process, the continuous refrigeration is obtained by inducing a continuous flow of a pre-cooled  $^3\text{He}$  phase into a  $^4\text{He}$  one.

To get this continuous flow, the dilution unit is separated in different stages (see figure 2.1).

- Firstly, the  $^3\text{He}$  rich phase is cooled from room temperature to 4 K by the He bath surrounding the Isolating Vacuum Chamber (IVC) in which is located the dilution unit. Next, the incoming  $^3\text{He}$  rich phase is cooled to 1.2 K by the 1K-pot. To reach that temperature, the 1K-pot, which is a reservoir of  $L^4\text{He}$ , is continuously filled with  $L^4\text{He}$ , and pumped to decrease the temperature from 4.2K to 1.2K.
  - The continuous and discrete exchangers cool down the incoming  $^3\text{He}$  with the outgoing one. The cold plate separating these two stages is typically at 65 mK.
  - Finally, the flow reaches the mixing chamber where the dilution process takes place. The  $^3\text{He}$  phase is evaporated and pumped in the still, closing the loop.
-

The base temperature of the used refrigerator was about 40 mK at the mixing chamber stage and 60 mK on the sample holder. Radiation from 4 K and imperfect thermal anchoring can explain this difference.

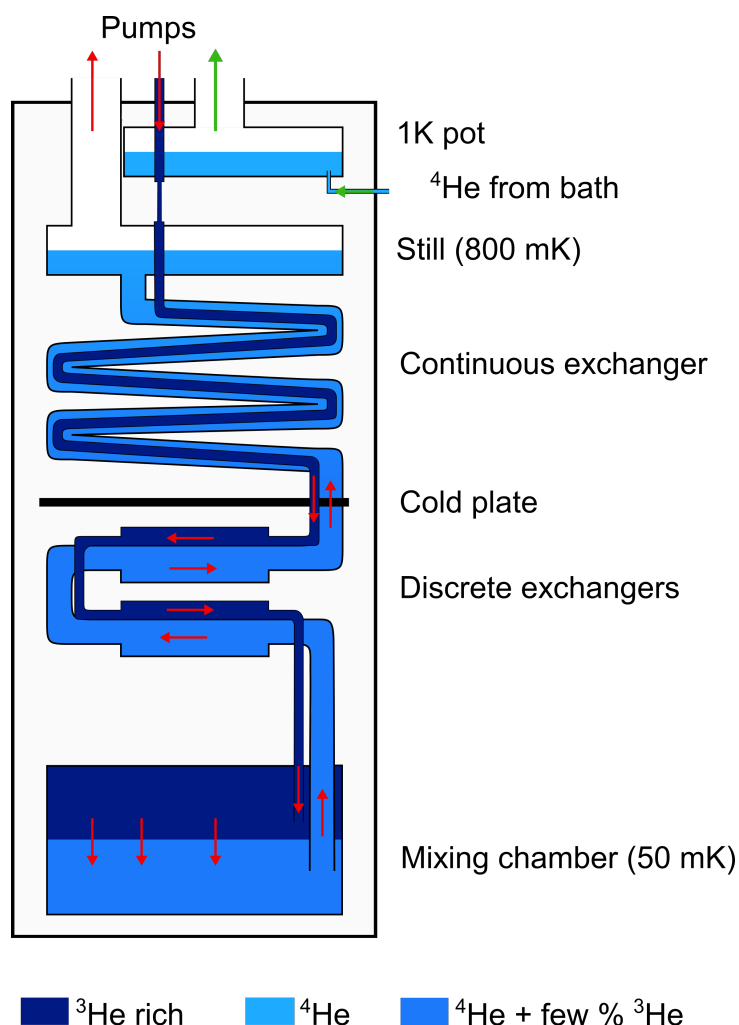


**Figure 2.1** – Sketch of the dilution refrigerator used for this work. The incoming  $^3\text{He}$ , pre-cooled to 4 K by the He bath, gets into the 1K-pot which cools it down to 1.2 K. The  $^3\text{He}$  phase is further cooled down by thermal exchange with the outgoing phase in the still, continuous and discrete exchangers before reaching the mixing chamber. There, the dilution process takes place. The sketch represents the inner part of the isolating vacuum chamber (IVC) that thermally decouples the dilution unit from the  $^4\text{He}$  bath by a secondary vacuum.

### 2.1.2 DC and RF connections

Several DC and RF connections, either for slow or fast manipulations, connect the room temperature instruments to the sample. Since each type of connection has different requirements, different wires and materials are used. Therefore, depending on the type of wire, the heat is brought to the sample via different mechanisms (thermal conduction or radiation from room temperature). Then, a careful choice of the materials and thermal anchoring are required to ensure a low electronic temperature and limiting the electrical noise.

### 2.1.2.1 DC connections

The DC connections are used for the manipulations from constant voltages to the microsecond pulses. In term of wiring, two types of lines are used, coaxial lines and Constantan wires.

First, concerning the coaxial lines, they are used because of the absence of crosstalk between them and the possibility to perform microsecond pulses.

From room temperature to the entrance of the IVC, we employ copper (Cu) beryllium (Be) coaxial lines. The inner conductor of CuBe is a rather good electrical conductor but a poor thermal one, while the outer conductor made of Stainless Steel is a poor electrical and thermal conductor.

From here and down to the mixing chamber they are replaced by Thermocoax<sup>TM</sup> wires which filter the high frequency noise. The electrical connection between the two, CuBe coaxial lines to Thermocoax<sup>TM</sup>, is performed in a copper gold plated support as presented in Fig. 2.2 hosting smallest boxes. Each small box hosts 4 connections and is filled with black Stycast<sup>R</sup> to maximise thermal anchoring. They are closed with a copper gold plated top for a full shielding. By using such small boxes, the cross talk is limited and the shielding to external radiations is ensured. The thermocoax<sup>TM</sup> coaxial lines are composed by an inner conductor of Nickel/Chrome, the outer conductor of stainless steel and in between, the dielectric is magnesium oxide. Such coaxial lines exhibit a low-pass filter behaviour with a cutoff frequency about  $\sim 100$  MHz [72]. Since, the longer the wire, the higher its thermal resistance, the wires length is increased up to two meters. For spacing issue they are split in two sets and rolled around a plastic tube. Two rounds are separated by nylon string to avoid thermal connection and maintain everything tightened, see 2.2.

The last part of the wiring is performed with copper (Cu) silver (Ag) coaxial lines to optimise the thermal connections between the mixing chamber and the sample. Here again the electrical connection between the two type of wires is done within a copper gold plated box with mini SMP connectors. Actually, because of their size, the SMP connectors are a limitation to the use of these coaxial lines. Indeed, besides the experimental difficulties to do all the connections and thermal anchoring, there is a spacing issue. Each coaxial line needs an individual connector which is 3.5 mm diameter. Since our experiment requires a large number of lines, there is not enough space to do these connections for the 42 lines of the fridge. Instead, Constantan wires are used, with the Fig. 2.3 which summarises these connections and thermal anchoring.

The Constantan wires benefit from the fact that 30 of them can be inserted into a CuNi capillary of 3 mm diameter. These wires are an alloy of Copper/Nickel/Manganese with a ratio about 58%/40%/2%, inserted into the capillary and filled with Ecosorb<sup>TM</sup> which is a compound containing magnetic particles which act as a microwave absorber. The aim of this assembly is to filter the high frequency signals which could propagate from room temperature with a cutoff frequency about  $\sim 10$  MHz.

The capillary is thermally anchored at each stage thanks to a copper wire rolled and soldered around it (see Fig. 2.2). The wires are then thermally anchored at 800 mK with a male/female connector embedded in copper box filled with black Stycast<sup>R</sup>, and again on the mixing chamber stage thanks to copper strip lines in a gold plated copper box. The different copper boxes are plated to avoid heating from the 4K radiations present in the IVC and avoids its oxidation. From this last box to the cold finger, copper wires

in a CuNi capillary are employed to maximise the thermal connection.

The advantage of using a capillary is the full shielding from room temperature down to the sample. On the other hand, the drawback of such method is the large density of wires leading to important cross talk between them, preventing us to use them for  $\mu s$  or fastest manipulations.

The detail of the connections and thermal anchoring are shown in the figure 2.3.

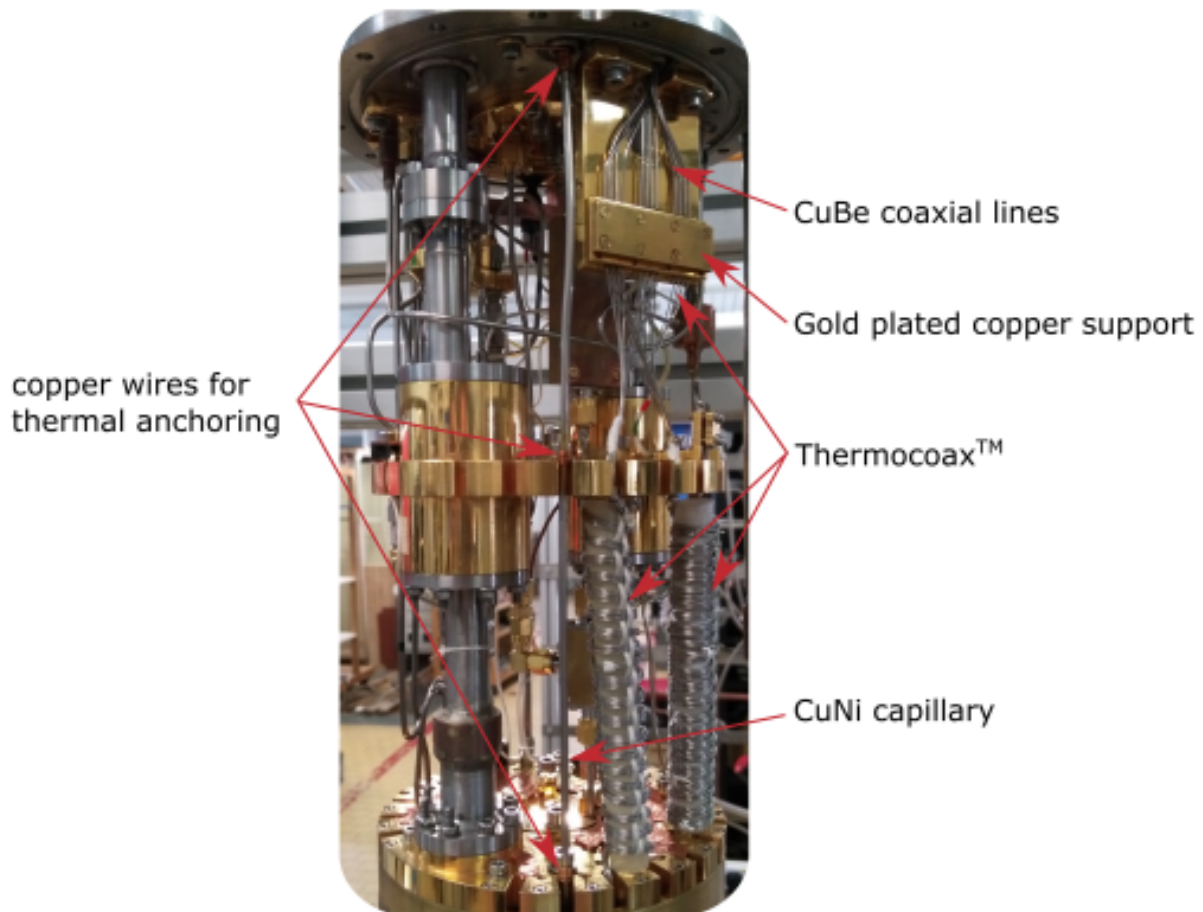


**Figure 2.2** – Picture of the IVC showing the DC wiring from the entrance of the IVC down to the cold plate stage. The different stages of thermal anchoring are indicated with the red arrows.

### 2.1.2.2 RF connections

As presented in the previous chapter subsection 1.6.2 the spin dephasing time is about  $T_2^* \sim 10$  ns. Then, to be able to manipulate coherently the spin, 1 ns voltage pulses are required meaning a manipulation bandwidth  $\sim$  GHz. Such bandwidth are reachable by using RF lines, but since they are designed and adapted for high frequency signals, the previous techniques of thermal anchoring and filtering cannot be used anymore. The inner conductor is particularly difficult to thermal anchored. Since it is decoupled to the outer material, it cannot be done by thermal conduction from the outside through the outer connector. A standard way to do it is to use cryogenic attenuators (from XMA Corp.) inserted at different stages.

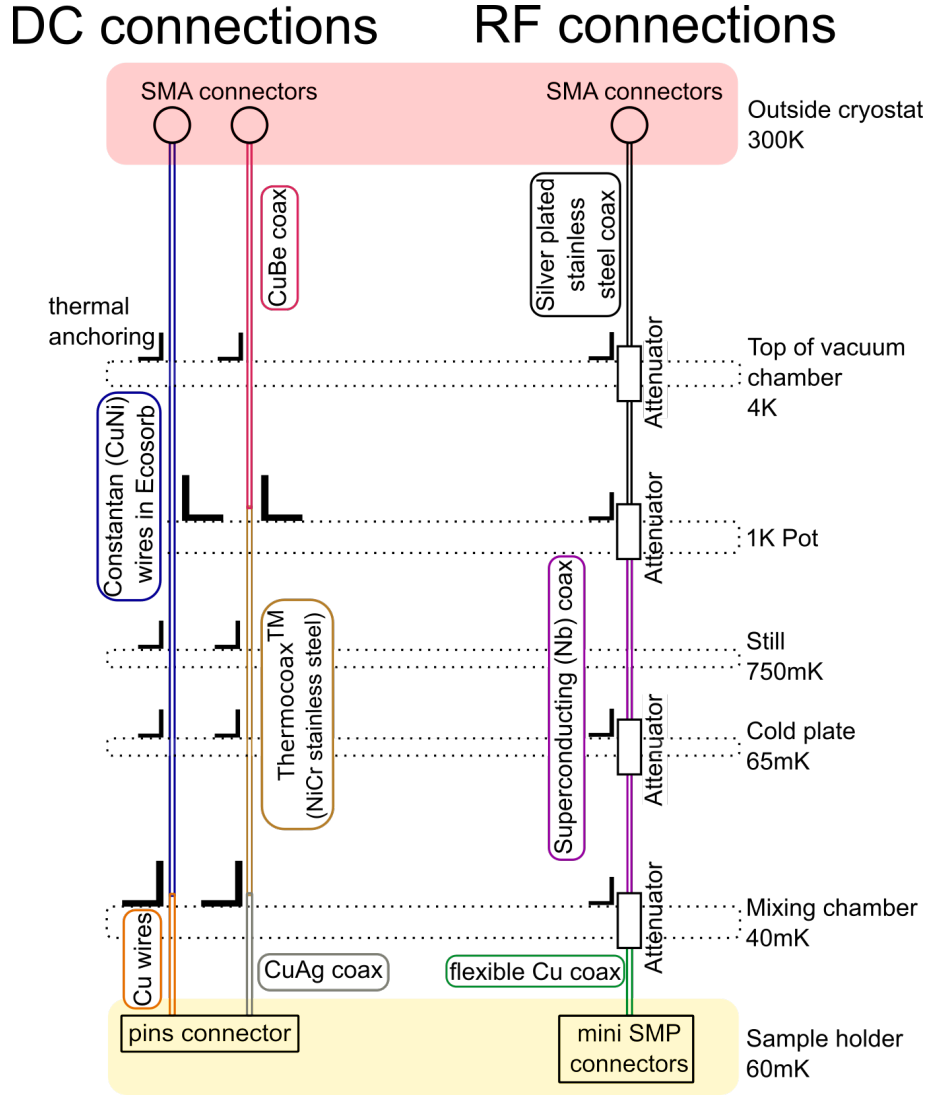


**Figure 2.3** – Scheme of the experimental wiring.

The input and output temperature of an attenuator are linked as follow:

$$T_{\text{out}} = D^2 T_{\text{in}} + (1 - D^2) T_{\text{stage}} \quad (2.1)$$

with  $D = 10^{\text{att}(dB)/10}$ . Attenuators are placed at 4 different stages, see Fig. 2.3 for their location. 4 RF lines connected to the sample (see Fig. 2.4) are dedicated to the nanosecond pulses, three of them with an attenuator set (20 dB, 6 dB, 6 dB and 1 dB), and (10 dB, 20 dB, 3 dB and 1 dB) for the last one. For technical reasons the same attenuators and chain of attenuation cannot be employed for the 4 lines. Using the equation 2.1, the inner conductor temperature can be estimated to 100 mK for the three identical lines and 200 mK for the last one. The drawback of using attenuators is the limitation of the pulse amplitude. Experimentally we choose to limit the attenuation into the cryostat to the previous set, and additional attenuator are placed at room temperature (3 dB) to further limit the pulse amplitude ensuring the safety of the sample. This way the heat brought to the sample is highly reduced, it is kept safe and there is still

an adjustable element.

Besides using attenuators, such as for the DC lines, different materials are employed. From room temperature to 65 mK, silver plated stainless steel coaxes are used. Since the high frequency current flow only in a few skin depth of the surface, a poor thermal conductor such as stainless steel is used for the inner part, covered with a good conductor like silver.

From 65 mK to the mixing chamber the connections are made in Niobium (Nb) which is superconducting below 10 K (very low thermal conduction). Finally, to ensure the good thermal contact between the sample and the mixing chamber, flexible copper coaxial cables are used.

The details of the RF chain of measurement is presented in the section 2.4.2.1, and the connections are presented in Fig. 2.3.

## 2.2 DC electronics

### 2.2.1 DC voltages

Since the experiment is electrically controlled, a fine resolution, a low noise and a high stability for the 17 DC gates of the sample are required. To this end, a home-made system based on a commercial 16 bits digital-to-analog converter (DAC) chip (Linear Technology LTC2604) is used. The chip is included in an electronic card which contains also a low voltage power line filtering and a low noise amplification stage of the output. Each source exhibits an operating range of  $\pm 5V$  with a fast rise time of  $t_{rise} < 2 \mu s$  and a typical noise spectral density of  $\sim 25 \text{ nVHz}^{-1/2}$ .

Each card hosts 8 sources with a coaxial output, permitting a full shielding down to the sample holder. Over the 35 hosts sources, 20 were used and each of them could be changed every  $16 \mu s$ . The DACs are controlled via a field programmable gate array (FPGA) from National Instruments (NI sbRIO-9208). Allowing experimental sequence to be programmed in advance on a computer and send to the FPGA via an ethernet connection.

Finally, to avoid any issue of communication between the controlling PC, the FPGA and the other instruments, an ethernet card of the computer is devoted to the FPGA.

### 2.2.2 DC measurements

The current flowing through the 2DEG, the QPC current, is pre-amplified with a home-made current to voltage converter (I/V converter) based on a Texas Instruments TLC2201 operational amplifier. The I/V converter operates from DC to  $\sim 1 \text{ kHz}$  while the gain is changed from  $10^6 \text{ V A}^{-1}$  to  $10^9 \text{ V A}^{-1}$ . The voltage is measured by a 12 bits analog-to-digital converter (ADC) card from National Instruments (NI PCI-6023E) with a sampling rate of 200 kS/s, interfaced with a host computer. Notice that this setup is only used for the DC measurements (*e.g.* DC stability diagrams). For the fast manipulations the RF-QPC was used with its dedicated setup described in the section 2.4.

---

### 2.2.3 Controlling software

The control of the experiment is performed using a home-made Labview program running on the host computer. The software is in charge of the control of the FPGA, allowing microsecond manipulation of the different voltages, and the triggering of the other instruments, plus the collection and the storage of the experimental data.

## 2.3 RF manipulations and detection

Before coming to the RF-QPC development and characterisation, the experimental methods employed to benefit from the fast detection ability of the RF-QPC are presented.

### 2.3.1 RF manipulations

The necessity to perform the fast manipulations as already been mentioned, with a required  $\sim$  GHz manipulation bandwidth. Therefore, the previous DC setup, limited to a  $\sim$  MHz bandwidth is not suitable. Instead, the required nanosecond pulses are implemented thanks to a Tektronix 5014 arbitrary waveform generator (AWG) having a sampling rate of 1.2 GS/s (0.8 ns/point). The waveforms run by the AWG are generated thanks to a python program, and are synchronised with the rest of the setup using the FPGA trigger (see Fig. 2.5).

The RF connections described in section 2.1.2.2 are used to perform these fast manipulations with the four RF gates colourised in the SEM image of Fig. 2.4. These gates are devoted to these RF manipulations and are directly connected to the AWG output. Taking into account their set of attenuation, 36 dB for three of them and 37 dB for the last one, and the AWG voltage amplitude 4.5 V, the expected maximum amplitude of the AWG pulses are  $\sim$  65 mV and  $\sim$  57 mV respectively. In the following, the voltages of the RF gates will be expressed with these expected values on the sample.

Actually, the chip carrier was only hosting 4 RF connections, while we need five of them, four connections for the RF gates, and a last one dedicated to the RF-QPC. Then, from the mixing chamber down to the sample, 3 RF gates and the RF-QPC are connected to the SMP connectors of the chip carrier, the last RF gate was connected to the sample via a CuAg coaxial line (green one in Fig. 2.4 but not used in the work presented in this manuscript).

### 2.3.2 RF detection

All along my thesis, most of the implemented experiments were spin manipulations performed within 500  $\mu$ s. Then, in order to optimise the acquisition and avoid dead times, the measurement procedure has been optimised to reduce the communications between the instruments, and more precisely with the computer. A python program has been developed in order to set the entire experiment on the AWG memory and requiring only a trigger to start it. For the detection, the ADC is replaced by an oscilloscope (LeCroy WaveRunner HRO 64Zi), triggered by the AWG, which is able to do post-processing before sending the results to the computer. In our case the oscilloscope performs either signal averaging or

---

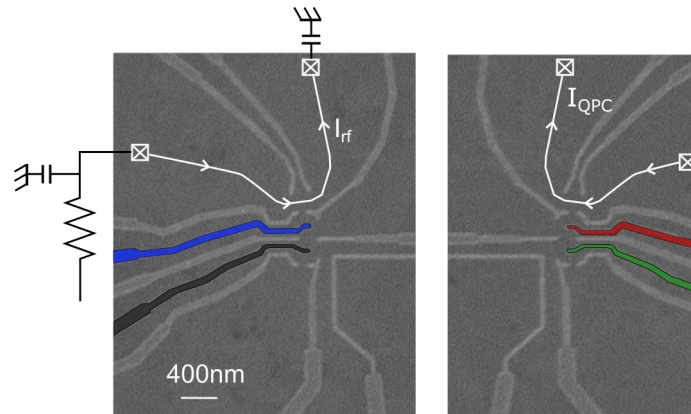


**Figure 2.4** – Scanning electron micrograph of the sample. The RF gates are colourised. The blue, red and green gates have an attenuation of 36 dB from room temperature, and the black gate a 37 dB attenuation (cf. 2.1.2.2). For the experiments presented in this manuscript, only the blue, black and red are used. On the left picture the components of the tank circuit are also shown, see 2.4.2.2 for more details. The inductor is 820 nH, the capacitance is 0.8 pF and the capacitance to the ground is 1  $\mu$ F.

pass/fail tests for the single shot spin readout.

The oscilloscope has two different modes of acquisition, one named single and the other segment acquisition. The single acquisition configuration consists in recording a single trace and then post-process it. The advantage of using this instrument is the second mode, the segment acquisition which permits to acquire a full experiment in a row, performing post-processing like averaging, and then send the averaged data to the computer. This mode is advantaging because, first, it limits the number of communication with the computer to two, to start the experiment and collect the data. Second, the full experiment being recorded in a row, it is submitted to a rather similar low frequency noise environment.

This gain on the communications leads to a total acquisition time close to the experimental one, and roughly three time faster than the single acquisition mode. Considering in addition the low frequency noise which is avoided and it explains why this mode was preferentially employed.

For the single shot measurements, the pass/fail post-processing mode was used, this mode is developed and optimised at the end of this chapter in section 2.5. Basically, it consists in checking if a signal is superior or not to a threshold. With this post-processing, the segment acquisition mode could not be used. Hence, the measurements were longer and each point being recorded independently, the low frequency noise advantage just mentioned is not accessible anymore. Associated to the increase of processing time and the fine tuning required to succeed the single shot detection were restricting its use. However, it remains a technique permitting to extract directly the triplet spin state probability of an experiment contrary to the signal averaging method as detailed in the following.

## 2.4 RF-QPC

In our system, the only accessible information is the charge, so to measure the electron spin, a spin to charge conversion is required. An interest of using a double quantum dot is the fact that the Pauli spin blockade can be used to do so. This technique details in the next chapter, section 3.3.1, relies on the measurement of the double quantum dot charge configuration just after the spin manipulation, if the charge state is (1,1) it means a triplet spin state, if it is (2,0) a singlet one. The only limitation of this technique is the necessity to perform the charge readout before the relaxation of the spin state, so within  $T_1$  which is about  $\sim 30 \mu\text{s}$  in our experimental conditions. Thus, the detection bandwidth has to be larger than  $T_1$ , preventing us to use a QPC with its kHz bandwidth. To circumvent this issue and therefore be able to perform the single shot spin readout, the RF-QPC has been developed permitting to reach a detection bandwidth of few MHz.

The RF-QPC and its characteristic are first presented before coming to its characteristics and the development of the single shot spin readout.

### 2.4.1 RF-QPC: working principle

The detection bandwidth limitation of the QPC is not due to the QPC in itself, but to its DC chain of detection. A QPC is a charge detector having a pretty high resistance,  $\sim 50 \text{ k}\Omega$ , and taking into account the shunt capacitances of the wires,  $\sim 100 \text{ pF}$ , results in a RC time, so a cutoff frequency  $f_c = \frac{RC}{2\pi} \approx 30 \text{ kHz}$ . Since the target detection bandwidth is  $\sim \text{MHz}$ , a major improvement of the wiring is required. Furthermore, only increasing the bandwidth is not enough. In DC experiments, the noise spectrum goes from DC to the upper limit of the detection bandwidth. So the measurement is submitted to the  $1/f$  noise plus some white noise, as sketch in the figure 2.6. Hence, increasing the detection bandwidth results in an increase of the range of noise submitted to the sample.

To circumvent these difficulties, we use an impedance matching network, transforming the high resistance of the QPC to the  $Z_0 = 50 \Omega$  impedance of the transmission lines, and performing homodyne detection around a carrier frequency of few 100 MHz. Thanks to this method, a higher detection bandwidth can be reached while remaining in a white noise regime, cf. sketch of Fig. 2.6. Using such matching impedance circuit detection bandwidth larger than hundred MHz have been obtained [73]. In a sample similar to ours, Reilly *et al.* shown a charge sensitivity  $\sim 5 \cdot 10^6 e^2/h \text{ Hz}^{-1/2}$  with a bandwidth of 8 MHz [74], equivalent to our expectations.

The detection principle is the following, the impedance matching network (or tank circuit) is a LCR circuit with the inductance L and capacitance C which are added components while the resistance R is the QPC resistance. The impedance  $Z$  of the tank circuit is defined with these three components where only the resistance is a variable element. When  $Z$  is tuned such that  $Z \sim Z_0$ , any change of resistance R, or  $g_{\text{QPC}}$ , due to a charge tunneling event for instance changes the tank circuit impedance  $Z$ . Hence, a RF signal tuned at the resonance frequency of the tank circuit is more or less reflected by the tank circuit depending on  $g_{\text{QPC}}$ , it is modulated in amplitude by the variations of  $g_{\text{QPC}}$ . The demodulation is performed by mixing the reflected signal with the reference RF carrier using a Local Oscillator (LO). The resulting signal is low pass filtered, removing the high frequency sideband while keeping the low

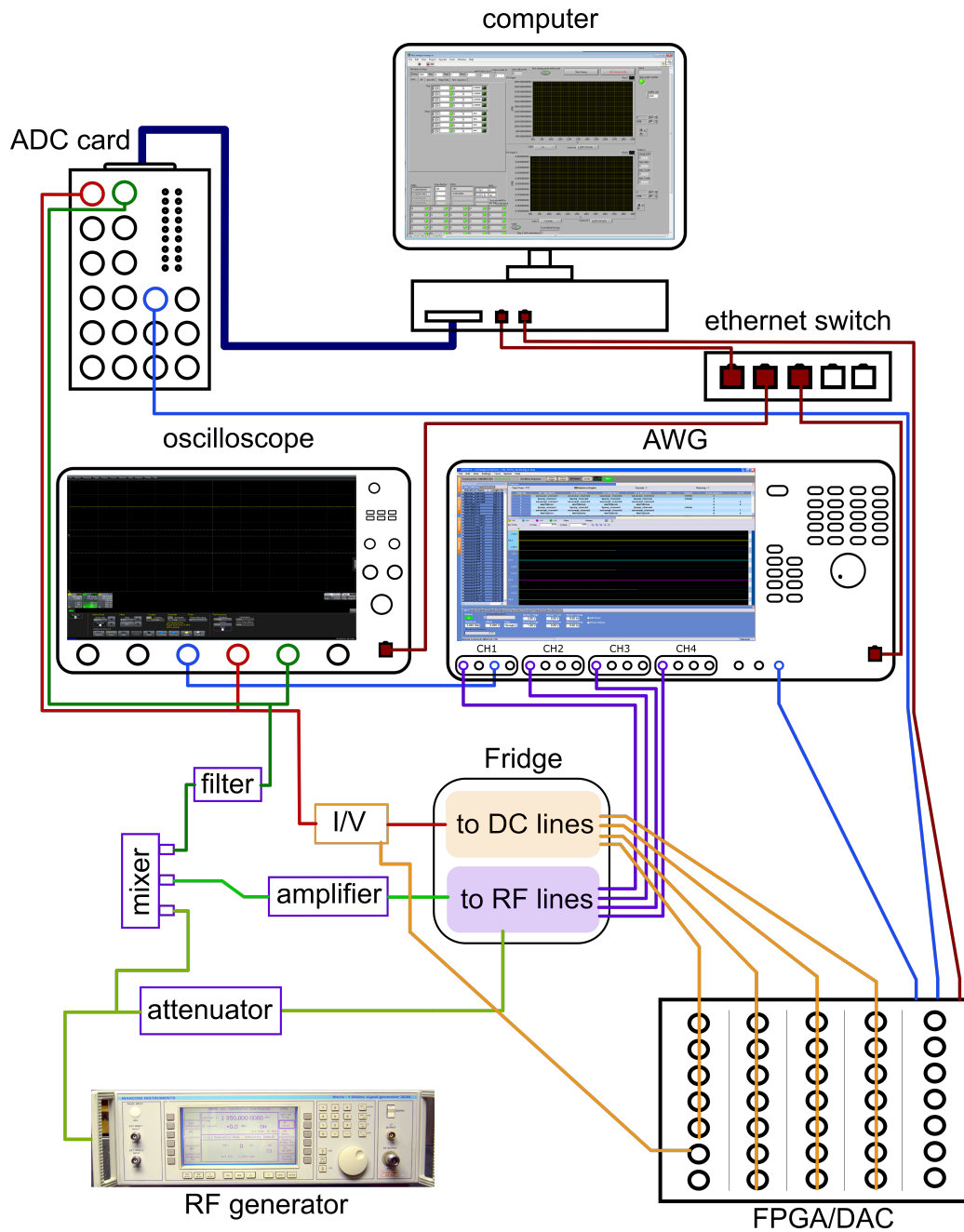


**Figure 2.5** – Scheme of the complete experimental setup with the DC and RF instruments. Orange elements corresponds to the DC chain of measurement, and in purple the RF one. The red line represents the DC current, in green the RF carrier, modulated and demodulated signals. Blue lines indicate the different triggers. Finally, in dark red the ethernet connections between the computer and the instruments.

frequency one, yielding to a voltage signal  $V_{\text{RF}}$  proportional to  $g_{\text{QPC}}$ .

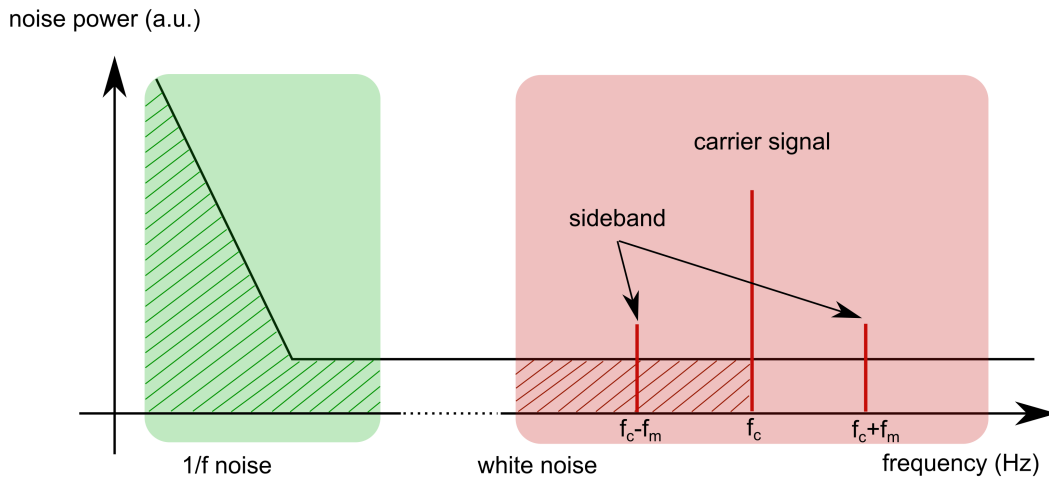


**Figure 2.6** – Schematic plot of the noise power spectral density as a function of the frequency. The green box corresponds to the detection bandwidth for a DC detection, the red one for a RF-QPC. The dashed lines represent the integrated noise for a same detection bandwidth for a DC detection (in green) or using a RF-QPC (in red) and the low frequency sideband of the modulated carrier as we do. The noise is much more important for the DC configuration than for the RF-QPC because of the  $1/f$  noise suppressed at high frequency. The sidebands are the result of the carrier signal modulation at  $f_c \pm f_m$ , where  $f_c$  is the carrier frequency and  $f_m$  the modulation frequency. In practice, this modulation can be due to a charge tunneling event in the double quantum dot for example leading to a change of the QPC conductance so reflection of the carrier signal by the tank circuit.

## 2.4.2 Complete RF-QPC setup

A brief review of our tank circuit and its development is here discussed, for further details about the development of a RF-QPC, the reader can refer to the following thesis [75]. The development of the RF-QPC was done in collaboration with a post-doc Konstantinos ROGDAKIS and the RF components were home-made by Christophe HOARAU, RF engineer at the Neel Institute.

To describe the complete chain of detection of the RF-QPC, the travel of the RF signal is followed to present each component of it before focusing on the tank circuit and its characteristics.

### 2.4.2.1 Measurement chain

The setup for the detection with a RF-QPC is not only composed of the tank circuit and the mixers, c.f. sketch in Fig. 2.7. In the detail, a RF generator (Marconi signal generator 2030) emits a carrier signal at fixed power and frequency finely tuned at the tank circuit resonance. The power is set to have the carrier signal on the LO of the mixer (Mini-circuits<sup>R</sup> mixer ZP-SMH-S+) at the required 11 dBm. Taking into account the 3 dB insertion loss inherent to the splitter, the RF source is set to 14 dBm. Such power is too high to be directly send to the sample, so a variable attenuator (Lab Brick Digital Attenuator), controlled by computer, is used at room temperature attenuating the RF carrier by  $\sim 70$  dB.

In the cryostat, the first component is a directional coupler mounted on the 1K-pot stage to redirect the RF signal. It is a 3-port component, one corresponds to the input, a second one is connected to the sample, and the third is the output (see figure 2.7). Additionally to the redirection capability, it contains a 30 dB

attenuator for thermally anchoring the incoming signal, and a capacitance ( $\sim 10 \mu\text{F}$ ) to block the DC component. With this component, the RF signal is sent to the tank circuit where it is modulated, and the reflected signal is redirected toward a 4 K amplifier where the signal is amplified by  $\sim 40 \text{ dB}$  and then  $\sim 22 \text{ dB}$  at room temperature. The demodulation is performed with the mixer, and after a low pass filter, being in reality a 47 dB amplifier, the resulting  $V_{\text{RF}}$  is recorded by either the ADC or an oscilloscope. The complete chain of RF measurement is represented in Fig. 2.7, and the full setup of the experiment in Fig. 2.5.

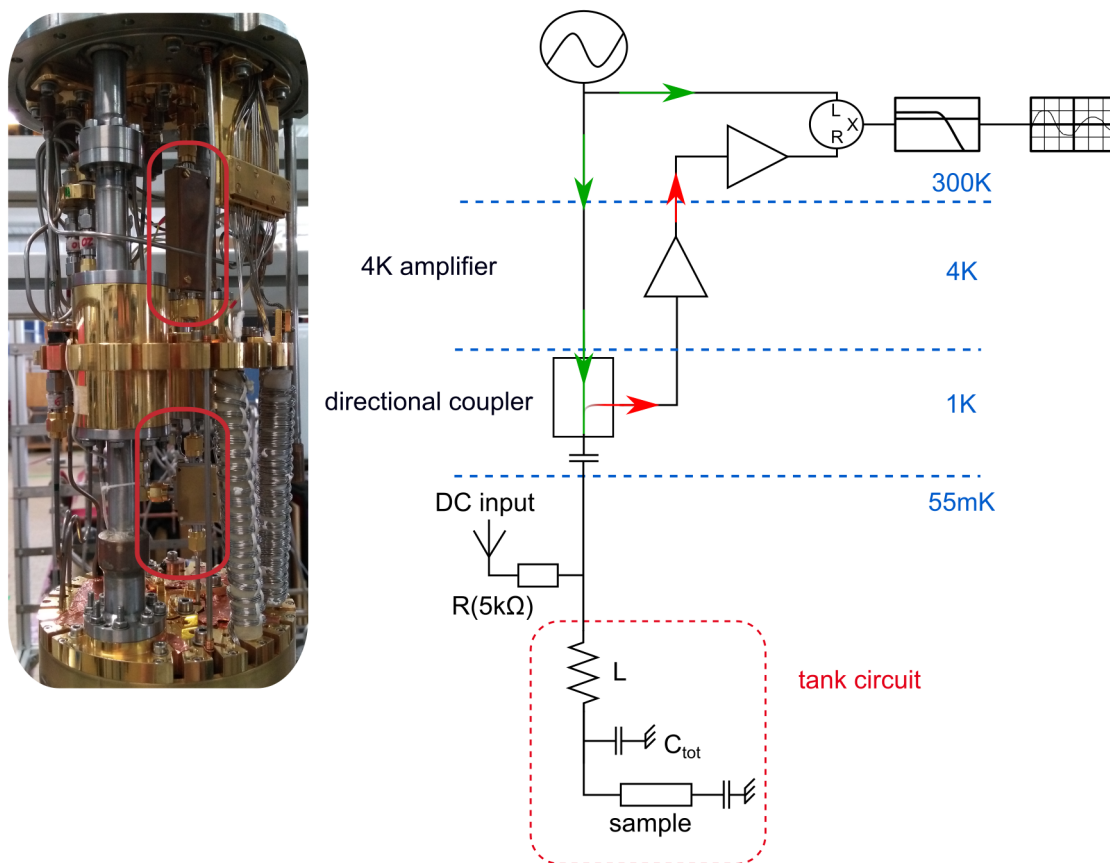


**Figure 2.7** – *a)* Picture of the isolating vacuum chamber from its top part to the cold plate stage. The amplifier located at 4K and the directional coupler are encircled in red. *b)* Electrical scheme of the RF-QPC measurement chain. The green arrows indicate the carrier signal, and the red ones the modulated one. The split carrier signal goes down to the tank circuit via the directional coupler. The modulated signal goes back to room temperature after amplification at 4K and is amplified again at room temperature. The modulated and carrier signals are mixed with the frequency mixer, the high frequency sideband filtered out with an amplifier used as low pass filter before having the signal recorded by either an ADC card or an oscilloscope depending on the performed measurement. The tank circuit represented by the red dashed line box includes a 820 nH inductor, a total capacitance (an added capacitance plus parasitic one, see 2.4.2.2) of  $\sim 0.8 \text{ pF}$ , and a capacitance to ground of  $1 \mu\text{F}$ . In order to applied a DC bias, a bias tee is added with the  $5 \text{ k}\Omega$  resistance.

### 2.4.2.2 Tank circuit components and its tuning

The tank circuit is the key component of the detection chain. Indeed, it defines the detection bandwidth and the charge sensitivity of the RF-QPC while having to satisfy different constraints. There are three main requirements, the first one is the resonance frequency defined as  $f = \frac{1}{2\pi\sqrt{LC}}$  which should be of few hundred of MHz to be only submitted to the white noise of the amplifier. The second is the impedance of the circuit,  $Z = Z_L + \frac{RZ_C}{R+Z_C}$  with  $Z_L$ ,  $Z_C$  the impedance of the inductance and capacitance, which should be as close as possible to  $Z_0 = 50\ \Omega$  of the transmission line. The tank circuit impedance for which the impedance mismatch is minimal is called matching impedance. The third requirement is a matching resistance close to  $50\ \text{k}\Omega$ . This resistance is the one of the QPC for which the tank circuit is at the matching impedance, so optimal transmission of the RF signal to the tank circuit, i.e. optimal amplitude modulation. This value of  $50\ \text{k}\Omega$  corresponds to the typical QPC resistance close to the pinchoff, which is usually the region where it is the most sensitive.

In the literature, different tank circuit have been developed [73, 76, 77], but Reilly *et al.* [74] have a similar sample than we have with characteristics similar to our target values, so first the same recipe has been followed. However, experimentally it was not possible to reach the matching resistance, which was out of our accessible range, probably above  $100\ \text{k}\Omega$ , meaning that the optimal configuration of detection was unreachable. This point have been studied and solved as described in the appendix A. After solving this issue, the tank circuit was composed by an inductance of  $820\ \text{nH}$ , the resistance is the QPC, and a total capacitance  $C_{\text{tot}} = C + C_p$ , where  $C$  is an added capacitance of  $0.2\ \text{pF}$ ,  $C_p$  being the parasitic ones from the chip carrier, bonding wires, sample tuning, 2DEG, etc...

The main difficulty in the development of this tank circuit was the required fine tuning of the added components, the inductance and capacitance, while their characteristics change depending on the experimental conditions. These variations can be seen in Figs. 2.8 and 2.9 showing the evolution of the resonant peak for different temperatures, applied magnetic fields or sample tunings.

First regarding the temperature, a shift of resonance frequency is observed between each temperature,  $300\ \text{K}$  ( $\sim 147\ \text{MHz}$ ),  $4\ \text{K}$  ( $\sim 185\ \text{MHz}$ ) and  $60\ \text{mK}$  ( $\sim 183\ \text{MHz}$ ). The resonance frequency being  $f = \frac{1}{2\pi\sqrt{LC_{\text{tot}}}}$ , these variations are either due to a change of capacitance or inductance. Contrary to the inductance, the parasitic capacitances are expected to vary when cooling-down the sample. Using the resonance frequency their values can be estimated. At room temperature the resonance is close to  $147\ \text{MHz}$  and  $183\ \text{MHz}$  at  $60\ \text{mK}$ , giving parasitic capacitances of  $1.2\ \text{pF}$  and  $0.7\ \text{pF}$ . Notice that the parasitic capacitances are the main contribution of the total one, the added one is only  $0.2\ \text{pF}$ . These shifts being rather reproducible they can be compensated by simply measuring the resonance at  $4\ \text{K}$  and adjusting the added capacitance.

Contrary to the shift in temperature, the ones with the magnetic field or the sample tuning are much more difficult to compensate. The variations with the magnetic field were not expected and are attributed to the evolution of the inductance with the magnetic field. Its composition being unknown it might contain magnetic materials. Compensating these shift is difficult experimentally since it requires to cool-down

the sample and looking at the resonance depending on the magnetic field. For our experiment it turns out that only the range 250 – 350 mT (see Fig 2.9) was unusable. A change of parasitic capacitance might also occur because of the increase of electron confinement with the magnetic field, but it should not induce such important shifts especially in this range of low magnetic field.

The main issue with our circuit was related to the matching resistance. This resistance corresponds to the one of the QPC for which the impedance matching so the amplitude modulation of the carrier signal is optimal. This resistance being defined by the characteristics of the tank circuit, it is not necessarily obtained for the optimal QPC tuning. The two resonance peaks presented in Fig. 2.8 have been obtained with the same sample tuning, except a difference about 0.2 V on the QPC gate  $V_{3:3}$ . The blue trace corresponds to the optimal QPC configuration, the QPC gate voltage for which its charge sensitivity is maximal (c.f. section 2.5), with a peak amplitude of about  $\sim 10$  dB. By shifting the gate voltage, the matching resistance configuration is obtained with a peak of about  $\sim 50$  dB (purple trace in Fig. 2.8). This large difference of peak amplitude illustrates the fact that for the optimal QPC configuration the modulation of the carrier signal is not optimal and since the matching resistance is obtained when the QPC is not sensitive, we cannot use the full potential of our RF-QPC in term of charge sensitivity. In addition, because of the electron confinement which is increasing with the magnetic field, it means that the intrinsic QPC resistance varies and increase with it too.

In the end, associated to the other shift of the tank circuit, the inductance one, the matching resistance and by extinction the RF-QPC charge sensitivity was decreasing with the magnetic field and was limiting us to work with an applied one inferior to approximately 500 mT. Referring to the Shubnikov de Haas oscillations presented in the previous chapter section 1.7 we set the magnetic field to  $B = 430$  mT for which the current is only carried by the ECs and the rest of the manipulations will be presented for this value.

A complete characterisation of the RF-QPC is now presented by explaining how the detection bandwidth can be estimated, such as the experimental noise or charge sensitivity, and finally the maximum power which can be applied to the sample.

### 2.4.3 Detection bandwidth

The detection bandwidth of the RF-QPC can be estimated by two different approaches, either by fitting the resonance peak, or from a non demodulated signal and by studying the evolution of the sidebands peaks, i.e. secondary peaks about the RF carrier resulting from its modulation, see Fig. 2.6.

First, from the resonance peaks of the tank circuit the detection bandwidth is by definition the width of this peak at  $-3$  dB. To determine this value, the peak can be fitted with a Lorentzian function and the width extracted from it. This analysis has been implemented for different magnetic fields, but because of the difficulty to define precisely the base line of the peaks, as it can be seen in Fig. 2.9, the obtained values are only rough estimations. The extracted values fluctuate between 10 and 25 MHz, indicating

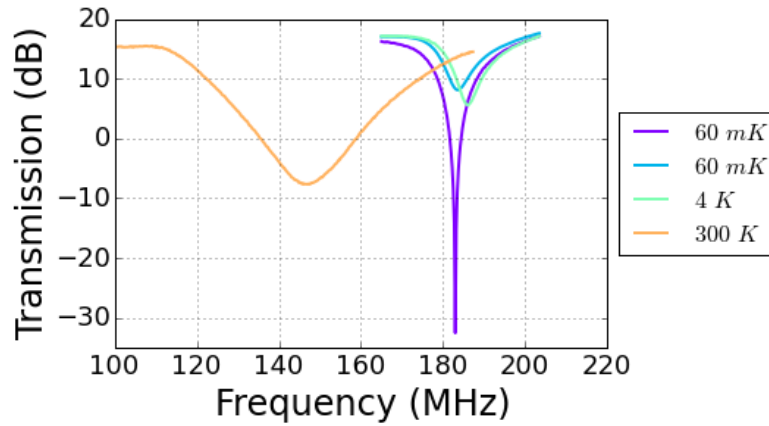


**Figure 2.8** – Transmission signal  $S_{21}$  of the RF-QPC system before room temperature amplification and demodulation recorded at various sample temperatures and sample tunings. The shift of resonance frequency is explained by an evolution of the parasitic capacitance variation with the temperature. For the purple and blue trace recorded at 60 mK, the only difference is the RF-QPC tuning, i.e. its resistance. The purple one is recorded at the matching resistance  $V_{3;3} = -0.525$  V, so optimal transmission of the RF carrier to the tank circuit, while the blue one is obtained for an optimisation QPC charge sensitivity  $V_{3;3} = -0.747$  V, see section 2.5.

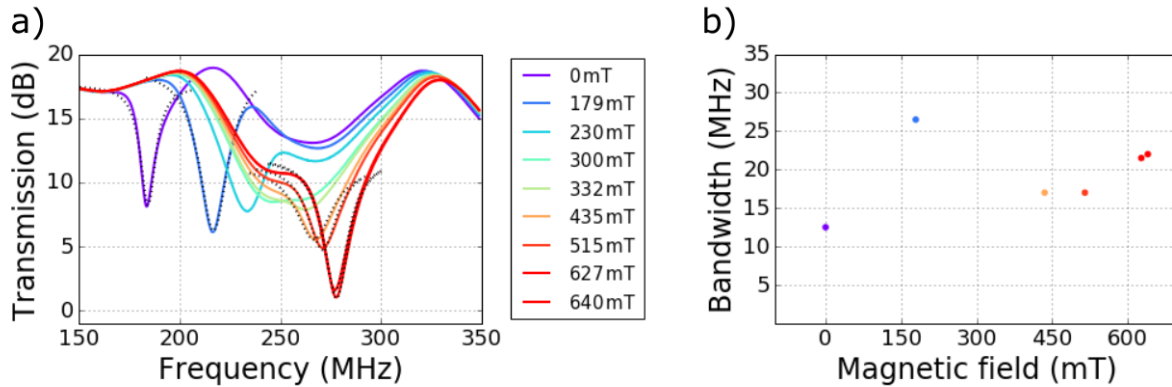


**Figure 2.9** – **a)** Transmission signal  $S_{21}$  of the the RF-QPC system before room temperature amplification and demodulation recorded at 60 mK for different magnetic fields in the range 0 to 640 mT, with the sample tuned for an optimised charge detection cf. Fig. 2.8. The black dashed lines are the Lorentzian fits used to estimate the detector bandwidth. The resonance frequency is changing with the magnetic field, and the resonant peak disappears in the range 250 – 350 mT. The shift in the resonance frequency is explained by an evolution of the inductance with the magnetic field. The evolution of the peak amplitude is due to a variation of the impedance matching between the tank circuit and the transmission line. **b)** Estimated detection bandwidth of the resonant circuit extracted from the Lorentzian fit of the resonant peak presented in a) for the different magnetic fields. Because of the absence of resonance speak in the range 250 – 350 mT, the detection bandwidth is not estimated.

that the bandwidth is large enough for our purpose.

The second method consist in studying the sidebands of the carrier signal, see Figs 2.10. The prin-

cedure is to record the amplitude modulation (AM) spectrum, so before demodulation, while applying a RF signal to a RF gate at a given amplitude, 75 mV, and for different excitation frequencies. This RF signal is used to control and induce variations of QPC conductance, simulating charge tunneling events basically. A typical AM trace is shown in Fig. 2.10c with the carrier separated from the two sidebands by the excitation frequency of 1 MHz here. The detection bandwidth is extracted from the dependency of the Signal-to-Noise Ratio (SNR) as a function of the excitation frequency as represented in Fig. 2.10a. With the SNR being the ratio of the height of the sidebands to the noise floor within a resolution bandwidth  $\Delta f$ . The detection bandwidth is defined as the frequency for which the SNR starts to decrease, here about  $\sim 15$  MHz for the used magnetic field of 430 mT, which is in agreement with the estimation from the fit of the resonance.

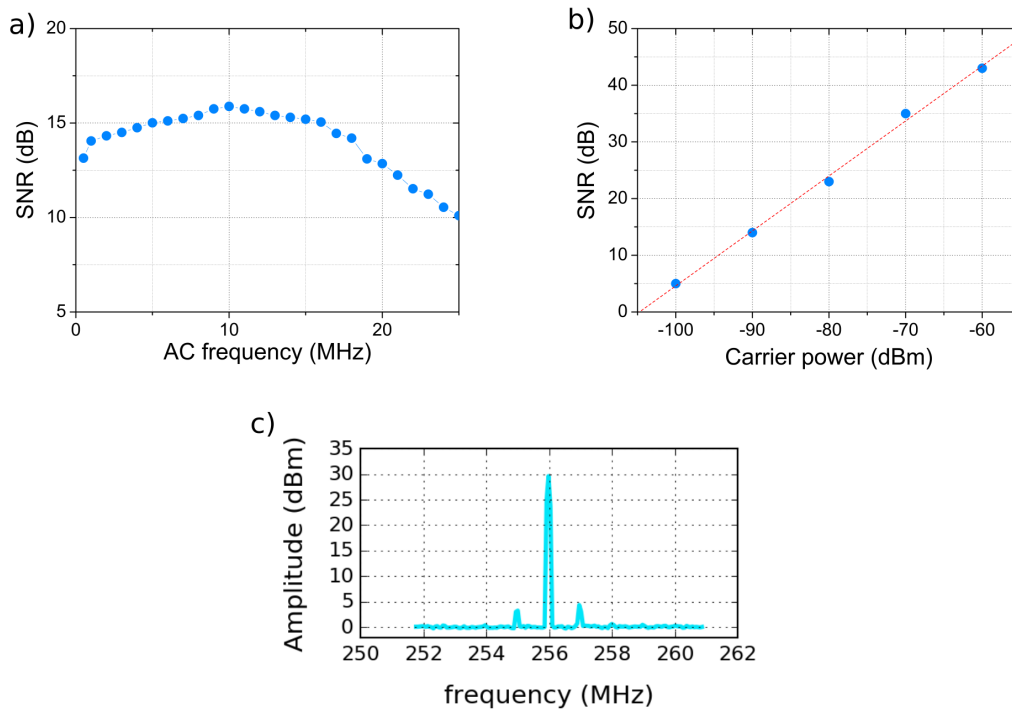


**Figure 2.10** – **a)** Signal to noise ratio (SNR) of the RF-QPC for different modulation frequencies of a RF gate with an applied voltage of 75 mV as explained in the main text. **b)** SNR dependence on the RF carrier power for an AC modulation set to the same gate and voltage than for a). A linear fit of the data is plotted as the red dashed line. **c)** Typical trace of amplitude modulated (AM) signal, before demodulation, for an AC modulation of 1 MHz with a subtracted base line of  $-78$ . Measurements shown in a) and b) were recorded with the tank circuit and sample as presented before, but in a different setup than the one presented here.

### 2.4.4 Signal to Noise Ratio and charge sensitivity

After the detection bandwidth, the experimental noise and the charge sensitivity of the employed RF-QPC can be investigated.

Concerning the noise of the experiment, its nature and spectral density can be determined. The nature of the noise is extracted from the evolution of the SNR with the RF carrier power. To do so, the same experiment than just described is performed, except that the excitation frequency and amplitude are set, here to 1.5 MHz and 300 mV, and the RF carrier power is swept, here in the range -110 to -84 dBm. The resulting trace is presented in fig. 2.10b, where the linear increase of the SNR is commonly associated to the white noise.

The spectral density of the noise can be extracted either from the AM trace, either from a single shot trace.

From the AM trace, like Fig. 2.10c, the base line is at -78 dBm (removed for clarity) taking into account the different amplification of 22 dB at room temperature and 40 dB at 4 K leads to a noise spectral density about  $0.4 \text{ nV Hz}^{-1/2}$  for the 60 kHz frequency resolution bandwidth of this measurement.

Value which can be compared with the one obtained from the single shot detection, a typical trace is presented in Fig. 2.13. In this trace, the noise amplitude peak to peak is about  $V_{pp} \approx 100 \text{ mV}$  leading to  $V_{RMS} \approx 35 \text{ mV}$ , with the 40 dB, 22 dB and 47 dB of amplification, and taking into account the  $\sim 70 \text{ kHz}$  of cutoff frequency of the filter/amplifier of the detection chain leads to a noise spectral density about  $0.5 \text{ nV Hz}^{-1/2}$ .

These two values are of the same order, and remain close to the expected white noise spectral density of the employed 4K amplifier of about  $0.5 \text{ nV Hz}^{-1/2}$ .

Finally, from the same data it is possible to extract the charge or conductance sensitivity which is defined as  $S_g = (1/2)d_{g_{QPC}}(\Delta f)^{-1/2}10^{-SNR/20}$ . The shift of conductance  $d_{g_{QPC}}$  is determined by recording the variation of  $V_{RF}$ , the demodulated RF-QPC signal, when the same RF signal of 300 mV amplitude is applied to a RF gate. This variation is converted in shift of conductance afterwards. The resolution bandwidth  $\Delta f = 1 \text{ MHz}$  is the same one than for the SNR analysis, this analysis has been performed for a carrier power of -86 dBm so a SNR about 18. Then, our conductance sensitivity is about  $\sim 1.5 \cdot 10^{-6} \text{ e}^2/\text{h Hz}^{-1/2}$ , comparable to the one obtained by Reilly *et al.* [74] which was  $\sim 5.10^{-6} \text{ e}^2/\text{h Hz}^{-1/2}$  with a similar RF-QPC.

### 2.4.5 RF carrier power

Finally, a last element can be determined, it is the maximum RF power which can be applied to the tank circuit. In DC measurements and for spin manipulations, the QPC bias is limited to  $\leq 500 \mu\text{V}$  to avoid any inter-spin states excitation [78]. But when using a RF-QPC, it is the carrier power which is controlled, so we have to estimate the equivalent limit value. Following [75], the voltage across the tank circuit is given by:

$$V_0 = V_{\text{QPC}} \left( 1 + iL\omega \frac{1 + (R+r)jC_{\text{tot}}\omega}{R(1 + rjC_{\text{tot}}\omega)} \right) \quad (2.2)$$

where  $Z$  is the total impedance,  $V_{\text{QPC}} = 500 \mu\text{V}$  the maximum allowed bias to the QPC,  $\omega = \frac{1}{\sqrt{LC_{\text{tot}}}}$  the angular frequency,  $R$  the resistance of the tank circuit,  $C_{\text{tot}}$ ,  $L$  its capacitance and inductance and  $r$  a parasitic resistance described in the appendix A. The maximum bias which can be applied to the tank circuit, labelled  $V_{\text{in}}$ , is equal to:

$$V_{\text{in}} = \frac{V_0}{1 + \Gamma} \quad (2.3)$$

we introduced here the reflection coefficient  $\Gamma = \frac{Z - Z_0}{Z + Z_0}$ . Finally, the maximum power which can be applied to the tank circuit is:

$$P_{\text{in}} = \frac{|V_{\text{in}}|^2}{Z_0} (1 - |\Gamma|^2) \quad (2.4)$$

This power is the one delivered to the tank circuit, the power delivered by the RF generator is  $P_{\text{source}} = P_{\text{in}}(|\Gamma|^2 - 1)$ .

Finally, for a maximum applied voltage  $V_{\text{QPC}} = 500 \mu\text{V}$  the maximum delivered power by the generator to the tank circuit should be  $P_{\text{source}} = -76 \text{ dBm}$ .

## 2.5 Single shot spin detection

From the previous analysis, the RF-QPC detection bandwidth and SNR are probably large enough to succeed the single shot spin readout in our experimental conditions considering our constraints of spin relaxation time limited to few tens of microseconds.

We can remind that the goal of my PhD was to detect single shot a single electron travelling in the ECs of the QHE. This detection is a two stages detection, the first one is performed by the qubit detector which stores the information of the passage of the electron for a time being the spin relaxation time  $T_1$ . The second stage is the readout of this information, equivalent to the readout the spin state of the spin qubit. It is the development of this single shot spin readout already implemented in different systems [65, 79] which is now described.

For the spin manipulations, as presented in the previous chapter with the two electron spin states, section 1.5, the spin manipulation can be performed with either the (1,1)-(2,0) charge transition or the (1,1)-(0,2). For the spin readout, a spin to charge conversion technique is required since the charge is the only accessible information with the RF-QPC. The spin to charge conversion will be performed thanks to the Pauli spin blockade technique presented in detail in the next chapter, section 3.3.1. The basic idea of this detection is measuring the charge state of the double quantum dot, if the state is (1,1) the spin state is a triplet  $|T_0\rangle$ , if it is (2,0) the spin state is a singlet  $|S\rangle$ . Then, being able to detect the spin single shot is equivalent to be able to measure the charge state of the double quantum dot single shot. In a first approach the (1,1)-(2,0) charge transition will be used since the charge sensitivity is larger for a loading in this (2,0) charge state as explained in the first chapter section 1.4.

A first experiment can be implemented to verify the ability to detect such charge tunneling event single

shot. The base idea is to force an electron tunneling. First, the charge state is initialised in the (1,0) charge configuration (point B of the stability diagram of Fig. 2.11) by waiting a time long enough to let an electron tunnel out of the quantum dot. Then, a pulse is applied to the RF gates to reach the (2,0) region (point A of Fig. 2.11), here again for a time long enough to let the tunnelling event occur. If the loading time is long enough and the QPC sensitive enough, two type of signal variations are expected, a large one corresponding to coupling with the RF gates, and a small one associated to the charge tunneling. The points A and B used in this sequence are set around a tunnel barrier showing stochastic events, then the tunnel coupling is estimated close to  $\sim$  kHz (cf. section 1.4 of the first chapter) so the tunneling time is large enough to be detected.

This pulse sequence has first been implemented with the same QPC tuning configuration than in the previous chapter, meaning using only the gate 3 : 3 for instance while 3 : 2 is grounded, the second gate of the QPC being 3 : 4. A signal evolution equivalent to this tuning can be observed in the right part of the pinch-off curve of Fig. 2.11a, with a QPC tuning configuration corresponding to the orange dot. With this tuning, while sometimes conductance plateaus are obtained (like in Fig. 1.4a), being the optimal configuration of a QPC, most of the time they are not and the current is simply decreasing such as in the right part of Fig. 2.11a. Since only one of the two QPC gates is active, one defining the nearby quantum dot chemical potential, we have to content ourselves with such current evolution. When implementing this pulse sequence with such QPC tuning, the resulting trace is the orange one in Fig. 2.11d, where there is no signal variation. Even the coupling to the RF gate which induces a large signal variation, much larger than the single electron tunneling, is not visible. It means that the charge sensitivity of the QPC is too weak to detect an electron tunneling.

Notice that, the averaging time per point was about 500 ns for this curve instead of 1.6 ms for the pinch-off curve, explaining the difference of SNR between the two.

In conclusion, the QPC tuning is not sensitive enough to perform the single shot charge detection, nevertheless, by combining the transport measurement described in the first chapter (section 1.2.1) to the QPC detector it is possible as the blue curve of 2.11 proves it.

## Sensing dot

The maximum sensitivity of a conventional QPC is obtained by setting the working position between two conductance plateaus. However, as explained just before, such detector is only composed by a single adjustable gate potential. This lack of tunable node can lead to a situation where the quantum dots tuning is such that this optimal configuration with conductance plateaus cannot be obtained with this single adjustable gate voltage. Contrary to a QPC, a Sensing Quantum Dot (SQD) is composed by at least three gates, see SEM image of Fig. 3.1, one is used for the nearby quantum dot (3 : 4) and with the two others (3 : 2 and 3 : 3) it is possible to define a quantum dot forming a so-called sensing dot.

The principle of a SQD charge detector is to do transport measurement through this sensing dot. Doing this, as discussed in the first chapter section 1.2.1, Coulomb peaks are obtained like the one in Fig. 2.11a, for  $V_{3:3} = -0.73$  V. The advantage of using this transport measurement relies of the presence

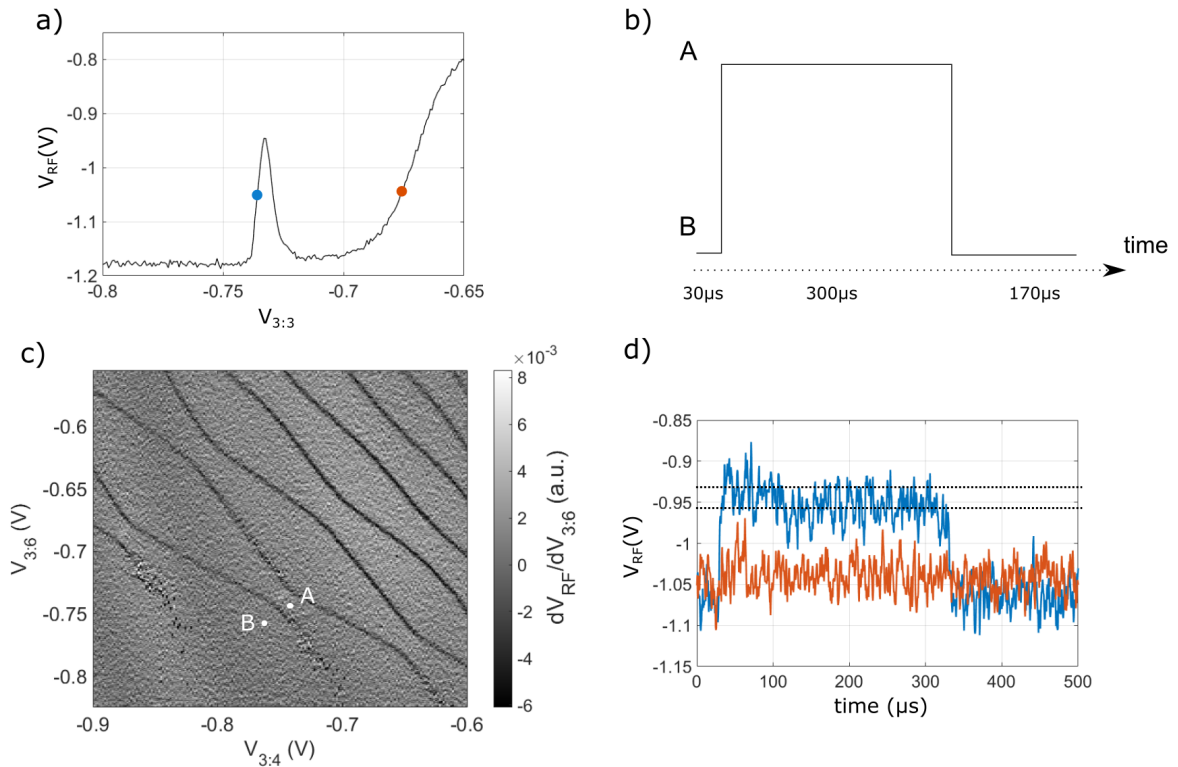


**Figure 2.11** – *a)* RF-QPC signal  $V_{RF}$  as a function of the gate voltage  $V_{3:3}$  where the two regimes of quantum point contact (QPC) and scanning quantum dot (SQD) are reachable. The colour dots indicate the working positions for the single shot charge detection shown in *c)*. For  $V_{3:3}$  corresponding to the blue (orange) dot, the charge detector is in a SQD (QPC) configuration. *b)* Sketch of the pulse sequence used to optimise the charge detection. First the initialisation in the (2,0) charge configuration is performed at the point B of the stability diagram, then by applying a pulse to reach the point A an electron tunnels into the quantum dot before coming back to the initialisation position. *c)* Stability diagram in which the derivative of the RF-QPC signal  $dV_{RF}/dV_{3:6}$  is plotted against  $V_{3:4}$  along the x axis, and  $V_{3:6}$ , along the y axis, with the position of the points A and B. *d)* Measured voltage  $V_{RF}$  during the pulse sequence, plotted as blue and orange curves, a SQD or QPC tuning, respectively. For the trace recorded in the SQD tuning, the step up from  $t = 30\mu\text{s}$  to  $t = 330\mu\text{s}$  is due to the capacitive coupling between  $V_{RF}$  and the RF gate manipulation. The higher signal corresponds to the (2,0) charge configuration. The step down, at  $t = 110\mu\text{s}$  is the tunnelling into the quantum dot of an electron, highlighted with the black dashed lines. In QPC tuning, the step up arising from the capacitive coupling to the gate is not visible because of the reduced charge sensitivity of this tuning configuration.

of these Coulomb peaks. As it can be seen with the blue dot of Fig 2.11, the current slope, so the charge sensitivity is larger for a Coulomb peak than for a QPC regime (orange dot). In this trace for instance, the current slope is approximately five times larger for the Coulomb peak than for the QPC regime.

Furthermore, another advantage is the fact that, thanks to the additional gate potential, it is possible to define a Coulomb peak at almost every point of the stability diagram, any set of quantum dot gate voltages. Resulting in a charge sensitivity which can be maximal for almost any tuning of the nearby quantum dot tuning, contrary to a QPC. In equivalent sample it has been shown that a RF-SQD is up to up to 30 times more sensitive than a RF-QPC [35].

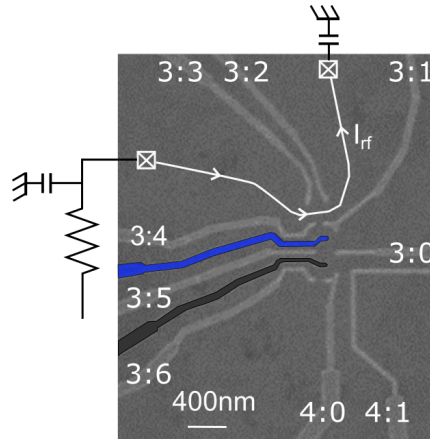


**Figure 2.12** – Scanning electron micrograph of the left double quantum dot, the RF gates are coloured. The components of the tank circuit are also drawn.

The same experiment of forcing electron tunnelling events can be performed with such SQD tuning corresponding to the blue curve of Fig. 2.11d. Two elements are noticeable, the first one is the step in signal between 30 and 330  $\mu\text{s}$ . This step is due to the capacitive coupling between the RF gates and the charge detector. It indicates the two charge states, with the (1,1) charge state being the lower  $V_{\text{RF}}$  signal, and the (2,0) one the higher one.

The second element is the step of signal, stressed out with the black dashed line, within this higher signal region which corresponds to the tunnelling of an electron into the quantum dot since the step is positive.

### Optimisation of the pass/fail test

The single shot charge tunneling detection being demonstrated, the single shot spin readout is also possible using the Pauli spin blockade based spin readout. To use this ability experimentally and implement the spin manipulation with the single shot spin readout, the experimental procedure of detection should be developed and the charge sensitivity of the SQD optimised.

As mentioned previously subsection 2.3.2, the employed oscilloscope has an acquisition mode called pass/fail test which is well adapted for the single shot detection. This test consists in checking if the difference of signal averaged over two time windows is superior or not to a threshold. For our experiment, it is equivalent to check if a charge state of the quantum dot is (1,1) or not, so if a  $|T_0\rangle$  spin state has been detected or not.

In practice, the signal is averaged over two time windows, a base line one and a measuring one just after the manipulation with the difference  $\Delta V_{\text{RF}}$  of signal between the two windows which is compared to a set threshold. If the signal difference is higher than the threshold, a tunnelling event occurred and the test is successful, otherwise nothing happens and the test is failed.

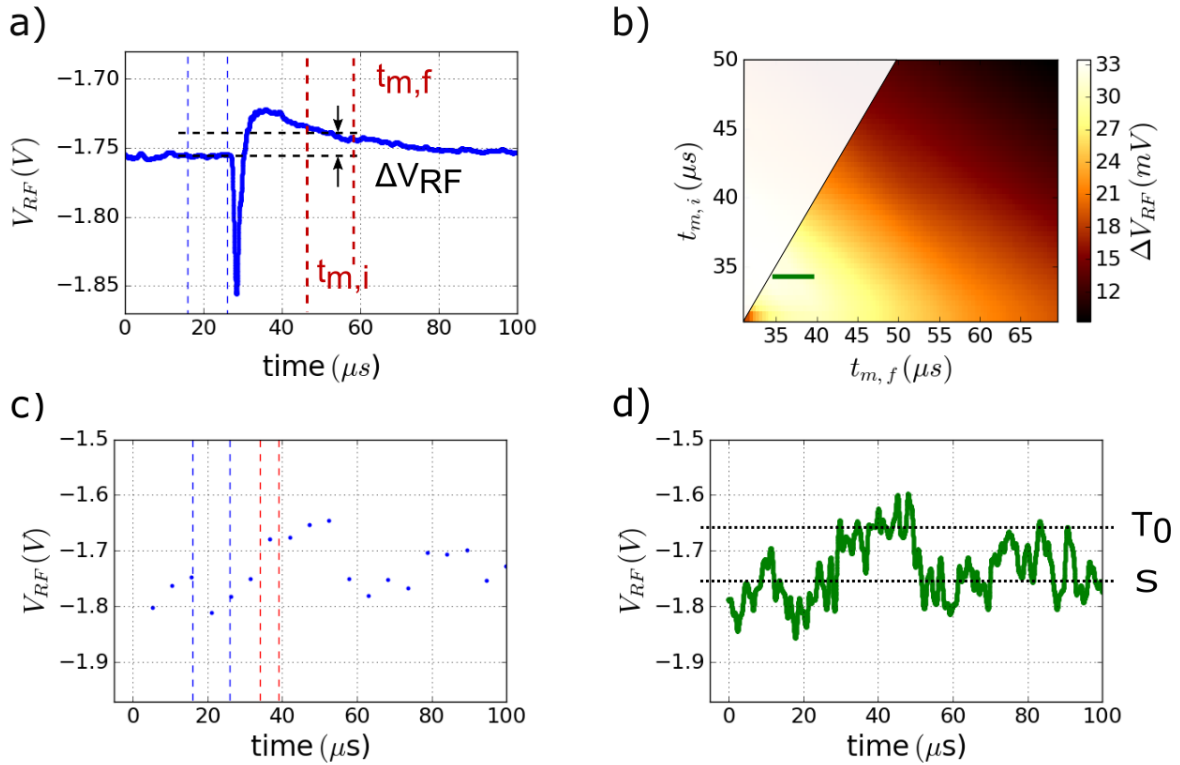


**Figure 2.13** – *a*) RF-QPC signal  $V_{RF}$  plotted as a function of the time. This trace is the result of the average over 2000 traces of single shot spin readout attempts. The first part of the trace is the initialisation of the singlet state  $S(2,0)$ . The deep at 30  $\mu s$  corresponds to the manipulation time, and the exponential decay is the indication of the tunnelling of an electron into the upper quantum dot, associated to the triplet relaxation. The blue dashed lines indicate the base line time window, the red ones the measuring window described in the main text. The difference of averaged signal over each time window  $\Delta V_{RF}$  is also illustrated. *b*) Colour plot of  $\Delta V_{RF}$  for different  $t_{m,i}$  and width of the measuring window. The base line integration delay and duration is set as represented in *a*) to 16 and 10  $\mu s$ , respectively. The irrelevant white triangle corresponds to a initial point occurring after the final point. The evolution of  $\Delta V_{RF}$  is explained in the main text, the optimal measurement window is 34 – 39  $\mu s$ , highlighted with the green line. *c*) Signal  $V_{RF}$  probed by the oscilloscope with a numerical averaging of 5  $\mu s$  per point corresponding to the width of the optimal measurement window. The dashed lines represent the optimal base line window (in blue) and the measuring one (in red) as established with the 2D colour map. The step of signal for  $t = 39 - 55 \mu s$  is a tunnelling event associated to a triplet spin state. *d*) Raw signal used for the numerical processing shown in *c*). The sampling rate is fixed at 10 ns per point. The tunnelling event is less visible since the noise is not averaged out.

To develop the experimental procedure, before improving the charge sensitivity it is necessary to optimise this test and the two time windows. The first windows ( $t_{bl,i}$ ,  $t_{bl,f}$ ) defines the base line, so its width is not critical. The measuring windows ( $t_{m,i}$ ,  $t_{m,f}$ ) is more critical since it corresponds to the time spend in the excited state. If the windows is too long, some excited state would have time to relax, while if it is too short, wrong click can happen because of the detection RC time and experimental noise which is not averaged enough. Regarding the spin readout, the consequence of a wrong tuning of this window is the non detection of a triplet  $|T_0\rangle$  spin states, so a limitation of the spin readout fidelity. It is therefore

a key element of the detection.

To determine precisely the optimal time window width and starting point, an equivalent pulse sequence to the ones shown before is implemented. However, this optimisation is performed in the same experimental conditions than for the spin manipulations, meaning that here the recorded signal, the tunnelling event, corresponds to the  $|T_0\rangle$  spin state. The detail of the experimental procedure is presented in the next chapter section 3.3.1 with the explanation of the Pauli spin blockade. As mentioned, the spin readout is based on the readout of the double quantum dot charge state, is it (1,1) or (2,0). The distinction between the two being possible until the relaxation toward the (2,0) charge state, so it involves a charge tunneling happening in a timescale  $T_1$ , the spin relaxation time. Since a charge tunneling event is a probabilistic event, by averaging many spin readout attempts, an exponential decay is recorded as the one presented in Fig. 2.13a. In this trace, obtained by averaging 2000, the peak at  $30\ \mu\text{s}$  is the cross talk with the RF gate manipulation, and the amplitude of the exponential is the probability to measure a triplet  $|T_0\rangle$ .

Before coming to the use of this trace to define the two time windows of the pass/fail test of the oscilloscope, a first comment about it can be made. From approximately  $30$  to  $35\ \mu\text{s}$ , a rising time of the signal  $V_{\text{RF}}$  can be noticed. It comes from the experimental setup and more precisely from the room temperature amplifier/filter. This rising is a drawback of our setup and it limits our capacity for the single shot spin readout. Indeed, during this rising time some triplet states to measure can relax and therefore could not be detected, reducing the fidelity of the readout. An estimation of this reduction is possible thanks to this exponential decay by extrapolating the trace to compensate the rising time as shown in Fig. 2.14. According to this extrapolation the real step signal is about  $40\ \text{mV}$ , while the measured one is  $33\ \text{mV}$ . The measurable signal with our setup is therefore of the order of  $80\%$  of the real one, setting an upper limit of the spin readout fidelity. Notice that this fidelity reduction is large because the spin relaxation time is evaluated to  $T_1 = 30\ \mu\text{s}$ , while the rising time is about  $4\ \mu\text{s}$ , so it is not negligible. For longer  $T_1$  this reduction would be smaller.

This rising time being a limit of our experimental setup, it could not be avoided. Coming back to the development of the single shot spin readout procedure, the two time windows of the test are optimised thanks to this exponential trace. To do so, the difference  $\Delta V_{\text{RF}}$ , see Fig. 2.13a, is calculated for different location and width of these windows in order to find the conditions where it is maximal.

To perform this calculation, the base line width is set to  $10\ \mu\text{s}$  just before the manipulation, blue dashed line Fig. 2.13a. For the measuring window, its initial position is changed in the range  $t_{m,i} \in [30, 50]\ \mu\text{s}$  and the final position  $t_{m,f} \in [30, 70]\ \mu\text{s}$ . The result of this calculation are presented as a 2D colour map where the colour corresponds to  $\Delta V_{\text{RF}}$ , see Fig. 2.13b.

From this map and the short times,  $t_{m,i} = 30\ \mu\text{s}$  and  $t_{m,f} < 35\ \mu\text{s}$ ,  $\Delta V_{\text{RF}}$  is increasing just like in the Fig. 2.13a. This increase is due to a RC time in the detection chain just described.

After this region,  $\Delta V_{\text{RF}}$  is maximal for  $t_{m,i} < 40\ \mu\text{s}$  and  $t_{m,f} < 45\ \mu\text{s}$ , light yellow region of the colour map, before decreasing for larger width or starting point, some triplet states already relaxed to the ground state. Using this map, we chose as time windows  $t_{m,i} = 34\ \mu\text{s}$  to avoid the RC time, and  $t_{m,f} = 39\ \mu\text{s}$  to stay in the optimal region. This window is the green line in the 2D colour map.

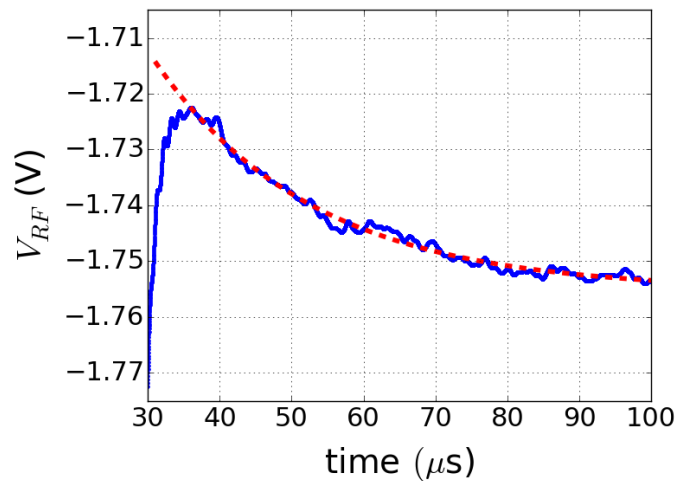


**Figure 2.14** – The RF-QPC signal  $V_{RF}$  is shown as a function of the measuring time. In blue, the trace corresponding to the average of 2000 single shot spin readouts. The red dashed line is an exponential fit of the experimental data. The exponential decay is the signature of the triplet  $|T_0\rangle$  spin state relaxation toward the ground singlet state  $|S\rangle$ . During the first 4  $\mu\text{s}$ , the detected signal is dominated by the rising time of the detection chain. Therefore, the full amplitude of the exponential decay cannot be experimentally measured, but it has to be evaluated from a fitting procedure.

The improvement thanks to this averaging can be noticed by comparing the raw data obtained with 10 ns per point, and the equivalent to 5  $\mu\text{s}$  per point of the averaged signal Figs. 2.13d and c, where in both cases the single shot spin readout is visible.

### Single shot spin readout analysis

After defining these windows and demonstrating the single shot spin readout, the experimental procedure for this type of detection is almost ready, remains only to set a threshold value. In addition, this procedure can be simulated with the previous set of data in order to investigate the spin readout fidelity which could be obtained with it in practice.

To implement this simulation of the test, the two time windows are chosen as the one determined with the previous analysis. For the threshold, from the single shot traces Fig. 2.13 c and d, the step signal between the two spin states is about 80 mV, the threshold has been set to 50 mV to limit the false clicks. The resulting histogram obtained with the failed test is presented as Fig. 2.15a, the successful tests Fig. 2.15b.

First, concerning the successful tests, Fig. 2.15b, a double Gaussian behaviour can be seen, despite their large overlapping, as expected for the detection of the two spin states  $|S\rangle$  and  $|T_0\rangle$ . To establish this histogram, the considered measurement time windows has been reduced to  $[10 \mu\text{s}, 50 \mu\text{s}]$  to have approximately the same time spend in the singlet or triplet spin state. The Gaussian corresponding to the singlet spin state is the one centred around  $\Delta V_{RF} = 0 \text{ V}$  highlighted with the red dashed line being its Gaussian fit, the triplet one is about  $\Delta V_{RF} = 0.65 \text{ V}$  with its fit being the green dashed line.

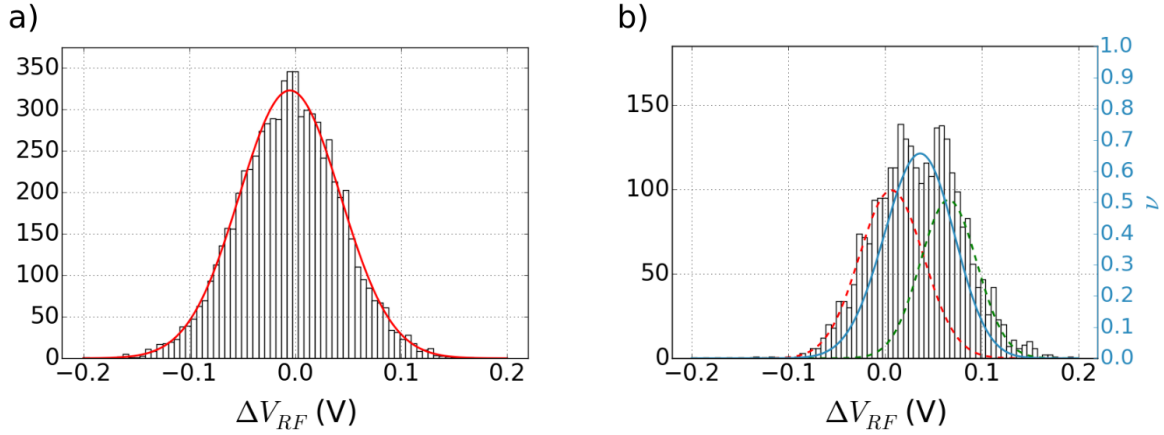


**Figure 2.15** – *a)* Histogram of the measured voltage amplitudes  $\Delta V_{RF}$  of the RF-QPC signal. This histogram is obtained from the traces how failed the simulated test performed by the oscilloscope (1427 over 2000) for a threshold set to 50 mV, so it is associated to the spin  $|S\rangle$ . A peak of counting for  $V_{RF} = 0$  mV is masked by setting it equal to the previous bin value. The red line is the result of the Gaussian fit of this histogram. *b)* Similar histogram but for the remaining 573 traces passing successfully the test, meaning the detection of a triplet  $|T_0\rangle$  for each trace. The considered time window of the measurement has been reduced to 10 – 50  $\mu$ s to have approximately the same time spend in the singlet and triplet spin state. The red and green dashed line are the Gaussian fits associated with the  $|S\rangle$  and  $|T_0\rangle$  spin states, respectively. The blue curve plotted against the right y axis is the ability to distinguish  $|T_0\rangle$  from  $|S\rangle$ , as known as the distinction fidelity. Its estimation is explained in the main text.

To determine what can be called the fidelity of the distinction  $\nu$  between the two states, the Gaussian fit can be used to calculate it. It is equal to  $\nu = 1 - \alpha - \beta$ , where  $\alpha$  is the probability to detect a singlet  $|S\rangle$  while it is actually a triplet  $|T_0\rangle$ , and vice versa for  $\beta$ . The normalised probability of each misjudging can be calculated by:

$$\alpha_i = \frac{\int_{-0.2}^{0.2} G_{T_0}}{\int_{-0.2}^{0.2} G_{T_0}} \quad (2.5)$$

where  $G_{T_0}$  is the Gaussian function associated to the singlet  $|T_0\rangle$  spin state, and similarly with  $\beta$  and  $G_S$ . This fidelity is represented with the blue line in Fig. 2.15b, having a maximum about  $\sim 65\%$  for  $V_{RF} \approx 0.035$  V. It indicates that in such detection conditions, only  $\sim 65\%$  of the spin states can be distinguished properly. Associated to the 80% of measurable signal on which this test can be implemented, due to the RC time of the detection chain, in the end, the fidelity of the single shot spin readout is limited to  $\sim 50\%$ .

This value can be verified by the success rate of this simulated pass/fail test implemented to obtain these histograms, which is about 30%. Here, for the experimental procedure used to get these data, explained in the next chapter, the theoretical triplet probability should be equal to 50%. Considering our estimated spin readout fidelity of 50% we get approximately the same 30% of triplet probability.

The second histogram of the failed tests can be commented too, Fig. 2.15a. It is a single Gaussian so it confirms the possibility to properly distinguish the two spin states with this detection procedure.

In conclusion, the experimental procedure for the single shot spin readout is defined with a spin readout fidelity estimated to 50%. Before coming to the spin manipulations, it can be first used to optimise the charge sensitivity of the RF-SQD.

### SQD gate optimisation

The optimisation of the SQD charge sensitivity is performed in two steps, by adjusting its two gates one after the other.

Experimentally we implement it by first sweeping the voltage on a gate, while stepping the second one as presented in Fig. 2.16a where  $V_{3:2}$  is stepped and  $V_{3:3}$  is swept. In this figure one can see the change of Coulomb peak amplitude while stepping  $V_{3:2}$  due to the change of confinement in the SQD vicinity. The optimal charge sensitivity is obtained for the largest peak amplitude so  $V_{3:2} = -0.415$  mV.

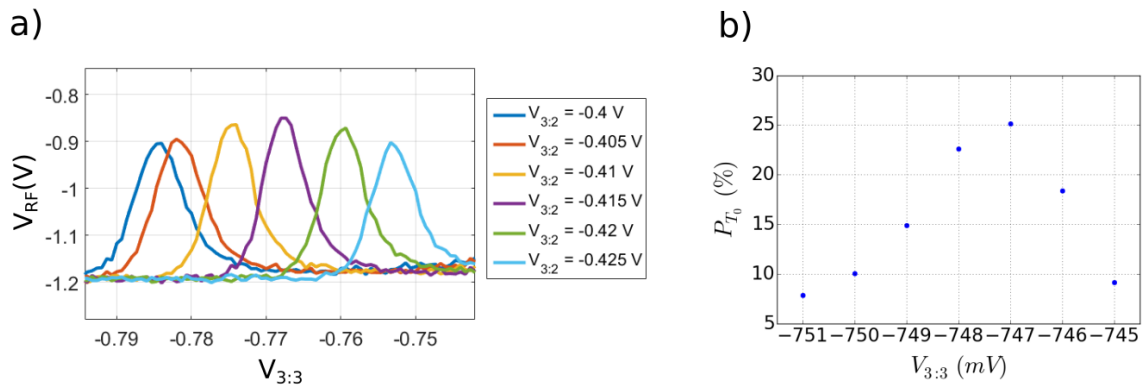


**Figure 2.16** – **a)** RF-QPC signal  $V_{RF}$  plotted as a function of  $V_{3:3}$  for different values of  $V_{3:2}$ , used for the SQD charge sensitivity optimisation. The largest sensitivity is obtained for the maximum Coulomb peak amplitude, here  $V_{3:2} = 0.415$  mV. **b)** Triplet spin state probability  $P_{T_0}$  as a function of  $V_{3:3}$ . By changing  $V_{3:3}$ , the charge sensitivity so the spin fidelity readout is changed. The optimal configuration is obtained for the maximum of the triplet probability at  $V_{3:3} = -0.747$  mV.

To optimise the second gate, the pass/fail tests can be used to record the triplet probability for different  $V_{3:3}$  voltages, with  $V_{3:2}$  kept unchanged. The aim is to perform the same spin manipulation, so with the same triplet probability after the manipulation, but for different charge sensitivity. Changing this sensitivity can be seen as changing the separation between the Gaussian of each spin state, see Fig. 2.15a, so it directly influences the distinction fidelity  $\nu$ . Thus, the measured triplet probability will be maximal for the largest charge sensitivity of the RF-SQD.

A typical evolution of the triplet probability for such experiment is presented in Fig. 2.16b. The increase and decrease of the probability is due to the SQD working position which is going from one side of the Coulomb peak to the other. The best working position is obtained for  $V_{3:3} = -0.747$  V.

## 2.6 Conclusion

In conclusion, these last measurements demonstrate our ability to detect single shot the electronic spin state, meaning that the qubit detector outcome can be readout single shot. This part of the single shot detection being proven, it remains to develop the qubit detector and verify if its interaction with a single travelling electron is large enough to permit its full single shot detection.

---

---

## Singlet-triplet spin qubit as charge detector

---

### 3.1 Introduction

In this chapter are presented the different steps leading to the elaboration of the spin qubit detector. The first one is to demonstrate the control of the charge considering the constraints imposed by the coherent spin manipulations. As introduced in the first chapter section 1.6.2, the typical dephasing time of the electron spin is  $T_2^* \sim 10$  ns, so the main requirement is on the speed of the manipulations which should be increased to keep the coherence of the manipulated spin state. Thus, 1 ns voltage pulses are necessary and implemented by using RF gates controlled by an Arbitrary Waveform Generator (AWG). The transition from slow to fast manipulations, DC to RF gates, is first presented with in particular a characterisation of the coupling to the electron reservoirs. Once the fast control of the charge demonstrated and the sample tuned in a configuration permitting the spin manipulations, the Pauli spin blockade based spin readout is introduced. The rest of the chapter will be dedicated to the characterisation and development of the singlet-triplet spin qubit as charge detector. A first part will be focused on the development of the coherent exchange oscillations, which are coherent oscillations of the spin state with their frequency sensitive to the electrostatic environment. Finally, we demonstrate the sensitivity of such oscillations to the electron density of the edge channels (ECs) of the Quantum Hall effect, introducing its use as detector to travelling charges in these same channels.

### 3.2 Charge manipulation with RF gates

All along the rest of the manuscript, the charge manipulations will be performed by using the RF gates (colourised one in Fig. 3.1) controlled by the AWG while the DC gates will be kept at constant voltages. As introduced in the first chapter section 1.3, the basic measurement demonstrating the control of the charge is the one of a stability diagram. First, the implementation of a RF stability diagram will be presented, followed by its use to study the different couplings of the system. Indeed, to be able to manipulate the spin, the interdot tunnel coupling should be large, typically of the order of  $\sim$  GHz. In addition, a  $\sim$  MHz coupling to the electron reservoirs is desired to be in a regime where the spin qubit detector is highly coupled to the ECs.

These two points will be treated in that order, first the stability diagram and then its use to investigate the couplings.

#### 3.2.1 RF stability diagram

A stability diagram is a map of the charge configurations of the quantum dots obtained by sweeping the voltage on a gate, while stepping the one on a second gate. To perform such map with the RF gates and the AWG, the constraints of the instrument must be considered. One is the reduced voltage range, the other is on the speed of the measurement.

The first restriction comes from the limited voltage amplitude of the AWG, 4.5 V, associated to the attenuation along the coaxial lines. Attenuations which are respectively 37 dB for the gate rf-black and 36 dB for rf-blue, so the maximum applied voltages on the sample are respectively 57 mV and 65 mV. In comparison to the few volts range available for the DC gates, it implies that only a restricted region of

charge configurations are accessible.

In the first chapter section 1.5, it has been introduced that the singlet-triplet spin qubit is defined around the (1,1)-(2,0) charge transition. Therefore, we aim to center the RF stability diagram on it, which means setting the DC voltages to values permitting to reach it with the RF gates. In a first approach one could choose voltages close to the transition to compensate the reduced voltage window. However, a second element must be considered, it is the  $\alpha$ -factor, or gate efficiency, of these RF gates. Since they are deposited almost on top of the estimated quantum dots location, see SEM image of Fig. 3.1, this factor is expected to be much larger than the DC gates one. In the end, the DC gates are set to voltages less negative corresponding to the point A in the DC stability diagram Fig. 3.2a.

In addition to the voltage amplitude, the sampling rate and the intern memory of the instrument are also limited. The minimum sampling rate is 10 MHz, so the slow manipulations like the millisecond per point of the DC stability diagram are avoided. Contrary to the previous restriction this point is not a limitation, it is even useful to investigate the coupling to the electron reservoirs. Indeed, as introduced in the first chapter section 1.3, the coupling can be estimated from the speed of the measurement, time per point. A short measuring time cannot detect slow events. Since the target coupling is about  $\sim$  MHz, the RF stability diagram will be implemented with 1  $\mu$ s per point.

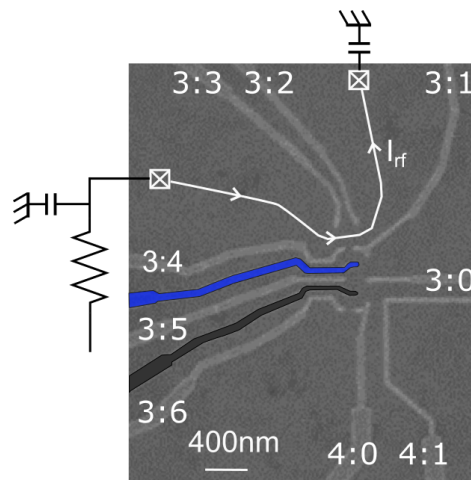


**Figure 3.1** – Scanning electron micrograph of the left double quantum dot with the RF gates coloured in blue and black.

To implement such stability diagram, a sequence where the gate labelled rf-black is swept and the second one, rf-blue, is stepped with this 1  $\mu$ s per point has been developed. The DC and RF stability diagrams should provide the same results. The only differences might be the higher  $\alpha$ -factor of the RF gates and a shift of the position indicating a low coupling to the electron reservoirs, position observable by the stochastic events in Fig. 3.2a. The speed of the measurement being increased by three orders of magnitude, the limit of detection of slow events is necessarily not the same.

A typical RF stability diagram is presented in Fig. 3.2b where the signal is averaged over 30 traces, i.e. 1  $\mu$ s per point repeated 30 times, and a DC one measured with 1.4 ms per point Fig. 3.2a.

Several comments can be made regarding this RF stability diagram. First, the expected large  $\alpha$ -factor of the RF gates can be estimated by comparing the voltage 'distances' for the DC and RF gates with the points B-C and B'-C' of the stability diagrams of Fig. 3.2. From the DC diagram,  $\delta V_{3:6} \approx -50$  mV and  $\delta V_{3:4} \approx -30$  mV, while  $\delta \text{rf-black} \approx -20$  mV and  $\delta \text{rf-blue} \approx -10$  mV. Calculating the ratio of these voltage distances give the RF gates close to three times more efficient than the DC ones. Second, in the RF stability diagram, the window in which the charge degeneracy lines are visible is pretty small. Only a part of the most vertical line is visible, and for the most horizontal one, even less. Furthermore, on this horizontal line, a change of colour, indicating a change of signal shift for a tunneling event, can be observed for approximately rf-blue  $\approx -0.015$  V. These two elements are due to the charge detection which is performed with a SQD, so on the side of a Coulomb peak, the change of sign arises from the change of flank on the peak.

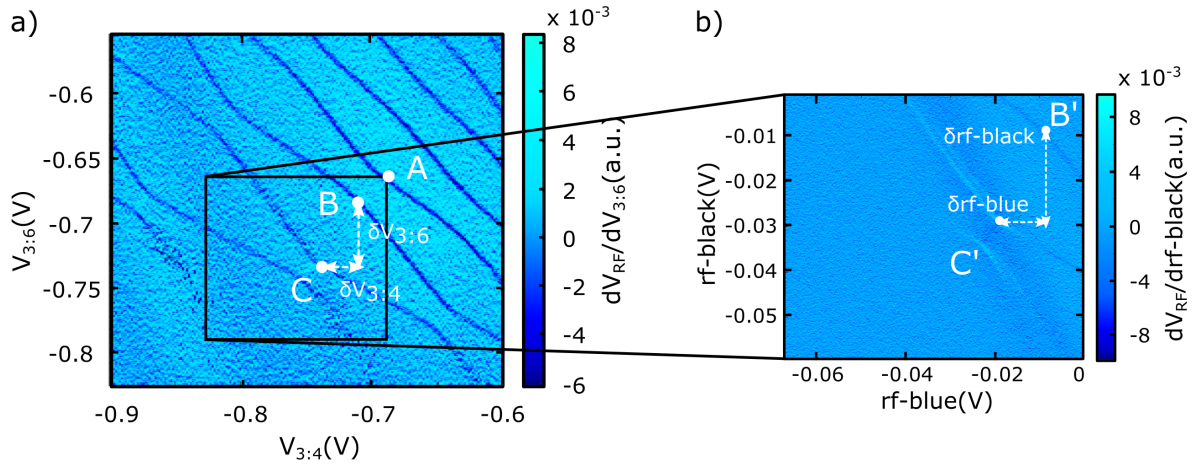


**Figure 3.2** – *a)* Stability diagram in which the derivative of the RF-QPC signal  $dV_{\text{RF}}/dV_{3:6}$  is plotted as a function of  $V_{3:4}$  along the  $x$  axis, and  $V_{3:6}$ , along the  $y$  axis. In this map the point A corresponds to the set DC gate voltages for the implementation of the RF stability diagram. The points B and C are used to compare the efficiency of the DC and RF gates. *b)* Stability diagram using only the RF gates. The derivative of the RF-QPC signal with respect to  $V_{\text{rf-black}}$ ,  $dV_{\text{RF}}/dV_{\text{rf-black}}$ , is plotted as a function of the swept rf-black gate voltage ( $y$  axis) and stepped rf-blue one ( $x$  axis). This map is measured with  $1 \mu\text{s}$  per point repeated 30 times. The voltages are the estimated values on the sample taking into account the AWG amplitude and the attenuation of the coaxial lines. The opposite colours, so change in  $V_{\text{RF}}$  due to a tunnelling event, between the DC and RF stability diagrams is only due to a compensation of the  $\Delta V_{\text{RF}}$  evolution, coming from the use of a RF-QPC, only taken into account for the RF diagram. The points B' and C' are the equivalent position than the B and C one of the DC stability diagram.

Last comment about the RF stability diagram, the disappearance of the most vertical line for rf-blue  $\approx -0.02$  V (rf-black  $\approx -0.04$  V) is due to the low coupling to the reservoir, not the charge sensitivity. The measuring time being  $1 \mu\text{s}$  per point (repeated 30 times), the coupling to the electron reservoir has to be rather close to few tens of microseconds to be measurable. This low coupling is also visible for the same charge degeneracy line in the DC diagram with the stochastic events indicating a

coupling  $\sim$  kHz observable for  $V_{3:6} \approx -0.75$  V.

In conclusion, by measuring a stability diagram with the RF gates we can now have access to the different charge configurations of the double quantum dot, offering the possibility to perform the fast charge manipulations and investigate the different couplings of the system. In addition, the two degeneracy lines being visible with this measuring speed, it indicates that we are close to the target  $\sim$  MHz coupling to the reservoir.

### 3.2.2 Charge manipulations with the RF gates

For our purpose the  $\sim$  MHz coupling is important because it ensures a high coupling between the double quantum dot, so the spin qubit detector, and the ECs. However, so far it is only an estimation relying on the measuring speed, so it should be verified experimentally.

To investigate precisely these couplings, the same experiment than the one performed in the previous chapter (section 2.5) consisting in forcing electron tunnelings is implemented. The experimental procedure is the following: a charge state is initialised by waiting at either the point A(C) of Fig. 3.3, depending on the studied coupling to reservoir, before pulsing to the point B(D). The pulse lengths are arbitrary chosen to values large enough to let the tunneling process occurs.

Three different signal variations are expected, a large one corresponding to the two charge states (by capacitive coupling with the RF gates), point A and B for instance. The two others variations are related to the tunneling event, either an increase of the signal for a charge unloading, or a decrease for an electron loading. Moreover, the charge tunneling being a probabilistic process, from an experiment to the other it will not happen at the same time, so by averaging over many attempts two exponential evolutions are expected, one associated to the electron loading the other to the unloading. The coupling, or tunneling time can be extracted by fitting such data with the following expression:

$$V_{\text{RF}} = a.e^{(-t/\tau)} + \text{offset} \quad (3.1)$$

for the loading of an electron, and for the unloading:

$$V_{\text{RF}} = 1 - a.e^{(-t/\tau)} + \text{offset} \quad (3.2)$$

To verify if the charge tunneling happens in the target quantum dot, the amplitude of the exponentials can be compared between the two measurements, i.e. for each tunnel barrier. The largest signal amplitude is expected for a tunneling event with the quantum dot the closest to the QPC, here for the most vertical line so for the points A and B.

The results of such manipulations are presented in Fig. 3.3 where the three expected signal variations are observable for the two traces. For the trace b of this figure, corresponding to the pulse sequence for the (1,1)-(2,1) charge configurations, the step of  $\Delta V_{\text{RF}}$  for  $t = 200 \mu\text{s}$  indicates the change of charge configuration, with the higher (lower) signal corresponding to the measurement at the point A (B). The

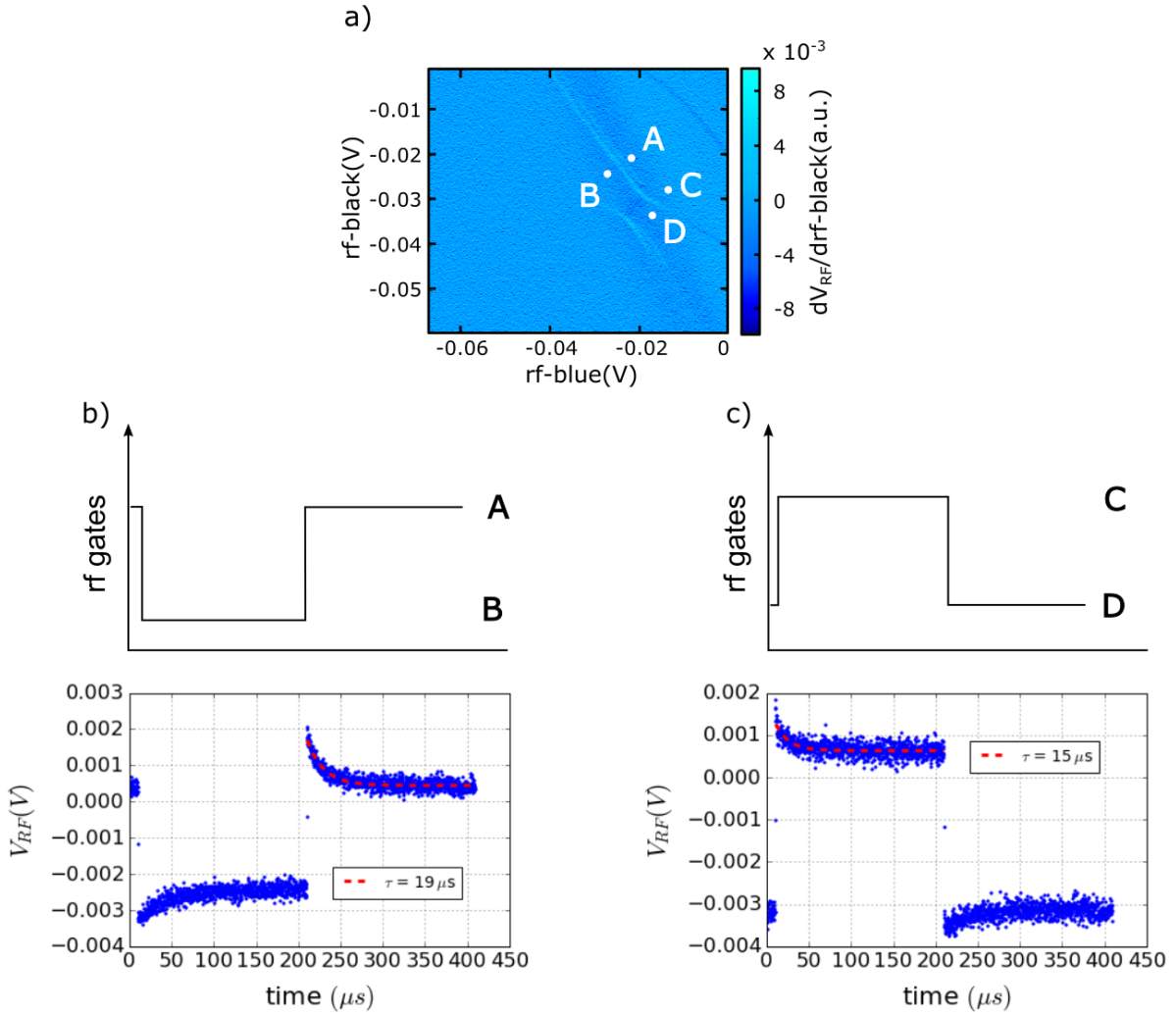


**Figure 3.3** – **a)** RF stability diagram in which the derivative of the RF-QPC signal  $dV_{RF}/drf - black$  is plotted against  $rf-black$  along the  $x$  axis, and  $rf-blue$ , along the  $y$  axis. In white are indicated the different points used to study the coupling to the electron reservoirs. **b)** Pulse sequence around the A and B points according to the RF gates amplitudes to illustrate the different measuring positions. Below is the RF-QPC signal  $V_{RF}$  averaged by repeating this pulse sequence around the  $(1,1)$ - $(2,1)$  charge configurations, showing the two exponential behaviours associated to the unloading and loading of an electron in the lower quantum dot here. The loading of the electron starting at  $200 \mu s$  is fitted with an exponential decay with its expression given in the main text. The result of the fit is represented with the red dashed line with the tunneling time  $\tau$  as legend. **c)** Same than **b)** but for the points C and D so the other tunnel barrier.

electron loading, so the exponentially decreasing  $\Delta V_{RF}$ , is fitted giving a tunneling time of the order of  $19 \mu s$ , consistent with the estimation from the RF stability diagram. For the Fig. 3.3c, the same analysis gives a loading time at the point C of  $15 \mu s$ . As estimated from the RF stability diagram the coupling to the electron reservoirs are in the desired regime.

Finally, the exponential amplitudes are larger in Fig. 3.3b than in Fig. 3.3c, meaning that we are really controlling the charge of each quantum dot.

There is another coupling in our system, the interdot tunnel coupling  $t_c$ , but determining it is more complex than the previous measurements because the target value  $\sim$  GHz, is larger than the detection bandwidth which is only  $\sim$  15 MHz, c.f. previous chapter section 2.4.3. As we will see in the following, a precise estimation of its value, or even indications of it, requires to do spin manipulations.

### 3.3 Preliminary spin measurements

The first requirement to any spin manipulations is the development of the spin readout technique, for us the Pauli spin blockade. An indication of the possibility to use this method is obtained by a similar sequence than the previous one, except that it is implemented around the (1,1)-(2,0) charge transition. The signature of the Pauli spin blockade is an asymmetry in the charge tunneling detection as the one presented in Fig. 3.4a where no tunneling event detected in the (1,1) charge configuration, while a 'slow', few tens microseconds, electron tunneling in (2,0) is measured. As explained in the following, this asymmetry means that the tunneling in (1,1) is defined by the tunnel coupling, larger than the detection bandwidth, while the electron loading in (2,0) is limited by the spin relaxation  $T_1$ .

From the previous measurements the fast charge manipulations have been demonstrated, such as the target coupling to the electron reservoir. If the asymmetry just described is observed experimentally it is an indication that the spin readout via the Pauli spin blockade is possible. In this section this asymmetry is first explained with the description of the Pauli spin blockade, such as the way to measure it. Second, before coming to the different spin manipulations necessary to the development of the coherent exchange oscillations, the measuring position is optimised in order to have the largest spin signal.

#### 3.3.1 Pauli spin blockade based spin readout

The Pauli spin blockade is a spin to charge conversion technique based on the spin selective tunneling process. To understand it, the discussion can be reduced to four spin states, the singlets  $S(1,1)$ ,  $S(2,0)$  and the triplets  $T_0(1,1)$ ,  $T_0(2,0)$  as represented in Fig. 3.4c. A magnetic field being applied the triplets  $|T_+\rangle$  and  $|T_-\rangle$  are repelled by the Zeeman energy. First proposed and measured by [59, 80, 81], this technique relies on the difference of charge configuration depending on the electron spin state in a reduced detuning region (cf. Fig. 3.4c). As introduced in the first chapter 1.5, the two anti-crossing between the spin states  $S(1,1)$ - $S(2,0)$  and the  $T_0(1,1)$ - $T_0(2,0)$  one are not located at the same detuning. The triplet spin states being higher in energy than the singlet, their anti-crossing is at higher energy, larger detuning. Then, locally the (2,0) charge state is preferential for the singlet spin states while it is the (1,1) one for the triplets. The Pauli spin blockade relies on this difference of preferential charge state which appears experimentally while pulsing from the (1,1) to the (2,0) charge configuration in the detuning region coloured in Fig. 3.4c. If the spin states was  $S(1,1)$ , the charge tunneling toward  $S(2,0)$  happen within few nanoseconds defined by the interdot tunnel coupling  $t_c$ . Tunneling event which cannot be measured, the RF-QPC detection bandwidth being 15 MHz. Instead, if the initial state was a triplet  $T_0(1,1)$ , such charge tunneling is not possible because  $T_0(2,0)$  is at higher energy. Consequently, the

---

electrons stay blocked in this metastable  $T_0(1,1)$  spin state until relaxation to the ground state  $S(2,0)$ . Since this relaxation involves a spin flip process, the relaxation time  $T_1$  is rather long, in our configuration it is typically of few tens of microseconds. The charge tunneling is sufficiently delayed so the  $(1,1)$  charge state is maintained for a time large enough to be measured with the RF-QPC.

In the end, if a tunneling event is detected it means that the spin state was a triplet  $|T_0\rangle$ , otherwise it was a singlet  $|S\rangle$ .

The procedure permitting to observe this spin blockade is similar to the one used in the previous section. The base idea is to force the detection of triplet spin states, so force the detection of a charge tunneling event. To do so, first a spin state has to be initialised. The  $S(2,0)$  spin state being a ground state of the system, it is the perfect candidate obtained by waiting in the  $(2,0)$  charge configuration until the complete relaxation of the spin state,  $500\ \mu\text{s}$  for us. To have a measurable information, a triplet  $|T_0\rangle$  is necessary, provided thanks to the  $|S\rangle$ - $|T_0\rangle$  spin mixing in the  $(1,1)$  charge configuration. This spin mixing is detailed in the following, section 3.5, and for the moment it is only regarded as a process changing the 100% of initialised  $|S\rangle$  to an equal mixture of  $|S\rangle$  and  $|T_0\rangle$  after a mixing time larger than  $T_2^*$ , typically  $t_{\text{mixing}} = 100\ \text{ns}$ . Finally, the detection is performed by pulsing back to the  $(2,0)$  charge configuration. If the spin state was a singlet, there is no signal variation, while a tunneling event is detected for a triplet state.

The spin relaxation being probabilistic, by averaging such sequence over many attempts an exponential decay similar to an electron loading is obtained. Just like the one used in the previous chapter section 2.5, also presented in Fig. 3.4b. The asymmetry of tunneling event mentioned previously and shown in Fig. 3.4a is precisely this sequence. The tunneling from  $(2,0)$  to  $(1,1)$  is not measurable since defined by the tunnel coupling larger than the detection bandwidth, and only the triplet states when pulsing from  $(1,1)$  to  $(2,0)$  are detected since the spin relaxation time is long enough to be recorded.

By fitting such exponential decay, two information can be extracted. The first one is the triplet probability corresponding to the voltage amplitude  $\Delta V_{\text{RF}}$  shown in Fig. 3.4b. The second is the spin relaxation time  $T_1$  which is the characteristic time of the exponential decay. Another advantage of this spin to charge conversion technique is the spin initialisation and measurement which are performed in the same time. Indeed, to extract precisely the triplet probability, the complete relaxation of the spin state is necessary, which corresponds to the initialisation of the singlet for the next point.

In conclusion, by using this Pauli spin blockade as spin to charge conversion technique, the triplet probability and the spin relaxation time  $T_1$  can be obtained with a high level of confidence. In addition, it is extremely simple to implement since only one voltage pulse toward the  $(2,0)$  charge state is required. In the same time, it initialises the spin state with a success rate close to 100%.

As presented in the previous chapter, the single shot spin readout can be employed in addition to the RF-QPC signal averaging method just described with this exponential fit. To distinguish between the two methods and avoid a rough conversion from the voltage amplitude  $\Delta V_{\text{RF}}$  to percentage, the results of the single shot acquisition mode are expressed in percentage while  $\Delta V_{\text{RF}}$  of the signal averaging acquisition mode is only expressed in volt.

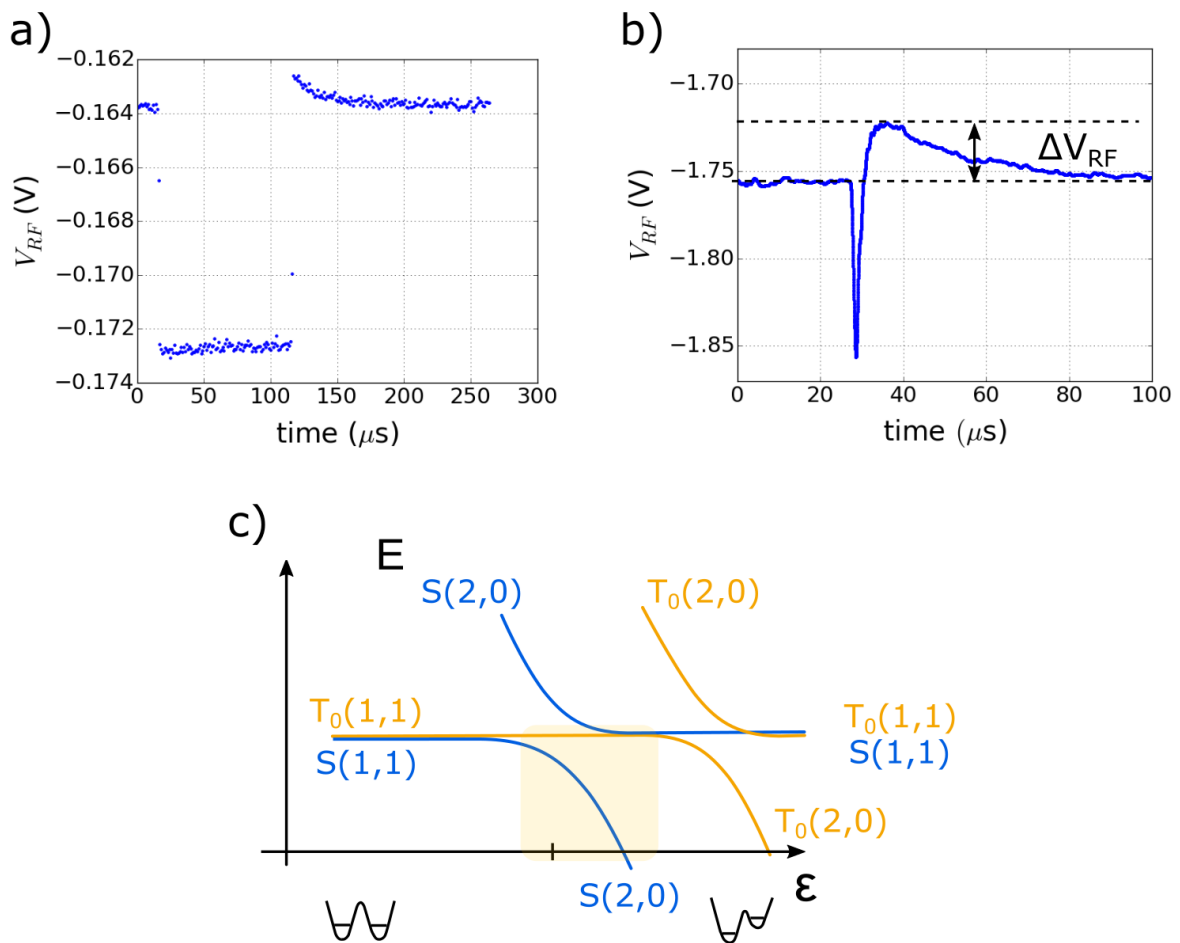


**Figure 3.4** – *a)* The RF-QPC signal  $V_{RF}$  is shown as a function of the measurement time, this trace is obtained by averaging  $V_{RF}$  while repeating a pulse sequence around the (2,0)-(1,1) charge transition. The lower signal is associated to the (1,1) charge configuration while the upper one the (2,0) one. There, the exponential decay of  $V_{RF}$  is the characteristic behaviour of a tunneling event, not observed in the other charge configuration. This asymmetry is the signature of Pauli spin blockade. *b)* Similar trace with here 100 ns spend in the (1,1) charge configuration. It is the result of the average over 2000 traces of single shot spin readout attempts. The first part of the trace is the initialisation of the singlet state  $S(2,0)$ . The deep at 30  $\mu\text{s}$  corresponds to the manipulation time. The exponential decay is the signature of the triplet  $|T_0\rangle$  spin state relaxation toward the ground singlet state  $|S\rangle$ . This decay is fitted with a similar expression to the 3.1 one to extract the voltage amplitude  $\Delta V_{RF}$  of the spin triplet RF-QPC signal and the spin relaxation time  $T_1$ , here about 30  $\mu\text{s}$ . *c)* Energy diagram restricted to the four spin states the singlets  $S(1,1)$ ,  $S(2,0)$  and the triplets  $T_0(1,1)$ ,  $T_0(2,0)$ . The coloured box corresponds to the detuning region over which the Pauli spin blockade described in the main text can be obtained.

### 3.3.2 Measuring position using the Pauli spin blockade

The principle of the Pauli spin blockade being presented, we can now describe how to find the optimal measuring position for the following spin manipulations. Indeed, this spin blockade is only measurable in a restricted region of detuning, this non access to the  $T_0(2,0)$  spin state being only true for a finite range of detuning (cf. Fig. 3.4c).

To investigate the spin readout efficiency and by this way find the optimal measuring position, the same procedure than the one described previously is implemented but for different measuring positions.

After initialising the S(2,0) spin state by waiting at the measuring/initialising position for 500  $\mu\text{s}$ , the spin mixing is forced in the (1,1) charge configuration, point C of Fig. 3.5, for a time  $t_{mixing} = 100$  ns. The spin readout takes place at a position stepped between B and A of the same figure. The experimental procedure is represented in the Fig. 3.5 with the experimental points A, B and C indicated in the stability diagram. The result of this experiment are presented in Fig. 3.5c, where the blue dots correspond to the triplet probability and the red ones the spin relaxation time  $T_1$ .

The evolution of the triplet probability and the relaxation time can be understood as follow. First, the measuring position like the point B being in the (1,1) charge configuration, there is no spin to charge conversion, the spin signal is equal to zero. This non zero  $\Delta V_{RF}$  signal is just an artefact of the signal extraction. For  $\varepsilon \sim 0$  the spin readout is possible but limited by the hybridisation of the singlets S(1,1), S(2,0). Indeed, the spin to charge conversion is only possible if the charge states are different, so it is only possible between  $T_0(1,1)$  and S(2,0). The relaxation from  $T_0(1,1)$  to S(1,1) cannot be detected with the charge detector. The lifting of this hybridisation being progressive, the spin to charge conversion efficiency is increasing with the S(2,0) proportion, corresponding to the  $\varepsilon = -1$  to  $\varepsilon = 3$  mV region in Fig. 3.5c.

In this region, the spin relaxation time  $T_1$  is limited by the  $|S\rangle$ - $|T_0\rangle$  spin mixing in the (2,0) charge configuration [59, 60, 82]. This mixing is similar to the one used previously and explained in the section 3.5.2. To understand the evolution of  $T_1$ , we can just mentioned that it induces a rotation of the spin state between  $T_0(1,1)$  and S(1,1), as sketched in the orange box of Fig. 3.5a, with an efficiency depending on their energy separation. In this detuning region, the energy splitting is rather constant, see energy diagram Fig. 3.5a, explaining why  $T_1$  is stable to 30  $\mu\text{s}$  approximately.

For larger detuning, another hybridisation has to be taken into account, the  $T_0(1,1)$ ,  $T_0(2,0)$  one. Similarly to the singlet hybridisation, this one impacts the efficiency of the spin to charge conversion, a part of the triplet being already in the (2,0) charge state. Here again, by sweeping the detuning toward more positive values the amount of  $T_0(2,0)$  is increasing, so the spin readout efficiency is dropping. This evolution is visible experimentally by the decrease of  $\Delta V_{RF}$  in the second half of the experiment starting from  $\varepsilon = 4$  mV.

Concerning the relaxation time, as it can be noticed in the energy diagram of Fig. 3.5a, at this anti-crossing between  $T_0(1,1)$ ,  $T_0(2,0)$  the energy splitting between S(1,1) and  $T_0(1,1)$  is increasing with the detuning. It induces a reduction of the  $|S\rangle$ - $|T_0\rangle$  spin mixing efficiency, lifting the limitation on the spin relaxation. Experimentally observed by its progressive increase up to more than 100  $\mu\text{s}$  starting from  $\varepsilon = 7$  mV.

From these results, we select the working position as the position where the spin to charge conversion is the most efficient, corresponding here to  $\varepsilon = 3$  mV, with a spin relaxation time  $T_1 \approx 30$   $\mu\text{s}$ . The initialisation for 500  $\mu\text{s}$  is therefore sufficiently long to ensure a perfect initialisation in the singlet S(2,0) spin state.

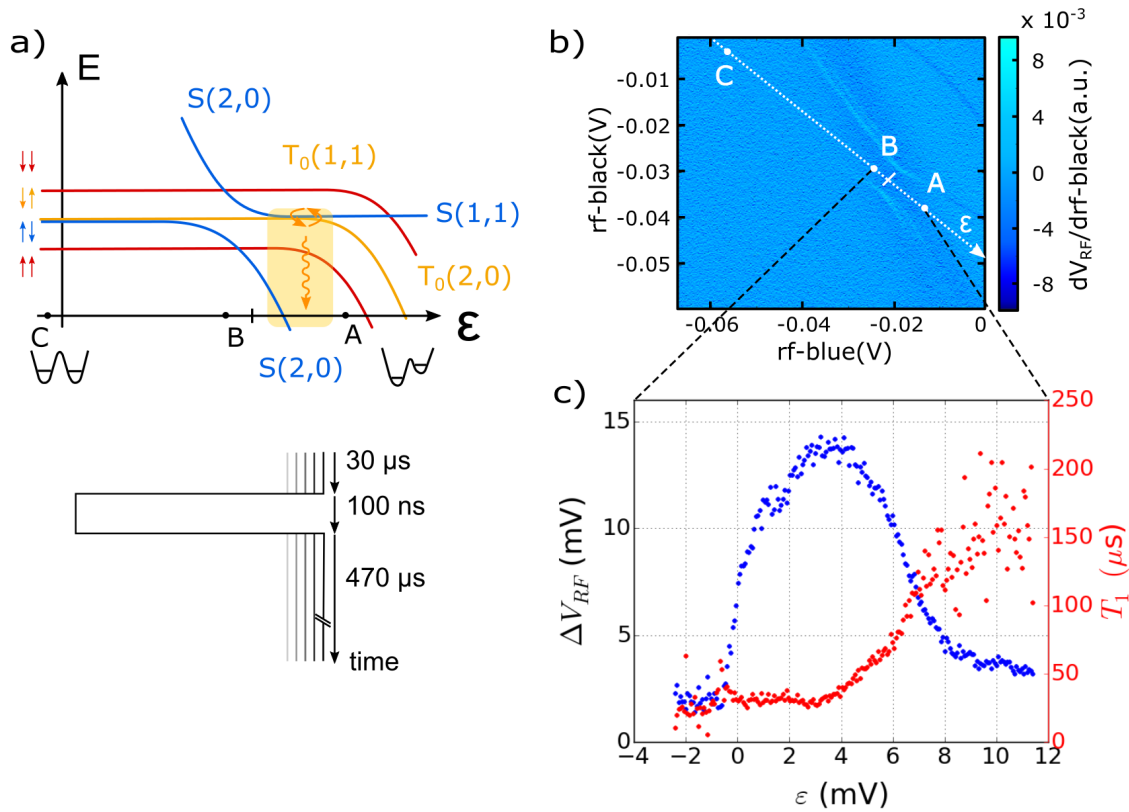


**Figure 3.5** – *a*) Energy diagram of the different spin states for the (1,1)-(2,0) charge transition, and the points used in the pulse sequence sketched just below. The orange box highlighted the region where the  $S(1,1)$  and  $T_0(1,1)$  can be mixed via the  $|S\rangle - |T_0\rangle$  spin mixing. The pulse sequence is composed by an initialisation of the  $S(2,0)$  spin state at the measuring position before applying a detuning pulse toward the point C for a time  $t_{mixing} = 100$  ns. Finally the spin readout using the Pauli spin blockade is performed at a position stepped between B and A. *b*) RF stability diagram in which the derivative of the RF-QPC signal  $dV_{RF}/drf$  – black is plotted against  $rf$ -black along the x axis, and  $rf$ -blue, along the y axis. The white dashed arrow corresponds to the detuning axis, and the different experimental points are labelled in white. *c*) The voltage amplitude  $\Delta V_{RF}$  of the spin triplet RF-QPC signal in blue and the spin relaxation time  $T_1$  in red are plotted as a function of the detuning  $\epsilon$  being here the measuring position. For negative detuning the spin signal is zero, the  $\Delta V_{RF} \approx 2$  mV is an artefact of the signal extraction. The triplet signal  $\Delta V_{RF}$  is increasing from  $\epsilon \approx 0$  to  $\epsilon \approx 4$  mV due to the progressive lifting of the  $S(1,1)$ ,  $S(2,0)$  hybridisation. For larger detuning the hybridisation between  $T_0(1,1)$ ,  $T_0(2,0)$  lifts the Pauli spin blockade inducing the decrease of the spin to charge conversion efficiency so of  $\Delta V_{RF}$ . The spin relaxation time is first limited by the  $|S\rangle - |T_0\rangle$  spin mixing as sketched in the energy diagram. For large  $\epsilon$  this mixing is losing in efficiency, so  $T_1$  is less limited and therefore increases with  $\epsilon$ .

### 3.4 Detuning mapping of the (1,1)-(2,0) spin states

The optimal measuring position with the Pauli spin blockade being defined, the development of the sequence to implement the coherent exchange oscillations can start. These oscillations are induced when an initialised state in the  $|\uparrow\downarrow\rangle, |\downarrow\uparrow\rangle$  spin basis is non-adiabatically brought in the  $|S\rangle, |T_0\rangle$  one. However, as presented previously the spin readout and initialisation are performed in the singlet-triplet spin basis.

Therefore, during the implementation of these oscillations, presented in the section 3.6, a change of spin basis is necessary. First from  $|S\rangle, |T_0\rangle$  to  $|\uparrow\downarrow\rangle, |\downarrow\uparrow\rangle$ , after the spin initialisation, and vice versa for the spin readout. This transfer involves the passage of the manipulated spin state through three crossings. The first one is the S(2,0)-S(1,1) anti-crossing already mentioned, the second one is  $|S\rangle, |T_+\rangle$  crossing, and finally in the (1,1) charge configuration the change of eigen spin basis in itself between  $|\uparrow\downarrow\rangle, |\downarrow\uparrow\rangle$  and  $|S\rangle, |T_0\rangle$ . Before coming to the implementation of the spin oscillations, we focus on the study of these crossings since we have to control the passage through them, depending on the crossed one the pulse has to be adiabatic or not. This notion of adiabaticity is developed in the next section, but before studying in detail the nature of the pulse, these crossings have to be localised. One is already known, the S(2,0)-S(1,1) one, remains the two last ones.

To localise them, the singlet-triplet mixing similar to the one used previously can be used. Before describing the measurement procedure, we explain why these two crossings are important for the coherent exchange oscillations and how such mixing can provide the information of their location.

The  $|S\rangle, |T_+\rangle$  crossing is studied to avoid a mixing between these two spin states during the implementation of the oscillations, so to avoid a change of the initialised singlet spin state. Even so, this mixing can be used to get a measurable information with the spin blockade, the spin readout being similar for the triplet  $|T_+\rangle$  than for the  $|T_0\rangle$ .

The final change of spin basis is more critical in the implementation of the coherent exchange oscillations since it corresponds to the spin state initialisation in the  $|\uparrow\downarrow\rangle, |\downarrow\uparrow\rangle$  spin basis. In order to be optimised it has to be performed in a 'pure'  $|\uparrow\downarrow\rangle, |\downarrow\uparrow\rangle$  spin basis, cf. section 3.6. However, in this (1,1) charge configuration, due to the exchange interaction, the two spin bases of the system can hybridised. The degree of hybridisation between them is given by the ratio of two energies: the Zeeman energy due to the difference of nuclear polarisation  $\Delta B_{nuc,z}$  between the two quantum dots (cf. first chapter section 1.6.2), and the exchange energy  $J(\varepsilon)$  (see Fig. 3.6). This ratio being also responsible of the efficiency of the  $|S\rangle$ - $|T_0\rangle$  spin mixing, cf. section 3.5, it can be used to study the degree of hybridisation between these two spin bases. The 'pure'  $|\uparrow\downarrow\rangle, |\downarrow\uparrow\rangle$  basis is obtained when  $J(\varepsilon) \sim 0$ , observed experimentally by the most efficient spin mixing, largest triplet probability, when the system has been initialised as a singlet spin state.

In practice, the experimental sequence is rather simple and equivalent to the one followed in the previous section, except that here, it is the mixing position which is stepped. After initialisation of the singlet spin state via relaxation at the measuring/initialising position, point M of Fig. 3.6, the mixing takes place at a position stepped between C and M of Fig. 3.6 for a time  $t_{mixing} = 100$  ns, before performing the spin readout at this point M.

The first mixing position being deeply in the (1,1) charge configuration, the eigen spin basis is  $|\uparrow\downarrow\rangle, |\downarrow\uparrow\rangle$ , with  $J \sim 0$ . Hence, the hybridisation with the  $|S\rangle, |T_0\rangle$  spin basis is weak and the mixing should be the most efficient, so the triplet probability should be large. This probability should even be maximal and then decrease when moving  $\varepsilon$  toward 0 mV. Indeed, as it can be noticed in the energy diagram, by displacing  $\varepsilon$  in that direction,  $J$  is increasing. The  $|S\rangle - |T_0\rangle$  spin mixing is therefore losing in efficiency, indicating the change of spin basis. This change is observed by a reduction of the triplet probability until being zero down to the measuring position.

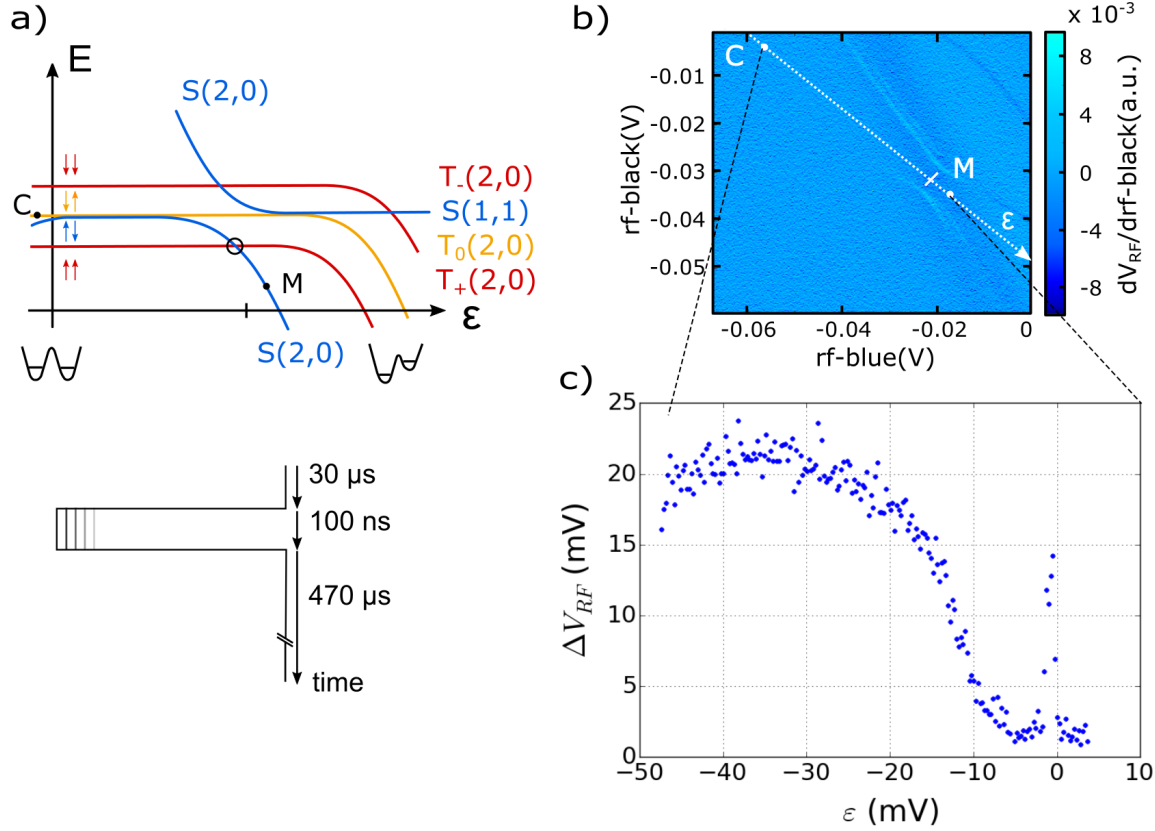


**Figure 3.6** – **a)** Energy diagram of the different spin states for this (1,1)-(2,0) charge transition with the representation of the experimental pulse sequence and the different points of it. The  $|S\rangle$ ,  $|T_+\rangle$  crossing is circle and the exchange energy  $J(\epsilon)$  is also represented. **b)** RF stability diagram in which the derivative of the RF-QPC signal  $dV_{RF}/df - \text{black}$  is plotted against  $\text{rf-black}$  along the  $x$  axis, and  $\text{rf-blue}$ , along the  $y$  axis. The white dashed arrow corresponds to the detuning axis, and the different experimental points are labelled in white. **c)** The voltage amplitude  $\Delta V_{RF}$  of the spin triplet RF-QPC signal is shown as a function of the mixing position  $\epsilon$ . Starting from negative  $\epsilon$ ,  $\Delta V_{RF}$  increases, reaches a plateau and starts to decrease until being zero starting from  $\epsilon \approx -6$  mV. This evolution is related to the efficiency of the  $|S\rangle - |T_0\rangle$  spin mixing explained in the main text. The peak for  $\epsilon = -2$  mV corresponds to the  $|S\rangle$ ,  $|T_+\rangle$  crossing.

Contrary to the  $|S\rangle - |T_0\rangle$  spin mixing, the  $|S\rangle - |T_+\rangle$  one is only possible for a restricted range of detuning (c.f. subsection 3.5.2), circle in Fig. 3.6a, it will be observed by a peak of triplet probability expected for a detuning close to  $\epsilon = 0$ . The spin blockade being similar for the two triplet spin states, there is no possible distinction between the two in the spin signal.

The result of such experiment is presented in Fig. 3.6c where the triplet signal  $\Delta V_{RF}$  follows its expected evolution. The largest signal is obtained for the most negative detuning before decreasing to zero while sweeping the detuning toward  $\epsilon = 0$ . Here again the non zero  $\Delta V_{RF}$  is an artefact of the signal extraction. The peak of  $\Delta V_{RF}$  for  $\epsilon = -2$  mV corresponds to the  $|S\rangle$ ,  $|T_+\rangle$  crossing.

The evolution of  $\Delta V_{RF}$  for the detuning range of  $[-45$  mV,  $-35$  mV] can be discussed more in detail

since it does not correspond precisely to the earlier explanation, with first an increase and a stabilisation. As mentioned, this probability, traducing here the efficiency of the spin mixing, depends on the value of the exchange energy  $J(\varepsilon)$ . As represented in the full energy diagram in the first chapter Fig. 1.6, it is increasing while moving from (1,1) to the (2,0) charge configuration, but also from (1,1) to (0,2). Then, this increase of triplet RF-QPC signal from  $\varepsilon = -45$  mV to  $-35$  mV simply indicates a decrease of the exchange energy associated to this second charge transition, until being close to zero.

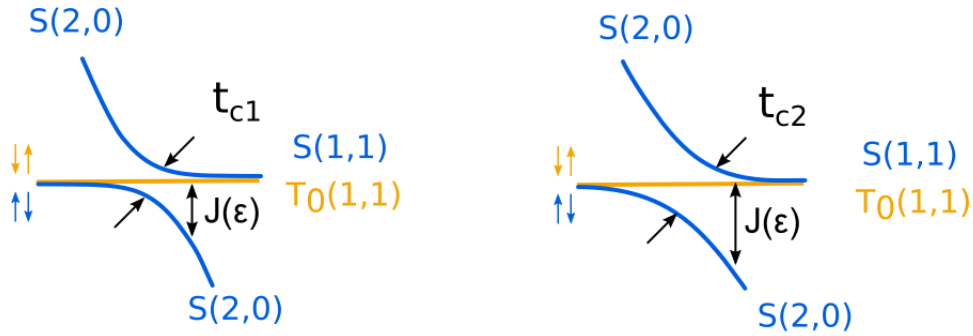


**Figure 3.7** – Sketch of the effect of the tunnel coupling on the exchange energy  $J(\varepsilon)$  and the energy separation between  $S(1,1)$  and  $T_0(1,1)$ , with  $t_{c1} < t_{c2}$ . For the largest tunnel coupling  $t_{c2}$ ,  $J(\varepsilon)$  is larger than for a smallest tunnel coupling  $t_{c1}$  at the same detuning position. The same way, the  $S(1,1)$ ,  $T_0(1,1)$  energy separation increases with  $t_c$ .

Besides the location of the two researched crossings, this measurement indicates also that the tunnel coupling is close to the target regime. This information is also extracted and related to the efficiency of the  $|S\rangle - |T_0\rangle$  spin mixing.

Around the  $|S\rangle$ ,  $|T_+\rangle$  crossing the triplet probability is equal to zero, meaning that the  $|S\rangle - |T_0\rangle$  mixing is already not possible anymore for such detuning values, i.e. the exchange energy  $J(\varepsilon)$  is large enough to prevent it. This energy is indirectly related to the tunnel coupling via the  $S(2,0)$ - $S(1,1)$  anti-crossing as sketched in Fig. 3.7. For the same  $\varepsilon$ ,  $J(\varepsilon)$  will be larger for a large  $t_c$  than for a small one. This relation between tunnel coupling and exchange energy can be found when the two quantum dots are aligned, so  $\varepsilon = 0$ , in the Hubbard approximation [83, 84, 85], where  $J = 4t_c^2/E_c$ , with  $E_c$  the charging energy (c.f. first chapter section 1.1.3). Then, the tunnel coupling influences  $J(\varepsilon)$  so the efficiency of the  $|S\rangle - |T_0\rangle$  spin mixing. Experimentally we noticed that  $\Delta V_{RF}$  is zero around this  $|S\rangle$ ,  $|T_+\rangle$  crossing when  $t_c$  is close to the target value  $\sim$  GHz.

The two researched crossings are now localised and the adiabaticity of the pulse through them can be investigated. This investigation is important because an incomplete control of the adiabaticity of the pulses would lead to a lower quality of the manipulations. The quality of the manipulations is given by the spin visibility which can be seen as the proportion of spin state controlled during the experiment. For the final experiment, the single travelling electron will induce a variation of the spin states population, a shift in the measured triplet probability. This variation of population concerning only the controlled

spin states, if the spin visibility is small, the step signal, the shift of triplet probability will be small too, so difficult to detect. Thus, to facilitate the detection, the spin visibility has to be as large as possible, meaning having a quasi perfect control of the spin state during its manipulation.

### 3.5 Concept of adiabaticity and singlet triplet mixing

As we will see, having a high spin visibility means controlling the adiabaticity or non-adiabaticity of the passage through these three crossings. First, this notion of adiabaticity is explained, focussed on the S(2,0)-S(1,1) anti-crossing, followed by the explanation of the  $|S\rangle - |T_0\rangle$  spin mixing and how it can be used to determine the nature of the pulse through this anti-crossing.

The two other crossings will be studied in the following during the development of the experimental procedure to realise the coherent exchange oscillations, subsection 3.6.1.

#### 3.5.1 Concept of adiabaticity

To understand the concept of adiabaticity, an equivalent system than ours is considered with two ground states  $|1\rangle$ ,  $|2\rangle$ , and their respective excited states  $|1'\rangle$ ,  $|2'\rangle$ , see Fig. 3.8. The Hamiltonian describing it is:

$$H = \begin{pmatrix} -\varepsilon/2 & \theta \\ \theta & \varepsilon/2 \end{pmatrix} \quad (3.3)$$

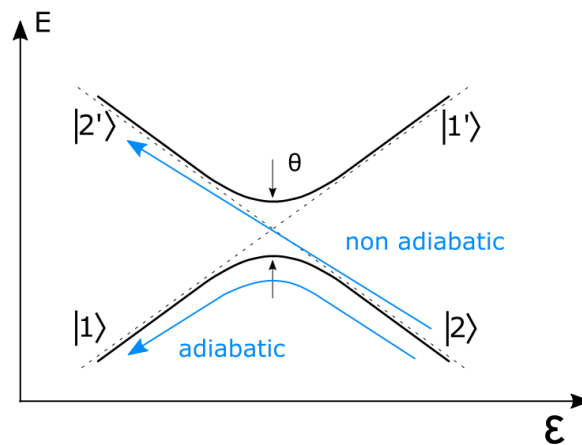


**Figure 3.8** – Sketch used in the Landau-Zener theory, with two ground states  $|1\rangle$  and  $|2\rangle$  and their respective excited states  $|1'\rangle$  and  $|2'\rangle$ , by changing the detuning  $\varepsilon$  one can go from a ground state to the other. The Landau-Zener theory gives the probability for a initial  $|2\rangle$  to tunnel toward its excited state corresponding to a non-adiabatic tunneling with respect to the tunnel coupling  $\theta$ . If the probability is close to zero the pulse is considered as adiabatic.

Here also, the detuning  $\varepsilon$  indicates what is the correct ground state among the two, and when these states are coupled with a tunnel coupling  $\theta$  an anti-crossing appears, see Fig. 3.8.

The notion of adiabaticity or non-adiabaticity arises while pulsing  $\varepsilon$ , transporting a prepared state  $|2\rangle$

toward the  $|1\rangle$  one. The question is, will it actually reach this state or not? The answer depends on the speed of the transfer with regards to the tunneling  $\theta$ , how fast the anti-crossing is crossed. If the pulse is too fast the system reach the excited  $|2'\rangle$ , otherwise it stays in the ground state for a slow transfer or high tunnel coupling. The Landau-Zener theory [86] models this situation and gives the probability to end up in the excited state:

$$P_{LZ} = e^{-2\pi\Gamma} \quad , \quad \Gamma = \frac{\theta^2}{\hbar d\varepsilon/dt} \quad (3.4)$$

with  $\hbar$  the Planck constant,  $d\varepsilon/dt$  is the speed in  $\varepsilon$ .

A word on the relation between adiabaticity and spin visibility. For the spin manipulations, the problem of uncontrolled adiabaticity is the fact that, at the end of the pulse, a part of the manipulated spin states will not reach the target state. For instance, if the pulse is designed to be adiabatic, a part of the manipulated spin state, defined by the Landau-Zener probability, cross it non-adiabatically. Meaning that after the pulse, only a part of the prepared state are still controlled and following the designed sequence. The full procedure of the coherent exchange oscillations passes two times through each crossings, so, if the adiabaticity of the pulses are not precisely controlled, quickly the spin visibility drops.

From the previous measurements, the nature, adiabaticity or non-adiabaticity, of the pulse through the S(2,0)-S(1,1) anti-crossing cannot be clearly defined. This pulse is designed to induce an equipartition of the  $|S\rangle$ ,  $|T_0\rangle$  spin states, but it is obtained in both configuration. For an adiabatic pulse, this equipartition is induced after initialising a singlet and applying a pulse toward the (1,1) charge configuration to force the mixing in the  $|\uparrow\downarrow\rangle$ ,  $|\downarrow\uparrow\rangle$  spin basis. In case of non-adiabatic pulse, the prepared singlet state becomes an excited S(2,0) spin state. Excited state which relaxes to the  $|\uparrow\downarrow\rangle$  spin state, ground state of the  $|\uparrow\downarrow\rangle$ ,  $|\downarrow\uparrow\rangle$  eigen spin basis in this (1,1) charge configuration, in a time theoretically estimated to be subnanosecond [87]. The projection of this  $|\uparrow\downarrow\rangle$  spin state by the Pauli spin blockade gives in the end 50% of triplet and 50% of singlet, same result than for an adiabatic pulse.

The situation is more complex for small negative  $\varepsilon$  position of mixing, when the two spin bases are coexisting, but basically for the mixing in the pure  $|\uparrow\downarrow\rangle$ ,  $|\downarrow\uparrow\rangle$  spin basis region, the distinction between adiabatic and non-adiabatic pulse is not possible from the previous measurements.

The difference between these two pulses is observable for the short mixing time, the timescales to reach the equipartition being different. For a non-adiabatic pulse, the full mixing is obtained after few nanoseconds [87], while it is obtained for approximately  $2.T_2^* \sim 20$  ns for an adiabatic one.

Regarding the development of the coherence exchange oscillations, this pulse has to be adiabatic, which regarding the Landau-Zener probability is possible when having a large tunnel coupling. Thus, by studying the short  $|S\rangle - |T_0\rangle$  spin mixing time the nature of the pulse can be determined. If the pulse is adiabatic it means that  $t_c$  is large enough to implement the coherent exchange oscillations, confirming the indication of the previous measurements with the mapping of the  $|S\rangle$ ,  $|T_0\rangle$  spin mixing.

### 3.5.2 singlet-triplet spin mixing

The spin mixing, here the  $|S\rangle - |T_0\rangle$  one, refers to the equipartition of these two spin states after the oscillation of the spin state with a frequency related to the gradient of nuclear spin between the two quantum dots,  $\Delta B_{nuc,z}$ . This mixing happens when a singlet  $|S\rangle$ , or a triplet  $|T_0\rangle$ , is brought non-adiabatically in a spin basis where it is not one of the eigenstate, the  $|\uparrow\downarrow\rangle, |\downarrow\uparrow\rangle$  one. There, it starts to oscillate around the quantisation axis with a frequency defined by the Zeeman energy arising from  $\Delta B_{nuc,z}$  labelled  $E_{Z,nuc}$  with  $E_{Z,nuc} = g\mu_B\Delta B_{nuc,z}$ . The probability to measure a triplet state after an oscillating time  $t$  is calculated as follow:

$$|\Psi(t)\rangle = \frac{1}{\sqrt{2}} \left( |\uparrow\downarrow\rangle e^{i\frac{g\mu_B\Delta B_{nuc,z}t}{2\hbar}} - |\downarrow\uparrow\rangle e^{-i\frac{g\mu_B\Delta B_{nuc,z}t}{2\hbar}} \right) \quad (3.5)$$

$$|\Psi(t)\rangle = \frac{1}{2} \left( |S\rangle \left( e^{i\frac{g\mu_B\Delta B_{nuc,z}t}{2\hbar}} + e^{-i\frac{g\mu_B\Delta B_{nuc,z}t}{2\hbar}} \right) - |T_0\rangle \left( e^{i\frac{g\mu_B\Delta B_{nuc,z}t}{2\hbar}} - e^{-i\frac{g\mu_B\Delta B_{nuc,z}t}{2\hbar}} \right) \right) \quad (3.6)$$

$$|\Psi(t)\rangle = |S\rangle \cos\left(\frac{g\mu_B\Delta B_{nuc,z}t}{2\hbar}\right) + i|T_0\rangle \sin\left(\frac{g\mu_B\Delta B_{nuc,z}t}{2\hbar}\right) \quad (3.7)$$

Finally, the triplet probability is:

$$P_{T_0}(t) = |\langle T_0|\Psi(t)\rangle|^2 = \frac{1 - \cos\left(\frac{g\mu_B\Delta B_{nuc,z}t}{\hbar}\right)}{2}. \quad (3.8)$$

This expression stands for a single experiment, but in practice many measurements are realised, so the fluctuations of the nuclear spin bath introduced in the first chapter (section 1.6.2) should be considered. Since in average  $\Delta B_{nuc,z} = 0$ , then  $\cos\left(\frac{g\mu_B\Delta B_{nuc,z}t}{\hbar}\right) \approx 1$  and it remains only the dephasing term [67]:

$$P_{T_0}(t) = \frac{1 - e^{-(t/T_2^*)^2}}{2} \quad (3.9)$$

the Gaussian envelop arises from the Gaussian distribution of the nuclear spin polarisation, see first chapter section 1.6.2.

The previously mentioned notions of hybridisation and spin mixing efficiency between the two spin bases of our system can now be explained in detail assuming an adiabatic pulse through the S(2,0)-S(1,1) anti-crossing. It has been mentioned that it is the ratio of the Zeeman energy  $E_{Z,nuc}$ , and the exchange energy  $J(\varepsilon)$  which is defining it. When  $J \ll E_{Z,nuc}$ , so  $J \sim 0$  since  $E_{Z,nuc} \approx 100$  neV, it means that the eigen spin basis is  $|\uparrow\downarrow\rangle, |\downarrow\uparrow\rangle$ . Thus, the pulse toward the (1,1) charge configuration brings non-adiabatically every, at least a large proportion, manipulated spin states in this spin basis. The spin mixing is therefore the most efficient so it leads to the largest triplet probability. On the contrary, if  $J \sim E_{Z,nuc}$ , the two spin bases are hybridised, and only a part of the manipulated spin state are brought in the  $|\uparrow\downarrow\rangle, |\downarrow\uparrow\rangle$  spin basis, so the mixing is less efficient. In the case where  $J \gg E_{Z,nuc}$ , the eigen spin basis is  $|S\rangle, |T_0\rangle$  so there is no mixing.

The  $|S\rangle - |T_+\rangle$  mixing can also be discussed since it was used to localise the crossing between these two spin states. Actually, it is the same phenomenon than the one just described, except that it is the transversal nuclear spin polarisation  $\Delta B_{nuc,x,y}$  which is involved in the oscillations. The resulting Zeeman energy being small, this crossing is crossed non-adiabatically almost every time, preventing the change of spin state only possible for an adiabatic pulse as described in [58, 66, 68]. Then, this mixing occurs only at the crossing position, explaining why it is observed only with a peak of triplet probability, see Fig. 3.6c.

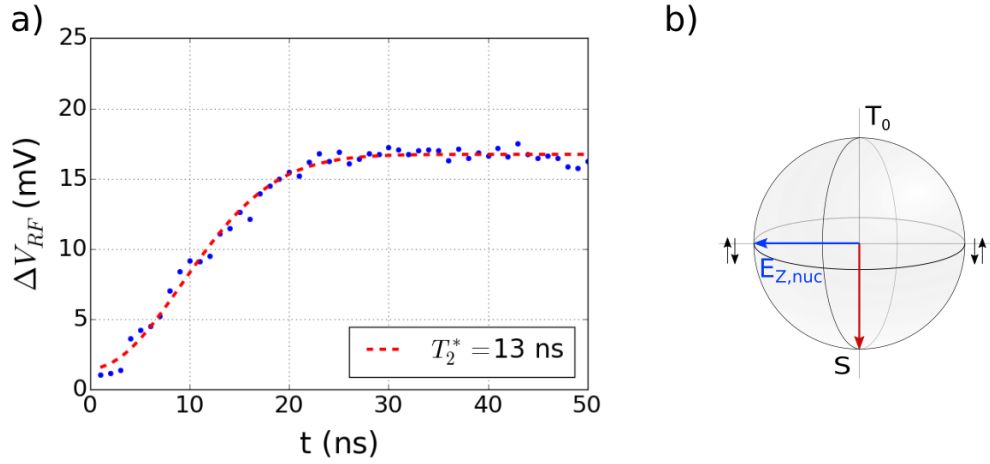


**Figure 3.9** – **a)** Voltage amplitude  $\Delta V_{RF}$  of the spin triplet RF-QPC signal as a function of the mixing time  $t$  in the  $(1,1)$  charge configuration, at point C of Fig. 3.6. The red dashed line is the result of the fit with the expression 3.9. The dephasing time  $T_2^* = 13$  ns is extracted from the fit. **b)** Representation of this experiment in a Bloch sphere, with the initialised  $|S\rangle$  spin state oscillating around the quantisation axis  $E_{Z,nuc}$ , between the states  $|S\rangle$  and  $|T_0\rangle$ .

Coming back to the study of the third crossing, the  $S(2,0)$ - $S(1,1)$  anti-crossing, it has been explained that studying the short mixing time permits to conclude on the nature of the spin evolution resulting from the pulse. Oscillations in the  $|\uparrow\downarrow\rangle, |\downarrow\uparrow\rangle$  spin basis or relaxation from the excited  $S(2,0)$ , with two different timescales to reach the complete spin mixing. There is another element which can add an argument to this differentiation, it is the shape of the mixing trace. In case of adiabatic pulse, the trace should have a Gaussian shape. The non-adiabatic pulse means a relaxation process, which is associated to an exponential behaviour. By combining the shape of the trace and the mixing time, it is possible to distinguish the two pulses nature with a reasonable level of confidence.

The experimental procedure to measure this  $|S\rangle - |T_0\rangle$  spin mixing is similar to the previous ones. The initialisation via relaxation at the measuring/initialising position is followed by a voltage pulse to reach the mixing position, point C of the stability diagram of Fig. 3.6, for a mixing time stepped between 1 – 50 ns, before measuring the resulting triplet probability.

The data points and the result of the fit are presented in Fig. 3.9, with the fitted dephasing time being  $T_2^* = 13$  ns consistent with the values found in the literature [39, 88, 89] for a  $|S\rangle - |T_0\rangle$  spin mixing.

We can also recognise the Gaussian shape of the triplet probability, which can be compared with the experimental data shown in appendix B associated to a non-adiabatic pulse, where the dephasing time is about 4 ns for an equivalent mixing position than the one used here.

In conclusion, the result of the experiment has both criteria of a  $|S\rangle - |T_0\rangle$  spin mixing so the pulse through the S(2,0)-S(1,1) anti-crossing is adiabatic, meaning that the tunnel coupling is in the desired regime. The coherent exchange oscillations can now be discussed more in detail.

### 3.6 Coherent exchange oscillations

Thanks to the results of the previous experiments, the singlet-triplet qubit presents the characteristics indicating that the coherent exchange oscillations can be implemented. The optimal measuring position with the Pauli spin blockade has been determined. A mapping of the spin states for negative detuning reveals the location of the 'pure'  $|\uparrow\downarrow\rangle, |\downarrow\uparrow\rangle$  spin basis, such as the  $|S\rangle, |T_+\rangle$  crossing position. The short mixing time indicates finally that the tunnel coupling is large enough to reach adiabatically the S(1,1) spin state.

The coherent exchange oscillations are the oscillations of the spin state in the  $|S\rangle, |T_0\rangle$  spin basis where the oscillating frequency is defined by the exchange energy  $J(\varepsilon)$  [39]. We can remind that  $\varepsilon$  is the difference of chemical potential between the two quantum dots, it can therefore be modified by the different gate voltages, or the electrostatic fluctuations. Consequently, any fluctuations of  $\varepsilon$  induces a variation of  $J(\varepsilon)$ . Since  $J(\varepsilon)$  varies highly with  $\varepsilon$ , it is expected to be exponential [39, 40, 90], any small variation of  $\varepsilon$  induces a large variation of  $J$ , and eventually a phase shift large enough to be recorded. In our project the electrostatic fluctuation/modification is induced by travelling charges in the edge channels passing nearby the double quantum hosting this singlet-triplet qubit.

Before coming back to this final experiment, a basic one can be realised aiming to verify this sensitivity to the electrostatic environment. This experiment is the so called chevron pattern first realised by Petta *et al.* in 2005 [39]. It is a 2D map where coherent exchange oscillations are measured for different detunings, showing the acceleration of the oscillation frequency while increasing  $\varepsilon$  so  $J(\varepsilon)$ .

The full procedure to implement such oscillations is a bit complex compare to the previous ones, mostly because the spin is oscillating in the  $|S\rangle, |T_0\rangle$  spin basis, so it has to be initialised first as a  $|\uparrow\downarrow\rangle$  spin state. To initialise in this  $|\uparrow\downarrow\rangle, |\downarrow\uparrow\rangle$  spin basis, a method consisting in sweeping slowly the detuning is employed to transform adiabatically a prepared singlet state S(2,0) as a  $|\uparrow\downarrow\rangle$  one.

In the detail, the pulse sequence and its illustration in Bloch spheres are presented in Fig. 3.10. The first step is the initialisation as a singlet S(2,0) by relaxation as before. Then, to avoid the mixing of the initialised spin state with  $|T_+\rangle$  during the incoming slow detuning sweep, a non-adiabatic pulse is applied to reach a detuning point just after the  $|S\rangle, |T_+\rangle$  crossing, pulse from M to B in Fig. 3.10. This pulse aim to prevent two different mixings, the one with the triplet  $|T_+\rangle$  but also one with the triplet  $|T_0\rangle$ . This last one is avoided by pulsing to a detuning value, point B, where  $\Delta V_{RF} = 0$ , typically for  $\varepsilon = -5$  mV of the

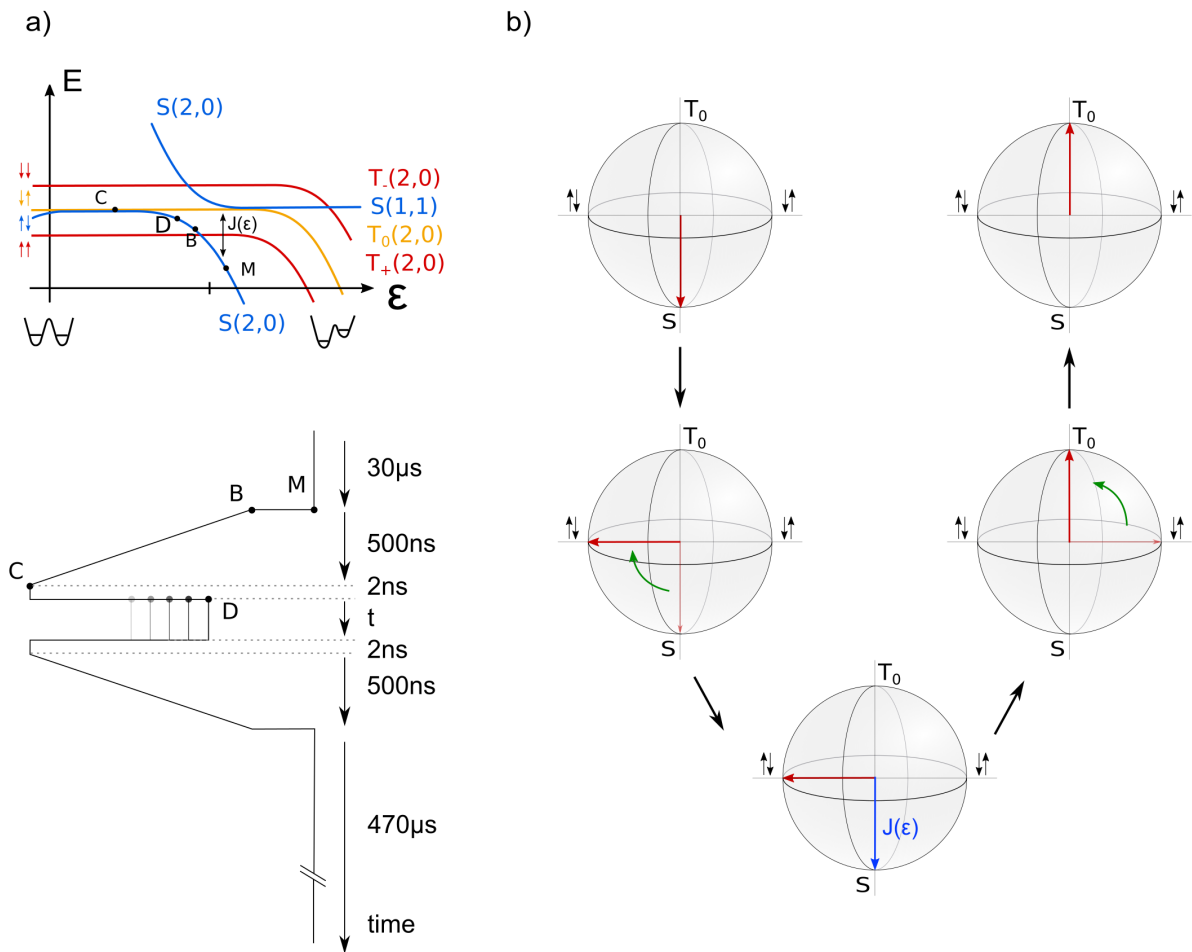


**Figure 3.10** – **a)** Energy diagram of the considered charge transition (1,1)-(2,0) and the sketch of the experimental sequence. The spin state is initialised as a  $S(2,0)$  at the point M, before applying a pulse to avoid the  $|S\rangle$ ,  $|T_+\rangle$  crossing (point B) and performing an adiabatic ramp to reach the point C changing the prepared singlet state to a  $|\uparrow\downarrow\rangle$ . An exchange pulse is applied to start the oscillations of the spin state at the point D for a time  $t$ . The mirror detuning sequence is performed, to stop the oscillations and come back to the measuring position. **b)** Representation of this pulse sequence in Bloch spheres. The initialised spin state is along the south pole before reaching the equatorial plan with the  $\pi/2$  pulse equivalent to the adiabatic ramp. The oscillations starts with the exchange pulse with a frequency defined by the exchange energy  $J(\epsilon)$ , for a time  $t$  equivalent here to a  $\pi$  shift. After stopping the oscillation, the projection is realised in the  $|S\rangle$ ,  $|T_0\rangle$  spin basis with the second  $\pi/2$  pulse.

Fig. 3.6c.

Then, to initialise the  $|\uparrow\downarrow\rangle$  spin state, instead of crossing this change of spin basis non-adiabatically and induce the  $|S\rangle - |T_0\rangle$  spin mixing as before, the transfer should be adiabatic, so the detuning should be swept slowly toward the 'pure'  $|\uparrow\downarrow\rangle$ ,  $|\downarrow\uparrow\rangle$  spin basis position defined in section 3.4, point C of Fig. 3.10. This ramp corresponds to the  $\pi/2$  rotation of the spin state toward the equatorial plane of the Bloch sphere represented with a green arrow in Fig. 3.10.

The spin state is then pulsed in the  $|S\rangle$ ,  $|T_0\rangle$  spin basis with a non-adiabatic pulse inducing the oscillations of the spin state for a time  $t$ . In the following, this pulse will be called exchange pulse. This oscillating

position corresponds to the point D of Fig. 3.10

Finally, the mirror detuning sequence is implemented, first to stop the oscillations, then to comeback in the  $|S\rangle, |T_0\rangle$  spin basis and perform the spin readout after avoiding the  $|S\rangle, |T_+\rangle$  crossing to reach the measuring position.

### 3.6.1 adiabaticity

To implement this sequence experimentally, a last element has to be determined, it is the length of the adiabatic ramp performing the change of eigen spin basis, the  $\pi/2$  spin rotation in Fig. 3.10. This adiabaticity is different than the one explained before with the study of the  $|S\rangle - |T_0\rangle$  spin mixing, where the adiabaticity was regarding the fixed tunnel coupling. Here, the ramp is adiabatic with respect to the ratio of  $E_{Z,nuc}$  and  $J(\varepsilon)$ , which is varying exponentially with  $\varepsilon$  since  $J(\varepsilon) \propto \exp(\varepsilon)$ . To calibrate it, the same sequence than the exchange oscillations one is implemented, except the exchange pulse which is removed. In this way, besides checking the absence of mixing with the triplet spin states  $|T_+\rangle$  and  $|T_0\rangle$ , the ramping time can be established experimentally. To ensure a complete mixing in case of non-adiabatic ramp, the time spend in the (1,1) charge configuration is set to 100 ns and the experiment is performed for different ramping time in the range 10 ns to 500 ns.

Following such procedure, the triplet probability is expected to decrease quickly with the ramping time. In addition, in the absence of mixing with the two triplet states, the signal should be zero for the long ramping time.

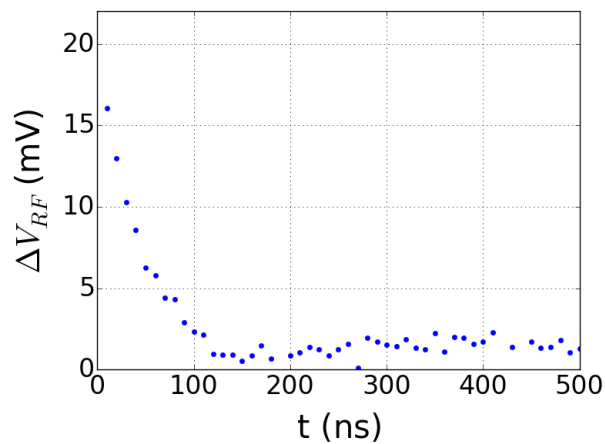


**Figure 3.11** – The voltage amplitude  $\Delta V_{RF}$  of the spin triplet RF-QPC signal is shown as a function of the adiabatic ramp length. The decrease of  $\Delta V_{RF}$  means a reduction of the  $|S\rangle - |T_0\rangle$  spin mixing efficiency, so the change from the  $|S\rangle, |T_0\rangle$  to  $|\uparrow\downarrow\rangle, |\downarrow\uparrow\rangle$  spin basis is performed more and more adiabatically.

The experimental data are shown in Fig. 3.11, where the triplet probability is pretty high for the first tens nanoseconds, indicating the  $|S\rangle - |T_0\rangle$  spin mixing of the prepared singlet spin state so the non-adiabaticity of the change of spin basis. Then,  $\Delta V_{RF}$  is decreasing quickly, meaning that the ramp is more and more adiabatic, until being zero starting from a ramping time of about  $\sim 150$  ns. Here again,

the signal does not go exactly to zero because of the signal extraction artefact.

According to these results the ramping time is set to 500 ns. Furthermore, the triplet probability goes to zero and does not stabilise to any other value, meaning that, first the change of spin basis is complete and also that there is no mixing between the prepared singlet and the triplets  $|T_+\rangle$  or  $|T_0\rangle$ . At least if there is one it is sufficiently weak not to be detected in this range.

In conclusion, thanks to the different measurements performed so far we verified that the three crossings are crossed as they should, adiabatically for the change of spin basis and the S(2,0)-S(1,1) anti-crossing, non adiabatically for the  $|S\rangle$ ,  $|T_+\rangle$  crossing. Furthermore, the results indicate that the spin state should be well controlled all along the experimental sequence of the coherent exchange oscillations, so the spin visibility is expected to be large.

### 3.6.2 chevron pattern

The full sequence of the coherent exchange oscillations is now ready to be implemented to measure a chevron pattern. In addition to validate the acceleration of the oscillations when increasing  $J(\varepsilon)$  via the amplitude of the exchange pulse, this experiment permits to extract other interesting information about the singlet-triplet spin qubit. From it we will determine the evolution of the exchange energy  $J(\varepsilon)$  with the detuning, plus the tunnel coupling  $t_c$  of our spin qubit. It will also be used to compare the spin visibility of the measurement for the two acquisition modes, the single shot spin readout or the signal averaging used so far.

The experimental sequence is exactly the same than the one described previously, the oscillating time is swept from 1 to 50 ns, with the detuning of the oscillating positions stepped between  $\varepsilon = -13$  and  $-2$  mV.

The resulting 2D colour map is presented in the figure 3.12a, recorded thanks to the single shot spin readout acquisition mode, with a slice along the black dashed line being Fig. 3.12c. An equivalent trace but recorded with the signal averaging mode, and for a slightly different detuning, is shown as Fig. 3.12d. For this trace the red dashed line is the result of the fit of the data used to evaluate the exchange energy presented in Fig. 3.12b.

Focussing on the 2D map, the acceleration of the oscillation frequency with the detuning is confirmed and to study it, the data are fitted using the same procedure than for the  $|S\rangle - |T_0\rangle$  spin mixing. The probability to measure a triplet  $|T_0\rangle$  after an oscillating time  $t$  is:

$$P_{T_0}(t) = \frac{1 - e^{-(t/T_2^*)^2} \cos\left(\frac{t}{\hbar} \int_0^t J(\varepsilon(t)) dt\right)}{2} \quad (3.10)$$

where the exchange energy is calculated from:

$$J(\varepsilon(t)) = J_0 + J_1 \cdot e^{\frac{\varepsilon(t)}{\sigma}} \quad (3.11)$$

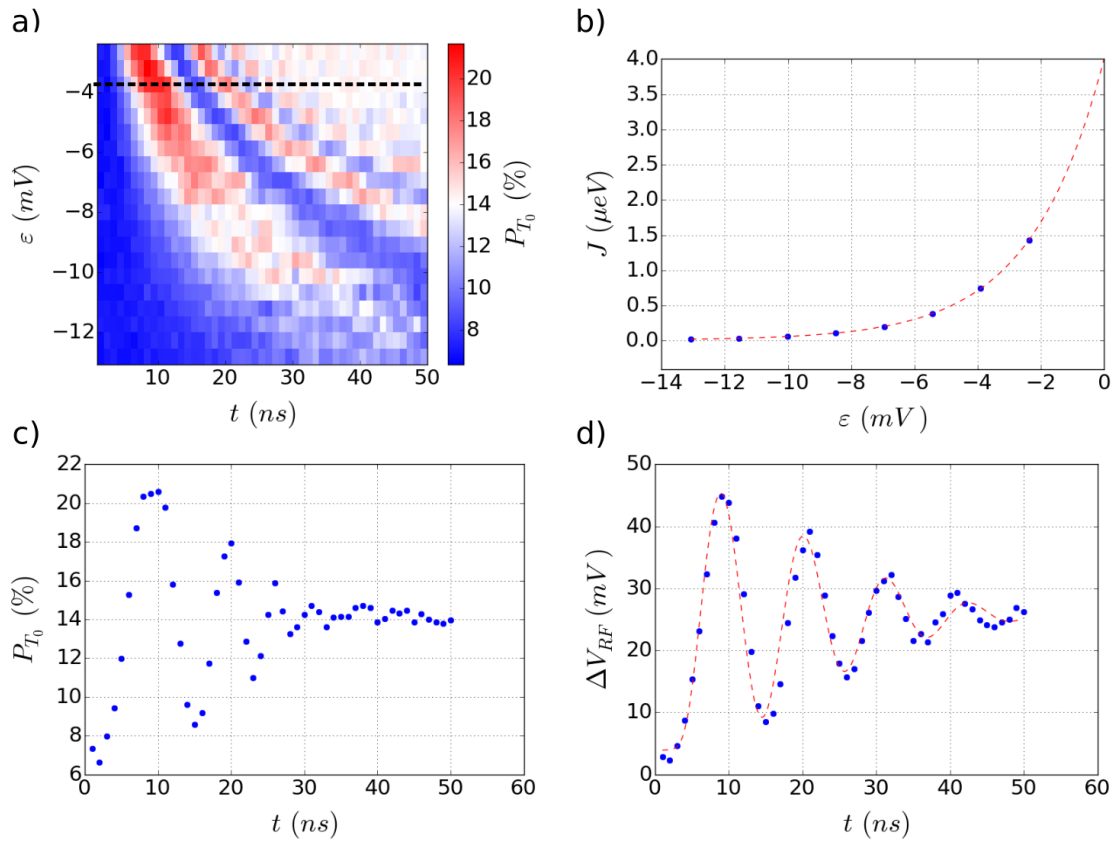


**Figure 3.12** – **a)** The triplet probability  $P_{T_0}$  from the single shot acquisition mode is shown as a function of the oscillating time along the  $x$  axis and the oscillating position  $\varepsilon$  along the  $y$  one.  $P_{T_0}$  is plotted in colour scale with in blue(red) the low(high) intensity. This map is the so-called chevron pattern showing the acceleration of the coherent exchange oscillations when increasing the detuning value  $\varepsilon$  of the oscillating position. The black dashed line indicates the cut along which the curve shown in **c)** is extracted. The small signal for smallest  $\varepsilon$  is due to the partial adiabaticity of the exchange pulse explained in the main text. **b)** Evolution of the exchange energy  $J(\varepsilon)$  as a function of the detuning value  $\varepsilon$  of the oscillating position. The red dashed line is the result of the fit with its expression 3.14 given in the main text. The interdot tunnel coupling  $t_c$  is  $J(0) \approx 4 \mu\text{eV}$ . **c)** Single trace of coherent exchange oscillations extracted at the oscillating position indicated by the black dashed line of **a)**. **d)** Same coherent exchange oscillation trace (for a slightly different  $\varepsilon$ ) recorded with the signal averaging acquisition mode, the red line is the result of the fit using expression 3.13 given in the main text.

the detuning is:

$$\varepsilon(t) = (a_0 - a_1 \cdot e^{-t/\tau})\varepsilon_{AWG} - \varepsilon_0 \quad (3.12)$$

In the expression 3.10,  $T_2^*$  is the dephasing time,  $\hbar$  the Planck constant. The accumulated phase during the oscillating time  $t$  is obtained from the integration of the exchange energy over  $t$  to take into account a short rising time from the AWG. The exchange energy expression 3.11, has the exponential behaviour already mentioned and observed in different experiments [39, 40, 90]. The term  $J_0$  corresponds to the remaining exchange energy in the  $|\uparrow\downarrow\rangle, |\downarrow\uparrow\rangle$  spin basis which is not zero because of the tunnel

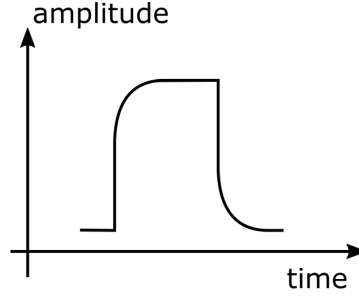


**Figure 3.13** – Sketch of the exchange pulse illustrating the impact of the AWG rising time.

coupling between the states  $S(2,0)$  and  $S(0,2)$ . The two last terms are defining the acceleration and the gate lever arm. Finally, the detuning expression 3.12 takes into account the deformation of the exchange pulse arising from the AWG rising time. Here we only consider the rising time for the first front of the exchange pulse, its impact on the total accumulated phase for the second front is neglected. Indeed, as sketched in Fig. 3.13, the remaining detuning amplitude due to this rising time is small, so it induces a negligible additional phase. The term  $\varepsilon_{AWG}$  corresponds to the applied voltage and  $\varepsilon_0$  is a constant corresponding to the voltage for which  $\varepsilon = 0$ .

Finally, the data can be fitted with the following parameters:

$$P_{T_0}(t) = \frac{1 - e^{-(t/20.10^{-9})^2} \cos\left(t \int_0^t \frac{J(\varepsilon(t)) \cdot dt}{\hbar}\right)}{2} \quad (3.13)$$

$$J(\varepsilon(t)) = 1.10^{-8} + 4.10^{-6} e^{\frac{\varepsilon(t)}{2.10^{-3}}} \quad (3.14)$$

$$\varepsilon(t) = (1 - 0.7e^{-t/1.10^{-9}}) \varepsilon_{AWG} - \varepsilon_0 \quad (3.15)$$

The evolution of  $J(\varepsilon)$  is presented as Fig. 3.12b, from which the tunnel coupling  $t_c$  corresponds  $J(\varepsilon = 0) \approx 4 \mu\text{eV}$ , which is consistent with the previous measurements.

The fit is only performed for the trace recorded with the signal averaging mode, the single shot data being too noisy to be properly fitted.

Coming back to the 2D colour map, for the smallest detuning the spin visibility, amplitude of the first oscillation, is pretty small and is increasing with it, as it can be observed for the  $\pi$  spin rotation where first the triplet probability is about 14% and rises up to  $\sim 20\%$  for the fastest oscillations. This phenomenon is related to the adiabaticity of the exchange pulse. As presented with the Landau Zener theory, section 3.5.1, the adiabaticity depends on  $d\varepsilon/dt$ . For the first oscillating position, the exchange pulse amplitude  $d\varepsilon$  is not large enough to ensure a full non-adiabatic pulse. Thus, instead of having all the prepared  $|\uparrow\downarrow\rangle$  spin states which are oscillating as expected, only a part of them is oscillating, the other states are changed to  $|S\rangle$  as sketched in Fig. 3.14. By increasing the amplitude of the exchange pulse, it is getting more and more non-adiabatic. Hence, the proportion of oscillating spin state is increasing, so

does the spin visibility. This phenomenon has already been observed and studied in the past [90].

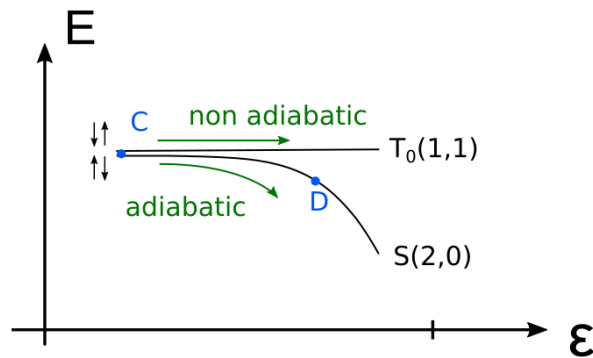


**Figure 3.14** – Sketch illustrating the adiabaticity or not of the exchange pulse in the energy diagram.

From the two traces Figs. 3.12 c and d, measured for a slightly different detuning for experimental reason, the spin visibility and fidelity of the two type of acquisition modes, single shot spin readout and signal averaging, can be discussed.

As presented at the end of the previous chapter, an important notion is the fidelity of the spin readout, the ability to distinguish between the two spin states  $|S\rangle$  and  $|T_0\rangle$ . For the single shot acquisition mode, the spin readout fidelity has been estimated to be maximum 50% (cf. section 2.5), but so far it is unknown for the signal averaging measurements. To determine it, we can use the spin mixing trace, Fig. 3.9, where we know that for the long mixing time the triplet probability is equal to 50%. Then, we have to convert the measured voltage to percentage and compare it to this value. This conversion from voltage to percentage is only a rough estimation because of the high sensitivity of the QPC tuning. Indeed, this conversion requires to define the step signal of  $V_{RF}$  for a charge tunneling event, which is equivalent to a triplet probability of 100%. Consequently, it depends highly on the charge sensitivity at the measuring position. Since we are using a SQD having a tuning even more sensitive than a QPC and which was drifting in time, it adds another uncertainty. Nevertheless, for this spin mixing experiment shown in Fig. 3.9, the step signal of a charge tunneling event was about 38 mV, so the measured triplet signal  $\Delta V_{RF} \approx 17$  mV for the long mixing time is equivalent to a triplet probability of about  $\sim 45\%$ . In comparison to the expected 50% gives a measurement fidelity about  $\sim 90\%$ . This fidelity is the result of the multiplication of three fidelities, the one of the spin readout, of the spin manipulation and the spin initialisation. Such mixing experiment is only composed by a single voltage pulse, so the spin manipulation fidelity is large, the spin initialisation is performed for a time much longer than  $T_1$ , so it is also expected to be quasi perfect. Thus, the fidelities of manipulation and initialisation are assumed to be close to the unity, and the measurement fidelity of this spin mixing experiment,  $\sim 90\%$ , is therefore assumed as limited only by the spin readout fidelity. In the following, for this signal averaging acquisition mode, the spin readout fidelity will be considered as equal to  $\sim 90\%$ .

Notice that thanks to the fit of the spin relaxation used with the signal averaging mode, the drawback of the rising time of detection chain limiting the single shot readout is avoided, cf. section 2.5 of the

previous chapter.

Coming back to the chevron pattern, the spin visibility of this experiment using the signal averaging acquisition mode is about 45 mV (see Fig. 3.12d), with a step signal of a charge tunneling event for this specific experiment evaluated to 58 mV, this spin visibility converted in percentage is therefore about  $\sim 85\%$ . For the first  $\pi$  spin rotation, the spin visibility is limited by the measurement fidelity, the dephasing time has no impact yet. Then, the measurement fidelity is equal to  $\sim 85\%$  and should be equal to the  $\sim 90\%$  of spin readout fidelity for a perfect spin manipulation and initialisation. Here it is not the case, meaning that either the spin initialisation or manipulation fidelities are not equal to the one, like for the spin mixing trace of Fig. 3.9. The initialisation being similar than for this spin mixing experiment, it is therefore also assumed as equal to one. Thus, it is the spin manipulation fidelity which is lower and evaluated about  $\sim 95\%$  for this coherent exchange oscillation experiment to explain this reduction from expected  $\sim 90\%$  to the measured  $\sim 85\%$ .

Concerning the single shot readout, the spin visibility is about  $\sim 15\%$ . If the spin readout of this experiment was perfect, so 50% (cf. section 2.5), using the  $\sim 95\%$  of spin manipulation fidelity and a perfect spin initialisation, the measured spin visibility should be equal to  $\sim 47\%$ , much larger than the obtained value. The only explanation of this difference from the expected  $\sim 47\%$  to the measured  $\sim 15\%$  is the fidelity of the spin readout. To evaluate this  $\sim 47\%$  we just considered a perfect tuning of the single shot spin readout which was therefore not the case for this experiment and was probably about  $\sim 15\%$ , because of a wrong tuning of the threshold.

In conclusion, from this chevron pattern the acceleration of the coherent exchange oscillations with  $\varepsilon$  has been verified, confirming their sensitivity to the electrostatic environment. In addition, the evaluated manipulation fidelity being large,  $\sim 95\%$ , it confirms the good control of the spin state during the implementation of the coherent exchange oscillations, necessary for our purpose as discussed at the end of the section 3.4.

### 3.7 $|S\rangle - |T_0\rangle$ spin qubit as charge detector

The chevron pattern shows that for this type of oscillations, the accumulated phase highly depends on the electrostatic environment, which was materialised by the detuning  $\varepsilon$ . This principle of phase accumulation depending on the environment has already been exploited experimentally [91, 92]. Either to perform coherent operations with such qubit, controlled by the charge state of a neighbour double quantum dot [92], or to change the coherent exchange oscillation frequency in a controlled qubit by the charge state of a target on [91]. The working principle of our qubit detector relies on the same idea than Schulman *et al.* [91], except that the oscillation frequency is affected by a single electron travelling into the ECs of the QHE. This approach has already been employed in the group [42, 43] with a less optimised sample design and experimental setup.

Before using the singlet-triplet spin qubit as charge detector, it can be interesting to present more in detail the proposed experiment of single electron detection, which stress out the remaining elements to

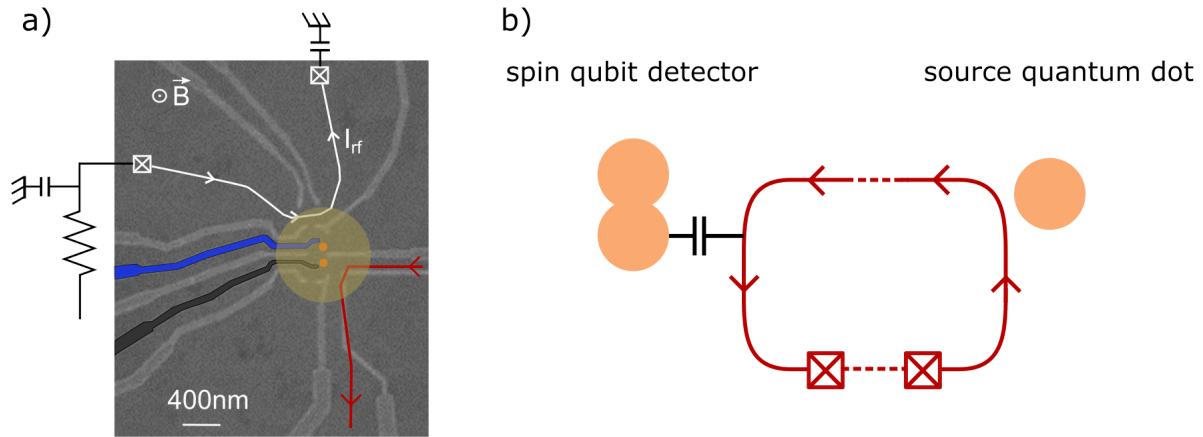


**Figure 3.15** – *a)* Scanning electron micrograph of the double quantum dot used as a spin qubit detector, which is capacitively coupled to the nearby edge channels (only one is represented), the orange disk sketch the area over which the qubit detector is sensitive. *b)* Sketch of the single electron detection principle. A source dot is used to inject a single electron into the edge channels. This electron is carried toward the detector, where it interacts with the qubit detector by capacitive coupling.

develop and characterise.

The full experiment consists in a charge to spin to charge conversion. The sketch of the experiment is presented in Fig. 3.15b, where a source quantum dot acts as a single electron source. In the first chapter section 1.3, we shown that it is quite simple to confine a single electron in a single quantum dot and to force the tunneling in and out of it by applying voltage pulses, cf. subsection 3.2.2. The aim is to use a voltage pulse to force an electron to tunnel out toward the electron reservoir hosting the ECs. Since they are like optical fibers for electrons, the injected electron travels without interacting with the defects and at constant velocity, estimated to  $v = 10^4 - 10^5 \text{ m s}^{-1}$  [93, 94, 95], from the source to the vicinity of the qubit detector. Via capacitive coupling, the electron interacts with the qubit and affects the oscillation frequency, performing a charge to spin conversion. Then, thanks to the Pauli spin blockade this phase shift is recorded, being the spin to charge conversion. Ideally, the phase shift is large enough to induced a  $\pi$  rotation of the spin state, offering the possibility to perform the full experiment single shot. The single shot spin readout being already proven in the previous chapter section 2.5. The major difficulty of this experiment is the sensitivity of the qubit detector which has to be large enough first, to have a measurable phase shift, and eventually this  $\pi$  phase shift. A way to illustrate this required high sensitivity is the interaction time of the electron with the detector. Assuming the detector interacting with its electrostatic environment over 500 nm, distance between the farthest quantum dot and the QPC corresponding to the orange disk of 3.15, gives an interaction length of about 1  $\mu\text{m}$ . Depending on the electron speed in the ECs gives the interaction time is of about 1 – 10 ps, in comparison to the nanoseconds of oscillating time used so far.

To implement and succeed this final experiment, different elements have to be develop or define. First, the coherent exchange oscillations sensitivity to the travelling electrons in the ECs is expected but has to be demonstrated experimentally. It is the subject of the last part of this chapter, associated to the determination of the direction of propagation within these ECs. The last chapter will be dedicated to the

optimisation of the qubit detector for the detection of a single travelling electron, before discussing the experimental results.

### 3.8 Detection of travelling electrons into the ECs

To verify the use of the coherent exchange oscillations as base component of the qubit detector, their sensitivity to the travelling in the ECs should be verified. As sketch in Fig. 3.15, the electron reservoir common to the source dot and the qubit detector host two ohmic contacts. One can therefore be used as electron source, via application of a DC bias, and the second one grounded can be the electron drain. As explained in the following, from the implementation of this experiment for the two contacts and the two perpendicular to the plane magnetic field orientation, it is possible to validate the sensitivity of the coherent exchange oscillations to the travelling electrons in the ECs, but also their propagation direction. It worth to highlight that the qubit detector is only sensitive to the density of electrons in its vicinity, the global current flowing in the ECs is thus irrelevant for the present discussion.

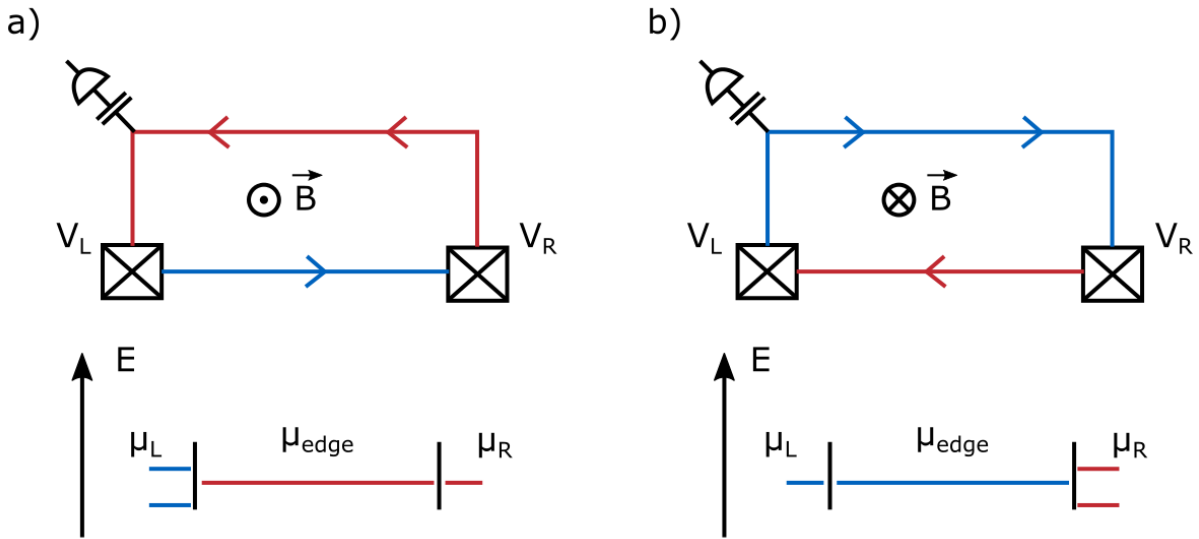


**Figure 3.16** – *a)* Sketch of the sample with the edge channels represented by a single line, the colour indicates which ohmic contact set their chemical potential, blue for the left, red for the right. The edge channels passing close to the qubit detector, capacitively coupled to it, has a chemical potential defined by the right ohmic contact,  $\mu_{edge} = \mu_R = E_F - eV_R$ . Furthermore,  $\mu_{edge}$  is insensitive to the changes of the potential applied to the left contact. *b)* Same sketch but for an opposite magnetic field, here  $\mu_{edge} = \mu_L = E_F - eV_L$ .

From the Landauer-Buttiker formalism [96, 97, 98] we know that the chemical potential of the ECs is given by the contact which is emitting them as depicted in Fig. 3.16. Then, labelling the chemical potential of the ECs passing nearby the qubit detector  $\mu_{edge}$ , for a positive magnetic field, the electrons travel anti-clockwise, so  $\mu_{edge} = \mu_R$ , without any dependence on  $\mu_L$  as sketched in Fig. 3.16a. By reversing the magnetic field orientation, the direction of propagation within the ECs is also reversed, so

the electrons travel clockwise and finally  $\mu_{edge} = \mu_L$ , see Fig. 3.16b.

The expected effect of the travelling electrons in the ECs on the coherent exchange oscillations can be understood by assimilating the ECs to a polarised gate. Indeed, depending on their polarisation, the ECs can have a gate like effect on the location of the oscillating electrons and inducing a detuning shift  $\delta\varepsilon$ . This detuning shift and the induced phase variation can be understood as follow.

So far the singlet-triplet spin qubit is obtained from the (1,1)-(2,0) charge transition, where the (2,0) charge state is the confinement of the two electrons in the quantum dot the farthest to the ECs. Considering a positive magnetic field,  $\mu_{edge} = \mu_R = E_F - eV_{bias}$  with  $E_F$  the Fermi energy and  $e$  the elementary charge. For a negative bias, the electron density of the ECs is increased, so they can be assimilated to a gate negatively polarised pushing the oscillating electrons toward the (2,0) charge configuration. A shift toward this charge configuration is equivalent to a positive  $\delta\varepsilon$ , a larger  $J(\varepsilon)$ , so the oscillations are accelerated. The same way around, a positive  $V_{bias}$  induces a smaller  $\varepsilon$  so a deceleration of the oscillations.

The only acting parameter on the phase shift is the electron density controlled by  $V_{bias}$ , so the phase shift should evolve linearly with it. Furthermore, because of the chirality of the ECs, it should be observed only for one contact per magnetic field orientation, the other contact changing the electron density of the ECs between the two ohmic contacts, see Fig. 3.15b.

This effect is verified in practice by performing the same coherent exchange oscillations than before with the exchange pulse amplitude set such that several oscillations are visible in our time window of 1 to 100 ns. The bias applied to the two ohmic contacts, one after the other, is stepped from  $-300\ \mu\text{V}$  to  $300\ \mu\text{V}$ , and the magnetic field set to  $B = \pm 430\ \text{mT}$

The results of the four experiments are presented in Fig. 3.17 with the oscillating time along the x axis and the applied bias along the y one.

The main observation about these data is the expected presence of a phase shift for only two configurations, for  $B = 430\ \text{mT}$  while changing  $V_{bias,R}$ , and for  $B = -430\ \text{mT}$  with  $V_{bias,L}$ . Validating the previous explanations and so confirm the sensitivity of the qubit detector to the electron density of the ECs.

Furthermore, from which contact has an impact on the oscillations it is possible to determine the direction of propagation of the ECs as sketched in Fig. 3.16. For the applied  $B = 430\ \text{mT}$ , the phase shift is observed while stepping the right contact, which means that  $\mu_{edge} = \mu_R$  so the B field has a positive orientation with respect to the sample. Conclusion validated by the results of the opposite magnetic field where, this time, the phase shift is induced by stepping the bias to the left contact, so  $\mu_{edge} = \mu_L$ .

For the future manipulations the magnetic field is maintained to  $430\ \text{mT}$  since it is the direction for which the ECs are going from the source dot to the detector without ohmic contact in between.

Some comments also concerning the detuning shift and the resulting variation of exchange energy. First, as expected the negative bias induces fastest oscillations, and a positive one slow them down, confirming also the previous explanation. For the shift of detuning, referring to positive magnetic field and for

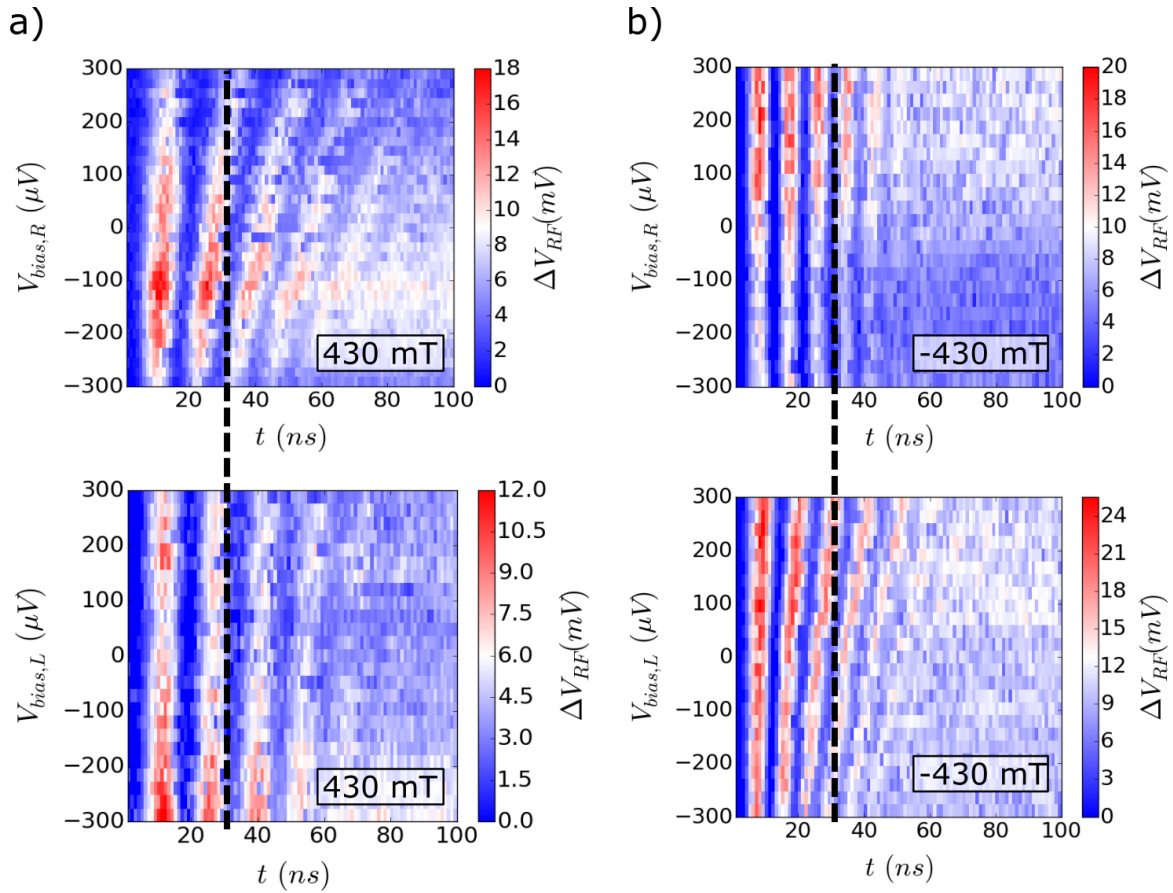


**Figure 3.17 – a)** The voltage amplitude  $\Delta V_{RF}$  of the spin triplet RF-QPC signal is shown as a function of the oscillating time  $t$  along the  $x$  axis and the DC bias  $V_{bias,R}$  ( $V_{bias,L}$ ) along the  $y$  one.  $\Delta V_{RF}$  is plotted in colour scale with in blue (red) the low (high) intensity. These coherent exchange oscillations have been measured with the oscillating time swept from 1 to 100 ns and  $V_{bias,R}$  or  $V_{bias,L}$  are stepped from  $-300$  to  $300 \mu\text{V}$ . For these two measurements the magnetic field was set to 430 mT. The dashed line is a guide for the eye to highlight the shift of oscillating frequency when  $V_{bias,R}$  is stepped, while it remains constant when stepping  $V_{bias,L}$ . The evolution of signal amplitude within a map is due to the instability of the RF-QPC charge sensitivity. **b)** Same measurements but for the reversed magnetic field. This time the shift of oscillation frequency is observed when stepping  $V_{bias,L}$ . For these maps the coherent exchange oscillations are faster because of a small sample tuning variation when reversing the magnetic field.

$t = 30$  ns, the phase shift is about  $2\pi$  for a stepped of  $600 \mu\text{V}$ . Corresponding to a variation of exchange energy calculated with  $\delta J = \frac{2\pi \cdot \hbar}{t} \approx 0.15 \mu\text{eV}$ .

The analysis can be implemented with the opposite magnetic field, where the tuning of the sample changes a bit, it is not perfectly symmetric about 0 T, inducing oscillations at larger detuning, so fastest. There, the phase shift is about  $5\pi/2$  leading to a variation of exchange energy  $\delta J = \frac{5\pi \cdot \hbar}{2 \cdot t} \approx 0.17 \mu\text{eV}$ .

Finally, few words on the signal amplitude which is clearly not constant from a map to the other, but also within a map. Moreover, here the signal is smaller compare to the chevron pattern presented previously. These variations are due to the QPC tuning, which was first, less optimised than for the chevron pattern, but it was also unstable, so the charge sensitivity was drifting in time.

In conclusion, by these four measurements the propagation direction of the ECs has been determined, but in particular the sensitivity of the exchange oscillations to the travelling charges in ECs is confirmed. This sensitivity to the travelling charges being demonstrated, the qubit detector can now be optimised for the single travelling electron detection. It will induce the implementation of a new type of coherent exchange oscillations, and the development of the single electron source to replace the DC current.

---



---

## Towards single electron detection

---

## 4.1 Introduction

The last measurements demonstrate the sensitivity of the coherent exchange oscillations to the electron density of the nearby ECs of the QHE. However, the implementation of these experiments is not adapted to the single electron detection. Indeed, the interaction time between a single electron travelling at the Fermi velocity and the qubit detector is estimated about  $1 - 10$  ps. It is therefore much shorter than the few nanoseconds we have used so far. As a consequence, the exposure time of the qubit detector, the oscillating time, should be reduced to a minimal amount of time.

The implications of setting the oscillating time will be presented with the implementation of another type of coherent exchange oscillations. Then, the origin of spin dephasing during these exchange oscillations limiting the qubit detector charge sensitivity is investigated. Once the qubit detector in its optimal configuration, largest charge sensitivity, the step signal  $\delta V_{\text{RF}}$  of spin triplet RF-QPC signal expected for the detection of a single electron propagating in the ECs is determined. Finally, after the development of a quantum dot as a single electron source, the detected edge magneto plasmon (EMP) are discussed such as the different techniques employed to implement the single travelling electron detection.

## 4.2 Coherent exchange oscillations in amplitude

In order to use the qubit detector as a charge detector, not only the exposure time has to be tuned, but also its working position.

We just mentioned the necessity to adjust the qubit detector exposure time to match the interaction time with the element to detect, here the single travelling electron. As discussed, it is about  $1 - 10$  ps, as we will see with the development of the single electron source the propagating wavepacket is of the same order of magnitude. These values are inaccessible with our experimental setup, therefore we set the oscillating time to the lowest reachable value by the AWG, 1 ns.

The qubit detector exposure time being set, now it is its working position which has to be defined. This detuning position corresponds to the oscillating position for which the interaction with the travelling electron induces the largest phase shift of the coherent exchange oscillations, so the largest variation of triplet probability. To find this working position, since the accumulated phase during the oscillations depends on the exchange energy  $J(\varepsilon)$  and the oscillating time  $t$ , set to 1 ns, it remains only the detuning  $\varepsilon$  as adjustable parameter.

In the following, coherent exchange oscillations will be implemented with a set exposure time and by sweeping the oscillating position, i.e. the exchange pulse amplitude. We call this experiment: coherent exchange oscillations in amplitude.

In the current section, these oscillations are first presented more in detail with in particular a discussion of the dephasing mechanism limiting their contrast which is, as we will see, the main limitation of the qubit detector charge sensitivity.

### 4.2.1 Experimental procedure and results

The procedure to implement the coherent exchange oscillations in amplitude is similar to the one developed along the previous chapter and sketched in Fig. 3.10. The only difference is the swept element which now is the detuning value of the oscillating position. Since the accumulated phase is defined as  $\int_0^t \frac{J(\varepsilon(t))dt}{\hbar}$ , with  $J(\varepsilon) \propto \exp(\varepsilon)$ , this feature is experimentally observed by the oscillations which are faster with an increasing detuning.

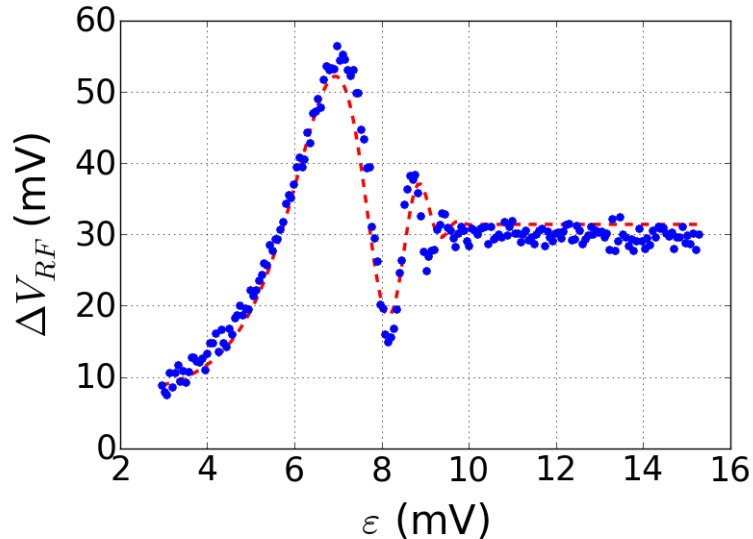


**Figure 4.1** – The voltage amplitude  $\Delta V_{RF}$  of the spin triplet RF-QPC signal evolution is plotted as a function of the corrected detuning  $\varepsilon$  (see main text). For such coherent exchange oscillations in amplitude the oscillating time is set to 1 ns. The experimental data are fitted (red dashed curve) using the model discussed in the main text.

A typical trace of such experiment is presented in Fig. 4.1 with the fit of the data being the red dashed line. There are two main elements to discuss about this trace. First, the specificity of this experiment which induces changes in the fit of the experimental data. Second, the short dephasing noticed with only two visible oscillations.

In these coherent exchange oscillations in amplitude, the exchange energy has to be large enough to compensate for the short oscillating time. A large  $J(\varepsilon)$  is obtained for large exchange pulse amplitude. This point is illustrated by these oscillations which are performed at positive detuning now, see Fig. 4.1, while the chevron pattern in the previous chapter was measured only with negative detuning. The implication of this necessity to reach large detuning, is a change of regime for the evolution of the exchange energy.

As demonstrated in the previous chapter section 3.6.2, the exchange energy is increasing exponentially with increasing but only for negative detuning. Indeed, for larger  $\varepsilon$  it has been already measured that it is no longer true [40]. When  $\varepsilon$  is positive, the two electrons are in the same quantum dot, and the energy splitting  $J(\varepsilon)$  is constant as sketched in Fig. 4.2a. Meaning that the evolution of  $J(\varepsilon)$  passes

from an exponential evolution for negative  $\varepsilon$  to a saturation for positive one. Transition expected at the  $T_0(1,1) - T_0(2,0)$  anti-crossing position which, according to the measurement performed in the previous chapter section 3.3.2, is localised close to  $\varepsilon \sim 5$  mV, so within the detuning range used here for the coherent exchange oscillations in amplitude. This change of regime is further explained and verified experimentally in the appendix C. For the case of stack, in our experiment it is incomplete and only materialised by a slower increase of  $J(\varepsilon)$  with  $\varepsilon$  compared to simple exponential increase.

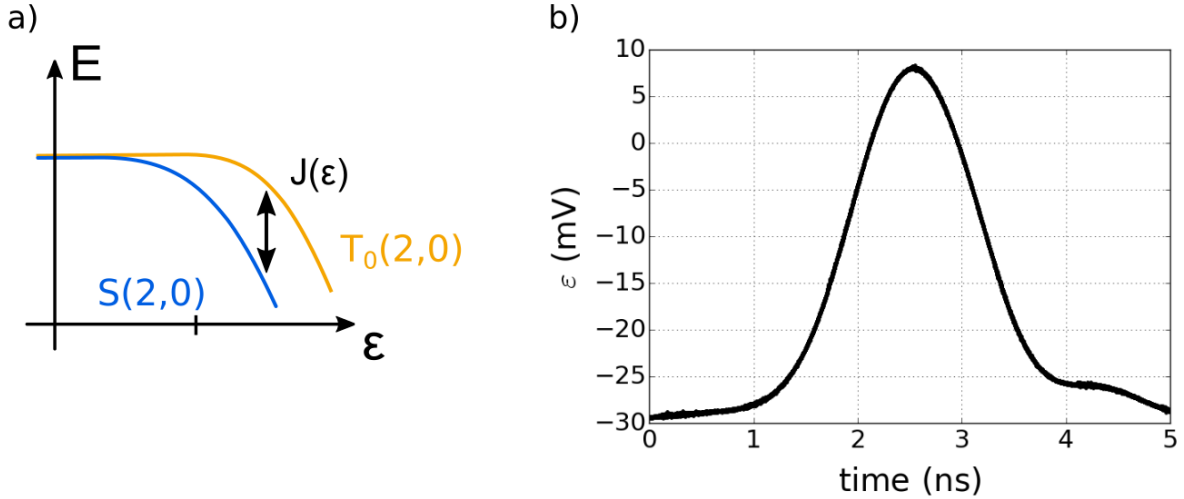


**Figure 4.2** – **a)** Sketch illustrating the exchange energy  $J(\varepsilon)$  as a function of the detuning  $\varepsilon$ . For large positive  $\varepsilon$   $J(\varepsilon)$  is saturating. **b)** Exchange voltage pulse measured at the output of the AWG with its amplitude renormalised to the expected one on the sample considering the attenuation along the coaxial line and the amplitude reduction due to the AWG rising time calibrated in the previous chapter section 3.6.2.

With this type of coherent exchange oscillations, a second element must be considered in the fit of the experimental data: the convolution of the exchange pulse with the rising time of the AWG leads to a Gaussian shape, as it can be seen in Fig. 4.2b. The general shape of the pulse is obtained by measuring the voltage pulse at the output of the AWG, and fitted with a Gaussian function in order to determine its general shape. Its voltage amplitude, attenuated compare to the designed pulse, is estimated using the fitting model used in the previous chapter to describe the chevron pattern experiment, section 3.6.2. This method leads to an attenuation factor of 0.75 for the exchange pulse applied on the double quantum dot system. This technique has the advantage of providing an in-situ calibration of the applied voltage amplitude. It is worth noting that the estimated detuning values reported in the different figures of this chapter take into account such reduction.

In the end, taking into account these two elements and the coherent exchange oscillations in amplitude can be fitted with the expressions and parameters defined in the previous chapter with the chevron pattern section 3.6.2. These expressions are:

$$P_{T_0}(t) = \frac{1 - e^{-(t/T_2^*)^2} \cos\left(t \frac{J(\varepsilon(t))dt}{\hbar}\right)}{2} \quad (4.1)$$

$$J(\varepsilon(t)) = J_0 + J_1 e^{\frac{\varepsilon(t)}{\sigma}} \quad (4.2)$$

$$\varepsilon(t) = \alpha e^{-\left(\frac{t-t_0}{\tau}\right)^2} \varepsilon_{att} - \varepsilon_0 \quad (4.3)$$

In the detuning expression 4.3,  $t_0$  and  $\tau$  are respectively the center and width of the Gaussian shaped exchange pulse, and  $\varepsilon_{att}$  is the attenuated amplitude of the pulse calibrated in the previous chapter section 3.6.2. The term  $\varepsilon_0$  is a constant defined as  $\varepsilon = 0$ ,  $\alpha$  stands for the slower increase of the exchange energy with  $\varepsilon$ , so its attenuation compared to the used exponential increase for the chevron pattern. This point is due to the mentioned incomplete change of regime in our detuning range. The other terms are already known and have been explained in the previous chapter section 3.6.2. Notice that here, the dephasing time is not a constant anymore since  $T_2^* \propto \frac{\hbar}{dJ/d\varepsilon}$  [40].

The different value of the parameters are presented in the following table:

$J_0$ (eV)	$J_1$ (eV)	$\sigma$ (V)	$\alpha$	$t_0$ (ns)	$\tau$ (ns)
$1 \cdot 10^{-8}$	$4 \cdot 10^{-6}$	$1.5 \cdot 10^{-3}$	0.84	$2.55 \cdot 10^{-9}$	$0.85 \cdot 10^{-9}$

A comment about the spin visibility of the experiment which, as explained in the previous chapter section 3.6.2, can be evaluated after conversion from the measured  $\Delta V_{RF}$  to triplet probability. Using the charge tunneling step signal of this measurement gives a spin visibility of about  $\sim 95\%$ . This value has to be compared with  $\sim 85\%$  obtained in the chevron pattern experiment of the previous chapter shown in Fig. 3.12. The experimental procedure being similar in both experiments, the measurement fidelity is unchanged. This increased spin visibility is therefore related to the manipulation, to the larger amplitude of the exchange pulse. After applying this voltage pulse, the probability to induce the oscillation of the manipulated spin state is defined by the Landau-Zener probability (cf. third chapter section 3.5.1). As introduced, this probability depends on  $d\varepsilon/dt$ . The larger the exchange pulse amplitude  $d\varepsilon$ , the larger the probability to have a non-adiabatic pulse and therefore to oscillate. Since the oscillations are performed for a larger exchange pulse amplitude in comparison to the chevron pattern, the spin visibility is also larger. This phenomenon has been observed for the single shot spin readout too as shown at the end of this chapter in Fig. 4.26.

Finally, the fast dephasing observed for these oscillations should be commented, with only two visible oscillations, the third one can barely be seen, referring to Fig. 4.1. We can remind that these coherent exchange oscillations in amplitude are implemented in order to define the working position of the qubit detector, to study the charge sensitivity of the qubit detector. This sensitivity being defined as  $dJ/d\varepsilon$ , it is increasing with  $\varepsilon$ . Then, the short dephasing is an issue because it narrows down the maximal range of detuning usable as working position, so it limits the qubit detector charge sensitivity. Therefore, the optimisation of the qubit detector requires necessarily an investigation and reduction of this dephasing process.

### 4.2.2 Noise origin

These oscillations being implemented to investigate the qubit detector charge sensitivity to the electrostatic environment, then, one can expect that this large sensitivity to the environment is at the origin of the dephasing. Meaning that the main source of noise is expected to be the charge noise materialised by fluctuations of the detuning.

The impact of these fluctuations on the coherence of the oscillations is similar to the ones of the nuclear polarisation for the  $|S\rangle - |T_0\rangle$  spin mixing introduced in the first chapter section 1.6. Here, the oscillation frequency is defined by the exchange energy  $J(\varepsilon)$ , so indirectly by the detuning  $\varepsilon$ . Then, if  $\varepsilon$  fluctuates, from a measurement to the other the oscillation frequency varies, and therefore, by repeating such manipulation many times a dephasing process occurs.

To verify this hypothesis of charge noise, a simulation of its effect can be implemented in equivalent experimental conditions than for the previous measurement. The same triplet probability expression is used with in addition a random term  $\delta\varepsilon$  with an amplitude in the range  $[-400 \mu\text{V}, 400 \mu\text{V}]$  standing for the charge noise:

$$P_{T_0} = \frac{1}{2} \left( 1 - \cos \left( \int_0^t \frac{J(t) dt}{\hbar} \right) \right), \quad J(t) = J_0 + J_1 e^{(\varepsilon(t) + \delta\varepsilon)/\sigma} \quad (4.4)$$

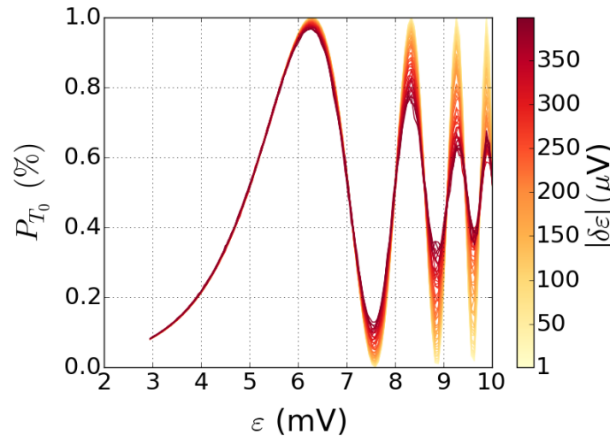


**Figure 4.3** – Simulated triplet probability  $P_{T_0}$  as a function of the detuning value  $\varepsilon$  of the oscillating position. The different colours correspond to various amplitudes of charge noise  $\delta\varepsilon$  (see main text). The figure is a simulation of the effect of a charge noise  $\delta\varepsilon$  on coherent exchange oscillations in amplitude. The noise effect is larger for large detuning where the damping of the oscillation is already visible for the smallest noise amplitude, light orange traces.

This simulation is presented in Fig. 4.3, where the same behaviour than what is experimentally observed can be noticed. Even for small noise amplitude, corresponding to the light orange colour in the simulation, the third and fourth oscillation amplitudes are highly reduced while the two first ones are almost unchanged. By further increasing the noise amplitude  $|\delta\varepsilon|$ , the second oscillation amplitude starts to be reduced while the first one is still poorly affected.

In conclusion, this simulation of a charge noise presents the same behaviour than what is experimentally

observed, so we can consider that we are experimentally limited by this type of noise.

### 4.2.3 Reduction of the charge noise

The origins of the charge noise are multiples and it is a large topic of discussion with different experiments performed to study it in our system [40, 99]. The intrinsic charge noise like the non trapped electrons hopping from a donor to the other should be distinguished from the extrinsic origins like the fluctuations of the applied voltages, the RF power for the RF-QPC, etc... In order to optimise the qubit detector, the dephasing has to be reduced, involving a reduction of this charge noise. This reduction is only possible for its extrinsic origins, so we can only act on the voltage fluctuations from the different DC and RF connections to the sample and the RF power of the detection procedure.

The effect of the RF power on the coherence of the exchange oscillations is a point to investigate. In the literature, with similar system and when a RF-QPC is employed [40, 74, 82], a triggering of the RF power is commonly implemented to have the RF power send to the sample only during the readout, not the manipulation. However, these measurements are performed at large RF power,  $-75$  dBm while we work at  $-86$  dBm, so the impact of our reduced power on the coherence of the spin oscillations should be verified experimentally.

This signal being an AC excitation at fixed frequency, it leads to a periodic excitation of the QPC 2DEG, so in the vicinity of the qubit detector. By capacitive coupling this excitation induces fluctuations of  $\varepsilon$ . The carrier frequency (250 MHz) being much smaller than the qubit detector exposure time, 1 ns, this excitation cannot be averaged over this time window. It can therefore be regarded as a slow noise equivalent to a charge noise. As presented in the second chapter section 2.4.5, the RF power is already limited to avoid the inter spin state excitations, but it might not be enough to avoid the dephasing. To investigate this point, coherent exchange oscillations in amplitude are implemented for different continuous RF power,  $-84$  dBm and  $-86$  dBm, the results are presented in Fig. 4.4.

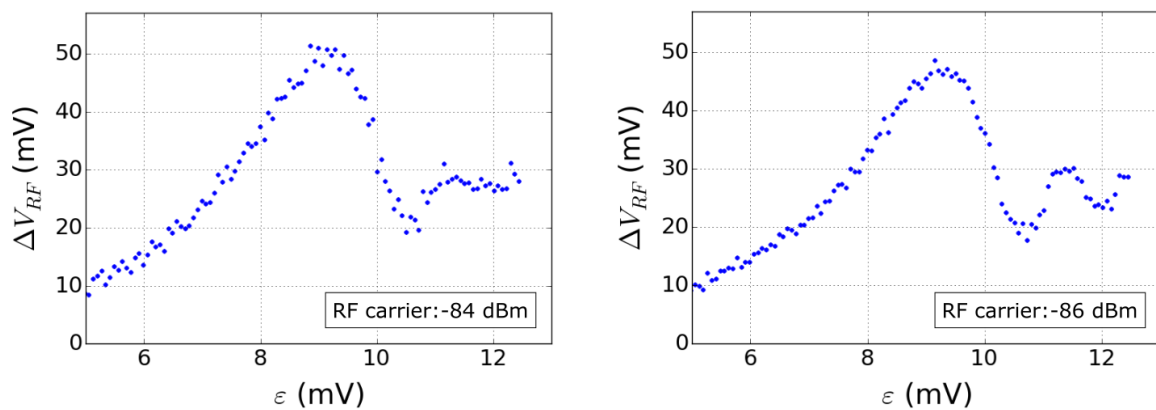


**Figure 4.4** – The voltage amplitude  $\Delta V_{RF}$  of the spin triplet RF-QPC is shown as a function of the oscillating position  $\varepsilon$ . These coherent exchange oscillations in amplitude have been measured with different continuous RF power,  $-84$  dBm and  $-86$  dBm, with a charge noise like effect noticeable for the larger power.

The effect of the RF power is mainly observable focusing on the second oscillation which is not visible for the larger RF power,  $-84$  dBm while it can be observed with the reduced power of  $-86$  dBm. The harmful effect of the RF power being verified, the triggering of the RF carrier has been developed in our setup to apply it only during the readout. However, by using it no improvement of coherence have been noticed whereas the signal extraction was more difficult because of signal rising times. One due to the chain of detection forcing the addition of a waiting time in the experimental sequence, so for each data point, and a second one for the first points of the experiment with an unknown origin. The benefit of such triggering being unobserved while the additional experimental constraints are important, we decided to pursue with the continuous power. Nevertheless, for safety it has been further reduced to  $-89$  dBm, a larger power reduction is not possible since it would deteriorate the SNR of the detection.

To suppress the noise from the DC and RF connections, the basic idea consists in improving the filtering of the lines to reduce the charge noise bandwidth on the sample. The voltage source having a non zero noise spectral density, typically  $\sim 25$  nV Hz $^{-1/2}$  for us, by reducing the cutoff frequency of the lines, the noise amplitude on the sample is reduced.

This reduction is possible by adding filters, but for the RF connections it is not possible since it would also restrict the bandwidth of the manipulations. Instead, one could think about adding attenuators to these lines to limit the fluctuations amplitude, but it will restrict also the available voltage range for these RF gates. For the implementation of the coherent exchange oscillations in amplitude presented so far, the full range was already needed, so in the end these RF gates are kept unchanged.

Contrary to the RF connections, the DC gates, already filtered thanks to the wiring techniques, can be further filtered. So far, the different lines have cutoff frequency of  $\sim 100$  MHz for the Thermocoax  $^{TM}$ , and 10 MHz for the Constantan wires, cf. 2.1.2.1 of the second chapter. These gates being only used for the constant voltages, their bandwidth can be further reduced and DC filters with a cutoff frequency of 1.9 MHz have been added at room temperature. The charge noise bandwidth being reduced, its impact on the sample is expected to be reduced too.

The benefit of using such filters can be noticed by comparing the two traces of Fig. 4.5. As it can be observed, by adding these DC filters, the first oscillation amplitude increases and the second oscillation is now visible.

These ameliorations were the only ones which could be performed with our experimental setup. However, we can notice that these modifications improved significantly the coherence of the exchange oscillations. This last trace with filter or the one of Fig. 4.1 corresponds to the fully optimised measuring conditions of the coherent exchange oscillations in amplitude. Now that the qubit detector cannot be further optimised, its charge sensitivity is discussed more in detail.

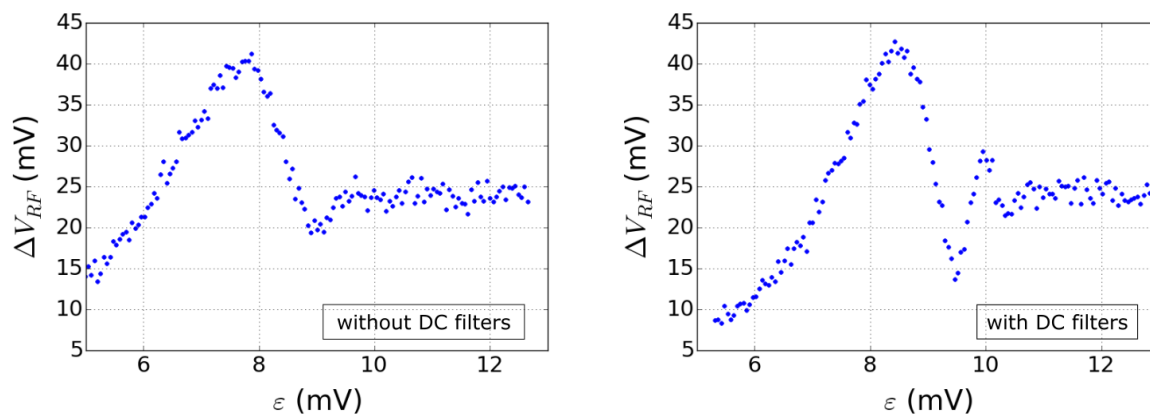


**Figure 4.5** – Voltage amplitude  $\Delta V_{RF}$  of the spin triplet RF-QPC as a function of the oscillating position  $\varepsilon$ . These coherent exchange oscillations in amplitude have been measured in similar experimental conditions except that in one case DC filters with a cutoff frequency of 1.9 MHz were added on the DC lines controlling the double quantum dot. The benefit of using the filters is clearly visible with the second oscillation visible when using the filters while it is not without them. These two measurements were performed with a continuous RF power set to  $-89$  dBm.

### 4.3 Estimation of a single electron influence from a DC excitation

The qubit detector being now optimised for the single electron detection, the question of its sensitivity arises, is it large enough to detect the single travelling electron, and what is its optimal working position?

We can remind that the working position is defined as the detuning for which the phase shift induced by the interaction with the single travelling electron is the largest, meaning the largest variation of triplet probability (i.e.  $\Delta V_{RF}$ ). To define this position, a trade-off has to be made between the high sensitivity to the travelling charge and a limited impact of the charge noise. Indeed, for a high sensitivity, the phase shift induced by the travelling charge might be large but compensated and masked during the averaging of the signal extraction because of the dephasing. In practice, it means that the optimal working position is not necessarily obtained for the largest detuning.

From the trace of Fig. 4.1, we can assume that the optimal working position will be located for the  $3\pi/2$  (7 mV) or  $5\pi/2$  (8.5 mV) spin rotation position where the sensitivity  $dJ/d\varepsilon$ , the slope of  $\Delta V_{RF}$ , seems to be the largest. In a first approach, one could expect the  $5\pi/2$  position as preferential, but the charge noise prevent it. Indeed, the  $[\pi, 2\pi]$  spin rotation is performed within  $d\varepsilon \approx 1$  mV, which is larger than the  $[2\pi, 3\pi]$  one performed in  $d\varepsilon \approx 0.5$  mV. However, the dephasing has not been considered yet, the amplitude of these oscillations are also different by a factor two, so in the end the two slopes  $dJ/d\varepsilon$ , so these two positions are expected to be rather similar.

To verify this assumption and, in particular, to establish if the single electron detection is possible, the step of triplet RF-QPC signal, labelled  $\delta V_{RF}$ , associated to the interaction with a single electron is evaluated. To perform this calibration, similarly to the previous chapter, the same idea of measuring the

evolution of the accumulated phase by the qubit detector under the effect of a DC bias is exploited. Different steps are necessary before coming to the estimation of  $\delta V_{\text{RF}}$ . First, the experiment has to be implemented followed by the extraction of the detuning shift  $\Delta\varepsilon$  induced by the DC bias. The conversion from DC bias to the number  $N_e$  of electrons interacting with the qubit detector will follow. Then, these two information will be used to define the detuning shift, also called gate like effect,  $\delta\varepsilon$  induced by a single electron. Finally,  $\delta\varepsilon$  is used to determine this step signal  $\delta V_{\text{RF}}$ . This last step will be performed for each detuning value of a trace of coherent exchange oscillations in amplitude in order to define the working position of the qubit detector. This position will corresponds to the detuning  $\varepsilon$  for which this  $\delta V_{\text{RF}}$  is the largest.

These different steps are now described one after the other.

### 4.3.1 Coherent exchange oscillations in amplitude influenced by the ECs electron density

The first step to the estimation of a single electron effect on the qubit detector is measuring the effect of many electrons, which is equivalent to measure the phase shift of the oscillations induced by a DC bias. The phase shift origin is similar to what have been explained in the previous chapter section 3.8, and is briefly remind here.

By applying a DC bias to the ohmic contact defining the chemical potential of the ECs, it is possible to control their electron density since  $\mu_{\text{EC}} = E_F - eV_{\text{bias}}$ . This bias is applied to the ohmic contact defining the chemical potential of the ECs passing nearby the qubit detector as sketched in Fig. 4.6b. When a negative bias is applied for instance, this density is increased and the ECs, being mostly coupled to the lower quantum dot, act like a negatively polarised gate pushing the confined electrons toward the upper quantum dot. So far, the singlet-triplet qubit is defined using the (1,1)-(2,0) charge transition of the double quantum dot, and this shift is toward the (2,0) charge configuration. Consequently, this shift means an increase of  $\varepsilon$ , so  $J(\varepsilon)$ , corresponding to an acceleration of the oscillations. The other way around, a positive bias induces a deceleration of the oscillations.

Such measurement has been implemented with  $V_{\text{bias}}$  stepped between 0 and  $-300 \mu\text{V}$ . The bias being negative, the oscillations accelerate with it, which is experimentally visible by a drift of the oscillations toward smaller detuning values. Indeed, this acceleration means that, with these coherent exchange oscillations in amplitude, the same phase will be accumulated earlier in terms of  $\varepsilon$  because of this gate like effect of the ECs. This effect being linear with  $V_{\text{bias}}$ , since it is due to the ECs electron density, the phase shift is expected to be linear with it too.

The results of this experiment are presented in Fig. 4.6, with a single trace of it at  $V_{\text{bias}} = 0$  being the trace of Fig. 4.1. In the 2D map presented here, the expected phase shift can be observed. For instance, the  $\pi$  spin rotation position is moving from  $\varepsilon \approx 7 \text{ mV}$  to  $\varepsilon \approx 6.5 \text{ mV}$  with a step of  $-300 \mu\text{V}$ .

The phase shift observed in this experiment can be compared with the one of the previous chapter section 3.8. Here, a  $\pi$  shift of the spin state is typically performed for a step bias of  $200 \mu\text{V}$ , while it was performed for more than  $300 \mu\text{V}$  in the previous chapter. This difference illustrates the higher charge

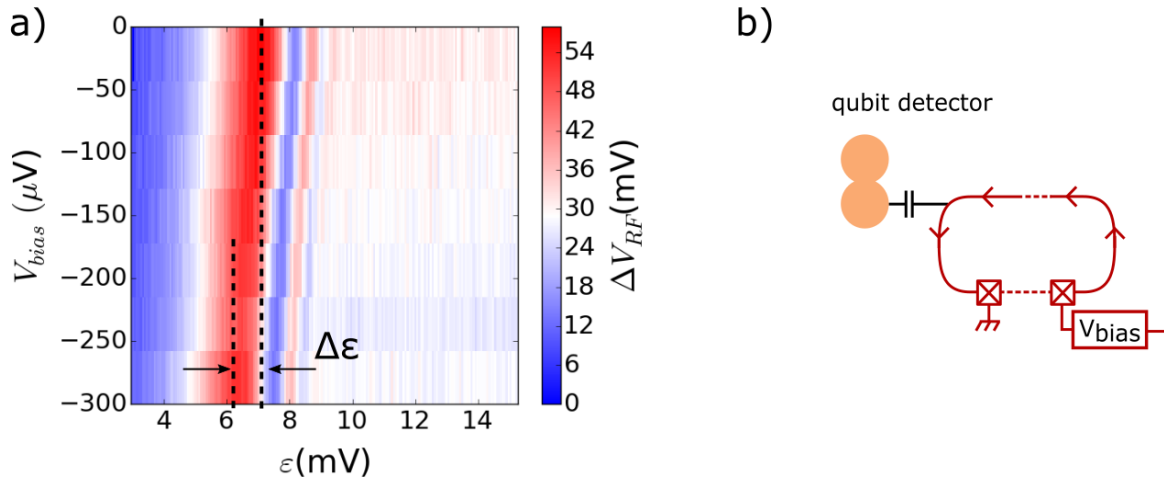


**Figure 4.6 – a)** Voltage amplitude  $\Delta V_{RF}$  of the spin triplet RF-QPC signal is shown for different oscillating positions  $\epsilon$  and DC bias  $V_{bias}$  applied to the EC. The voltage amplitude  $\Delta V_{RF}$  increases from blue to red,  $\epsilon$  is along the x axis and  $V_{bias}$  along the y axis. This map shows coherent exchange oscillations in amplitude measured for different EC electron density controlled by  $V_{bias}$ , since  $\mu_{EC} = E_F - eV_{bias}$ . By applying a negative  $V_{bias}$ , the density is increasing resulting in an acceleration of the oscillations, visible by this shift toward smaller  $\epsilon$ . The linear evolution is explained by this gate like effect of the 'polarised' EC inducing a detuning shift linear with the EC electron density so  $V_{bias}$ . **b)** Sketch of the experiment.

sensitivity of these oscillations which is only due to their implementation at larger detuning where  $dJ/d\epsilon$  is larger.

From this experiment, the detuning shift  $\Delta\epsilon$  induced by the travelling electrons in the ECs can be extracted. However, at this point of the discussion it will only be expressed as a function of the DC bias, so we have to go one step further and define the number  $N_e$  of electrons interacting with it. To do so, we can benefit from the flowing current in the ECs as a function of this DC bias and using the following expression:

$$N_e = \frac{I \cdot \tau_{int}}{e} \quad (4.5)$$

With  $\tau_{int}$  the interaction time between the electrons and the qubit detector, and  $e$  the elementary charge. The current  $I$  flowing in every EC can be easily measured as a function of the DC bias by performing a so called IV curve, remains the estimation of the interaction time which is actually not trivial.

### 4.3.2 Qubit detector exposure time

So far, the exposure time of the qubit detector, the interaction time  $\tau_{int}$ , was regarded as the set value to the AWG so 1 ns. This evaluation has to be verified since the pertinent information is the time spend to accumulate the phase during the oscillations of the spin state, not the temporal width of the exchange pulse. In addition, the accumulated phase depending on  $J(\epsilon)$  which itself evolves exponentially with  $\epsilon$ , most of the phase is accumulated for the largest detuning value, resulting in a reduction of the effective exposure time. Furthermore, this point is particularly important for our experiment considering the

deformation of the exchange pulse by the rising time of the AWG.

We define the interaction time  $\tau_{\text{int}}$  as the time necessary to accumulate 50% of the total phase accumulated during the exchange pulse. To estimate it, a typical pulse corresponding to the set amplitude of the  $\pi$  spin rotation is recorded with a fast oscilloscope, renormalised to its amplitude on the sample and cut in different time bins. For each bin the accumulated phase is calculated thanks to the exchange energy expression obtained by the fit of the data, cf. section 4.2.1. Finally, since most of the phase is accumulated for the larger detuning, the interaction time is given by the time spend to accumulate from 25% to 75% of the total phase.

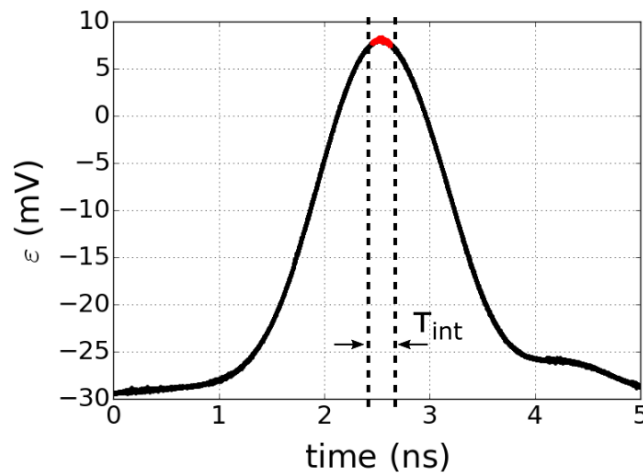


**Figure 4.7** – Exchange voltage pulse measured at the output of the AWG renormalised to its amplitude on the sample corresponding to the pulse inducing the  $\pi$  spin rotation. The coloured part of this pulse is the estimated time for which 50% of the total phase is accumulated, defining  $\tau_{\text{int}} \approx 200$  ps.

By following this procedure, the interaction time is estimated to  $\tau_{\text{int}} = 200$  ps. It corresponds to the coloured part of the detuning in the figure 4.7.

### 4.3.3 Single electron effect on the qubit detector

The interaction time and the phase shift being known, these information can now be used to determine the two researched information, the step signal and the working position of the qubit detector. We can remind that we expect this position to be either for the  $3\pi/2$  spin rotation position or the  $5\pi/2$ .

From the previous information, the gate like effect  $\delta\varepsilon$  of a single electron is first determined before being used to estimate the step signal  $\delta V_{\text{RF}}$ .

#### Gate like effect for one interacting electron

To determine this gate like effect  $\delta\varepsilon$ , the aim is to express the global detuning  $\Delta\varepsilon$  observed experimentally, cf. Fig. 4.6, as a function of  $N_e$ . To do so, on one hand this number is calculated from: the current flowing in the ECs, the interaction time just defined and using the expression 4.5.

On the other hand, the phase shift induced by the DC bias is extracted from the displacement of the  $\pi$  spin rotation position labelled  $\varepsilon_\pi$ .

The evolution of this point is plotted in Fig. 4.8 as a function of  $N_e$ . Finally,  $\delta\varepsilon$  is simply determined as  $\frac{\Delta\varepsilon}{\Delta N_e}$ , and is equal to  $\delta\varepsilon = -6\ \mu\text{V}$ .

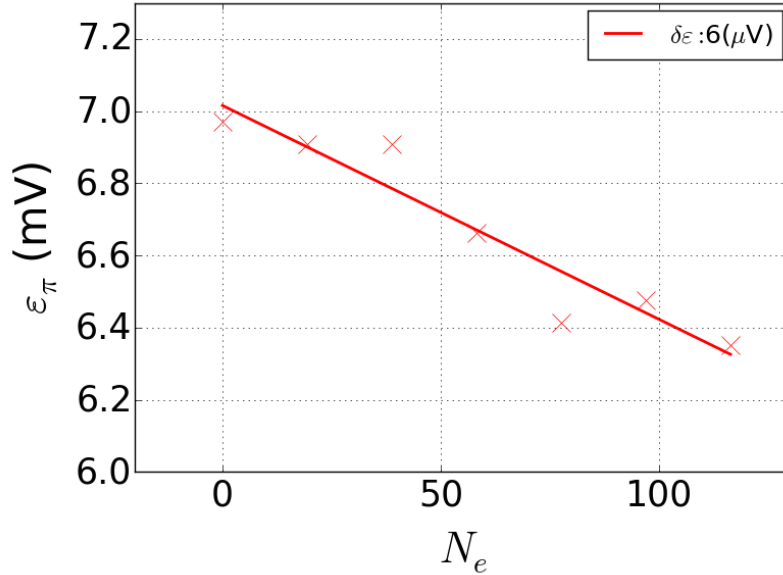


**Figure 4.8** – Value of  $\varepsilon_\pi$  inducing a  $\pi$  spin rotation shown as a function of the number of interacting electron with the qubit detector  $N_e$ . From the linear fit of the data points (red line), the step of detuning for a single electron is estimated which is in  $-6\ \mu\text{V}$ .

It is important to precise that for this estimation the influence of the travelling electron is averaged over every ECs since the single electron is considered as spread over the 10 of them. This point arises from the fact that the DC bias controls the chemical potential of every ECs, so the observed detuning shift is induced by the influence of each EC. Similarly,  $N_e$  corresponds to the total number of electrons flowing in the ECs. Combined, these two elements means that  $\delta\varepsilon$  is the gate like effect of an electron spread over every ECs, i.e. with an equiprobability to be in any of them.

### Step signal $\delta V_{\text{RF}}$ for a single charge

Finally, the step signal for a single electron can be determined for each detuning value of the range used in the measurement, it is calculated with:

$$\delta V_{\text{RF}} = \Delta V_{\text{RF}}(\varepsilon - \delta\varepsilon) - \Delta V_{\text{RF}}(\varepsilon) \quad (4.6)$$

In the expression  $\Delta V_{\text{RF}}(\varepsilon - \delta\varepsilon)$  the minus sign stands for the acceleration of the oscillations with this increase of ECs electron density.

These extracted values are the blue crosses in Fig. 4.9 with in brown the trace used for the calculation corresponding to the fit of the experimental data measured for  $V_{\text{bias}} = 0$ . The fit is used instead of the

experimental data to avoid the experimental noise.

The first element to comment about this calibration is the amplitude of the step signal which is small, the largest one is of the order of  $\delta V_{\text{RF}} = \pm 300 \mu\text{V}$ , for this reduced gate like effect of  $\delta\varepsilon = -6 \mu\text{V}$ . The first conclusion about this calibration is the impossibility to perform the detection of the single travelling charge in a single shot manner. Indeed, such single shot detection is possible if the interaction with the travelling charge induces a  $\pi$  phase shift, so a spin flip of the oscillating spin state. In our experiment we are far from it,  $\delta\varepsilon$  should be larger by several order of magnitude than what it is. Considering the  $[2\pi, 3\pi]$  spin rotation, this  $\pi$  phase shift is performed for  $d\varepsilon \approx 0.5 \text{ mV}$  (see Fig. 4.1). Then, the single shot detection, the  $\pi$  phase shift is possible for the interaction with approximately 80 electrons during this interaction time of  $1 - 10 \text{ ps}$ . The develop qubit detector has therefore a charge sensitivity of about  $8.10^{-5} \text{ e Hz}^{-1/2}$  which is close two orders of magnitude smaller than required, i.e.  $1.10^{-6} \text{ e Hz}^{-1/2}$  for one electron with  $1 \text{ ps}$  of interaction time.

In addition, performing this single electron detection by repeating and averaging the signal over many attempts appears as extremely difficult. As discussed in the second chapter section 2.4.4, the noise spectral density of the 4K amplifier is about  $0.5 \text{ nV Hz}^{-1/2}$ , with the amplification of the signal and the cutoff frequency of the low pass filter, it gives a typical noise of  $\sim 100 \text{ mV}$ . Then, to be able to observe  $\delta V_{\text{RF}} = \pm 300 \mu\text{V}$ , the averaging level of the measurement has to be large. As we will see, this will induce constraints in the experimental procedure because of the qubit detector instability and the required level of accuracy of the working position.

The second element to comment is the working position which is obtained for the two expected detuning of the  $3\pi/2$  and  $5\pi/2$  spin rotation position, confirming the harmful impact of the charge noise in our experiment. Indeed, as discussed at the beginning of this section, the  $[\pi, 2\pi]$  spin rotation is performed for  $d\varepsilon \approx 1 \text{ mV}$  whereas for the  $[2\pi, 3\pi]$  one  $d\varepsilon \approx 0.5 \text{ mV}$ . It means that the slope, so the sensitivity of the qubit detector at this  $5\pi/2$  position can be up to two times larger than the  $3\pi/2$  one. However, as explained previously, the dephasing induces a reduction of the signal amplitude for this oscillations sufficiently large to suppress this advantage and we end up in this configuration with two equivalent working positions.

Even if the step signal is small, the final experiment will be implemented requiring to select a working position. To choose between these two positions, the experimental constraints have to be taken into account. Since the averaging level has to be large, the measuring time will be long, so the largest qubit detector charge sensitivity has to be maintained over a long time.

For this selection, the instability of the sample must be considered. It is equivalent to a slow drift of the working position toward less or not sensitive position. The  $\pi$  rotation of the spin state is performed within approximately  $1 \text{ mV}$  for the first oscillation, while it is done in  $0.5 \text{ mV}$  for the second one. The safest working position is therefore for the first oscillation so the  $3\pi/2$  spin rotation position.

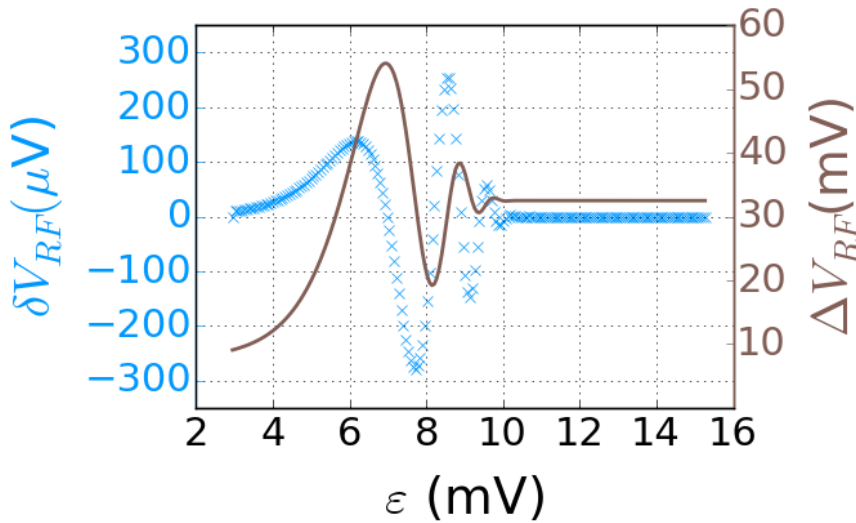


**Figure 4.9** – Estimated amplitude of the signal  $\delta V_{RF}$  step (left y axis, blue) and the voltage amplitude  $\Delta V_{RF}$  of the spin triplet RF-QPC signal (right y axis, brown) are plotted against the detuning  $\varepsilon$ .  $\delta V_{RF}$  is the estimated signal variation expected for the interaction with a single travelling electron inducing a gate like effect of  $-6 \mu\text{V}$ .  $\Delta V_{RF}$  is the result of the fit of the coherent exchange oscillations in amplitude measured with  $V_{bias} = 0 \text{ V}$ . The fit is employed instead of the experimental data points to avoid the noise fluctuations. The maximum signal is obtained for the  $3\pi/2$  and the  $5\pi/2$  spin rotation position, i.e.  $7.5 \text{ mV}$  and  $8.5 \text{ mV}$ .

## 4.4 Discussion on the qubit detector sensitivity

Before coming to the use of such qubit detector, some remarks and possible improvements of the qubit detector are discussed.

The previous measurement indicates that in such configuration, the single electron detection is probably not possible,  $\delta V_{RF}$  being too small, so to succeed this detection it has to be increased. It is defined by two elements, one is the qubit detector charge sensitivity, which is limited by the dephasing already optimised for us, remains the second element, the gate like effect induced by the travelling electron. In the current section, the different methods tried to improve it are presented.

### 4.4.1 (1,1)-(0,2) charge transition

A possible solution to the enhancement of the gate like effect  $\delta\varepsilon$  is to increase the capacitive coupling between the qubit detector and the ECs. To do so, a method is to directly increase the coupling to the electron reservoir hosting these ECs. However, it turns out that going toward larger coupling than  $\sim \text{MHz}$  induces an instability of the sample tuning. It is therefore not a suitable solution for us. Even so, there is another way.

So far, the considered charge transition is the (1,1)-(2,0) one, with the oscillations taking place in the (2,0) charge configuration, so in the quantum dot the farthest to the ECs. A solution of improvement could be to use the other charge transition (1,1)-(0,2). The aim is to implement these coherent exchange oscillations in the quantum dot the closest to the ECs. There, the capacitive coupling between the two

is expected to be larger, so the gate like effect should be enhanced. This transition was not used so far because the single shot spin readout cannot be implemented with it. The RF-QPC is not sensitive enough to detect single shot a charge tunneling event with this transition, the quantum dots being further away from it in such sample tuning configuration, so the single shot travelling charge detection is not possible.

From this charge transition, the singlet-triplet spin qubit is defined and optimised as presented in the previous chapter. Finally, the same experiment of changing the electron density of the ECs with a DC bias while performing coherent exchange oscillations in amplitude is implemented to investigate this new qubit detector charge sensitivity.

In addition to the expected larger gate like effect  $\delta\varepsilon$  of a single electron, the phase shift induced by the travelling charges is expected to be opposite to the one measured with the other charge transition. Again, the shift of detuning is explained by the gate like effect of the ECs. When they are negatively polarised, i.e. larger electron density, they repel the oscillating electrons toward the upper quantum dot. The same phenomenon is expected here but instead of accelerating the oscillations, it should slow them down. Indeed, pushing the electrons toward the upper quantum dot, so here the (1,1) charge configuration, is equivalent to a decrease of the detuning, so of the exchange energy.

The resulting 2D map of this experiment with the equivalent analysis than described previously are presented in the Fig. 4.10.

Different comments can be made about these results. First the expected deceleration of the oscillations is visible in the 2D map with the shift toward largest detuning while applying negative  $V_{\text{bias}}$ . The evolution of the spin visibility can also be commented since it is decreasing while going from negative to positive DC bias. This direction is also the one of the measurement, so we associate this decrease to the instability of the RF-QPC tuning which was drifting in time, i.e. its charge sensitivity was not stable.

Concerning the sensitivity of the qubit detector, as expected the single electron gate like effect is larger when using this charge transition. It is estimated to  $\delta\varepsilon \approx 16 \mu\text{V}$  which is close to three times larger than for the other charge transition.

In a first approach, this charge transition seems preferential, the gate like effect being larger than before. Except that, the weak charge sensitivity of the RF-QPC to the tunneling of an electron in/out of this lower quantum dot prevents it. Remember that the complete detector relies on a charge to spin conversion followed by a spin to charge conversion. Therefore, these two conversions have to be as efficient as possible to induce an important signal variation and so be detectable.

The first stage of detection relies on this gate like effect. The objective is to induce the largest shift of spin triplet probability measured with the Pauli spin blockade, the second stage of detection. As explained in the previous chapter section 3.3.1, this spin to charge conversion relies on the distinction of the charge state of the double quantum dot, (1,1) for the triplet spin state and (0,2) for the spin singlet. Then, the difference of signal amplitude between these two charge states should be large too to be easily detectable. Meaning that the charge sensitivity of the RF-QPC is also a key ingredient of the global qubit detector. In the end, because of the reduced charge sensitivity of the RF-QPC, the step signal is estimated to

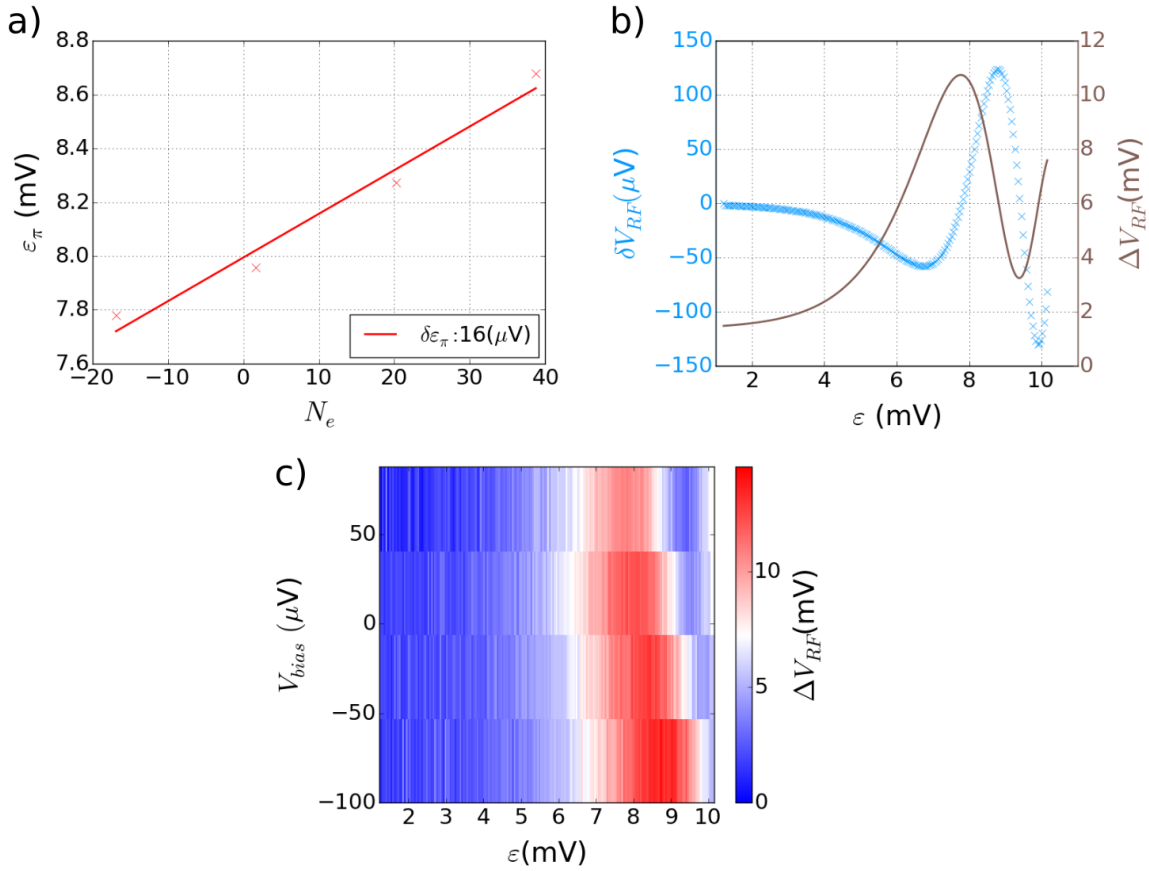


**Figure 4.10** – **a)** Evolution of  $\varepsilon_\pi$  the position of the  $\pi$  spin rotation position as a function of  $N_e$  the number of interacting electron with the qubit detector. The resulting gate like effect of an electron is  $\varepsilon_\pi = 16 \mu\text{V}$  for this (1,1)-(0,2) charge transition. **b)** The step signal  $\delta V_{RF}$  and the voltage amplitude  $\Delta V_{RF}$  of the spin triplet RF-QPC signal are plotted as a function of the detuning  $\varepsilon$ . The left y axis refers to the step signal  $\delta V_{RF}$  associated to the interaction with a single travelling charge is represented with light blue crosses, the right y axis corresponds to the result of the fit of a coherent exchange oscillations in amplitude trace measured with  $V_{bias} = 0 \mu\text{V}$  shown in c). The maximum step signal  $\sim 125 \mu\text{V}$  is obtained for the  $3\pi/2$  spin rotation position. **c)** The signal  $\Delta V_{RF}$  is shown as a function of the detuning  $\varepsilon$  along the x axis and the DC bias applied to the ECs  $V_{bias}$  along the y axis. The observed phase shift is explained in the main text.

$\sim 125 \mu\text{V}$ . This value is close to two times smaller than for the other charge transition, even if the single electron gate like effect is larger by a factor three, highlighting the importance of the RF-QPC charge sensitivity. This charge transition is therefore unsuitable for this single travelling charge detection.

#### 4.4.2 Number of ECs

The last measurement shows that the previous spin qubit developed around the (1,1)-(2,0) charge transition is preferential. Then, only this one will be considered in the following. To enhance the gate like effect, we just see that increasing the coupling is not possible for us. Another solution is to strengthen

the impact of these travelling charges by reducing the number  $\nu$  of ECs. This can be done by either increasing the magnetic field or using additional gates. Before describing how to implement it, the possible gain in term of travelling charge effect on the qubit detector due to this reduction of  $\nu$  is discussed.

To establish the effect of such ECs reduction, a distribution of the travelling electron over every ECs is considered just like in the calibration experiment with the DC bias. Another solution based on the higher probability to inject the electron in the closest EC to the source, because of the capacitive coupling scaling inversely to the distance, and the absence of electron tunneling between the ECs could be considered. This last point being motivated by the equilibration of electron density between two ECs which has not been measured over  $100 \mu\text{m}$  [100, 101, 102, 103]. But these measurements were performed at  $\nu = 2$  where the ECs are well defined and separated while we work at  $\nu = 10$  where it is not the case. Even if the probability to inject the electron is higher for the closest EC to the source dot, it will probably be distributed over all of them within the  $5 \mu\text{m}$  separating the source dot to the qubit detector. We expect therefore to be in a situation equivalent to the DC bias experiment with this equipartition of the travelling electron.

Then, the possible gain of such reduction of number of ECs is calculated from the effect of the travelling charge, labelled  $\delta$ , where we consider only the capacitive coupling between the ECs and the qubit detector. This effect is therefore proportional to  $\frac{\alpha}{x_i}$  with  $x$  the inter-EC distance and  $i$  the considered EC,  $\alpha$ , the overlap between the ECs and the qubit detector times the permittivity, is set equal to one in the following for simplification.

In this configuration, the global effect is proportional to  $\frac{1}{N} \sum_{i=1}^N \frac{1}{x_i}$  with  $N$  the number of ECs. We assume  $x$ , the distance inter-EC, equivalent to the distance between the qubit detector and the first EC, which is a reasonable assumption to get an order of magnitude.

The effect  $\delta$  of the travelling charge is normalised to the configuration of  $\nu = 1$ , and is presented in Fig. 4.11. According to this calculation  $\delta$  can be increased by a factor three approximately going from  $\nu = 10$  to  $\nu = 1$ . Such gain is not enough to reach the single shot detection, but it could be sufficient for an averaged detection experiment of a single travelling charge.

The implementation of such reduction of the number of ECs is now discussed. As mentioned, there is two possibilities, either using the magnetic field or polarised metallic gates, solutions which unfortunately were not working for us, it will be explained why.

The solution of the magnetic field is the simplest one and arises from the fact that the number  $\nu$  depends on the magnetic field. As introduced in the first chapter section 1.7  $\nu = \frac{ne\hbar}{eB}$ , so by increasing the magnetic field  $\nu$  is reduced. In our experimental conditions the magnetic field was limited to 430 mT because of the limits of our tank circuit and the RF-QPC charge sensitivity. This limitation is due to its components which are varying with the magnetic field and the temperature as discussed in the second chapter subsection 2.4.2.2. For larger magnetic field the charge sensitivity of the RF-QPC was too low to permit the fast charge manipulations. However, with another tank circuit this solution is simple to implement and this estimated gain could be verified experimentally.

Decreasing the number of ECs down to  $\nu = 1$  is not possible when using such spin qubit detector since it

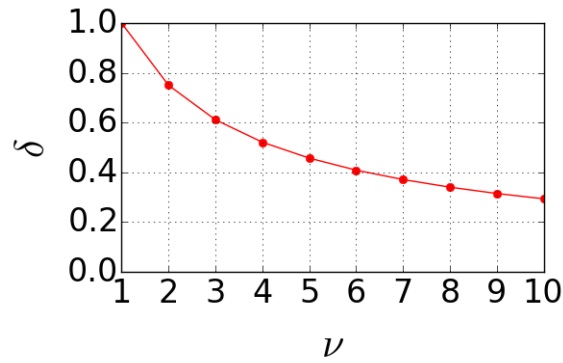


**Figure 4.11** – Normalized evolution of the estimated interaction strength of the travelling charge with the qubit detector  $\delta$  depending on the number  $\nu$  of EC. Here we consider an equipartition of the electron over the EC.

would imply to use a large magnetic field. The energy splitting between the spin singlet and triplet being decreasing with the magnetic field, for large magnetic field the singlet-triplet spin qubit cannot be defined anymore, the upper limit is about  $\sim 1$  T [61]. In addition, by increasing the magnetic field the electron confinement is more important too. Then, reaching a high coupling between the quantum dots and the electron reservoir, so the qubit detector and the ECs, is more difficult experimentally. Nevertheless a reduction to a few ECs seems possible without adding a too large experimental constraint.

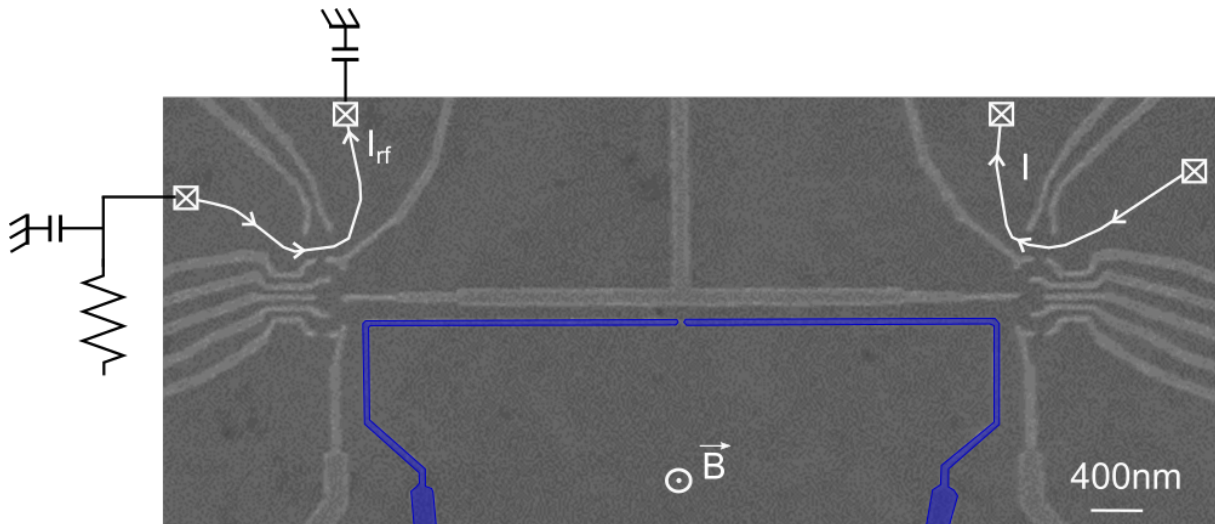


**Figure 4.12** – Scanning electron micrograph of the sample with colourised in blue additional gates designed to select the number of edge channels travelling between the source quantum dot and the qubit detector.

The second solution is to use polarised metallic gates to select the number of ECs passing nearby the qubit detector. The principle is the same than a QPC, by polarising such gates with negative voltages, the 2DEG can be depleted, reducing the number of allowed ECs. If these gates are localised all along the

path from the source dot to the qubit detector, as designed in our sample see Fig. 4.12, ideally only one EC can carry the travelling charge, even at low magnetic field.

Here also the required high coupling to the ECs has to be taken into account, and limits this technique. These gates being located nearby the double quantum dot, by polarising them the coupling to the electron reservoir is reduced. Reaching  $\nu = 1$  only by using polarised gates like these ones is probably too demanding in term of sample tuning. In our experiment we could only polarise slightly the left gate too less than ten millivolt without impacting the experiment, but with another design and the gates further away from the quantum dots, this solution should be useful to reduce  $\nu$ .

In conclusion, solutions exist to enhance the step signal  $\delta V_{\text{RF}}$  which could not be used for our experiment but with minor modifications it could be possible to employ them. In addition, here we focus only on the increase of the gate like effect of the travelling charges, a better filtering of the lines and a global work on the charge noise of the experiment would help to increase the charge sensitivity of the qubit detector. Improving the RF-QPC charge sensitivity is also a solution rather simple to implement. The calibration and optimisation of the qubit detector being finished, we will now focus on the implementation of the final experiment.

## 4.5 Injection of a single electron into the ECs

According to the previous calibration, the single electron detection will be difficult to reach since the step signal estimated to  $300 \mu\text{V}$  cannot be enhanced in our experimental conditions. However, it remains an estimation, besides, even if the single electron level cannot be reached, a few electrons wavepacket should be measurable. To verify this point, the final experiment will be implemented with few elements which remains to be developed, the main one being the single electron source.

As a single electron source we use a single quantum dot, called source dot, as [26]. In such system the different charge states are separated in energy by the charging energy  $E_c$  introduced in the first chapter section 1.1.3. This energy being of the order of  $\sim 1 \text{ meV}$  it is large enough to permit a single electron emission toward an electron reservoir when applying a short voltage pulse to the source dot chemical potential, see sketch Fig. 4.13b. Actually, by using such source, not only one electron is emitted but a hole too. Indeed, to come back to the initial charge state of the source dot, an electron is loaded from the Fermi sea to the source dot at the end of the voltage pulse, leaving a hole in the ECs as as sketch in Fig. 4.13b.

To implement this electron emission for our experiment, two information are required: verifying to which reservoir the source dot is coupled and setting the injecting position. This point means defining the source dot chemical potential and its coupling to the reservoir by setting the voltage of  $V_{4:4}$  and  $V_{4:3}$  (see Fig. 4.13a). The other gate voltages being already set to define the single quantum dot.

The investigation of coupling to the reservoir is first presented followed by the study of the electron injection with what we call an injecting voltage pulse (IVP). It is a square voltage pulse applied to the red RF gate (see Fig. 4.13a) using the AWG.

### 4.5.1 Single quantum dot

After tuning the second double quantum dot as a single one, as presented in the first chapter section 1.3, the next step is to verify to which reservoir it is coupled. Indeed, as it can be seen in the SEM image of Fig. 4.13a, two electron reservoirs are accessible for this source dot, the upper one labelled  $V_U$  and the lower one  $V_L$ . Since this source dot will be used to inject the electron to detect, it has to be coupled to the lower reservoir hosting the ECs passing nearby the qubit detector, sketched with the red line in Fig. 4.13.

Determining to which reservoir the source dot is coupled is possible by changing the conditions permitting to load or unload an electron from the reservoir. To force this change of loading/unloading condition, the Fermi sea level can be modified by applying a DC bias to it. If it is elevated, to emit or load an electron from this reservoir, the source dot chemical potential has to be elevated too, which is experimentally visible by a shift of the charge degeneracy line of a stability diagram.

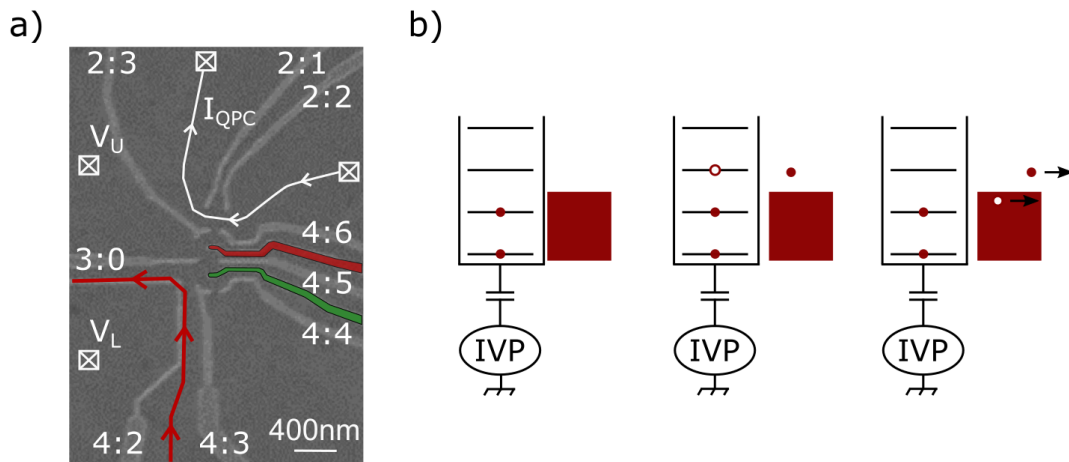


**Figure 4.13** – *a)* Scanning electron micrograph of the source dot with in white labelled the different gate voltages and electron reservoir mentioned in the main text. In the experiment only the red coloured RF gate is used. The red line represents the edge channels passing nearby the qubit detector. *b)* Sketch of the implementation of the single electron injection. When a non zero voltage pulse (called IVP in the text) is applied to the source dot, its chemical potential is brought above the Fermi sea inducing an electron emission toward the edge channels of the electron reservoir represented in the middle sketch. When the pulse amplitude is zero again, an electron is loaded into the source dot inducing the emission of a hole propagating also in the edge channels.

Such experiment is implemented by measuring stability diagrams of this source dot while DC bias of 0 and  $-300 \mu\text{V}$  are applied, one after the other, to the upper and lower electron reservoir. The applied bias being negative, it corresponds to the described situation where the Fermi sea is elevated, and therefore the charge degeneracy line should be shifted toward more negative DC gate voltages. Effect visible only when the bias is applied to the reservoir coupled to the source dot.

The resulting four stability diagrams are presented in Fig. 4.14, where the two upper ones correspond

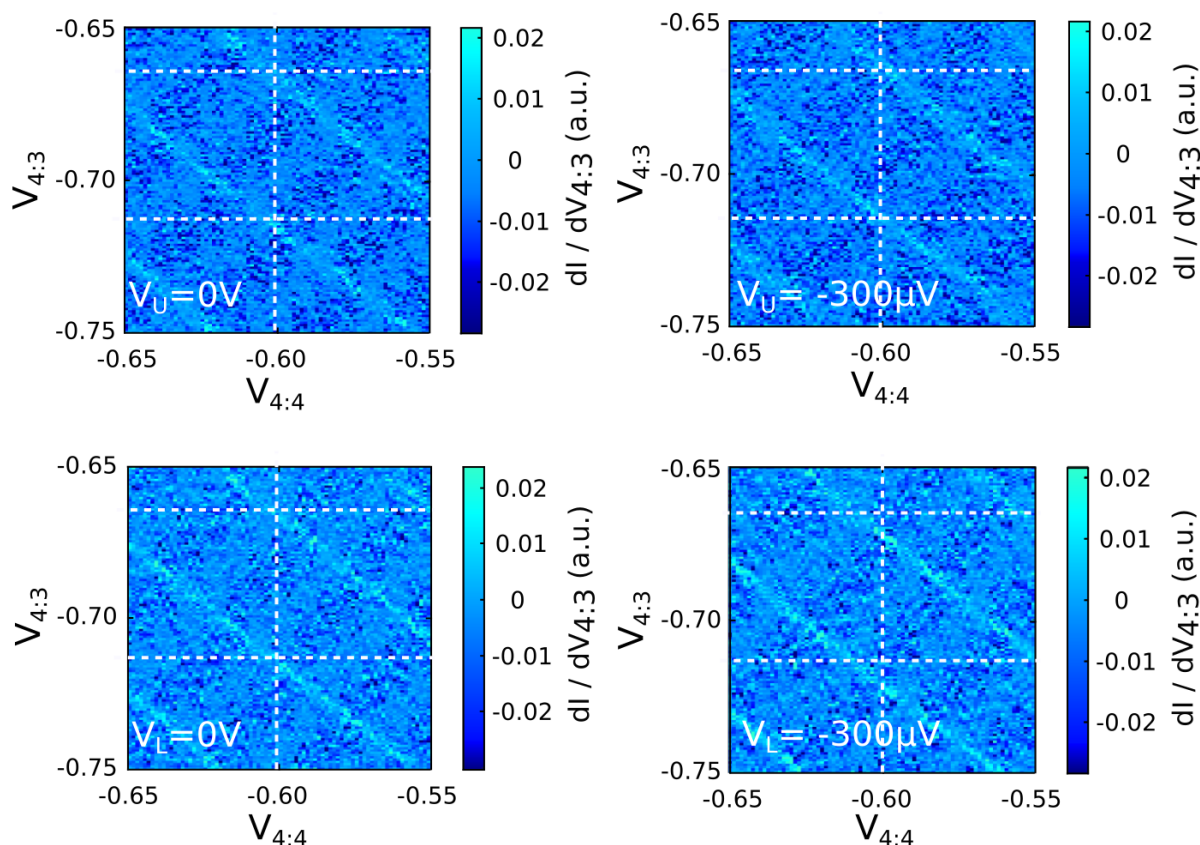


**Figure 4.14** – Stability diagrams of the source dot without (left) and with (right) DC bias applied to the two different reservoirs labelled  $V_U$  and  $V_L$  in Fig. 4.13. The differential value of the QPC current  $dI/dV_{4:3}$  is plotted as a function of  $V_{4:3}$  ( $y$  axis) and  $V_{4:4}$  ( $x$  axis). The white crosses are guide for the eyes to highlight the displacement of the degeneracy lines only when changing the bias applied to  $V_L$ , indicating that the source dot is only coupled to this electron reservoir.

to the bias applied to  $V_U$ , the two lower ones to the bias applied to  $V_L$  and the white crosses are guide for the eyes. When the bias is applied to the upper reservoir there is no change of the charge degeneracy lines position, while a shift toward more negative gate voltages is observed when the bias is applied to  $V_L$ . From this measurement we can conclude that the source dot is coupled to the lower reservoir hosting the ECs passing in front of the qubit detector as required. It remains now to study more in detail the electron emission by the IVP to set the injecting position responding to our experimental constraints.

## 4.5.2 Electron injection

Our constraints on the electron injection are double. One is the ability to emit only one electron with such pulse, this point is developed in the following with the study of the IVP efficiency. The second one is about the coupling to the reservoir, which here is equivalent to set the voltage of the gate  $V_{4:3}$  (first chapter section 1.3).

The target coupling to the reservoir is typically  $\sim$  GHz or larger in order to have the lowest incertitude

on the emission time, meaning inducing a travelling electron wavepacket shorter than the qubit detector exposure. As presented in the first chapter section 1.3, this regime is obtained when the charge degeneracy lines are getting broader, like for  $V_{4:3} = -0.67$  mV in Fig. 4.16a. There, the broadening is explained by the coupling which becomes larger than the thermal excitation. The electron temperature being of the order of 100 mK, thus, the coupling is of the order of  $\sim$  GHz, and increasing when  $V_{4:3}$  is getting less negative. To set the injecting position, this high coupling is necessary but the quantum dot should be well defined too. Hence, this position should not be too close to the disappearance of the lines, happening typically for  $V_{4:3} = -0.6$  mV according to the stability diagram of Fig. 4.16a. The injecting position should associate these two constraints on the coupling which are typically fulfilled for  $V_{4:3} = -0.65$  mV.

The coupling being defined, now it remains to adjust the chemical potential of the source dot with  $V_{4:4}$  by investigating the IVP effect. The ability to force a charge tunneling event by applying a short voltage pulse on a RF gate has been already used in the previous chapters, but here we should verify if only one electron is emitted. In addition, knowing for which voltage amplitude it is emitted would be a valuable information.

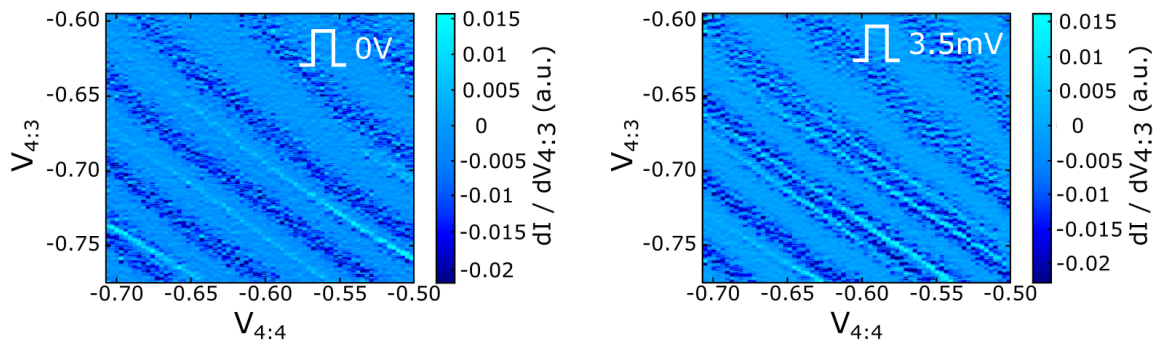


**Figure 4.15** – Derivative of the QPC current  $I$  with respect to the swept gate voltage  $V_{4:3}$ .  $V_{4:4}$  is stepped in the  $x$  axis. For these stability diagrams of the source dot, square voltage pulses with amplitudes of 0 and 3.5 mV estimated on the sample, were applied to the red RF gate, see Fig. 4.13 with a repetition rate of 10 MHz. When a non zero pulse is applied, the charge degeneracy lines, in light blue, are doubled with one line per square pulse extremum. The separation between them is dependent of the square voltage pulse amplitude, the larger the voltage amplitude the more separated are the lines.

This point can be investigated thanks to the evolution of the charge degeneracy lines when such voltage pulse is applied. Indeed, these lines indicate the tunneling of an electron, and the IVP controls the source dot chemical potential, so by looking at the evolution of these lines, it is the IVP effect which is observed. If a square pulse is applied for instance, instead of having only one chemical potential position to exchange an electron with the reservoir, two positions are possible, one per pulse extrema. This phenomenon is observed by a doubling of the charge degeneracy lines in a stability diagram. The separation in DC voltage  $\delta V$  of these two lines depends on the IVP amplitude, so by extracting  $\delta V$  as a function of this voltage pulse amplitude, a conversion from applied RF pulse to equivalent DC voltage shift is obtained. In the following this conversion will be used to determine the minimum IVP ampli-

tude required to cross a charge degeneracy, so to emit a single electron depending on the injecting position.

Such experiment has been performed with a square voltage pulse, equivalent to the IVP, having an amplitude estimated to 3.5 mV on the sample. The resulting maps, with and without pulse are presented in Fig. 4.15 where the doubling of the charge degeneracy lines can be observed when the pulse is applied. The distance  $\delta V$  between the lines has been measured for different voltage amplitudes and are presented in Fig. 4.16b. Referring to this figure, the maximum IVP amplitude,  $-32$  mV, is equivalent to a DC gate voltage shift of  $\delta V \approx 0.1$  V. According to the stability diagram of Fig. 4.16a, the DC gate voltage distance between two charge degeneracy lines is about 0.05 V. Thus, for the full IVP amplitude,  $\delta V \approx 0.1$  V, maximum two lines can be crossed when applying such pulse, meaning that maximum two electrons can be emitted. By reducing this amplitude the single electron injection is therefore possible. Finally, a typical injecting position is indicated with the point A on the stability diagram of 4.16. This point is for instance separated to the next degeneracy line, toward more negative voltages, by approximately  $-0.03$  V, thus, according to Fig. 4.16, the electron should be emitted starting from an IVP amplitude about  $-10$  mV.

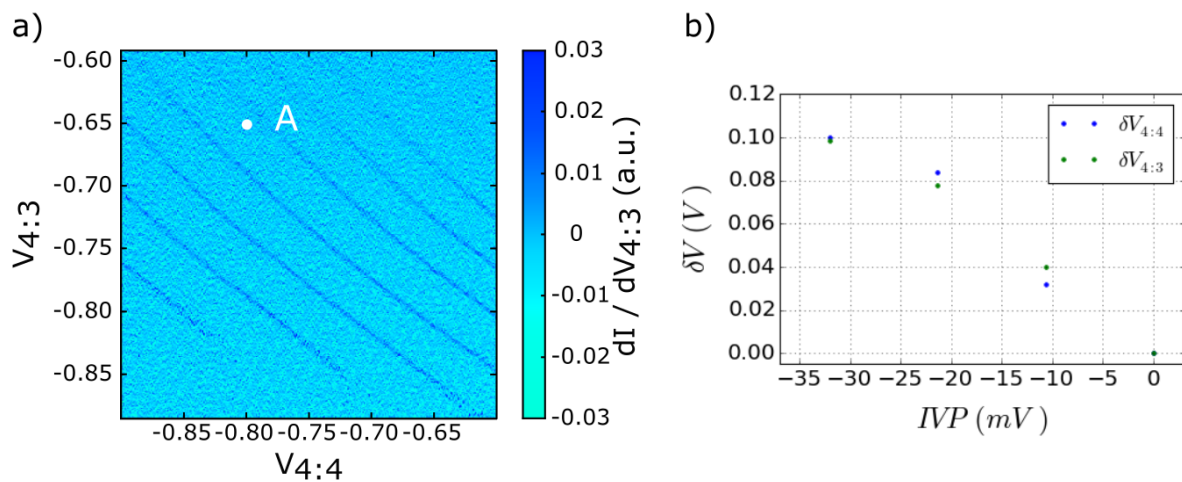


**Figure 4.16** – a) Stability diagram of the source dot as defined in Fig. 4.14 and Fig. 4.15, the point A corresponds to a typical injecting position. b) Voltage splitting  $\delta V$  between the doubled charge degeneracy line (cf. Fig. 4.15) as a function of the IVP amplitude. This curve permits a conversion from IVP amplitude to equivalent DC gate voltage shift. Depending on the injecting position, so distance to the next charge degeneracy line, it is a way to evaluate when an electron can be emitted.

## 4.6 Detection of Edge Magneto Plasmon

The final experiment aiming to the detection of the single travelling electron is composed by two components, the qubit detector and the single electron source. This source and the qubit detector being defined and optimised, this final experiment can almost be implemented. It remains only to combine these two elements by setting the delay between the electron injection (IVP) and the detection (1 ns

exchange pulse). In the following this delay will be called injection pulse delay. The implementation of this experiment is first presented before describing the adjustment of this delay thanks to the preliminary results of its implementation.

### 4.6.1 Experimental sequence

The two key elements of this single electron detection experiment are the two voltage pulses: the IVP of the source dot, and the exchange pulse of the qubit detector. The delay between these pulses, the injection pulse delay, is controlled by the channel skew of the AWG. Since its range is limited, it imposed a constraint on the width of the IVP pulse, not defined yet. The channel skew can varies in a range from  $-5$  ns to  $5$  ns. We would like to see the two fronts of the IVP in order to detect either the single injected electron by the IVP pulse, or the hole following it as sketched in Fig. 4.13b. In the same time, the pulse should be long enough to ensure the electron emission. In the end, the IVP width is set to  $6$  ns with an intrinsic delay  $\delta t_{int} = -2$  ns as sketched in Fig. 4.17a. With these settings, the detection pulse will be synchronised with the two fronts of the IVP for injection pulse delay of  $2$  ns and  $-4$  ns.

Now that the experimental procedure is defined, the expected results of its implementation can be discussed, with first the experimental signature of a single electron detection.

The electron is emitted for the first front of the IVP, synchronised with the detection for an injection pulse delay of  $2$  ns. As presented previously, cf. section 4.3, an increase of the ECs electron density leads to a negative step of  $\Delta V_{RF}$ . Thus, for this injection pulse delay of  $2$  ns, a negative step of  $\Delta V_{RF}$  with an amplitude of the order of the step signal  $\delta V_{RF}$  is expected. In addition, this step should be visible only when the IVP amplitude is large enough to emit an electron. The resulting expected signal is the upper sketch of Fig. 4.13b.

Similarly, for the second front of the IVP, synchronised with the detection for an injection pulse delay of  $-4$  ns, it is a hole which should be detected (cf. Fig. 4.16b). Since it is a decrease of the ECs density, its signature is a positive step of  $\Delta V_{RF}$  with an amplitude expected about  $\delta V_{RF}$ . Here also this step should be visible for every IVP amplitude above a certain threshold value as represented in the lower sketch in Fig. 4.13b.

However, these expectations could be verified experimentally only if the set delay to the AWG is the real one on the sample, which is not true experimentally. The imperfection of the experiment (AWG intern delays between the channels, coaxial lines with different lengths,...) add an unknown delay between the IVP and the exchange pulse of the qubit detector. An adjustment of these  $2$  ns and  $-4$  ns is therefore necessary. To adjust these values, we could benefit from the detection of edge magneto plasmon (EMP) resulting from the capacitive coupling between the IVP and the ECs, or the direct capacitive coupling between the qubit detector and the IVP.

EMP are collective excitation of the 2DEG, in our case they are a collective excitation of the ECs electrons due to the short voltage pulse on the nearby RF gate. Such EMP have been widely studied over the past years [93, 95, 104, 105], in these experiments they were excited by a voltage pulse applied to

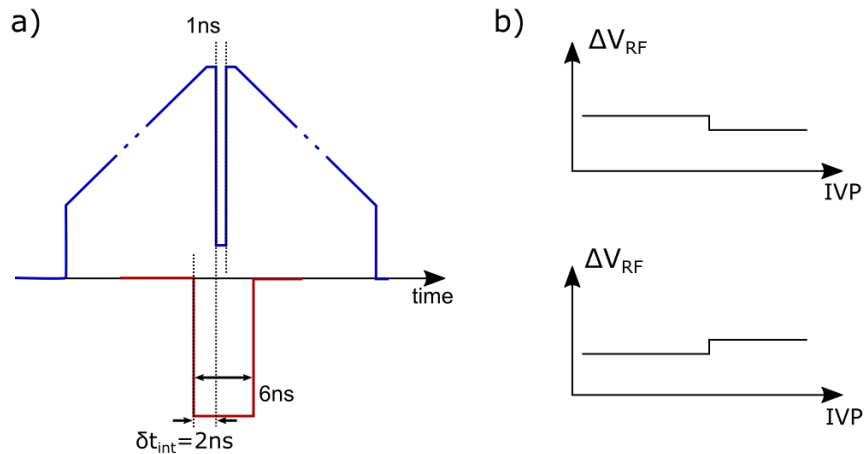


**Figure 4.17** – *a)* Sketch of the experimental sequence with the procedure of the coherent exchange oscillations of the qubit detector in blue and the IVP applied on the source dot in red. The different duration of the exchange pulse and the IVP one are indicated, as well the intrinsic delay  $\delta t_{int}$  added between them. *b)* Sketch of the expected signal for the detection of a single electron when the IVP amplitude is swept. Above a certain voltage threshold, which depends on the injecting position, the electron can be emitted. Being an increase of the edge channels electron density, it is measured as a negative step of the voltage amplitude  $\Delta V_{RF}$  of the spin triplet RF-QPC signal. This step should have an amplitude of  $\delta V_{RF}$ . *c)* Same as *b)*, except that here it corresponds to the detection of a hole, so a decrease of the electron density observed with such positive step. This signal should be observed 6 ns after the electron one, this time corresponds to the width of the IVP.

the ohmic contact, so directly to the ECs and measured by recording the current flowing into them. In our experiment the situation is different since the short pulse is not directly applied to the ECs but to a RF gate capacitively coupled to them. The effect of the IVP is similar to a short modification of the ECs path, which could result in the following ECs electron density variations. In between the two fronts of the IVP, the situation is at an equilibrium and no change are expected. However, for the two fronts, this pulse could induce two opposite electron density variations detectable with the qubit detector. The first front of negative amplitude leads to an excess of charge to evacuate. The magnetic field being set such that the bulk is insulating (cf. first chapter section 1.7), this increase of electron density is carried by the ECs until being absorbed by the next ohmic contact. Similarly, the second front being of opposite sign, positive amplitude, it is a propagating decrease of electron density which could be induced. These changes of electron density are what we call EMP in the following.

If these EMP are excited, since they are a collective excitation of several electrons, they should be measured more easily by the qubit detector in comparison to the single travelling charge. In addition, they should be detected for the same injection pulse delay than the single emitted electron (or hole) since they are excited/emitted at the same time. Concerning the signal variations, the first EMP corresponds to an increase of ECs electron density, so a negative peak of  $\Delta V_{RF}$ , the opposite for the other EMP with a positive peak. Finally, these EMP being excited by the IVP, these peak amplitudes are expected to increase linearly with the IVP one.

The other large signal which could be detected is the capacitive coupling between the detection and

the IVP. If this coupling exists, a step of  $\Delta V_{RF}$  with a width similar to the IVP one, 6 ns, is expected with an amplitude depending on the strength of this coupling.

#### 4.6.2 First detection : mapping of the injection pulse delay

As mentioned, before implementing the single electron detection, the delay between the IVP and the exchange pulse has to be adjusted precisely. To perform this adjustment, a first measurement consisting in the mapping of the full injection pulse delay window is implemented as a function of the full IVP amplitude. The aim is to eventually excite and detect EMP with the qubit detector or probe the effect of a direct capacitive coupling between it and the IVP. If at least one of these signals is recorded, since their amplitude is expected to be large, they could be used to determine the optimal injection pulse delay for the single electron detection, so set this delay between injection and detection pulses.

A two dimensions experiment is implemented with the IVP amplitude swept in its full range 0 to  $-32$  mV, and the same with the stepping of the injection pulse delay from  $-5$  to  $5$  ns. During the implementation of this experiment,  $\Delta V_{RF}$  should be constant, except if EMP and/or capacitive coupling are detected.

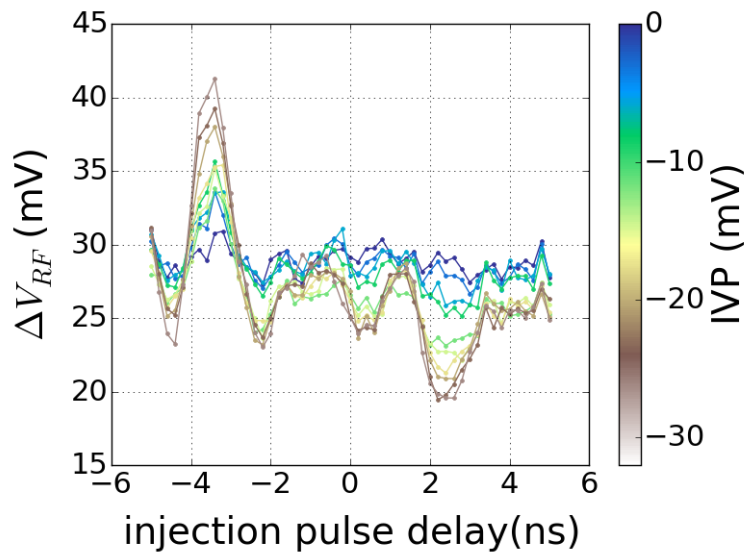


**Figure 4.18** – The voltage amplitude  $\Delta V_{RF}$  of the spin triplet RF-QPC signal is shown as a function of the injection pulse delay and the IVP amplitude. The injection pulse delay is stepped between  $-5$  ns and  $5$  ns and the IVP amplitude stepped from 0, the blue trace, to  $-32$  mV in brown. The different signals variations are discussed in the main text.

The results of its implementation are presented in Fig. 4.18 with the injection pulse delay as horizontal axis and the IVP amplitude is plotted with a colour gradient. In this figure, two main peaks of  $\Delta V_{RF}$  can be seen for injection pulse delays of approximately  $2.5$  ns and  $-3.5$  ns, such as secondary peaks at different values. Despite these peaks, there is no clear indication of step of signal having a 6 ns width, meaning that there is probably no capacitive coupling between the IVP and the qubit detector.

The two main peaks presents the characteristics expected for the detection of EMP excited by the fronts of the IVP. Indeed, they are localised only 500 ps after the expected value for the synchronisation between the two fronts of the IVP and the exchange pulse explained in the previous section. This hypothesis is supported by the amplitude of these two peaks which are of opposite sign. A negative amplitude for the first front of the IVP, here at an injection pulse delay of 2.5 ns, as expected for an increase of ECs electron density. A positive one for the second front of the IVP, at  $-3.5$  ns, corresponding to a decrease of electron density. In addition, these two peaks have the same amplitude of approximately 12 mV from 0 to  $-32$  mV for the positive one and 10 mV for the negative one. The difference between the two can simply be a decrease of the qubit detector charge sensitivity. Finally, these peaks have a temporal size of the order of 1 ns, which corresponds to the AWG rising time, so the IVP one.

A word on the presence of the secondary peaks of signal, around the positive main one for instance where they have an opposite amplitude, or for an injection pulse delay of 1 ns. These peaks are unexpected and their behaviour being similar to the main ones, they are probably EMP too but the origin of their excitation is unknown.

In conclusion, this experiment indicate the detection of EMP, so the detection of a travelling excitation in the ECs. Different verifications can be implemented to study them more precisely and validate this conclusion. The intrinsic delay  $\delta t_{int}$ , sketched in Fig. 4.17, can be changed, a better resolution in IVP amplitude can be used to verify the linear increase of the EMP peaks amplitude with the IVP one. Finally, by reversing the magnetic field the travelling nature of the detected excitation can be demonstrated.

### 4.6.3 Delay dependence

The first verification concern the change of the intrinsic delay  $\delta t_{int}$  to validate the displacement of the detected EMP peaks with it, so the relation between them and the IVP. For this measurement only one EMP peak is considered, the positive one, to increase the injection pulse delay resolution and reduce the measuring time so limit the drift of the qubit detector charge sensitivity.

This experiment was performed with a qubit detector less optimised than the one used in the previous measurement, with a smaller charge sensitivity. The DC filters were not added yet and an intermediate 1 ns step in the exchange pulse was added aiming to reduce the AWG rising time. The delay  $\delta t_{int}$  is stepped between  $-1$  and  $-3$  ns, the injection pulse delay is swept from  $-5$  to  $-1$  ns and the IVP amplitude is set to  $-28$  mV. According to the previous experiment where  $\delta t_{int} = -2$  ns, the positive peak was measured at an injection pulse delay of  $-3.5$  ns. Then, here it should move from  $-4.5$  ns to  $-2.5$  ns. The resulting traces are shown in Fig. 4.19, where for clarity an offset has been added to the traces of  $\delta t_{int} = -1, -2$  ns.

The expected displacement of the peak is observed with the stepping of 1 ns from a trace to the other. The peak amplitude are reduced compare to the previous experiment because of the smaller qubit detector charge sensitivity but it remains constant all over the experiment to  $\sim 4$  mV. The traces being measured independently, the variations of EMP peak amplitude between them can be explained by a difference of

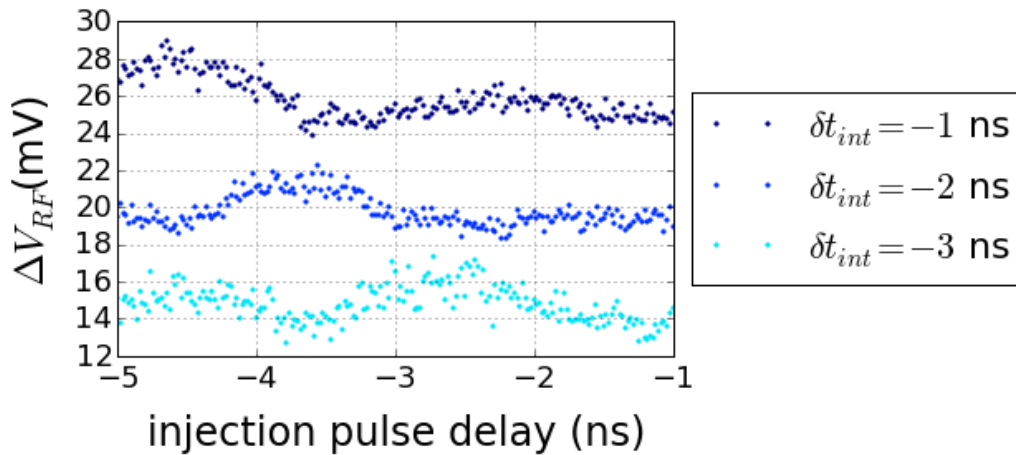


**Figure 4.19** – Voltage amplitude  $\Delta V_{RF}$  of the spin triplet RF-QPC signal as a function of the injection pulse delay for various intrinsic delay  $\delta t_{int}$ . The colour code of  $\Delta V_{RF}$  is indicated in the legend. For this experiment the IVP amplitude was set to  $-28$  mV. The different traces are separated by an offset of 12 and 4 mV added to the data of  $\delta t_{int} = -1, -2$  ns. The measurements were performed one after the other with a qubit detector less optimised than previously, without DC filter and with an intermediate 1 ns pulse in the exchange pulse of the coherent exchange oscillation aiming to reduce the effect of the rising time of the AWG.

qubit detector charge sensitivity. The same secondary peaks observed in the previous experiment are also visible around the main one, with the amplitude which is also approximately two times smaller than the main one. Thus, these secondary peaks are not an artefact of the previous measurement and are really related to the IVP.

#### 4.6.4 Amplitude dependence

In the full mapping of the injection pulse delay, Fig. 4.18, the linear rising of the EMP peaks was not obvious with the noise fluctuations. This expected linear evolution can be verified by increasing the IVP amplitude resolution and separating the measure of each peak to avoid the drift of the qubit detector sensitivity. Here also the qubit detector was not fully optimised at that time. The intrinsic delay is set to  $\delta t_{int} = -2$  ns and the IVP voltage amplitude swept from 0 to  $-32$  mV. The injection pulse delay is stepped in a time windows centred around the positive and negative EMP peaks. The experimental data for the positive and negative peak are presented in the figure 4.20.

To suppress the slow drift of the sample, since the injection pulse delay is stepped, the trace for the IVP amplitude of 0 V is equivalent to the reference signal and has been removed to the other ones, the resulting signal is labelled  $\Delta$ . The linear evolution of the EMP peak amplitude can be noticed in Fig. 4.20 showing the absolute value of the EMP peaks as a function of the IVP one. Here again, a difference of amplitude can be noticed between the two EMP peaks. The positive one, Fig. 4.20a, can be up to  $\sim 6$  mV while the negative one increases to  $\sim 3$  mV maximum, Fig. 4.20b. To explain this difference

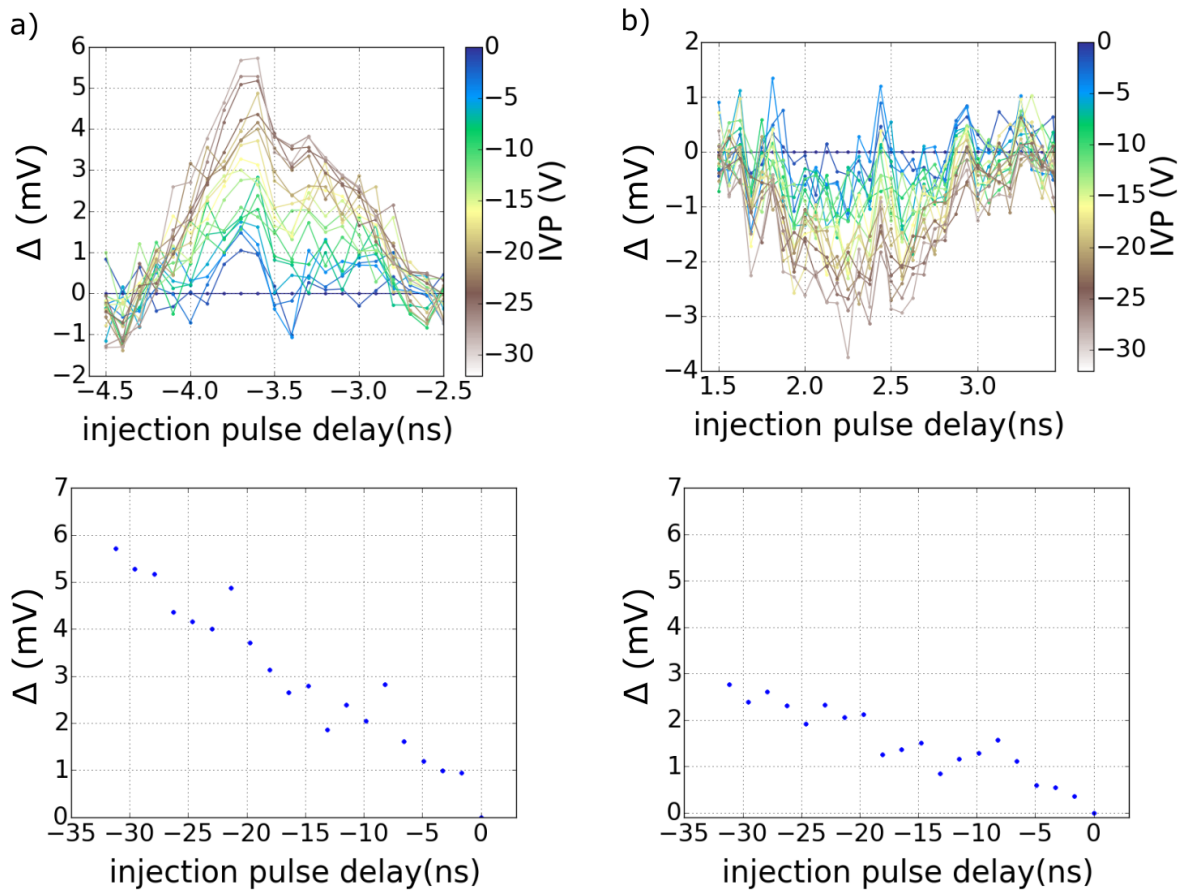


**Figure 4.20** – *a)* Evolution of  $\Delta$  as a function of the injection pulse delay and the IVP amplitude.  $\Delta$  is the signal  $\Delta V_{RF}$  to which has been subtracted the reference signal, i.e. trace measured without IVP. The IVP amplitude is swept in its full range from 0 in blue to  $-32$  mV in brown. The injection pulse delay is varied in the range corresponding to the positive EMP peak of Fig. 4.18. For this measurement, DC filters were not used yet explaining the smaller amplitude of the peak. Bottom, the expected linear increase of  $\Delta$  with the IVP amplitude is verified with the values extracted at an injection pulse delay of  $-3.6$  ns and for one trace over two. *b)* Similar analysis for the negative peak of  $\Delta V_{RF}$  in Fig. 4.18. The absolute value of  $\Delta$  extracted for an injection pulse delay of  $2.2$  ns is plotted as a function of the IVP amplitude. The same linear evolution is observed, with the smaller amplitude in comparison to a) explained by a difference of qubit detector sensitivity.

of amplitude, the drift of the qubit detector charge sensitivity between the two experiments is the most probable explanation rather than an intrinsic difference between the two EMP. The abrupt signal variation in Fig. 4.20b at  $2.5$  ns argue for this explanation of instability of the qubit detector tuning.

In conclusion, despite this amplitude difference these measurements permit to verify the expected linear increase of the EMP peaks amplitude with the IVP one.

To validate the detection of EMP, a last verification is implemented consisting in verifying the travelling nature of the detected signal.

### 4.6.5 Magnetic field dependence

To highlight this propagating nature of the detected excitation, the magnetic field setting the propagation direction of the ECs can be simply reversed. If EMP are really emitted and detected, by reversing the magnetic field orientation, no signal variations are expected. Indeed, the EMP would be emitted too but travelling in the other direction and therefore on the lower path, see sketch of Fig. 4.6. This path comporting an ohmic contact in between the source dot and the qubit detector, the EMP would be absorbed before reaching the qubit detector. Hence, by performing the same experiment than shown in Fig. 4.18 with the same fully optimised qubit detector, instead of measuring peaks of  $\Delta V_{RF}$  with an amplitude  $\sim 10$  mV, only the noise fluctuations should be observed. A potential step of signal associated to the capacitive coupling is still possible since it does not depend on the magnetic field orientation and could have been masked in the previous measurements.

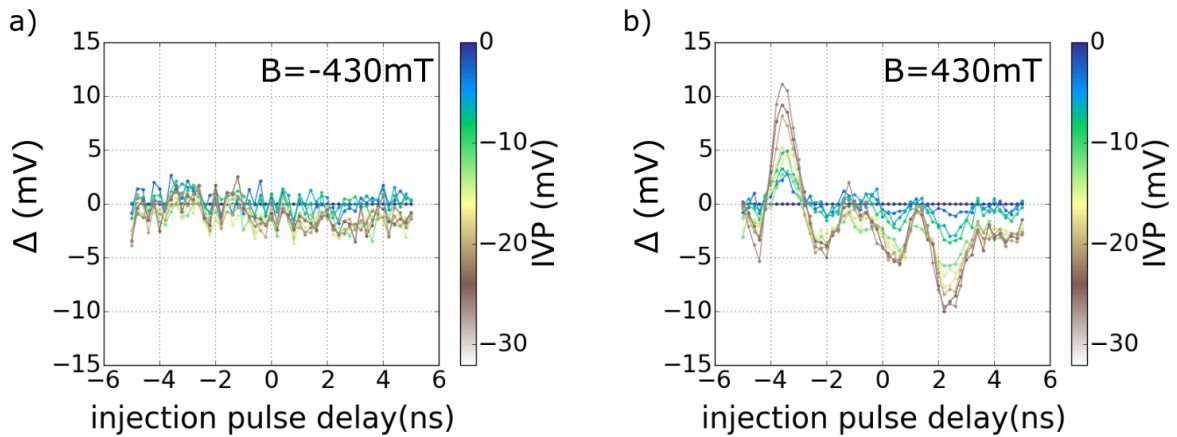


**Figure 4.21** – *a)* Signal  $\Delta$  as a function of the injection pulse delay and the IVP amplitude.  $\Delta$  is the voltage amplitude  $\Delta V_{RF}$  of the spin triplet RF-QPC signal from which the reference signal measured without IVP has been subtracted. The IVP is represented in colour scale with the colour evolving from blue to brown when the IVP amplitude is increasing in its full range. This measurement has been performed with a magnetic field set to  $-430$  mT. The absence of step in the signal indicates the absence of direct capacitive coupling between the IVP and the qubit detector. The absence of peak in comparison to the same experiment performed with the opposite magnetic field presented as the *b)* figure emphasize the detection of EMP. *b)* Same experiment than *a)* but with  $B = 430$  mT. These data are the same than the one presented in the Fig. 4.18 except that here the reference signal has been removed.

After verification of the qubit detector tuning for  $B = -430$  mT, the same experiment than before is implemented, so  $\delta t_{int} = -2$  ns, the injection pulse delay is stepped in the range  $\pm 5$  ns with the IVP amplitude swept between 0 and  $-32$  mV.

The figure 4.21 presents the result of this experiment with for comparison the one measured with  $B = 430$  mT of Fig. 4.18. For clarity the base line measured for an IVP amplitude of 0 mV has been removed for the two measurements, as before the resulting signal is labelled  $\Delta$ . The difference between these two experiments, two magnetic field orientations, is clearly visible with  $\Delta$  constant for the full injec-

tion pulse delay range with this reversed magnetic field. The travelling nature of the detected excitation is therefore demonstrated so the hypothesis of EMP detection is validated.

In addition, in Fig. 4.21a there is not step of signal from  $-3.5$  to  $2.5$  ns, emphasizing the absence or unobservable direct capacitive coupling with the IVP.

The detection of EMP being confirmed, it proves the ability of the qubit detector to detect in-flight a few electron wavepacket travelling at the Fermi velocity.

From the EMP peak amplitude an evaluation of the number of travelling electrons forming the EMP is possible. This estimation is rather rough since it depends highly of the qubit detector charge sensitivity during the experiment, which, as mentioned many times was drifting, nevertheless, it gives an order of magnitude. With the optimised qubit detector and the measurement presented in Fig. 4.18, the maximum number of detected electrons forming the EMP is about  $35 - 40$  with the step signal  $\delta V_{\text{RF}} = 300 \mu\text{V}$  and the EMP peak of  $10 - 12$  mV. The minimum number of detected electron can also be estimated from the noise amplitude of these traces. It is about  $1$  mV, so to be distinguished from it, the EMP were composed by at least 4 electrons according to our calibration. Once again these estimations give only an order of magnitude, but it seems that the qubit detector detects down to a few travelling electrons.

From these successive measurements, the detection of travelling EMP excited by the IVP is demonstrated, now they can be used to adjust the injection pulse delay for the implementation of the single charge detection. There is two possibilities to select this delay, either trying the detection of the injected electron, or the hole following it, corresponding to setting the delay on the negative or positive EMP peak. The two possibilities being similar for the qubit detector, except the sign of the step signal, we choose the positive peak and an injection pulse delay of  $-3.5$  ns corresponding to the detection of a travelling hole.

#### 4.6.6 EMP effect on coherent exchange oscillations in amplitude

So far, the working position was set according to the calibration implemented with the DC bias applied to the ECs. Now that a travelling signal induced by the IVP can be detected, this optimal working position for the  $3\pi/2$  spin rotation position can be verified. This verification is implemented by performing coherent exchange oscillations in amplitude while stepping the IVP amplitude to excite the EMP.

The injection pulse delay is set to  $-3.5$  ns, the IVP amplitude stepped from  $0$  to  $-32$  mV. For this delay, the detection is focussed on the positive EMP peaks where the IVP induces a decrease of the electron density. Hence, while increasing the IVP amplitude a drift of the oscillations toward larger detuning is expected.

This expectation is verified experimentally as shown in Fig. 4.22a with the linear shift highlighted with the black dashed line. The signal variation labelled  $\Delta$  induced by the EMP is extracted by subtracting the reference signal measured without IVP to the other traces. This variation is plotted as Fig. 4.22b with the colour scale indicating positive or negative shift of  $\Delta V_{\text{RF}}$ . The conclusion are the same than for the DC bias experiment, the signal variation is largest for the  $3\pi/2$  spin rotation position, followed by the

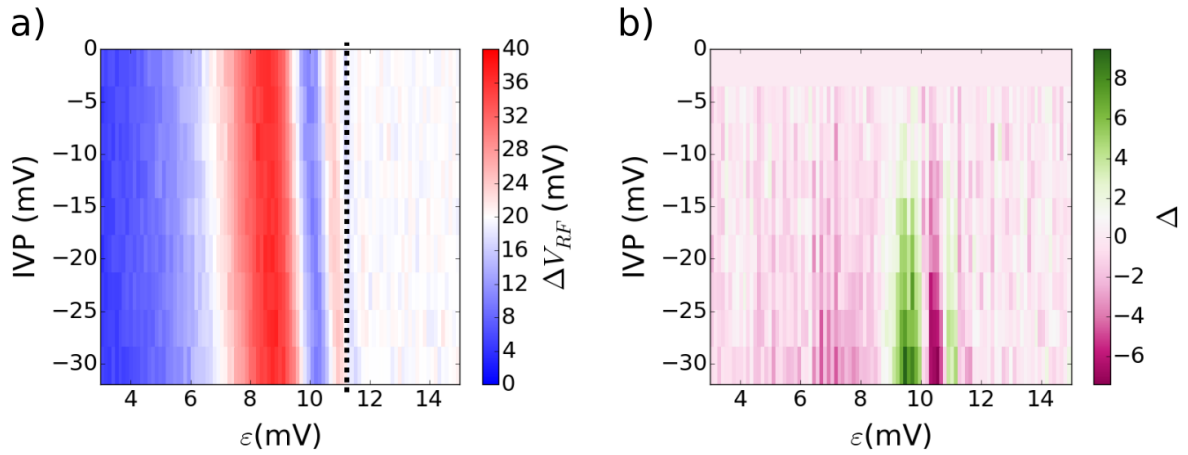


**Figure 4.22** – **a)** The voltage amplitude  $\Delta V_{RF}$  of the spin triplet RF-QPC signal is plotted in colour scale as a function of the detuning value of the oscillating position  $\epsilon$  along the  $x$  axis and the IVP amplitude along the  $y$  axis. The amplitude of  $\Delta V_{RF}$  is increasing with the colour evolving from blue to red. The black dashed line is a guide for the eyes, highlighting the linear phase shift of the oscillations due to the interaction with the EMP. **b)** Signal variation  $\Delta$  induced by the EMP obtained by subtracting to each traces of **a)** the one measured without IVP. Its colour scale goes from negative variation in purple to positive one in green. The largest variation, so the most sensitive position of the qubit detector is obtained for  $\epsilon \approx 9.5$  mV corresponding to the  $3\pi/2$  spin rotation position.

$5\pi/2$  one.

Thanks to this measurement the working position is confirmed at this  $3\pi/2$  rotation point, and now the final experiment is implemented.

## 4.7 Single travelling charge detection

The experimental procedure for the single charge detection is now ready, and the different approaches employed to perform it are described in the current section. Indeed, we are now looking for a small signal variation with an amplitude  $\delta V_{RF} = 300 \mu\text{V}$ , the large signal variation due to the EMP and our experimental constraints will have to be taken into account to facilitate its detection.

### 4.7.1 Fixed injecting position

In a first attempt, the same procedure than for the study of the EMP has been implemented. The injection position is set to the point A of Fig. 4.16, the full IVP amplitude is swept and the injection pulse delay is stepped between  $-4$  ns and  $-3.5$  ns.

With such experimental sequence, two signal variations are expected. First, a linear increase of  $\Delta V_{RF}$  with the IVP amplitude due to the detection of the EMP. Second, a positive step of signal with an amplitude  $\delta V_{RF}$ . This step, due to the travelling hole, should be visible once the IVP amplitude is large enough to induce the electron emission from the source dot towards the ECs. According to the calibration presented

in section 4.5.2, for this injecting position this emission is expected to be for an IVP amplitude of at least  $\sim 10$  mV.

This procedure of sweeping the IVP amplitude being performed for different injection pulse delays, this step should be observed for each of them. Indeed, stepping this delay only changes the qubit detector sensitivity to the travelling charges. As a consequence, if a step signal is measured for the same IVP amplitude and for each injection pulse delay, it is highly improbable to be an artefact of the experiment and therefore it corresponds to the researched travelling charge.

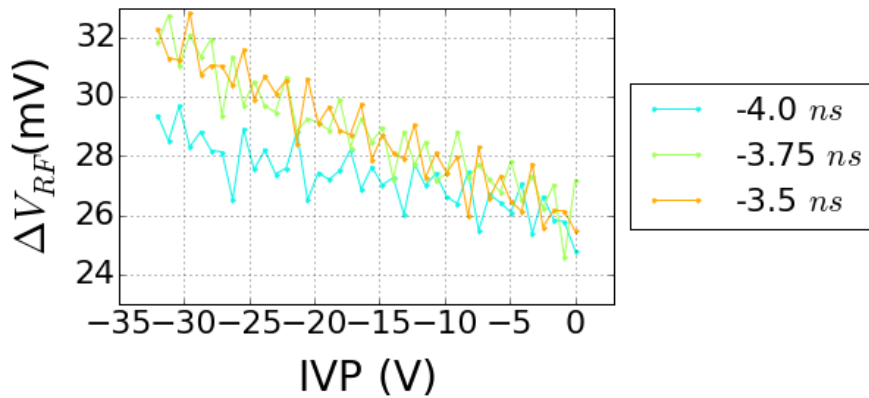


**Figure 4.23** – Evolution of the voltage amplitude  $\Delta V_{RF}$  of the spin triplet RF-QPC signal as a function of the IVP amplitude and for various values of injection pulse delay. The colour code of the  $\Delta V_{RF}$  traces are indicated in the legend. While sweeping the IVP amplitude,  $\Delta V_{RF}$  is increasing because of the EMP signal. The different slopes are due to the varying sensitivity of the qubit detector to the travelling EMP with the injection pulse delay. The noise fluctuations of this experiment are too large to be able to detect the step signal expected for an IVP amplitude about 10 mV and visible for each value of the injection pulse delay.

The result of this experiment are presented in Fig. 4.23 with different comments to be made about it. The first one is the absence of positive step for the different injection pulse delay, the noise amplitude being much larger than  $\delta V_{RF}$  it prevents its observation. This noise being a secondary mode of the 50 Hz most likely coming from the amplification chain, it cannot be further averaged. The second comment concerns the two sets of slope of the traces. Two of them having the same one measured with an injection pulse delay set to  $-3.5$  ns and  $-3.75$  ns. The third trace measured at  $-4$  ns has a smaller slope in comparison to the two other traces. This difference is simply due to the position on the EMP peak, the optimisation of the travelling charge detection by the qubit detector. Two traces being measured for an injection pulse delay corresponding to a maximum of the EMP peak, while the other one to its flank (cf. Fig. 4.18).

This experiment indicates mainly that this experimental procedure is not adapted for the single charge detection. The noise fluctuations with a larger amplitude than  $\delta V_{RF}$  plus the slope of  $\Delta V_{RF}$  prevent the observation of the travelling charge. To avoid these two limitations, slope and noise, another approach has been developed.

### 4.7.2 Sweeping of the injecting position using single shot spin readout acquisition mode

We can remind that in the charge emission, DC and RF voltages are involved. The DC ones are used to define the injection position while the RF voltage pulse is used to induce the charge emission. Since this IVP excite EMP in the same time which are at the origin of the slope of  $\Delta V_{\text{RF}}$  in the previous traces, instead of sweeping its amplitude, it is the injecting position which can be swept for a constant IVP amplitude. Using this procedure, this slope should be avoided and the same step signal is expected starting from a specific DC gate voltage. This measurement can be performed for different IVP amplitude to verify if an eventual step signal does not correspond to an artefact. In that case, the step should be observable for each IVP amplitude but for different DC gate voltage as sketched in Fig. 4.24.

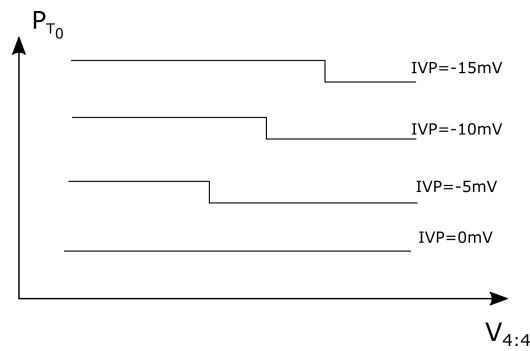


**Figure 4.24** – Sketch of the evolution of the triplet probability  $P_{T_0}$  when stepping the DC gate voltage  $V_{4:4}$  for different IVP amplitudes. The increase of the signal from an IVP amplitude to the other is due to the EMP peak. The step signal is associated to the detection of a single travelling hole. As shown in Fig. 4.16 the resulting DC gate voltage shift  $\delta V$  induced by the IVP is increasing with its amplitude, explaining the displacement of this step signal toward less negative DC gate voltage when increasing the IVP amplitude. There is no expected signal variation when crossing the charge degeneracy lines. The probability to emit an electron for each implementation of the experiment in a time window equivalent to our qubit detector exposure time of 200 ps is negligible.

In addition to this change of experimental procedure, to avoid the noise observed in the previous experiment, the single shot spin readout acquisition mode can be used. Indeed, the advantage of this technique is its insensitivity to the  $V_{\text{RF}}$  fluctuations since it relies on the detection of a step of it, as described in the second chapter section 2.5.

Consequently, before implementing this experiment, the calibration of the step signal  $\delta P_{T_0}$ , equivalent to  $\delta V_{\text{RF}}$  but for this single shot acquisition mode, should be performed. Estimation which is nevertheless faster to do since only the trace of a coherent exchange oscillation in amplitude is required, the gate like effect  $\delta \varepsilon$  being independent to the signal acquisition mode.

This analysis is presented in Fig. 4.25 where the estimated step signal is  $\delta P_{T_0} \approx 0.15\%$  with  $\delta \varepsilon = -6 \mu\text{V}$ , obtained here again for the  $3\pi/2$  spin rotation position.

One can notice the increase of spin visibility in comparison to the previous chapter, here it is about  $\sim 30\%$  while it was  $\sim 15\%$  in Fig. 3.12 of third chapter. This improvement is also observed for the signal averaging mode of detection as discussed at the beginning of this chapter section 4.2.1, associated

here to a better tuning of the single shot spin readout procedure (optimised threshold, cf. second chapter section 2.5). However, this fidelity remains much smaller than for the other acquisition mode ( $\sim 95\%$ ) explaining the lower quality of this trace.

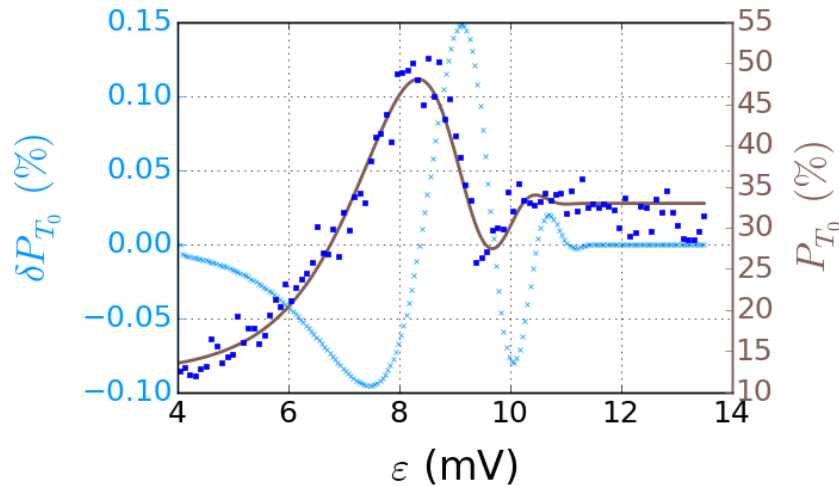


**Figure 4.25** – The triplet probability  $P_{T_0}$  and the step signal  $\delta P_{T_0}$  are plotted as a function of the detuning  $\varepsilon$ . The left axis is related to  $\delta P_{T_0}$  represented with light blue crosses. The right axis refers to the triplet probability  $P_{T_0}$ , with the blue dots being the raw data points extracted by single shot spin readout and the brown line is the result of the fit. The maximum step signal of  $\delta P_{T_0} \approx 0.15\%$  is calculated using a single electron gate like effect  $\delta\varepsilon = -6\ \mu\text{V}$ , cf. subsection 4.3.3.

Finally, the single electron detection experiment is implemented with this new detection procedure where the gate voltage  $V_{4:4}$  is swept about charge degeneracy lines, from  $-0.87\ \text{V}$  to  $-0.77\ \text{V}$  in Fig. 4.27a, with the IVP amplitude stepped from 0 to  $-15.5\ \text{mV}$ . The gate voltage  $V_{4:3}$  is still set to  $-0.65\ \text{V}$  and the injection pulse delay to  $-3.5\ \text{ns}$ . By implementing this experiment, in case of single hole detection a positive step of the triplet probability with an amplitude  $\delta P_{T_0}$  is expected with the similar evolution to the one sketched in Fig. 4.24. When crossing charge degeneracy lines there is no signal variation which are expected, the probability to emit an electron or hole during the detector exposure time of  $200\ \text{ps}$  for each experiment is negligible. Typical results of such experiment are presented in Fig. 4.26.

The first remark about this experiment is the absence of the step signal indicating the single hole detection, the noise amplitude preventing here again its observation. This noise could be reduced by increasing the level of averaging, however, as explained in the chapter 2 section 2.3.2, the measuring time with this acquisition mode is intrinsically longer than the other one. Then, considering also the sample instability and the implementation of the same experiment with a larger averaging level is not a suitable solution. Nevertheless, regarding the absence of slope of the triplet probability, it indicates that this detection procedure seems advantageous for the single charge detection. Notice that the steps of  $P_{T_0}$  from a trace to the other, are due to the EMP signal which is increasing with the IVP amplitude.

This experiment indicates that this procedure is suitable for the single charge detection but to avoid the

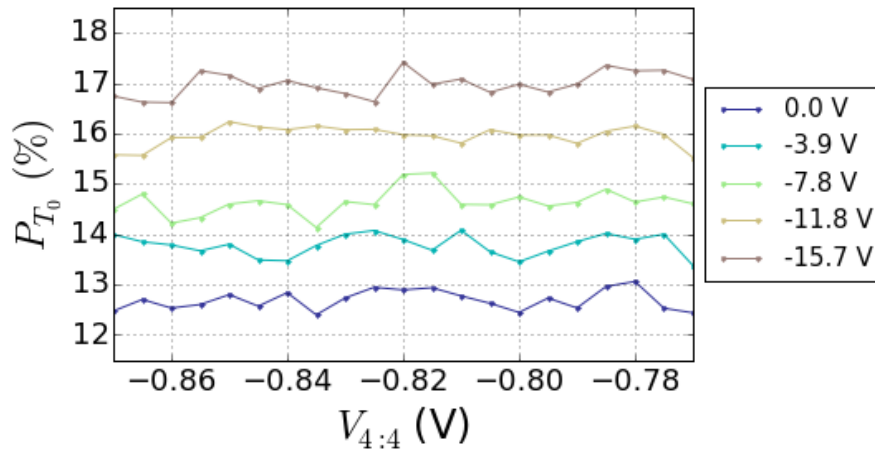


**Figure 4.26** – The triplet probability  $P_{T_0}$  extracted by single shot spin readout is shown as a function of the DC gate voltage  $V_{4:4}$ . From dark blue to brown the IVP amplitude is increasing with its values indicated in the legend. The absence of positive step of signal moving with the IVP as expected and sketch in Fig. 4.24 indicates that the single travelling hole is not detected. The step of triplet probability from a trace to the other is due to the EMP detection, the EMP signal increases with the IVP amplitude as discussed in the previous experiments.

drift of the qubit detector charge sensitivity and fasten the signal averaging it is preferential to implement it with the signal averaging acquisition mode.

### 4.7.3 Sweeping of the injecting position using signal averaging acquisition mode

The same procedure is therefore followed with a reduction of the IVP amplitude resolution to avoid the noise observed in Fig. 4.23. Then, the IVP is stepped between 0 and  $-8$  mV and  $V_{4:4}$  is swept about a charge degeneracy line in the range shown in the Fig. 4.27. Actually, while stepping the DC gate voltage in this range, two of these lines are crossed, for approximately  $V_{4:4} = -0.78$  V and  $V_{4:4} = -0.84$  V. Regarding the expected signal, it should be equivalent to the one sketched in Fig. 4.24. In addition, since this sequence is designed to study the electron emission when crossing the second charge degeneracy line with the IVP, the one of  $V_{4:4} = -0.84$  V, and considering the IVP efficiency (cf. Fig. 4.16), the step signal associated to the detection of the single travelling charge is expected for  $V_{4:4} = -0.83$  V for the first non zero IVP amplitude, and shifted by approximately  $+0.01$  V for each IVP value. Here also there is no signal variation expected when crossing the charge degeneracy lines. The results of this experiment are presented in Fig. 4.27.

The first observation is the absence of the step signal moving with the IVP amplitude, which indicates one more time that the single charge detection is failed, even if here the noise amplitude is low enough to permit its observation. This non detection is discussed in the following conclusion.

The second remark concern the slow increase of  $\Delta V_{RF}$  while increasing the DC gate voltage. This evolution is associated to a direct capacitive coupling with the gate voltage  $V_{4:4}$ . This slope was not observed

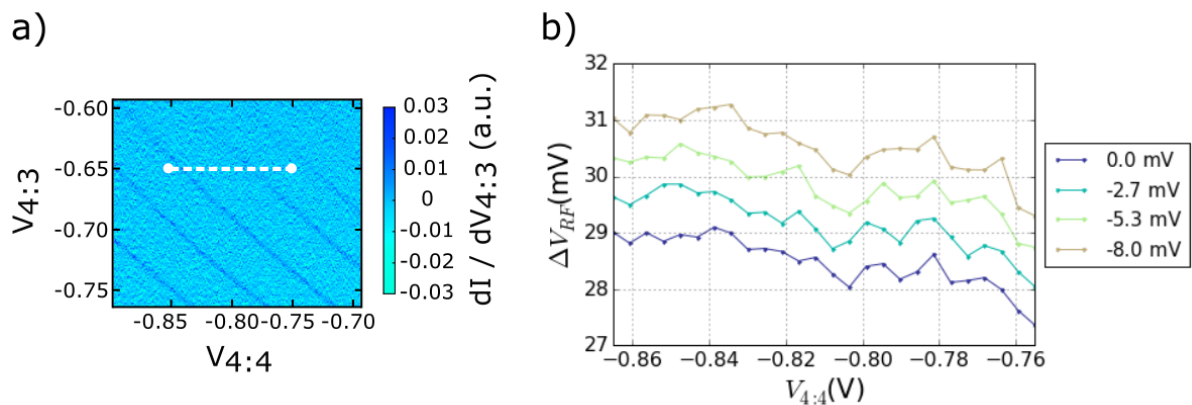


**Figure 4.27** – *a)* The derivative of the QPC current with respect to the swept gate voltage  $V_{4:3}$ , for a stepped  $V_{4:4}$  voltage is shown. In this stability diagram of the source dot, the range over which the DC gate voltage  $V_{4:4}$  is swept during the single travelling hole detection experiment described in the main text is represented with the white dashed line. *b)* The voltage amplitude  $\Delta V_{RF}$  of the spin triplet RF-QPC signal is plotted for various DC gate voltage  $V_{4:4}$ . The IVP amplitude is increasing from dark blue to brown. In this experiment the injection pulse delay is set to  $-3.5$  ns with the IVP amplitude stepped in the range  $[0 : -8]$  mV.  $\Delta V_{RF}$  is increasing with the IVP amplitude because of the EMP detection. The general increase of  $\Delta V_{RF}$  with  $V_{4:4}$  is explained by a capacitive coupling between the detection and this gate voltage. The kink of signal for  $V_{4:4} \approx -0.8$  V is study more in detail in the following and discussed in the main text. Since it is not related to the IVP amplitude it does not correspond to the research single travelling charge.

in the previous experiment with the single shot acquisition mode because there, the noise amplitude was too large to observe it.

Finally, a kink in the triplet probability can be seen for approximately  $V_{4:4} = -0.8$  V and for each trace at the same DC gate voltage position. These traces can be superposed one of top of the others. It is not the signature of a single travelling charge since the IVP has no influence on it. However, it could be related to the charge degeneracy line located at slightly more negative value than expected, i.e.  $V_{4:4} = -0.78$  V according to the stability diagram of fig. 4.27.

Another measurement has been implemented about this transition with a higher resolution and larger range of IVP amplitude to investigate it more precisely. The experimental data are presented as a 2D colour map in Fig. 4.28, with the same kink observed at the same location and for each IVP amplitude, it is therefore not an experimental artefact. This signal seems to be related to the crossing of the charge degeneracy line when sweeping the gate voltage  $V_{4:4}$ . It is not associated to multiple charge tunneling events which would be manifested by a peak of signal not a step like here. Since it is a step, it tends to indicate a direct capacitive coupling to the charge configuration of the source dot. This feature is for sure not related to the single electron injection but distinguishing between our hypothesis and another explanation is so far not possible to our knowledge.

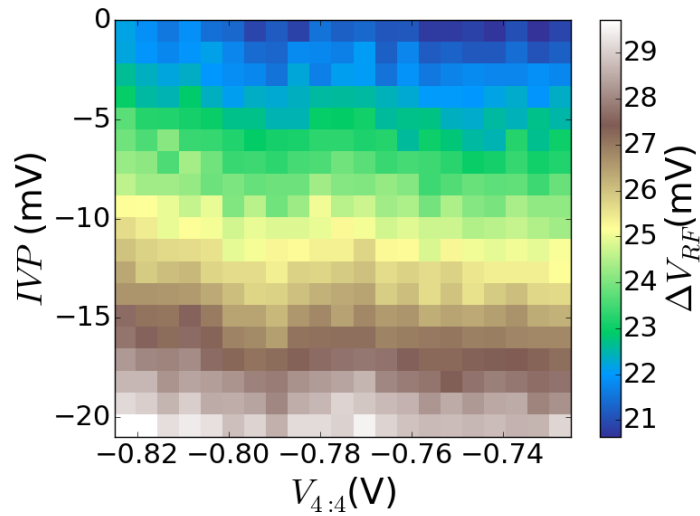


**Figure 4.28** – The voltage amplitude  $\Delta V_{RF}$  of the spin triplet RF-QPC signal is shown as a function of the DC gate voltage  $V_{4:4}$  along the x axis and the IVP amplitude along the y one.  $\Delta V_{RF}$  is plotted in colour scale with in blue(brown) the low(high) intensity. This measurement is similar to one presented in Fig. 4.27 with a higher resolution of gate voltage and IVP amplitude. The same kink of signal is observed for  $V_{4:4} = -0.78$  V and for every IVP amplitude meaning that it is not the single travelling charge, its origin is discussed in the main text.

#### 4.7.4 Conclusion

To conclude on the single electron detection, we could not reach the single charge level with different issues which might explain this fail. The first one being the wrong estimation of the step signal evaluated to be approximately  $300 \mu\text{V}$ . In particular, this estimation depends highly on the exposure time of the qubit detector which is itself an evaluation rather difficult to perform precisely. Thus, this estimation might be overestimated with the real step signal smaller than our calibration, so unobservable with our noise amplitude. Another explanation is the inconstant charge sensitivity of the qubit detector. As it can be seen in Fig. 4.9, these  $\delta V_{RF} = 300 \mu\text{V}$  are only obtained for a reduced range of detuning, smaller than  $1 \text{ mV}$ . In addition, in the section 4.4 has been highlighted the importance of the RF-QPC charge sensitivity. Considering these two elements, and even if we tried to maintain them to their maximum of charge sensitivity all along the measurements, regarding the required high level of accuracy on these tunings and the sample instability, it might not be true experimentally. Then, the averaged step signal over a full experiment might be smaller than the expected one and so smaller than the noise level.

In conclusion on the development of this singlet-triplet spin qubit detector development, the employed one has a charge sensitivity of about  $8 \cdot 10^{-5} \text{ e Hz}^{-1/2}$  for a detection bandwidth from DC to  $1 \text{ THz}$ . This charge sensitivity is too small to reach the single electron level, but a few electron wavepacket forming an EMP could have been detected.



---

## Conclusion & perspectives

---

The goal of my thesis was the development of an ultra-sensitive charge detector for the single shot detection of an electron travelling at the Fermi velocity. Such detector could have a direct application for electron quantum optics experiments using flying electrons. Our strategy was to detect a single travelling electron propagating in the edge channels (ECs) of the quantum Hall effect (QHE) by measuring the induced phase shift of a singlet-triplet spin qubit, referred as to the qubit detector. The single shot detection being only possible if the interaction with the travelling charge induces a complete  $\pi$  phase shift and the spin readout of the qubit detector being performed in a single shot manner. During the development of this ultra-sensitive detector, three major challenges have been encountered.

The first challenge was to maximise the interaction strength between the travelling electron and the qubit detector in its working conditions. To obtain a high capacitive coupling between these two elements, it is necessary to be in a regime of large coupling of the double quantum dot to the ECs, or electron reservoir, plus a small number of ECs. In the presented work, such strong coupling between the qubit detector and the ECs has been reached but its use was limited by a sample charge stability issue. The stronger this coupling is, the more unstable was the sample. To be able to use the qubit detector in its optimal working conditions while implementing multiple detections of the travelling electron, the coupling to the electron reservoir hosting the ECs was limited to the megahertz regime. The number of ECs was limited to ten as the out of plane magnetic field intensity had a negative impact on the charge sensitivity of the employed RF-QPC.

The two remaining challenges were more related to the qubit detector. First, the coherent exchange oscillations performed with the singlet-triplet spin qubit should be perfectly controlled from the spin initialisation to the sub-nanosecond interaction time with the travelling electron.

The last challenge was the single shot readout of the acquired information by the qubit detector during this interaction time. The information being encoded in the qubit detector spin state, this single shot spin readout has to be performed during the spin state lifetime reduced to few tens of microseconds in the operating conditions.

The single shot spin readout development is presented in Chapter 2. It relies on the use of a RF-QPC

---

associated to the Pauli spin blockade based spin to charge conversion. This readout is limited by our rather short spin relaxation time  $T_1 = 30 \mu\text{s}$  and the charge sensitivity of the RF-QPC. The development and optimisation of the readout procedure could allow us to reach a spin readout fidelity of about 50%. The implementation of the coherent exchange oscillations and the study of their sensitivity to the electron density of the ECs have been presented in Chapter 3. A phase shift of these oscillations due to the interaction with an imposed flow of electrons in the ECs has been observed. This flow of electrons was induced by a DC voltage bias applied on the ECs to tune their chemical potential.

The optimisation of the qubit detector for the single travelling charge detection is described in Chapter 4. We first reduced the exposure time to the minimal experimental duration of 1 ns, to match it as much as possible with the interaction time with the travelling charge evaluated of about 1 – 10 ps. Then, by the reduction of the charge noise being the main limit of the qubit detector sensitivity. A calibration of the qubit detector has been implemented using the same imposed flow of electrons by application of a DC bias. This calibration provides the expected signal variation induced by the interaction with a single travelling electron, and indicates the impossibility for us to implement this detection in a single shot manner. Our detector exhibits a charge sensitivity estimated about  $810^{-5} \text{ e Hz}^{-1/2}$  for a detection bandwidth from DC to 1 THz approximately. The sensitivity is almost two orders of magnitude smaller than required for a single shot detection. Finally this qubit detector has been employed to detect in average measurements an edge magneto plasmon composed by less than 5 electrons. However, the single electron level could not be reached in statistical measurement neither, the sensitivity of our qubit detector being too limited.

According to this work, this single charge detection seems nevertheless reachable with the following proposed improvements organised in two groups.

One is the further reduction of the charge noise. Actually, the charge noise is the main source of dephasing of the coherent spin oscillations and so the main limitation to the qubit detector charge sensitivity as discussed in the Chapter 4. A general work on the charge noise reduction by the filtering of the sample connections is the most obvious solution. Improving the matching impedance between the tank circuit of the RF-QPC and the transmission RF line could permit to implement this experiment with a reduced RF carrier power which turned out to be a source of dephasing too.

Increasing the impact of the travelling charge discussed in Chapter 4 is another axis of development. The reduction of the number of ECs is possible by working at larger magnetic field and using polarised metallic gates. These solutions could not be implemented in our experiment, however, with another sample design and without the charge sensitivity reduction of the RF-QPC at large magnetic field, a small reduction of  $\nu$  should permit to reach the single charge detection.

---

---

## Parasitic losses in the tank circuit

---

During the development of the RF-QPC tank circuit, in a first approach a recipe similar to the one of Reilly *et al.* [74] has been followed. In this experiment, the tank circuit is composed by an inductance of 820 nH, the resistance is the QPC and the capacitance corresponds to the parasitic ones labelled  $C_p$ . The same tank circuit has been elaborated and from the resonance frequency  $\left(f = \frac{1}{2\pi\sqrt{LC_p}}\right)$  the parasitic capacitance has been estimated about  $C_p \approx 0.8$  pF. However, with such tank circuit, we could not observe the matching impedance when performing a pinch off measurement. This measurement consists in sweeping the QPC gate voltage to constrain more and more the electron transport, which is therefore equivalent to sweep the QPC resistance. This non-matching impedance means that the optimal transmission of the carrier power to the tank circuit could not be reached in our experimental conditions, i.e. QPC resistance range.

This behaviour has been already observed and study in the following thesis [75], it can be simulated by adding a resistance  $r$  accounting for losses in series with the parasitic capacitance. Then, the relevant circuit is the one presented in Fig. A.1a, with the reflection of this new tank circuit being simulated with the following expressions:

$$Z_L = j\omega L \quad , \quad Z_C = r + \frac{1}{j\omega C_p} \quad (\text{A.1})$$

$Z_L$  is the impedance of the inductance (820 nH) and  $Z_C$  the one of the parasitic capacitance (0.8 pF) in series with a resistance  $r$ . Thus, the resulting impedance of the tank circuit with the resistance  $R$  of the sample is:

$$Z = Z_L + \frac{RZ_C}{R + Z_C} \quad (\text{A.2})$$

and the tank circuit reflection  $\Gamma$  is

$$\Gamma = \frac{Z - Z_0}{Z + Z_0} \quad (\text{A.3})$$

The tank circuit reflection has been calculated as a function of the QPC resistance  $R$  and for different resistances  $r$  presented in Fig. A.1. In this simulation, we can see that the matching resistance observable by the minimum of reflection is drifting toward large QPC resistance, as observed experimentally. To avoid this effect and bring the matching resistance in the accessible range of the QPC, the total capaci-

---

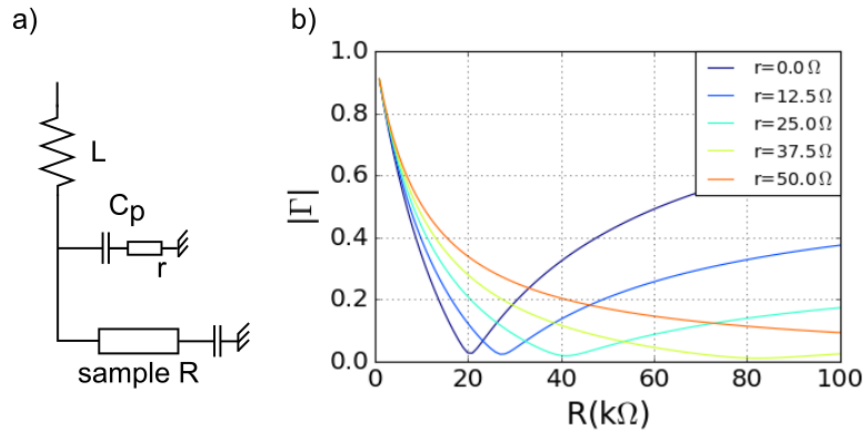


**Figure A.1** – a) Sketch of the tank circuit, where a resistor is added in series with the parasitic capacitor  $C_p$  to simulate the non matching impedance behaviour observed experimentally. b) Reflection  $|\Gamma|$  of the tank circuit as a function of the QPC resistance  $R$  for various resistances  $r$ . The resistance value is increasing from blue to orange. The inflection point corresponding to the minimum of  $|\Gamma|$  is moving toward high values of  $R$  with increasing values of  $r$ .

tance of the tank circuit should be increased as simulated and presented in Fig. A.2b where a resistance  $r = 30\ \Omega$  has been considered. The total capacitance is therefore composed by the parasitic one already presented plus an added one (cf. Fig. A.2a), resulting in  $C_{tot} = C + C_p$ . To solve this issue, we decided to add a capacitor of  $0.2\ \text{pF}$  in order to have the matching resistance between  $50 - 100\ \text{k}\Omega$ , so close to the pinch off value of the QPC.

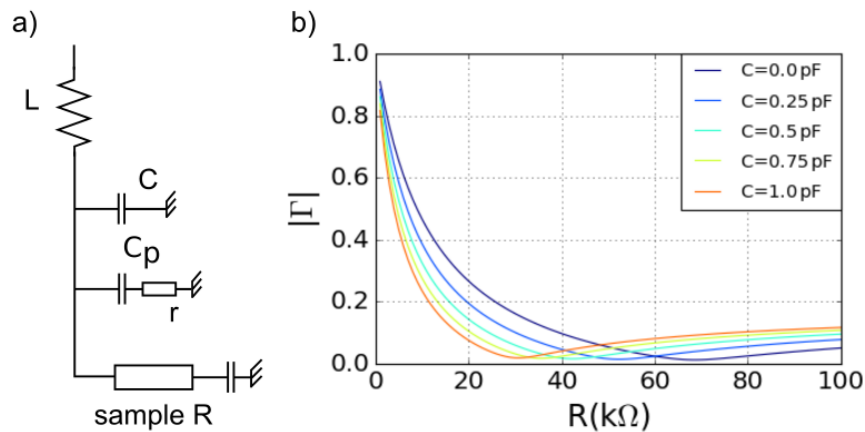


**Figure A.2** – a) Sketch of the tank circuit used in the simulation. An additional capacitor  $C$  is added in parallel to the parasitic one. b) Reflection  $|\Gamma|$  as a function of the QPC resistance  $R$  for various values of added capacitance  $C$ . For this simulation, the resistance  $r$  was set to  $r = 30\ \Omega$ . When  $C$  increases, the matching resistance moves toward smaller resistance values.

---

## Non adiabatic S(2,0)-S(1,1) transfer

---

In Chapter 3, the adiabaticity of the charge transfer from the S(2,0) configuration to S(1,1) realised by a detuning pulse of amplitude  $\varepsilon$  was studied by looking at the degree of  $|S\rangle - |T_0\rangle$  spin mixing. These two notions of spin mixing and adiabaticity are briefly reminded.

In such spin mixing experiment the aim is to bring non-adiabatically the initial singlet S(2,0) spin state into the  $|\uparrow\downarrow\rangle, |\downarrow\uparrow\rangle$  spin basis to induce a precession around the  $|S\rangle, |T_0\rangle$  axis. After an oscillating time of typically  $2T_2^* \sim 20$  ns, an equipartition of the spin singlet  $|S\rangle$  and spin triplet  $|T_0\rangle$  is obtained. This equipartition is obtained if a magnetic field is applied to repel the two other triplets  $|T_{+,-}\rangle$  spin states thanks to the Zeeman energy, and if the detuning pulse is adiabatic through the S(2,0)-S(1,1) anti-crossing. For our purpose, this  $|S\rangle - |T_0\rangle$  spin mixing is employed to verify the adiabaticity of the transfer from S(2,0) to S(1,1) as required for the implementation of the coherent exchange oscillations. This notion of adiabaticity is defined by the Landau-Zener theory, with the non-adiabaticity probability of the pulse being:

$$P_{LZ} = e^{-2\pi\Gamma} \quad , \quad \Gamma = \frac{\theta^2}{\hbar d\varepsilon/dt} \quad (\text{B.1})$$

with  $\hbar$  the Planck constant,  $d\varepsilon/dt$  is the speed in  $\varepsilon$ , and  $t_c$  is the tunnel coupling. Then, the adiabatic transfer from a singlet spin state S(2,0) to S(1,1) depends on the tunnel coupling value.

For a non adiabatic pulse, the  $|S\rangle, |T_0\rangle$  equipartition is also obtained but arises from a different process. A non-adiabatic pulse promotes the initialised S(2,0) spin singlet from ground to excited state in the (1,1) charge configuration. This spin state relaxes by phonon relaxation toward the spin state  $|\uparrow\downarrow\rangle$ . The spin readout of this state using the Pauli spin blockade by projection in the  $|S\rangle, |T_0\rangle$  spin basis provides also an equipartition of the measured spin state.

The distinction between this two regimes is observed for small mixing time. The phonon relaxation being fast, it can be theoretically up to subnanosecond [87], for a non-adiabatic pulse this equipartition is already obtained after few nanoseconds spend in the (1,1) charge configuration. For an adiabatic one, few tens of nanoseconds are necessary.

A mixing trace with an adiabatic pulse is presented in the Chapter 3 section 3.5.2, here we present

---

a non-adiabatic one. For this experiment the magnetic field was set to  $B = 730$  mT, with the following experimental procedure. A spin state is initialised as S(2,0) by waiting in the (2,0) charge configuration, the spin relaxation time was reduced to  $T_1 = 5 \mu\text{s}$  so this initialisation was performed by waiting  $50 \mu\text{s}$  at the measuring/initialising position. A detuning pulse is applied to reach the (1,1) charge configuration for a time  $t$  varying from 1 to 50 ns before implementing the spin readout at the initialisation position thanks to the Pauli spin blockade based spin to charge conversion. This mixing experiment has been implemented for different mixing positions  $\varepsilon$  in the range  $-20$  to  $-13$  mV.

For an adiabatic pulse, this experiment exhibits the same characteristic time  $\tau = T_2^* \sim 10$  ns to reach the spin state equipartition for the different mixing position in the (1,1) charge configuration. For a non-adiabatic pulse, so a tunnel coupling too small for our purpose, in addition to have this time  $\tau$  much shorter (typically few nanoseconds) it depends on the mixing position. Indeed, the energy relaxation of the excited state being a phonon relaxation process, the relaxation time depends on the phonon density which is energy dependent. The energy splitting between the excited S(2,0) and  $|\uparrow\downarrow\rangle$  varies with the detuning. Then the relaxation time, so  $\tau$  depends on the mixing position. This evolution can be observed with the result of such experiment presented in Fig. B.1.

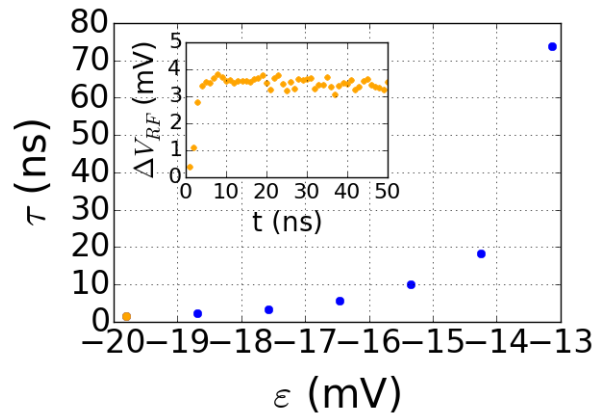


**Figure B.1** – Characteristic time  $\tau$  necessary to reach a singlet triplet equipartition shown as a function of the mixing position  $\varepsilon$ . These values are extracted from the mixing traces as the one shown in the insert using the expression given in the main text. (insert) The evolution of the voltage amplitude  $\Delta V_{RF}$  of the triplet RF-QPC signal is shown as a function of the mixing time  $t$ . This trace has been measured for a detuning  $\varepsilon = -19.8$  mV with  $\tau \approx 1.5$  ns.

A mixing trace, so the  $\Delta V_{RF}$  evolution as a function of the mixing time  $t$  is presented in the insert of Fig. B.1. For this trace, the equipartition was obtained in a characteristic time  $\tau \approx 1.5$  ns, and varying from 1.5 to 73 ns depending on the mixing position  $\varepsilon$ . These values have been obtained using the following expression:

$$\alpha(1 - e^{-\frac{t}{\tau}}) + \beta \quad (\text{B.2})$$

Here, contrary to what is shown in the third chapter section 3.5.2, this expression is an exponential function standing for the relaxation of the spin state while for an adiabatic pulse, the trace is fitted with a

Gaussian function related to the dephasing process of the oscillation of the spin state.

---

---

## Exchange energy evolution with the detuning

---

As explained in Chapter 4, in the implementation of the coherent exchange oscillations in amplitude, the short oscillating time of 1 ns is compensated by a large exchange energy  $J(\varepsilon)$  obtained for large exchange pulse amplitude, positive detuning  $\varepsilon$ . At large positive detuning, when the two electrons are in the same quantum dot, the energy splitting between the singlet  $|S\rangle$  and the triplet  $|T_0\rangle$  is the orbital energy introduced in the first chapter section 1.5. Then, a change in the evolution of this energy splitting  $J(\varepsilon)$  is expected for rather large positive detuning as already observed by [40]. More precisely this change is expected to occur about the anti-crossing between the triplet spin states  $T_0(1,1)$ - $T_0(2,0)$ . According to the measurement performed in the Chapter 3 section 3.3.2, this anti-crossing is localised about  $\varepsilon \simeq 5$  mV, so within the detuning range used for the coherent exchange oscillations in amplitude.

In our experiment this change of regime is not critical, and since it is incomplete, only the non exponential evolution of the exchange energy is of interest, because it implies a modification when fitting the exchange energy. To validate experimentally this change of regime, and verify if it is not simply an error in the detuning estimation performed to compensate the rising time of the AWG, we can benefit from the dephasing of the oscillations.

When the exchange energy  $J(\varepsilon)$  is in its exponential evolution regime, the number of visible oscillations is constant as it can be noticed in the chevron pattern of Chapter 3 Fig. 3.12. This is no longer true for positive detuning when  $J(\varepsilon)$  is not increasing exponentially with  $\varepsilon$ .

To demonstrate this change of regime, coherent exchange oscillations have to be measured for different ranges of detuning, from positive to negative values. To do so, a chevron pattern can be implemented with these coherent exchange oscillations in amplitude, meaning sweeping the detuning while increasing the oscillating time  $t$ . Indeed, by increasing  $t$  the same phase should be accumulated 'earlier', meaning shifting the oscillations toward smallest detuning. The experiment has been implemented for oscillating time stepped in the range 2 ns to 6 ns.

Two experimental traces of such chevron pattern are presented in Fig. C.1 extracted from 2 ns and 6 ns of oscillating time where the change of number of visible oscillations can be noticed. Two oscillations

---

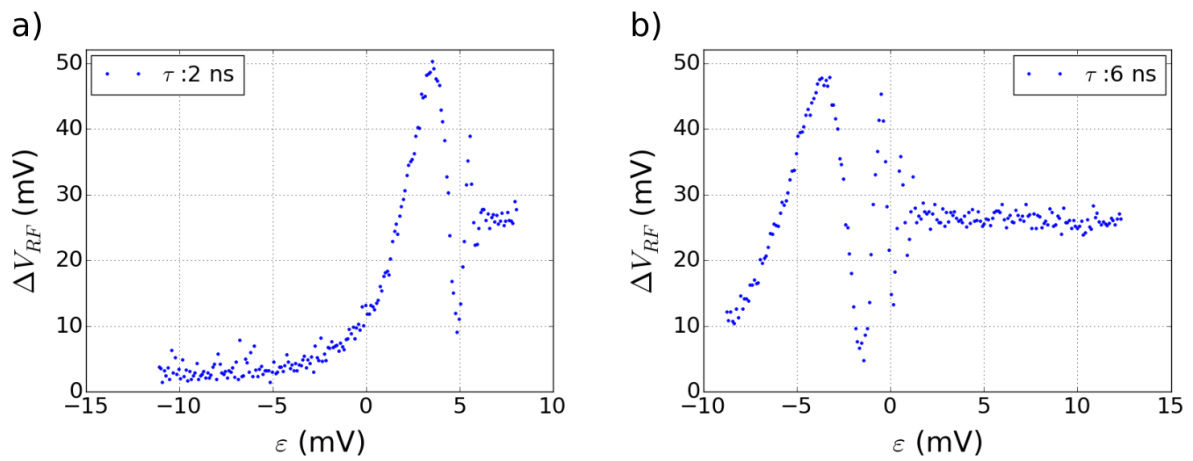


**Figure C.1** – **a)** The voltage amplitude  $\Delta V_{RF}$  of the triplet RF-QPC signal is plotted as a function of the detuning  $\epsilon$ . This coherent exchange oscillations in amplitude trace has been measured for an oscillating time of 2 ns. **b)** Same trace but for an oscillating time of 6 ns.

are visible for the 2 ns trace while four can be observed for the 6 ns one. This measurement confirms therefore the change of regime of the exchange energy.

---

## French summary

---

### Introduction

Alors que cela était illusoire pendant longtemps, le contrôle totale d'une charge élémentaire est aujourd'hui une tâche couramment réalisée amenant au développement d'un nouveau domaine de recherche dédié à l'observation et la compréhension des effets quantiques. En particuliers, il est aujourd'hui possible d'élaborer des échantillons qui une fois refroidi à température cryogénique ont une taille caractéristique inférieur à la longueur de cohérence de l'électron. Les propriétés de phase de l'électron étant préservées sur la longueur de la structure, des expériences d'interférence quantique peuvent être réalisées basées sur la nature ondulatoire de ces particules. Parmi les expériences pionnières de ce nouveau domaine appelé physique mésoscopique, l'observation en 1985 [1] des oscillations de Aharonov-Bohm dans des anneaux d'or est considérée comme un percée majeure.

Au fil du temps, les progrès constant de la science des matériaux, de la qualité de la nanofabrication et de l'électronique de contrôle ont participé au développement rapide de l'optique quantique électronique dont le but est de réaliser des expériences similaires à celles d'optique quantique mais en utilisant des électrons. Il y a un double intérêt à réaliser ces expériences d'optiques quantiques avec des électrons plutôt qu'avec des photons. Le premiers étant le fait que, comme les électrons sont des fermions contrairement aux photons qui sont des bosons, en faisant les mêmes expériences, comme de corrélation, des résultats radicalement différents peuvent être obtenus. L'exemple le plus parlant est l'observation de ce qui est appelé l'anti-bunching des électrons, en comparaison du bunching obtenue avec des photons, déjà démontré expérimentalement [2, 3, 4]. Le second avantage est le fait que, les électrons étant des particules chargées, on peut facilement les contrôler, les manipuler et les faire interagir par le biais de champs électrostatiques. Un tel niveau de contrôle n'existe pas pour les photons.

Pour réaliser de telles expériences, l'hétérostructure semi-conductrice d'aluminum arséniure de gallium/arséniure de gallium (AlGaAs/GaAs) contenant un gaz bidimensionnel d'électron (2DEG) environ 100 ns sous la surface est communément utilisée. Cela s'explique par sa qualité avec une mobilité électronique pouvant atteindre  $35 \times 10^6 \text{ cm}^2/\text{Vs}$  [5]. Par conséquent, les électrons peuvent se propager balistiquement sur plusieurs micro-mètres, donc sans collisions avec des défauts, préservant ainsi leurs propriétés de phase. En utilisant des grilles métalliques polarisées négativement, il est possible de sculpter

---

---

à volonté le 2DEG. En plaçant deux de ces grilles en face à face, on peut contraindre la propagation d'électrons dans le 2DEG, définir une barrière tunnel avec une transparence réglable. Cet outil est communément appelé un point quantique de contact (noté QPC) [6]. Quand la taille de la constriction induite est comparable à la longueur d'onde de Fermi, des plateaux de conductance apparaissent [7, 8]. En réglant la conductance du QPC entre les deux derniers plateaux de conductance on obtient un barrière tunnel avec une transparence de 50%, une lame semi-transparente pour électrons. De la même manière, si deux de ces grilles sont placées en parallèles, le 2DEG peut être redessiné de façon à définir un canal ballistic 1D, formant ainsi un guide d'onde pour électrons. Un tel canal balistique est également obtenue en utilisant les canaux de bords (ECs) de l'effet Hall quantique [9, 10]. Ces outils ont déjà été utilisés pour réaliser l'équivalent électronique de l'expérience d'interférence des deux fentes [11], ou l'interféromètre de Mach-Zehnder [12, 13, 14, 15]. De tels interféromètres sont par ailleurs considérés aujourd'hui comme des candidats pour des applications en information quantique [16, 17, 18] où les états du bit quantique (qubit) correspondent à la présence d'un électron dans chacun des bras de l'interféromètre. Cette approche a d'ailleurs déjà été démontrée expérimentalement avec ce qui est désormais appelé des qubit volants [19]. Les récentes expériences sur l'étude de la cohérence [20, 21, 22] et de la relaxation en énergie d'électrons [23, 24, 25] se propageant dans de tels circuits, dans des ECs plus précisément, peuvent être associées au développement de cette approche pour l'information quantique. Cependant, ces travaux ont tous été menés à partir de mesures DC. D'un point de vue fondamentale, pour continuer les expériences de corrélation avec des électrons et avoir accès à la full counting statistic, ou d'un point de vue information quantique pour continuer le développement de qubit volants, il est nécessaire de contrôler et détecter un électron unique.

Récemment, différentes approches ont été utilisées pour réaliser l'injection sur demande d'électron unique dans des canaux balistiques. On peut citer par exemple le condensateur mésoscopique [26], les ondes acoustiques de surfaces (OAS) [27, 28] ou encore de courts pulses Lorentziens [29, 30]. De tels sources à électron unique ont déjà été utilisées dans des expériences de corrélation, à une seule source dans une expérience dite de Hanbury-Brown-Twiss [31], à deux électrons indistinguables avec cette expérience de Hong Ou Mandel [29, 32]. Mais là aussi, alors que des sources à électron unique étaient utilisées, la mesure était statistique basée sur le bruit du courant, donc un grand nombre d'électron était nécessaire. La détection instantanée d'un électron unique se déplaçant dans des OAS a déjà été démontrée, mais ce système est relativement différent des autres canaux balistiques. En effet, avec des OAS l'électron est transporté dans une boîte quantique en mouvement, un puits de potentiel en mouvement, avant d'être attrapé et confiné dans une boîte quantique statique. Ainsi l'électron peut être figé pour un temps suffisamment long pour permettre sa détection avec un détecteur de charge conventionnel basé sur l'utilisation d'un QPC. Ces OAS permettent de transporter la charge dans un puits de potentiel 0D se déplaçant à une vitesse de l'ordre de  $\sim 3 \text{ km s}^{-1}$ , ce qui est très différent du transport dans les autres canaux balistiques 1D où les électrons se déplacent librement à la vitesse de Fermi, qui est typiquement  $\sim 10^5 \text{ m s}^{-1}$ . De plus, même si l'injection d'électron dans les OAS a été optimisée au fil des ans [33, 34], elle est toujours faite de façon statistique dans un train de boîtes quantiques en mouvement, ce qui n'est clairement pas adapté pour les expériences de corrélation. Pour détecter un électron se déplaçant dans les canaux balistique 1D, de la même façon on pourrait envisager d'attraper cet électron volant dans une boîte quantique. Cependant, en considérant la vitesse de propagation des électrons dans ces canaux, il faudrait

---

être capable de déclencher cette saisi dans une échelle de temps de l'ordre de la picoseconde, ce qui expérimentalement est inconcevable avec l'électronique conventionnel.

Dans les expériences utilisant des canaux balistique 1D, la difficulté de la détection d'un électron unique provient du temps d'interaction extrêmement court entre cette charge à détecter et le détecteur de charge. Ce temps est défini par la vitesse de l'électron, la taille du paquet d'onde ou encore la distance sur laquelle le détecteur est sensible. Dans ces systèmes où l'électron se déplace à la vitesse de Fermi, ce temps est typiquement inférieur à quelques picosecondes,  $1 - 10$  ps. Jusqu'à présent le meilleur détecteur de charge [35] requiert un temps d'interaction plus grand que celui ci par plusieurs ordres de grandeur, sa bande passante étant limitée à 10 MHz environ. En d'autres termes, cette détection d'un électron unique en mouvement est possible uniquement avec une sensibilité en charge de l'ordre de  $\sim 1 - 3 \cdot 10^{-6} e \text{ Hz}^{-1/2}$ , est une bande passante de  $0.1 - 1$  THz typiquement.

Alors que les sources à électron unique sont existantes, le détecteur capable de réussir une telle détection reste à développer afin de, notamment, pouvoir continuer le développement de ces expériences d'optique quantique électronique.

Récemment, les systèmes quantiques ont été identifiés comme étant extrêmement sensibles aux fluctuations de leur environnement, ils apparaissent donc comme de possible détecteurs [36]. Ils ont par exemple déjà été utilisés pour détecter un excitation phononique unique dans des systèmes nanomécanique [37]. Dans l'AlGaAs/GaAs, un qubit de charge dans une double boîte quantique ou un interféromètre de Mach Zehnder ont également proposés pour de telles applications [38]. Dans cette thèse, nous nous concentrons sur un autre type de détecteur, un qubit de spin singulet-triplet.

Ce qubit de spin est un système quantique défini dans une double boîte quantique par les états anti-parallèle de spin à deux électrons singulet  $|S\rangle$  et triplet  $|T_0\rangle$ , séparés en énergie par l'énergie d'échange  $J(\varepsilon)$ . Cette énergie dépend du couplage et du désaccord  $\varepsilon$  entre les deux boîtes quantiques. Le désaccord  $\varepsilon$  est la différence entre le potentiel chimique de chacune des boîtes quantiques et varie donc avec leur environnement électrostatique. Expérimentalement, des oscillations de l'état de spin peuvent être induites avec une fréquence d'oscillation qui est définie par  $J(\varepsilon)$ . Ces oscillations, appelées oscillations cohérentes d'échange démontrées pour la première fois en 2005 [39], sont sensibles à l'environnement électrostatique via le désaccord  $\varepsilon$  et ont déjà été utilisées comme détecteur de charge [40]. L'avantage d'utiliser ces oscillations pour la détection de charge est double, un temps d'exposition qui peut être très court, et l'information acquise qui peut être conservée sur une longue durée. Cela provient de la manipulation rapide des états de spin électronique qui permet un contrôle de l'énergie d'échange  $J(\varepsilon)$  sur de très courte échelle de temps. Le qubit de spin peut donc être transformé comme un détecteur de charge ultra-sensible avec une large bande-passante. Dans son utilisation, la détection de la charge se fait durant les oscillations de l'état de spin, avec l'information acquise encodée dans la phase des oscillations, donc l'état de spin du qubit. Cette information peut être conservée jusqu'à plusieurs centaines de microsecondes [41], ce qui est un temps suffisamment long pour permettre sa lecture avec un détecteur de charge conventionnel. Ce système apparait donc comme un candidat prometteur pour réussir la détection instantanée et en vol d'un électron unique se déplaçant dans des canaux balistiques.

---

Le but de ma thèse était de développer un tel qubit de spin pour la détection instantanée d'un électron se déplaçant à la vitesse de Fermi dans des canaux de l'effet Hall quantique. Ce projet a été initialisé par le travail de R.Thalineau [42, 43] dans lequel les contraintes expérimentales ont limité la sensibilité en charge de ce qui peut être appelé le spin qubit détecteur à la détection de quelques dizaines d'électrons. L'amélioration du dispositif expérimentale et du design de l'échantillon devraient nous permettre d'atteindre cette détection en vol et instantanée d'un tel électron unique en déplacement. L'expérience finale que l'on souhaite réaliser est de détecter une charge unique émise à partir d'une source à électron unique similaire à celle de Ref. [26], qui se propagera dans les ECs. Durant son transport elle interagira par couplage capacitif avec le spin qubit détecteur placé en proximité des ECs. Si des oscillations cohérentes d'échange sont en cours durant cette interaction, la charge en mouvement modifiant l'environnement électrostatique de la double boîte quantique induit une variation de phase des oscillations qui sera mesurée dans un second temps avec un détecteur de charge conventionnel. Pour réussir la détection instantanée de l'électron unique, il y a deux défis à réussir, deux étapes de détections. La première étant l'interaction entre l'électron en déplacement et le spin qubit détecteur qui doit induire une variation de phase de  $\pi$  pour parfaitement encoder la présence ou non de l'électron dans l'état de spin du qubit, induire un renversement de l'état de spin. Ensuite, la lecture de l'état de spin du qubit doit être instantanée. Si ces deux défis sont réussis, une correspondance directe entre la détection du passage d'un électron et l'état de spin qubit détecteur est obtenue.

Au cours de mon travail de thèse, décrit dans les chapitres qui suivent, j'ai développé un tel spin qubit détecteur dans l'objectif de réussir ces deux challenges. Le premier chapitre s'attache à décrire le confinement et la manipulation d'électrons dans des boîtes quantiques. Suivi de la présentation des états de spin à deux électrons dans une double boîte quantique. Enfin, la dernière section introduit l'effet Hall quantique et explique l'origine de ces ECs.

Le second chapitre présente le dispositif expérimental utilisé pour ce travail avec en particulier une présentation détaillée du RF-QPC (Radio Frequency Quantum Point Contact) employé. C'est une version améliorée du détecteur de charge conventionnel QPC ayant une bande passante répondant aux contraintes de la détection instantanée de l'état de spin du qubit de spin.

Dans le troisième chapitre est décrit le développement du spin qubit détecteur avec la présentation de résultats préliminaires démontrant la sensibilité de ce qubit de spin singulet-triplet à la densité en électron des ECs dans une expérience DC.

Enfin, le quatrième et dernier chapitre présente l'optimisation et l'utilisation de ce spin qubit détecteur pour la détection d'un électron unique dans une expérience pulsée.

## Confinement et manipulation

Ce chapitre ( 1) présente les concepts de bases nécessaires à la compréhension des différentes manipulations qui sont réalisées tout au long du manuscrit. Dans un premier temps le confinement des électrons dans des boîtes quantiques est présenté. Il est possible grâce à des grilles métalliques polarisées négativement déposées sur une hétérostructure d'AlGaAs/GaAs. Cette hétérostructure a une structure de bande bien particulière où à l'interface entre ces deux matériaux, localement un puits de potentiel est formé

---

et rempli d'électrons provenant d'atome de silicium dopant négativement la couche d'AlGaAs. Ainsi ce forme ce que l'on appel un gaz d'électrons bidimensionnel noté 2DEG (cf. Fig. 1.1). Ce 2DEG, localisé environ 100 nm sous la surface, peut être dépeuplé en appliquant un potentiel négatif sur des grilles métalliques déposées en surface. En designant la position de ces grilles, ainsi que les tensions appliquées, il est possible d'isoler une, deux îles d'électrons du reste du 2DEG (cf. Fig. 1.2). Ces îles sont les boites quantiques dans lesquelles on peut contrôler le nombre d'électrons jusqu'à l'électron unique. Le comportement de ces électrons confinés est décrit à l'aide du modèle d'interaction constante [47, 52] dans lequel les différentes interactions électrostatiques entre la charge et les grilles ou les réservoirs à électrons sont modélisées avec un réseau de capacités (cf. Fig. 1.3a).

Expérimentalement on peut vérifier ce contrôle à l'électron unique en utilisant un détecteur de charge local que l'on appel QPC par la suite. Ce détecteur consiste à mesurer le courant se propageant dans une constriction du 2DEG dans le voisinage des boites quantiques (cf. Fig. 1.2). Ce courant étant capacitivement couplé à la population électronique des boites quantiques, une modulation de sa conductance est réalisée (cf. Fig. 1.4c). En associant ce détecteur de charge à la manipulation des tensions appliquées sur deux grilles il est possible de caractériser les boites quantiques en mesurant ce que l'on appel un diagramme de stabilité que l'on peut obtenir pour une simple (cf. Fig. 1.4d) ou double boites quantiques (cf. Fig. 1.5a). Ces diagrammes ne sont rien d'autre que des cartes des états de charge du système.

Le spin qubit utilisé pour le développement du qubit détecteur est obtenu à partir de la manipulation de deux électrons confinés dans une double boite quantique. Lorsque il y a un électron dans chacune des boites quantique, on parle de l'état de charge (1,1), la base propre des états de spin est  $|\uparrow\downarrow\rangle, |\downarrow\uparrow\rangle$ , les électrons étant relativement indépendants l'un de l'autre. Lorsqu'ils sont dans la même boite, avec un état de charge noté (2,0), la base propre n'est plus la même puisque les électrons interagissent et elle est désormais formée des états de spin singulet et triplet  $|S\rangle, |T_0\rangle$ . A noter que d'autres états de spin sont présents mais sont ignorés de la discussion car ils peuvent être repoussés, séparés en énergie par l'effet Zeeman résultant de l'application d'un champ magnétique externe. La transition entre les deux bases de spin n'étant pas abruptes, à la transition entre ces deux états de charges elles sont hybridisées. En générale on représente les états de spin du système suivant un axe de désaccord  $\varepsilon$ , allant de l'état (0,2) à (1,1) puis (2,0) dans un diagramme d'énergie correspondant à la figure 1.6.

En plus de l'énergie de Zeeman appliqués aux états de spin  $|\uparrow\uparrow\rangle, |\downarrow\downarrow\rangle, |T_+\rangle$  et  $|T_-\rangle$ , d'autres énergies sont présentes dans ce système. Les états  $|\uparrow\downarrow\rangle$  et  $|\downarrow\uparrow\rangle$  ne sont pas dégénérés en énergie mais séparés en énergies par une énergie de Zeeman provenant de la différence de polarisation des spin nucléaires entre les deux boites quantiques notée  $\Delta B_z$  ( $\sim 100$  neV). Cette différence amène à un champ magnétique effectif ayant une amplitude de l'ordre de quelques milli Tesla [59, 63, 64]. Dans la base de spin singulet-triplet, les deux états  $|S\rangle, |T_0\rangle$  sont séparés en énergie par l'énergie d'échange  $J(\varepsilon)$  qui a une valeur maximum de  $500 \mu\text{eV}$ .

Dans la pratique, l'évolution des états de spin entre la transition (0,2)-(1,1) et (1,1)-(2,0) est équivalente, on considère uniquement la seconde transition pour laquelle la sensibilité en charge du QPC est plus importante. Par la manipulation des électrons entre ces deux états de charges, qui revient à manipuler l'état de spin entre ces deux bases de spin, deux oscillations de spin cohérentes sont possibles, une avec une fréquence définie par  $\Delta B_z$ , et une autre, celle utilisée pour le qubit détecteur, définie par  $J(\varepsilon)$  qui est

---

sensible à l'environnement électrostatique de la double boîte quantique via le désaccord  $\varepsilon$ .

Comme cela sera montré par la suite, les manipulations de spin sont contraintes par le couplage de notre système de spin à l'environnement qui induit une perte de l'information stockée dans le qubit de spin par deux processus différents schématisés dans la figure 1.7.

L'un est la relaxation de l'état de spin schématisée dans la figure 1.7b, qui correspond à la tendance qu'à n'importe quel système à tendre vers son état fondamentale par échange d'énergie avec l'environnement, dans notre cas des phonons [61]. Ce temps de relaxation noté  $T_1$  est typiquement de quelques dizaines de microsecondes dans nos conditions expérimentales. Pour notre expérience, la lecture de l'état de spin (cf. section 3.3.1) doit se faire avant sa relaxation [35, 59, 60], ce qui d'un point de vue technique signifie que pour être capable de le lire instantanément, une bande passante  $\sim$  MHz est nécessaire. La bande passante d'un QPC conventionnel étant typiquement  $\sim$  10 kHz, nous avons donc du utiliser une version optimisée de ce détecteur, un RF-QPC, pour réussir la lecture instantanée de l'état de spin du qubit. Ce RF-QPC et cette lecture de spin sont présentés dans le deuxième chapitre à partir de la section 2.4.

Le deuxième processus est le déphasage qui correspond à la perte de l'information de phase du spin schématisée dans la figure 1.7c. Ce processus apparaît typiquement quand des oscillations de l'état de spin sont réalisés avec une fréquence qui est inconstante dans le temps. Par exemple, quand les oscillations ont une fréquence définie par  $\Delta B_z$ , donc dépendent de la polarisation des spin nucléaires. Cette polarisation fluctuant dans le temps dans une échelle de temps de l'ordre de la seconde [65], d'une expérience à l'autre, la fréquence d'oscillation n'est pas exactement la même et la phase accumulée est finalement distribuée sur les différents essais. L'information de phase est perdue en un temps noté  $T_2^*$ , appelé temps de déphasage qui vaut typiquement  $T_2^* \sim 10$  ns [39, 88, 89]. Donc, pour être capable de faire des manipulations cohérentes de spin, cela signifie qu'il faut être capable de le manipuler plus vite que  $T_2^*$ .

Finalement, un dernier élément est introduit dans ce premier chapitre qui est l'effet Hall quantique [9]. Dans le régime de l'effet Hall quantique, la conduction du courant se fait uniquement sur les bords de l'échantillon, dans ce qui est appelé des canaux de bords noté ECs. Dans ces canaux la conduction des électrons est insensible à la présence de défauts de la structure, la direction de propagation est fixe et se fait à vitesse constante égale à la vitesse de Fermi qui est de  $10^4 - 10^5$  m s<sup>-1</sup> [93, 94, 95]. Ce régime qui apparaît dans des systèmes bidimensionnels, comme notre échantillon, soumis à un champ magnétique perpendiculaire peut être caractérisé en mesurant ce qui est appelé des oscillations de Shubnikov de Haas (cf. Fig. 1.8c). Cette mesure consiste à enregistrer la conductance du 2DEG en faisant varier l'amplitude du champ magnétique. La conductance oscille avec l'amplitude du champ magnétique, et chaque maximum indique que le transport du courant se fait uniquement dans les ECs dont le nombre diminue lorsque l'on augmente cette amplitude. Pour notre expérience le champ magnétique doit être réglé pour un tel maximum de conductance, et dans l'idéal nous voudrions avoir uniquement un canal de bord. Cependant cela n'est pas possible en considérant l'utilisation du qubit de spin singulet-triplet qui ne peut être défini que pour un champ inférieur à 1 Tesla typiquement [61]. En plus de cette contrainte, dans notre dispositif expérimental la sensibilité en charge du RF-QPC diminuait avec l'amplitude du champ magnétique, et à partir d'une champ de 500 mT elle était trop faible pour permettre la réalisation des expériences. Au final nous avons réglé le champ magnétique à 430 mT pour lequel on a 10 canaux

---

de bords. Ce qui est une limitation importante pour notre expérience puisque l'électron injecté est équiréparti sur tous les canaux. Comme il interagit avec le spin qubit détecteur par couplage capacitif qui diminue avec la distance, son impact sur le détecteur dépendra de sa position et en moyenne sera inférieur que pour un plus petit nombre de ECs.

## Dispositif expérimental

Dans le chapitre précédent on a vu que les énergies typiques associées à notre système sont faibles, en particuliers celles du qubit de spin avec la séparation entre les états de spin singulet et triplet qui est maximum de  $500 \mu\text{eV}$  ce qui est égale à  $5 \text{ K}$ . Il est donc nécessaire de refroidir l'échantillon à une température bien inférieure à  $1 \text{ K}$ . Cela est possible en utilisant un réfrigérateur à dilution qui se base sur la dilution d'une phase d' $^3\text{He}$  dans une phase d' $^4\text{He}$ . Ce processus étant endothermique, la réfrigération continue est obtenue en maintenant un flux constant d' $^3\text{He}$  dans cette phase d' $^4\text{He}$ . Pour l'expérience présentée dans ce manuscrit, la température de base de fonctionnement au niveau de l'échantillon était de  $60 \text{ mK}$ .

Pour le contrôle de la charge qui se fait par l'application de tensions, un grand nombre de lignes DC et RF font la connection de température ambiante jusqu'à l'échantillon. Pour éviter l'apport de chaleur et pour filtrer l'apport de bruit de charges, ces connections sont faites en suivant une procédure bien définie avec un choix des matériaux et un filtrage des lignes (cf. Fig. 2.2). Les lignes DC sont utilisées pour la réalisation de manipulations "lentes", limitées à une bande passante de typiquement  $\sim 1 \text{ MHz}$ . Les manipulations qui doivent se faire avant déphasage de l'information de spin, dans une échelle de temps inférieure à  $T_2^*$ , se font à l'aide des grilles rapides dites RF qui ont une bande passante  $> 1 \text{ GHz}$ .

Les tensions appliquées pour les lignes DC sont contrôlées à l'aide d'un convertisseur digital à analogue (DAC), développé au sein de l'Institut Néel qui est basé sur une carte (Linear Technology LTC2604). Cette carte contient différentes sorties ayant chacune une tension d'opération dans la gamme de  $\pm 5\text{V}$  avec un temps de montée  $t_{rise} < 2 \mu\text{s}$  et une densité spectrale de bruit de l'ordre de  $\sim 25 \text{ nVHz}^{-1/2}$ . Le DAC est contrôlé par un FPGA de National Instruments (NI sbRIO-9208) programmé à l'aide d'un programme Labview développé au sein du groupe de recherche.

Pour ce qui est des grilles RF, elles sont contrôlées à partir d'un générateur de tension arbitraire (AWG Tektronix 5014) ayant un échantillonnage de  $1.2 \text{ GS/s}$  et une gamme de tension sur l'échantillon de l'ordre de  $\sim 60 \text{ mV}$ . Cet instrument est contrôlé à partir d'un programme que j'ai développé permettant de générer en amont la séquence jouée par le AWG, et de la stocker sur sa mémoire. Sa réalisation et sa mesure sont synchronisées à partir d'un jeu de triggers.

Pour ce qui est de la mesure du courant pendant les manipulations DC, il est enregistré à l'aide d'un convertisseur courant tension (I/V) également développé au sein de l'institut Néel basé sur un amplificateur opérationnel de Texas Instruments (TLC2201). Ce convertisseur de tension opère de DC jusqu'à une fréquence de l'ordre de  $\sim 1 \text{ kHz}$  avec un gain allant de  $10^6 \text{ V A}^{-1}$  à  $10^9 \text{ V A}^{-1}$ . Le voltage est ensuite mesuré à l'aide d'un analog-to-digital converter (ADC) de National Instruments (NI PCI-6023E) avec un échantillonnage de  $200 \text{ kS/s}$ .

Pour les mesures rapides à l'aide des grilles RF, la chaîne de détection utilisée est bien particulière.

Ces manipulations sont réalisées pour une seule des deux double boîtes quantiques de l'échantillon, celle définissant le qubit de spin pour laquelle le détecteur de charge est un RF-QPC donc la chaîne de détection est maintenant décrite.

Dans le but de mesurer l'état de spin du qubit détecteur, un détecteur de charge ayant une bande passante de quelques mega-Hertz est nécessaire. Pour cela, un QPC ne peut pas être utilisé comme il a une bande passante de  $\sim 10$  kHz. Un RF-QPC est un détecteur de charge basé sur la modulation en amplitude d'un signal RF par un circuit résonant contenant l'échantillon [73, 75, 76, 77, 74]. Ce circuit est un circuit RLC dans lequel la résistance est celle du QPC, l'inductance et le condensateur sont des éléments ajoutés. Ces composants sont choisis de façon à avoir un accord d'impédance entre le circuit résonant et la ligne RF de transmission qui est  $50 \Omega$ . Ainsi, comme le seul élément variable du circuit résonant est la résistance du QPC, avec sa conductance qui est modulée par l'état de charge de la double boîte quantique, le signal RF envoyé sur ce circuit est plus ou moins réfléchi, donc modulé en amplitude, par la conductance du QPC. Après différentes étapes d'amplification, une démodulation et un filtrage passe-bas, un signal (noté  $V_{RF}$ ) directement proportionnel à la conductance du QPC est obtenu. Grâce à cette ajustement d'impédance une large bande passante peut être obtenue, de  $\sim 15$  MHz pour notre dispositif, avec une large sensibilité de charge,  $\sim 1.5 \cdot 10^{-6} e^2/h \text{ Hz}^{-1/2}$  pour nous. Malheureusement, l'inductance utilisée ainsi que la résistance du QPC pour laquelle la modulation est optimale varient avec l'amplitude du champ magnétique, débouchant sur une sensibilité en charge qui diminuait avec nous limitant à un champ magnétique de travail inférieur à 500 mT.

La fin de ce chapitre est dédié à l'étude et à l'optimisation de la sensibilité en charge du RF-QPC par le réglage des grilles de tension définissant le QPC. Cette optimisation se fait dans l'objectif de démontrer tout d'abord notre habilité à détecter de façon immédiate le tunneling d'un électron dans et en dehors d'une boîte quantique (cf. Fig. 2.11). Une fois ce point démontré, la procédure de détection développée en associant ce RF-QPC et un oscilloscope (LeCroy WaveRunner HRO 64Zi) qui peut faire des tests booléens consistant à vérifier l'état de charge de la boîte quantique est présentée. Cette procédure est développée et optimisée dans le cadre de la lecture instantanée de l'état de spin du qubit (cf. Fig. 2.13). Au final une fidélité de lecture de l'ordre de 50% est atteinte, cf. Fig. 2.15. Cette détection est limitée par différents facteurs, d'une part la sensibilité en charge du RF-QPC influencée par le champ magnétique (fixé à la limite permettant cette détection instantanée) et par un temps de montée de notre chaîne de détection.

Néanmoins cette détection instantanée de l'état de spin du qubit détecteur est démontrée, ce qui signifie que l'un des deux challenges pour la détection instantanée de l'électron unique en déplacement dans les canaux de bords de l'effet Hall quantique est atteint.

## **Qubit de spin singulet-triplet comme détecteur de charge**

Dans le chapitre précédent la détection instantanée de l'état de spin du qubit a été démontrée. Il reste maintenant à développer le spin qubit détecteur est plus précisément les oscillations cohérentes d'échange. Ce qui est l'objet de la première partie de ce chapitre, suivi de son utilisation dans une expérience de principe pour démontrer leur sensibilité à des électrons se déplaçant dans les ECs.

Pour développer ce qubit de spin, les manipulations de la charge doivent se faire dans une échelle de temps de la nanoseconde typiquement afin de garder la cohérence de l'état de spin, elles se font expérimentalement avec les grilles dites RF. Comme uniquement ces dernières seront utilisées par la suite, une caractérisation, un diagramme de stabilité, de la double boîte quantique dans laquelle est développée le qubit de spin est mesurée. Pour la réalisation de l'expérience finale, la détection d'une charge unique en déplacement, un large couplage  $> \text{MHz}$  aux réservoirs est préférable afin de faciliter la détection. L'étude de ce diagramme de stabilité mesuré (cf. Fig. 3.2) avec  $1 \mu\text{s}$  par point permet d'avoir une première indication du réglage ou non de l'échantillon dans ce régime de fort couplage. Une étude plus approfondie permet de valider ce point en étudiant directement le temps de tunneling d'un électron vers les réservoirs (cf. Fig. 3.3).

Ce régime étant atteint, les mesures de spin peuvent débuter avec tout d'abord une explication du blocage de spin de Pauli, qui est le principe sur lequel est basé la lecture de spin. En effet, dans notre système comme la charge est la seule information à laquelle nous avons expérimentalement accès, une conversion d'information de spin à information en charge est nécessaire. Le blocage de spin de Pauli correspond à la différence d'état de charge de la double boîte quantique suivant l'état de spin [59, 80, 81]. Dans une zone limitée de  $\varepsilon$  l'état de spin singulet est dans l'état de charge (2,0) alors que l'état de spin triplet est en (1,1) (cf. Fig. 3.4). Ainsi, en faisant un transfert de (1,1) vers (2,0) dans cette région de  $\varepsilon$ , si l'état de charge (1,1) est mesuré cela correspond à un spin triplet, si c'est (2,0) un spin singulet. Cette différence d'état de charge n'étant vrai que jusqu'à relaxation de l'état excité  $|T_0\rangle$  vers l'état de spin fondamentale  $|S\rangle$  se faisant dans un temps caractéristique  $T_1$  qui vaut dans notre expérience environ  $30 \mu\text{s}$ . Grâce à l'utilisation du RF-QPC nous sommes capables de faire cette mesure instantanément comme démontré dans le chapitre 2. En pratique, une telle lecture de spin par transfert de charge est réalisée un grand nombre de fois, et la moyenne du signal de RF-QPC  $V_{\text{RF}}$  a une forme de décroissance exponentielle associée à cette relaxation de l'état de spin. L'amplitude de cette exponentielle, notée  $\Delta V_{\text{RF}}$ , est donc proportionnelle à la probabilité de l'état de spin triplet après chaque manipulation de spin et sera l'information de spin utilisée dans ce manuscrit. A noter que pour l'extraction de cette information il faut attendre la relaxation complète de tous les états de spin, ce qui correspond au final à l'initialisation entant que singulet pour l'expérience suivante.

La première étape avant de développer la séquence permettant de réaliser des oscillations cohérentes d'échanges est l'optimisation de la mesure de spin, donc la recherche du  $\varepsilon$  pour lequel la conversion de spin à charge via le blocage de spin de Pauli est optimale. Cette étape correspond à la figure 3.5.

Le point optimal de mesure de spin étant défini, la séquence pour la réalisation de ces oscillations cohérentes d'échange peut maintenant débuter. Ces oscillations se font dans la base de spin  $|S\rangle, |T_0\rangle$  avec un état de spin initialement préparé dans la base  $|\uparrow\downarrow\rangle, |\downarrow\uparrow\rangle$ . Or, pour la lecture de spin et son initialisation, la base de spin  $|S\rangle, |T_0\rangle$  est préférentielle, par conséquent un changement d'une base de spin à l'autre est nécessaire. Ce changement se fait à l'aide d'une variation lente de  $\varepsilon$ , un transfert adiabatique d'une base de spin à l'autre, pendant laquelle des croisements avec d'autres états de spin sont traversés. Pour éviter de mélanger l'état de spin manipulé avec ces derniers, la façon de passer à travers ces croisements doit être parfaitement contrôlée, leur adiabaticité doit être contrôlée. Il faut

donc dans un premiers temps faire une cartographie des états de spin le long de l'axe de  $\varepsilon$  afin de les localiser, ce qui correspond à la figure 3.6. Ensuite, la notion d'adiabaticité est présentée (cf. Fig. 3.8), elle est liée à la vitesse à laquelle  $\varepsilon$  est modifié par rapport à une énergie caractéristique du croisement traversé. Puis sont étudiées la façon dont sont traversés ces croisements, d'abord le passage de S(2,0)-S(1,1) qui doit être adiabatique (cf. Fig. 3.9), celui entre  $|S\rangle$  et  $|T_0\rangle$  qui doit être non adiabatique et enfin le changement d'une base propre de spin à l'autre qui doit également être adiabatique (cf. Fig. 3.11).

Les figures 3.12c & d présentent la réalisation de ces oscillations mesurées avec les deux modes d'acquisition : la lecture instantanée de l'état de spin ( $P_{T_0}$ ) ou le signal moyenné du RF-QPC ( $\Delta V_{RF}$ ). Un chevron pattern est également présenté, il s'agit du carte montrant ces oscillations mesurées pour différents points d'oscillations  $\varepsilon$ , différentes fréquences d'oscillations qui augmentent avec  $\varepsilon$ . Cette carte permet d'une part de vérifier que ces oscillations dépendent bien de l'environnement électrostatique de la double boîte quantique, via  $\varepsilon$ , et en plus de cela elle permet de définir expérimentalement la valeur du couplage interboîte  $t_c$ , dans notre cas il est évalué à  $4 \mu\text{eV}$ .

L'étude plus approfondie de ces oscillations nous permet de vérifier que nous avons un très bon contrôle de l'état de spin durant cette séquence puisque la fidélité de la manipulation est évaluée à 95% avec une fidélité de mesure de 85% pour le mode de lecture moyenné de l'état de spin ( $\Delta V_{RF}$ ). Cette cartographie prouvant la sensibilité de ces oscillations à l'environnement électrostatique de la double boîte, leur sensibilité à un flux d'électrons se propageant dans les ECs est par la suite étudiée. Cette vérification se fait à partir de l'application d'une tension à deux contacts ohmiques du réservoir abritant les ECs reliant la source à électron au qubit détecteur. En raison de la chiralité de ces canaux de conduction [96, 97, 98], et du fait que leur potentiel chimique est défini par le contact ohmique qui les émet, une variation de phase de ces oscillations cohérentes d'échange doit être observée seulement en changeant le biais de l'un des contacts. L'autre doit avoir aucun effet. En effet, les ECs ont une trajectoire formant une boucle, avec une moitié de la boucle passant devant la source à électron et le spin qubit détecteur dont le potentiel chimique, donc sa densité en électrons, est définie par l'un des deux contacts. L'autre moitié de la boucle interagit ni avec la source ni avec le spin qubit détecteur, sa densité électronique est définie par la tension du second contact ohmique. De plus, comme la direction de propagation des ECs est définie par l'orientation du champ magnétique appliqué, suivant quel contact ohmique induit la variation de phase des oscillations, nous pouvons déterminer quel est la direction de propagation dans les ECs. La figure 3.16 présente un schéma résumant cette explication.

Des oscillations cohérentes d'échanges sont donc réalisées, à  $\varepsilon$  constant mais en faisant varier les biais de tension appliqués à ces deux contacts ohmiques, cela correspond aux cartes de la figure 3.17. Le résultat de cette expérience nous montre que effectivement une variation de phase est observée pour un seul contact pour une même orientation de champ magnétique. De plus, comme attendu, le contact induisant cette variation change en retournant l'orientation du champ magnétique. Cette expérience prouve donc que ce type d'oscillation est sensible au passage d'électrons dans la proche proximité de la double boîte quantique, et peut donc être utilisé pour détecter un petit nombre d'électrons en déplacement dans des canaux de bords.

A ce point de développement de notre détecteur, nous avons juste démontré sa sensibilité en charge, il reste maintenant à l'optimiser pour la détection d'un électron unique ainsi qu'à développer la source à électron unique.

## Vers la détection d'un électron unique

Dans le but de détecter un électron unique, deux éléments clefs de ces oscillations doivent être définis, le temps d'oscillation de l'état de spin et le désaccord  $\varepsilon$  auquel elles sont réalisés. D'une part, le temps d'oscillation qui est le temps d'exposition du détecteur, c'est à dire le temps pendant lequel il est sensible en charge, doit être défini. Ce temps doit être ajusté au temps d'interaction avec l'élément à détecter, en l'occurrence un électron unique se déplaçant à la vitesse de Fermi. Comme mentionné dans l'introduction, ce temps est de l'ordre de 1 – 10 ps. Par conséquent, dans l'idéal on souhaiterait limiter le temps d'oscillation à ces quelques picosecondes. Cependant, en pratique une telle échelle de temps n'est pas accessible avec notre AWG, on le fixe donc à la valeur la plus courte que l'on peut atteindre, 1 ns.

Le second élément à définir est le  $\varepsilon$  auquel sont réalisées ces oscillations, qui par la suite sera appelée position de travail du détecteur. Cette position correspond au  $\varepsilon$  pour lequel la phase accumulée durant cette nanoseconde d'oscillation est la plus sensible aux variations de l'environnement électrostatique. Pour définir cette position, des oscillations cohérentes d'échange sont induites en faisant varier la position à laquelle elles sont réalisées. Une trace typique correspond à la figure 4.1, et ces oscillations sont appelées oscillations cohérentes d'échanges en amplitude. La sensibilité en charge de ce détecteur augmentant avec  $\varepsilon$ , on voudrait fixer ce point de travail au plus grand  $\varepsilon$  possible. Cependant, le déphasage de ces oscillations nous l'empêche. Ce déphasage est étudié à l'aide d'une simulation (cf. Fig. 4.3) qui indique que le bruit de charge est à l'origine de ce processus. Pour le réduire, la puissance du signal RF utilisé pour le RF-QPC est tout d'abord réduite (cf. Fig. 4.4), ainsi que l'ajout de filtres pour les lignes DC utilisées pour définir cette double boîte quantique (cf. Fig. 4.5).

Après ces deux améliorations, la sensibilité en charge de ce spin qubit détecteur ne peut pas être augmentée et sa position de travail optimale est définie à partir de l'étude de l'effet résultant de l'interaction avec un électron unique se propageant dans les ECs. Cette calibration de l'effet d'un électron unique a pour but d'une part de définir ce point de travail mais également d'évaluer si la détection instantanée de cet électron est possible. Cette détection instantanée étant possible si cette interaction induit une variation de phase de  $\pi$ .

Cette calibration se fait dans un premiers temps par la détermination de la variation de désaccord  $\Delta\varepsilon$  du à l'interaction avec un grand nombre d'électrons à partir de la réalisation de la même expérience que celle avec un flux imposé d'électrons (cf. Fig. 4.6). C'est à dire que des oscillations d'échanges en amplitude sont réalisées en appliquant un biais de tension au contact ohmique définissant la densité en électron des ECs passant à proximité du détecteur.

Le nombre d'électrons  $N_e$  induisant cette variation est ensuite défini à partir de l'expression 4.5 pour laquelle il est nécessaire tout d'abord de déterminer le temps effectif d'exposition. En raison d'un temps

de monté de notre AWG, la montée en tension de  $\varepsilon$  est ralentie (cf. Fig. 4.7). Ce phénomène est important pour notre expérience puisque la phase accumulée augmente exponentiellement avec  $\varepsilon$  [39, 40, 90]. Par conséquent, la majeure partie de la phase est accumulée pour les plus grandes valeurs de  $\varepsilon$ , réduisant ainsi le temps effectif d'exposition du détecteur. On définit ce temps comme étant celui qui est nécessaire pour accumuler 50% de la phase durant ce pulse d'oscillation, appelé pulse d'échange, plus précisément de 25% à 75%. Finalement de temps d'exposition est évalué à 200 ps.

En combinant ces deux éléments,  $\Delta\varepsilon$  et  $N_e$ , on obtient la variation en  $\varepsilon$  induite par l'interaction du détecteur avec un seul électron qui vaut  $\delta\varepsilon = -6 \mu\text{V}$ . Enfin, la variation  $\delta V_{\text{RF}}$  de signal du à l'interaction avec une seule charge peut être calculée pour chacun des  $\varepsilon$  d'une trace d'oscillations cohérentes d'échanges en amplitude. La position de travail du spin qubit détecteur étant le point pour lequel  $\delta V_{\text{RF}}$  est maximale (cf. Fig. 4.7). Cette position optimale est obtenue pour  $\varepsilon$  pour lequel le spin fait une rotation de  $3\pi/2$ , avec une variation de signal de maximum  $\delta V_{\text{RF}} = -300 \mu\text{V}$  (cf. Fig. 4.9).

Cette calibration indique deux informations, d'une part le point optimal de travail du détecteur, d'autre part, elle nous indique que la détection instantanée de l'électron unique n'est pas possible. En effet, elle requiert une variation de phase de  $\pi$  qui est obtenue au minimum pour une variation de  $\varepsilon$ . Or un tel déphasage est obtenu pour un variation de  $\varepsilon$  de l'ordre de 0.5 mV alors qu'une charge unique induit une variation de seulement  $\delta\varepsilon = -6 \mu\text{V}$ . Néanmoins, la détection de l'électron unique va être tentée dans une expérience moyennée, dont le but sera de détecter cette variation de  $\delta V_{\text{RF}} = \pm 300 \mu\text{V}$  du à une charge unique.

Avant de tenter cette détection, différentes solutions d'amélioration ont été envisagées et sont présentées. D'une part en utilisant la seconde transition de charge (0,2)-(1,1) (cf. Fig. 4.10), ou en réduisant le nombre de ECs par deux solutions (cf. Fig. 4.11). Ces solutions ont été tentées mais n'apportent pas d'amélioration à nos conditions expérimentales.

Aucune amélioration n'étant possible, nous essayons de faire cette détection dans ces conditions, avec dans un premiers temps le développement de la source à électron unique. Elle est une simple boîte quantique avec l'émission de l'électron qui est induite par l'application d'un pulse de tension, noté IVP, arbitrairement fixé à 6 ns pour nous. Lorsque le pulse est appliqué un électron est émis, et à la fin, un électron tunnel dans la boîte quantique pour compenser celui qui a été émis, c'est donc une charge manquante (un trou) qui est généré dans les ECs (cf. Fig. 4.13). Pour caractériser cette source, tout d'abord le couplage au réservoir abritant les ECs est vérifié, cf. Fig. 4.14, suivi de la possibilité d'émettre un électron (associé à un trou) avec un tel pulse IVP cf. Fig. 4.15. A partir de ces informations on peut calibrer l'effet de ce pulse et définir la position d'injection, c'est à dire les tensions DC appliquées aux grilles définissant cette boîte quantique afin d'avoir un très fort couplage aux réservoirs  $> \text{GHz}$  cf. Fig. 4.16.

Avant de réaliser cette détection, soit de l'électron soit du trou il faut définir un dernier élément qui est le délais entre ce pulse d'injection et le pulse d'échange (de détection). A noter que le spin qubit détecteur étant uniquement sensible aux variations de densité électronique des ECs détecter un électron est équivalent à détecter un trou. Pour définir ce délais, on utilise l'excitation de edge magneto plasmon (EMP) qui est une excitation collective d'électrons de la mer de Fermi [93, 95, 104, 105]. Dans notre

cas ils sont du au couplage capacitif entre le IVP et cette mer de Fermi. Ce couplage induit l'excitation d'électrons, donc une augmentation de la densité en électron des ECs pour le premier front du IVP. Le second front résulte en une diminution de cette densité puisqu'il s'agit de la variation positive de tension du IVP. Ces deux variations locale de densité électronique se propagent dans les ECs et interagissent avec le spin qubit détecteur avant d'être absorbées par le contact ohmique. Ces EMP sont pour nous très intéressants puisque d'une part il s'agit d'une excitation collective, ils sont donc plus faciles à détecter qu'une charge unique. D'autre part ils sont excités en même temps que l'émission de l'électron de la source (ou du trou) avec le IVP. Donc, si nous sommes capables de détecter les EMP, le signal résultant peut être utilisé pour synchroniser la détection et émission d'une charge unique.

Une première expérience est réalisée dans le but de détecter ces EMP, il s'agit de la figure 4.18 dans laquelle il semblerait que l'on a effectivement détecté ces excitations. On vérifie cela par différentes expériences, en jouant sur le délai d'injection Fig. 4.19, l'amplitude du IVP Fig. 4.20. Une dernière vérification est faite qui consiste à changer l'orientation du champ magnétique pour renverser la direction de propagation dans les ECs. Ainsi, si l'on a effectivement détecté un paquet d'électrons du au IVP, i.e. EMP, il sera excité de la même façon mais se propagera dans l'autre direction et sera par conséquent absorbé avant d'avoir pu interagir avec le détecteur. Cette vérification correspond à la figure 4.21 où effectivement l'absence de variation de signal confirme que l'on a bien détecté un paquet d'électrons. Grâce à notre calibration on a pu vérifier que pour cette expérience on a été capable de détecter des EMP comportant au moins 4 électrons environ.

Finalement, on a réalisé l'expérience finale avec la détection d'une charge unique, et plus précisément nous essayons de détecter le trou induit par le IVP. Différentes procédures de détection ont été utilisées, tout d'abord en faisant varier l'amplitude du IVP, Fig. 4.23 mais cette procédure n'est pas adaptée. Une autre approche est utilisée en travaillant avec une amplitude de IVP constante mais en faisant varier les tensions DC de la position d'injection Fig. 4.26 associé à l'utilisation de la détection instantanée de l'état de spin (après sa calibration cf. Fig. 4.25). Cette dernière procédure semble favorable, mais ce mode de détection n'est pas le plus adapté. En effet, il est lent, trois fois plus que celui utilisant la détection moyennée, et associé à l'instabilité de l'échantillon, donc à la sensibilité en charge, nous empêche d'atteindre le niveau de bruit suffisamment faible pour détecter cette charge unique. Cette procédure est donc suivie mais avec en moyennant le signal de spin du RF-QPC. La réalisation de cette procédure est la figure 4.27 où, ici aussi on n'a pas réussi à détecter cette charge unique. La raison principale étant l'instabilité de l'échantillon associé au réglage du détecteur dans sa configuration optimale qui est très fin. Finalement, en moyenne la sensibilité du détecteur était probablement trop faible pour réussir cette détection de charge unique et on doit se contenter de la détection de quelques électrons sous la forme de EMP.

## Conclusion

Le but de ma thèse était de développer un détecteur de charge ultra-sensible pour la détection instantanée d'un électron se déplaçant à la vitesse de Fermi. Un tel détecteur pourrait avoir une application directe pour le domaine de l'optique quantique électronique en utilisant des électrons volants. Notre stratégie

---

---

était de détecter un électron unique se déplaçant dans des canaux de bords (ECs) de l'effet Hall quantique en mesurant la variation de phase induite d'un qubit de spin singulet-triplet, nommé qubit détecteur. La détection instantanée est uniquement possible si l'interaction avec la charge en mouvement induit a variation de phase de  $\pi$  et une lecture instantanée de l'état de spin du qubit détecteur. Durant le développement de ce détecteur ultra-sensible, trois challenges principaux ont été rencontrés.

Le premiers était de maximiser la force d'interaction entre la charge en mouvement et le détecteur dans ces conditions d'utilisation. Pour cela un fort couplage capacitif entre ces deux éléments est nécessaire, ce qui implique d'être dans le régime de fort couplage entre la double boîte quantique et les ECs, plus un petit nombre d'ECs. Dans le travail présenté dans ce manuscrit, un tel régime de fort couplage entre le détecteur et les ECs a été atteint mais il était limité par un problème d'instabilité de l'échantillon. Plus ce couplage étant élevé, plus l'échantillon était instable. Pour être capable d'utiliser le détecteur dans ces conditions optimales de travail tout en faisant une multitude de détection de cette charge unique en déplacement, nous avons limité ce couplage à quelques megahertz. Le nombre d'ECs était limité à dix puisque l'intensité du champ magnétique appliqué détériore la sensibilité en charge du RF-QPC utilisé. Les deux derniers challenges sont plus liés au spin qubit détecteur. D'une part la cohérence des oscillations d'échanges réalisées avec le qubit de spin singulet-triplet qui doivent être parfaitement contrôlée depuis l'initialisation de spin jusqu'au pulse sub-nanoseconde d'interaction avec la charge en déplacement.

Le derniers challenge est la détection instantanée de l'information acquise par le spin qubit détecteur durant cette interaction. L'information étant encodée dans l'état de spin du qubit, la lecture instantanée doit être faite durant la durée de vie de cette état de spin qui est réduit à quelques dizaines de microsecondes dans nos conditions de travail.

La lecture instantanée de l'état de spin est présentée dans le Chapitre 2. Il est basé sur l'utilisation d'un RF-QPC associé à la conversion de spin à charge grâce au blocage de spin de Pauli. Cette lecture est limitée par le relativement rapide temps de relaxation de l'état de spin  $T_1 = 30 \mu\text{s}$  et la sensibilité en charge du RF-QPC. Le développement et l'optimisation de ce procédé de lecture de spin nous permet d'atteindre une fidélité de lecture de spin d'environ 50%.

La réalisation des oscillations cohérentes d'échanges et l'étude de leur sensibilité à la densité électronique des ECs ont été présentés dans le Chapitre 3. Une variation de phase de ces oscillations induite par l'interaction avec un flux d'électron imposé dans les ECs a été observée. Ce flux d'électrons a été induit par l'application d'un biais de tension DC aux ECs pour contrôler leur densité électronique.

L'optimisation du détecteur pour la détection d'une charge unique est décrit dans le Chapitre 4. Tout d'abord nous avons réduit le temps d'exposition à sa valeur minimale expérimentalement de 1 ns, pour l'ajuster autant que possible à celui d'interaction avec cette charge en mouvement évaluée à environ 1 – 10 ps. Ensuite, par la réduction du bruit de charge qui est la limite principale de la sensibilité en charge du qubit détecteur. Une calibration fournie la variation de signal attendu pour l'interaction avec une telle charge unique, indiquant l'impossibilité pour nous de réussir cette détection instantanément. Notre détecteur a une sensibilité en charge estimée à environ  $8 \cdot 10^{-5} \text{ e Hz}^{-1/2}$  pour une bande passante allant de DC à 1 THz environ. Cette sensibilité est presque deux ordres de grandeur inférieure à ce qui

---

est requis pour réaliser cette détection instantanément. Finalement, le qubit détecteur a été utilisé pour détecter dans une expérience moyennée un edge magneto plasmon composé de moins de 5 électrons. Cependant, la détection d'un seul électron n'a pas été possible dans cette expérience moyennée non plus, la sensibilité de notre détecteur étant trop faible.

D'après ce travail, cette détection d'un électron unique est cependant atteignable avec les améliorations suivantes, répartis en deux groupes.

D'une part en réduisant encore plus le bruit de charge. Ce bruit est la source principale de déphasage de oscillations cohérentes de spin, et donc la principale limite de sensibilité en charge du détecteur comme discuté dans le Chapitre 4. Un travail global sur cette réduction de bruit de charge par le filtrage des connections de l'échantillon est la solution la plus évidente. Améliorer l'accord d'impédance entre le circuit résonant du RF-QPC et la ligne de transmission RF devrait permettre de réaliser ces expériences avec une puissance de signal RF plus faible qui est apparue comme étant également une source de déphasage.

Augmenter l'impacte de la charge en mouvement est un autre axe de développement présenté dans le Chapitre 4. La réduction du nombre de ECs est possible en travaillant avec un champ magnétique plus grand et en utilisant des grilles métalliques polarisées.

Ces solutions ne pouvaient pas être utilisées pour notre expérience, cependant, avec un autre design de l'échantillon et sans ce problème de réduction de sensibilité en charge du RF-QPC avec le champ magnétique, une réduction même faible du nombre de ECs devrait permettre d'atteindre la détection d'une charge unique.

---

---

# Acknowledgement

---

Cette thèse a été une sacrée aventure que je n'aurais pas pu finir sans l'aide de nombreuses personnes que je tiens à remercier.

Dans un premier temps merci à Tristan qui m'a donné la possibilité de venir travailler ces quelques années au bâtiment M. Tu as su me guider pour qu'on aille le plus loin possible dans ce projet en me donnant un coup de main pour me sortir des ornières.

Chris, merci beaucoup pour les leçons de cryo et de câblage ainsi que pour ta disponibilité pour répondre à nos questions quelles qu'elles soient.

Je souhaite remercier également Fabien Portier et Dominique Mailly d'avoir accepté d'être rapporteurs de mon travail et pour leur bienveillance surtout vis à vis des conditions particulières de fin de rédaction du manuscrit. Merci également à Pascal Degiovanni et Wiebke Guichard d'avoir participé et présidé mon jury ainsi que pour la discussion de la soutenance.

Un grand merci également à toutes les personnes de l'institut qui m'ont aidé durant ce projet. Déjà un immense merci à BB et PAM qui m'ont appris énormément de choses en plus de me driver. Si j'ai pu arriver au bout c'est en grande partie grâce à vos interventions. I'm very grateful to Kostas for the help and the development of the RF-QPC plus the discussions about basket, Crete and Olympiacos.

Les expériences présentées dans ce manuscrit n'auraient jamais été réalisables sans le soutien technique dont on peut bénéficier quotidiennement à l'Institut. Pour la cryo et le développement de ce frigo qui a été le seul élément à avoir fonctionné correctement pendant les manip, Pierre merci beaucoup pour tes nombreux coup de main. Christophe merci beaucoup pour ton aide et ta participation au développement du RF-QPC ainsi que tes réparations de l'ampli sans broncher. Merci aux membres du liquef, Johan, Raphaël et Kevin pour l'He disponible tous les jours et les discussions de midi. L'équipe de nanofab, Seb, Jeff, Bruno, Gwen et le général Thierry pour les bons moments passés en salle blanche. Merci également à l'équipe administrative, Caroline, Sabine, Florence, Otmane, Angélique,... pour tous les avenants, les factures, les feuilles de temps et j'en passe.

Je tiens à remercier les différentes personnes passées par le bâtiment M au cours de ces années pour la bonne ambiance et l'entre-aide. Quel que soit le jour ou l'heure il y avait toujours du monde disponible si besoin. Merci à Olivier et Clément sans qui je ne coderais probablement pas en python. Tobias, Etienne, Guillaume, Greg, Shintaro, Hanno, Bambi, Toutouille (jeune padawan du RF-QPC et garant de l'état de santé de Merlin), Martin, Urdamp, Manu (Klaus devrais-je dire mon acolyte de train et auto-proclamé psychologue), Herman, Giorgos... Une fois encore merci beaucoup à BB et PAM. Un mot en particulier

---

à Mathias dit 'El pitufo' pour tous les bons moments passés au labo et en dehors ainsi que les discussions sur tout et surtout n'importe quoi. Merci également à miss Toto, ma jumelle de thèse, souvent témoin de ces discussions et toujours d'accord pour me suivre et commander une bière blonde malgré les remarques d'El pitufo. Enfin merci à Serge et tous ceux que j'ai pu oublier.

Parce qu'il n'y avait presque pas que le labo, un grand merci à ma famille que j'ai peu vue mais qui a toujours été présente. Merci aux Donatiens pour les moments de décompressions jamais assez fréquents mais toujours bienvenus, et bien évidemment à Lise pour tout le soutien que tu m'as apporté.

---

---

# Bibliography

---

- [1] R. A. Webb, S. Washburn, C. P. Umbach, and R. B. Laibowitz. Observation of  $\frac{h}{e}$  aharonov-bohm oscillations in normal-metal rings. *Phys. Rev. Lett.*, 54:2696–2699, Jun 1985.
  - [2] R. C. Liu, B. Odom, Y. Yamamoto, and S. Tarucha. Quantum interference in electron collision. *Nature*, 391:263–265, Jan 1998.
  - [3] M. Henny, S. Oberholzer, C. Strunk, T. Heinzel, K. Ensslin, M. Holland, and C. Schönenberger. The fermionic hanbury brown and twiss experiment. *Science*, 284(5412):296–298, Apr 1999.
  - [4] W. D. Oliver, J. Kim, R. C. Liu, and Y. Yamamoto. Hanbury brown and twiss-type experiment with electrons. *Science*, 284(5412):299–301, Apr 1999.
  - [5] V. Umansky, M. Heiblum, Y. Levinson, J. Smet, J. Nübler, and M. Dolev. Mbe growth of ultra-low disorder 2deg with mobility exceeding  $35 \times 10^6 \text{ cm}^2/\text{v s}$ . *Journal of Crystal Growth*, 311:1658–1661, Mar 2009.
  - [6] M. Field, C. G. Smith, M. Pepper, D. A. Ritchie, J. E. F. Frost, G. A. C. Jones, and D. G. Hasko. Measurements of coulomb blockade with a noninvasive voltage probe. *Phys. Rev. Lett.*, 70:1311–1314, Mar 1993.
  - [7] B. J. van Wees, H. van Houten, C. W. J. Beenakker, J. G. Williamson, L. P. Kouwenhoven, D. van der Marel, and C. T. Foxon. Quantized conductance of point contacts in a two-dimensional electron gas. *Phys. Rev. Lett.*, 60:848–850, Feb 1988.
  - [8] D.A. Wharam, T.J. Thornton, R. Newbury, M. Pepper, H. Ahmed, J.E. Frost, D.G. Hasko, D.C Peacock, D.A. Ritchie, and G.A. Jones. One-dimensional transport and the quantisation of the ballistic resistance. *Journal of Physics C: Solid State Physics*, 21(8):L209, 1988.
  - [9] K. v. Klitzing, G. Dorda, and M. Pepper. New method for high-accuracy determination of the fine-structure constant based on quantized hall resistance. *Phys. Rev. Lett.*, 45:494–497, Aug 1980.
  - [10] M. Büttiker. Absence of backscattering in the quantum hall effect in multiprobe conductors. *Phys. Rev. B*, 38:9375–9389, Nov 1988.
  - [11] R. Schuster, E. Buks, M. Heiblum, D. Mahalu, V. Umansky, and H. Shtrikman. Phase measurement in a quantum dot via a double slit interference experiment. *Nature*, 385:417 – 420, Jan 1997.
-

- 
- [12] Y. Ji, Y. Chung, D. Sprinzak, M. Heiblum, D. Mahalu, and H. Shtrikman. An electronic machzehnder interferometer. *Nature*, 422:415–418, Mar 2003.
- [13] P. Roulleau, F. Portier, P. Roche, A. Cavanna, G. Faini, U. Gennser, and D. Mailly. Direct measurement of the coherence length of edge states in the integer quantum hall regime. *Phys. Rev. Lett.*, 100:126802, Mar 2008.
- [14] S. Takada, C. Bäuerle, M. Yamamoto, K. Watanabe, S. Hermelin, T. Meunier, A. Alex, A. Weichselbaum, J. von Delft, A. Ludwig, A. D. Wieck, and S. Tarucha. Transmission phase in the kondo regime revealed in a two-path interferometer. *Phys. Rev. Lett.*, 113:126601, Sep 2014.
- [15] S. Takada, M. Yamamoto, C. Bäuerle, K. Watanabe, A. Ludwig, A. D. Wieck, and S. Tarucha. Measurement of the transmission phase of an electron in a quantum two-path interferometer. *Applied Physics Letters*, 107(6):063101, Aug 2015.
- [16] R. Ionicioui, G. Amaratunga, and F. Udreă. Quantum computation with ballistic electrons. *International Journal of Modern Physics B*, 15(02):125–133, Jan 2001.
- [17] T. M. Stace, C. H. W. Barnes, and G. J. Milburn. Mesoscopic one-way channels for quantum state transfer via the quantum hall effect. *Phys. Rev. Lett.*, 93:126804, Sep 2004.
- [18] T. Bautze, C. Süssmeier, S. Takada, C. Groth, T. Meunier, M. Yamamoto, S. Tarucha, X. Waintal, and C. Bäuerle. Theoretical, numerical, and experimental study of a flying qubit electronic interferometer. *Phys. Rev. B*, 89:125432, Mar 2014.
- [19] M. Yamamoto, S. Takada, C. Bäuerle, K. Watanabe, A. D. Wieck, and S. Tarucha. Electrical control of a solid-state flying qubit. *Nature Nanotechnology*, 7:247–251, Feb 2012.
- [20] P. Roulleau, F. Portier, P. Roche, A. Cavanna, G. Faini, U. Gennser, and D. Mailly. Tuning decoherence with a voltage probe. *Phys. Rev. Lett.*, 102:236802, Jun 2009.
- [21] P.-A. Huynh, F. Portier, H. le Sueur, G. Faini, U. Gennser, D. Mailly, F. Pierre, W. Wegscheider, and P. Roche. Quantum coherence engineering in the integer quantum hall regime. *Phys. Rev. Lett.*, 108:256802, Jun 2012.
- [22] S. Tewari, P. Roulleau, C. Grenier, F. Portier, A. Cavanna, U. Gennser, D. Mailly, and P. Roche. Robust quantum coherence above the fermi sea. *Phys. Rev. B*, 93:035420, Jan 2016.
- [23] C. Altimiras, H. le Sueur, U. Gennser, A. Cavanna, D. Mailly, and F. Pierre. Non-equilibrium edge-channel spectroscopy in the integer quantum hall regime. *Nature Physics*, 6:34–39, Oct 2009.
- [24] C. Altimiras, H. le Sueur, U. Gennser, A. Cavanna, D. Mailly, and F. Pierre. Tuning energy relaxation along quantum hall channels. *Phys. Rev. Lett.*, 105:226804, Nov 2010.
- [25] H. le Sueur, C. Altimiras, U. Gennser, A. Cavanna, D. Mailly, and F. Pierre. Energy relaxation in the integer quantum hall regime. *Phys. Rev. Lett.*, 105:056803, Jul 2010.
-

- 
- [26] G. Feve, A. Mahe, J.M. Berroir, T. Kontos, B. Placais, D. C. Glattli, A. Cavanna, B. Etienne, and Y. Jin. An on-demand coherent single-electron source. *Science*, 316:1169–1172, May 2007.
- [27] R.P. McNeil, M. Kataoka, C.J. Ford, C.H. Barnes, D. Anderson, G.A. Jones, I. Farrer, and D.A. Ritchie. On demand single electron transfer between distant quantum dots. *Nature*, 477:439–442, Sep 2011.
- [28] S. Hermelin, S. Takada, M. Yamamoto, S. Tarucha, A.D. Wieck, L. Saminadayar, C. Bäuerle, and M. Meunier. Electrons surfing on a sound wave as a platform for quantum optics with flying electrons. *Nature*, 477:435–438, Sep 2011.
- [29] J. Dubois, T. Jullien, F. Portier, P. Roche, A. Cavanna, Y. Jin, W. Wegscheider, P. Roulleau, and D.C. Glattli. Minimal-excitation states for electron quantum optics using levitons. *Nature*, 502:659–663, Oct 2013.
- [30] L. S. Levitov, H. Lee, and G. B. Lesovik. Electron counting statistics and coherent states of electric current. *Journal of Mathematical Physics*, 37(10):4845–4866, 1996.
- [31] E. Bocquillon, F. D. Parmentier, C. Grenier, J.-M. Berroir, P. Degiovanni, D. C. Glattli, B. Plaçais, A. Cavanna, Y. Jin, and G. Fève. Electron quantum optics: Partitioning electrons one by one. *Phys. Rev. Lett.*, 108:196803, May 2012.
- [32] E. Bocquillon, V. Freulon, J.-M Berroir, P. Degiovanni, B. Plaçais, A. Cavanna, Y. Jin, and G. Fève. Coherence and indistinguishability of single electrons emitted by independent sources. *Science*, 339(6123):1054–1057, Mar 2013.
- [33] B. Bertrand, S. Hermelin, S. Takada, M. Yamamoto, S. Tarucha, A. Ludwig, A. D. Wieck, C. Bäuerle, and T. Meunier. Fast spin information transfer between distant quantum dots using individual electrons. *Nature nanotechnology*, 11:672–676, Apr 2016.
- [34] B. Bertrand, S. Hermelin, P.A. Mortemousque, S. Takada, M. Yamamoto, S. Tarucha, A. Ludwig, A.D. Wieck, C. Bäuerle, and T. Meunier. Injection of a single electron from static to moving quantum dots. *Nanotechnology*, 27(21):214001, May 2016.
- [35] C. Barthel, M. Kjørgaard, J. Medford, M. Stopa, C. M. Marcus, M. P. Hanson, and A. C. Gossard. Fast sensing of double-dot charge arrangement and spin state with a radio-frequency sensor quantum dot. *Phys. Rev. B*, 81:161308, Apr 2010.
- [36] S. Gleyzes, S. Kuhr, C. Guerlin, J. Bernu, S. Deleglise, U.B. Hoff, M. Brune, J.-M. Raimond, and S. Haroche. Quantum jumps of light recording the birth and death of a photon in a cavity. *Nature*, 446:297–300, Mar 2007.
- [37] A. D. O’Connell, M. Hofheinz, M. Ansmann, R. C. Bialczak, M. Lenander, E. Lucero, M. Neeley, D. Sank, H. Wang, M. Weides, J. Wenner, J.M. Martinis, and A. N. Cleland. Quantum ground state and single-phonon control of a mechanical resonator. *Nature*, 464:697–703, Apr 2010.
-

- 
- [38] I. Neder and I. Marquardt. Coherence oscillations in dephasing by non-gaussian shot noise. *New Journal of Physics*, 9(5):112, May 2007.
- [39] J. R. Petta, A. C. Johnson, J. M. Taylor, E. A. Laird, A. Yacoby, M. D. Lukin, C.M. Marcus, M.P. Hanson, and A.C. Gossard. Coherent manipulation of coupled electron spins in semiconductor quantum dots. *Science*, 309:2180, Sep 2005.
- [40] O. E. Dial, M. D. Shulman, S. P. Harvey, H. Bluhm, V. Umansky, and A. Yacoby. Charge noise spectroscopy using coherent exchange oscillations in a singlet-triplet qubit. *Phys. Rev. Lett.*, 110:146804, Apr 2013.
- [41] H. Bluhm, S. Foletti, I. Neder, M. Rudner, D. Mahalu, V. Umansky, and A. Yacoby. Dephasing time of gaas electron-spin qubits coupled to a nuclear bath exceeding 200us. *Nature Physics*, 7:109, Oct 2010.
- [42] R. Thalineau, A. D. Wieck, C. Bäuerle, and T. Meunier. Using a two-electron spin qubit to detect electrons flying above the Fermi sea. *ArXiv e-prints*, March 2014.
- [43] Romain Thalineau. *Spin qubits : from single electron spin manipulation and transport to its use as a ultra sensitive detector*. Phd thesis, Université de Grenoble, December 2012.
- [44] J. Park, A.N. Pasupathy, J.I. Goldsmith, C. Chang, Y. Yaish, J.R. Petta, M. Rinkoski, J.P. Sethna, H.D. Abruna, P.L. McEuen, and D.C. Ralph. Coulomb blockade and the kondo effect in single atom transistors. *Nature*, 417:722–725, Feb 2002.
- [45] D.L. Klein, P.L. McEuen, J.E. Bowen Katari, R. Roth, and A.P. Alivisatos. An approach to electrical studies of single nanocrystals. *Applied Physics Letters*, 68(18):2574–2576, 1996.
- [46] L. P. Kouwenhoven, D.G. Austing, and S. Tarucha. Few-electron quantum dots. *Reports on Progress in Physics*, 64:701, 2001.
- [47] L.P. Kouwenhoven, C.M. Marcus, P.L. McEuen, S. Tarucha, R.M. Westervelt, and N. S. Wingreen. *Electron Transport in Quantum Dots*, pages 105–214. Springer Netherlands, Dordrecht, 1997.
- [48] H.Flentje, B.Bertrand, P-A.Mortemousque, V.Thiney, A.Ludwig, Wieck A.D., C.Bäuerle, and T.Meunier. A linear triple quantum dot system in isolated configuration. *Applied Physics Letters*, 110(23):233101, Jun 2017.
- [49] R. Thalineau, S. Hermelin, A.D. Wieck, C. Bäuerle, L. Saminadayar, and T. Meunier. A few-electron quadruple quantum dot in a closed loop. *Applied Physics Letters*, 101, Sep 2012.
- [50] Michael J. Manfra. Molecular beam epitaxy of ultra-high-quality algaas gaas heterostructures enabling physics in low-dimensional electronic systems. *Annual Review of Condensed Matter Physics*, 2014.
- [51] S. Gehrsitz, H. Sigg, N. Herres, K. Bachem, K. Köhler, and F. K. Reinhart. Compositional dependence of the elastic constants and the lattice parameter of  $\text{al}_x\text{ga}_{1-x}\text{As}$ . *Phys. Rev. B*, 60:11601–11610, Oct 1999.
-

- 
- [52] X. Wang, S. Yang, and S. Das Sarma. Quantum theory of the charge-stability diagram of semiconductor double-quantum-dot systems. *Phys. Rev. B*, 84:115301, Sep 2011.
- [53] S. Tarucha, D. G. Austing, T. Honda, R. J. van der Hage, and L. P. Kouwenhoven. Shell filling and spin effects in a few electron quantum dot. *Phys. Rev. Lett.*, 77:3613–3616, Oct 1996.
- [54] W. G. van der Wiel, S. De Franceschi, J. M. Elzerman, T. Fujisawa, S. Tarucha, and L. P. Kouwenhoven. Electron transport through double quantum dots. *Rev. Mod. Phys.*, 75:1–22, Dec 2002.
- [55] D. Sprinzak, Y. Ji, M. Heiblum, D. Mahalu, and H. Shtrikman. Charge distribution in a kondo-correlated quantum dot. *Phys. Rev. Lett.*, 88:176805, Apr 2002.
- [56] J. M. Elzerman, R. Hanson, J. S. Greidanus, L. H. Willems van Beveren, S. De Franceschi, L. M. K. Vandersypen, S. Tarucha, and L. P. Kouwenhoven. Few-electron quantum dot circuit with integrated charge read out. *Phys. Rev. B*, 67:161308, Apr 2003.
- [57] R. Hanson, L. P. Kouwenhoven, J. R. Petta, S. Tarucha, and L. M. K. Vandersypen. Spins in few-electron quantum dots. *Rev. Mod. Phys.*, 79:1217–1265, Oct 2007.
- [58] S. Foletti, H. Bluhm, D. Mahalu, V. Umansky, and A. Yacoby. Universal quantum control of two-electron spin quantum bits using dynamic nuclear polarization. *Nature Physics*, 5:903 – 908, Oct 2009.
- [59] A. C. Johnson, J. R. Petta, J. M. Taylor, A. Yacoby, M. D. Lukin, C. M. Marcus, M.P. Hanson, and A.C. Gossard. Triplet singlet spin relaxation via nuclei in a double quantum dot. *Nature*, 435:925–928, May 2005.
- [60] J. M. Taylor, J. R. Petta, A. C. Johnson, A. Yacoby, C. M. Marcus, and M. D. Lukin. Relaxation, dephasing, and quantum control of electron spins in double quantum dots. *Phys. Rev. B*, 76:035315, Jul 2007.
- [61] T. Meunier, I. T. Vink, L. H. Willems van Beveren, K-J. Tielrooij, R. Hanson, F. H. L. Koppens, H. P. Tranitz, W. Wegscheider, L. P. Kouwenhoven, and L. M. K. Vandersypen. Experimental signature of phonon-mediated spin relaxation in a two-electron quantum dot. *Phys. Rev. Lett.*, 98:126601, Mar 2007.
- [62] D. Paget, G. Lampel, B. Sapoval, and V. I. Safarov. Low field electron-nuclear spin coupling in gallium arsenide under optical pumping conditions. *Phys. Rev. B*, 15:5780–5796, Jun 1977.
- [63] P.-F. Braun, X. Marie, L. Lombez, B. Urbaszek, T. Amand, P. Renucci, V. K. Kalevich, K. V. Kavokin, O. Krebs, P. Voisin, and Y. Masumoto. Direct observation of the electron spin relaxation induced by nuclei in quantum dots. *Phys. Rev. Lett.*, 94:116601, Mar 2005.
- [64] F. H. L. Koppens, J. A. Folk, J. M. Elzerman, R. Hanson, L. H. Willems van Beveren, I. T. Vink, H. P. Tranitz, W. Wegscheider, L. P. Kouwenhoven, and L. M. K. Vandersypen. Control and
-

- detection of singlet-triplet mixing in a random nuclear field. *Science*, 309(5739):1346–1350, Aug 2005.
- [65] C. Barthel, D. J. Reilly, C. M. Marcus, M. P. Hanson, and A. C. Gossard. Rapid single-shot measurement of a singlet-triplet qubit. *Phys. Rev. Lett.*, 103:160503, Oct 2009.
- [66] D. J. Reilly, J. M. Taylor, J. R. Petta, C. M. Marcus, M. P. Hanson, and A. C. Gossard. Suppressing spin qubit dephasing by nuclear state preparation. *Science*, 321(5890):817–821, Aug 2008.
- [67] I. A. Merkulov, A. L. Efros, and M. Rosen. Electron spin relaxation by nuclei in semiconductor quantum dots. *Phys. Rev. B*, 65:205309, Apr 2002.
- [68] J. R. Petta, J. M. Taylor, A. C. Johnson, A. Yacoby, M. D. Lukin, C. M. Marcus, M. P. Hanson, and A. C. Gossard. Dynamic nuclear polarization with single electron spins. *Phys. Rev. Lett.*, 100:067601, Feb 2008.
- [69] Steven M Girvin. The quantum hall effect : Novel excitations and broken symmetries. *Topological aspects of low dimensional systems*, Session LXIX.:53–175, 1998.
- [70] L. D. Landau and E. M. Lifshitz. *Quantum Mechanics: Non-relativistic theory*, volume 3 of *Course of Theoretical Physics*. Pergamon Press, Oxford; New York, third edition, 1989, c1977.
- [71] Frank Pobell. *Matter and Methods at Low Temperatures*. Springer-Verlag Berlin Heidelberg, 2007.
- [72] A. B. Zorin. The thermocoax cable as the microwave frequency filter for single electron circuits. *Review of Scientific Instruments*, 66(8):4296–4300, May 1995.
- [73] R. J. Schoelkopf, P. Wahlgren, A. A. Kozhevnikov, P. Delsing, and D. E. Prober. The radio-frequency single-electron transistor (rf-set): A fast and ultrasensitive electrometer. *Science*, 280(5367):1238–1242, May 1998.
- [74] D.J. Reilly, C.M. Marcus, M.P. Hanson, and A.C. Gossard. Fast single-charge sensing with a rf quantum point contact. *Appl. Phys. Lett.*, 91, Oct 2007.
- [75] Thomas Müller. *Radio-Frequency Quantum Point Contact Charge Detection*. Phd thesis, ETH Zurich, 2011.
- [76] T. Müller, B. Küng, S. Hellmüller, P. Studerus, K. Ensslin, T. Ihn, M. Reinwald, and W. Wegscheider. An in situ tunable radio-frequency quantum point contact. *Applied Physics Letters*, 97(20):202104, Nov 2010.
- [77] J. M. Hornibrook, J. I. Colless, A. C. Mahoney, X. G. Croot, S. Blanvillain, H. Lu, A. C. Gossard, and D. J. Reilly. Frequency multiplexing for readout of spin qubits. *Applied Physics Letters*, 104(10):103108, Mar 2014.
- [78] S. Gustavsson, M. Studer, R. Leturcq, T. Ihn, K. Ensslin, D. C. Driscoll, and A. C. Gossard. Frequency-selective single-photon detection using a double quantum dot. *Phys. Rev. Lett.*, 99:206804, Nov 2007.
-

- 
- [79] J. R. Prance, Z. Shi, C. B. Simmons, D. E. Savage, M. G. Lagally, L. R. Schreiber, L. M. K. Vandersypen, M. Friesen, R. Joynt, S. N. Coppersmith, and M. A. Eriksson. Single-shot measurement of triplet-singlet relaxation in a Si/SiGe double quantum dot. *Phys. Rev. Lett.*, 108:046808, Jan 2012.
- [80] H.A. Engel, V. N. Golovach, D. Loss, L. M. K. Vandersypen, J. M. Elzerman, R. Hanson, and L. P. Kouwenhoven. Measurement efficiency and  $n$ -shot readout of spin qubits. *Phys. Rev. Lett.*, 93:106804, Sep 2004.
- [81] K. Ono, D. G. Austing, Y. Tokura, and S. Tarucha. Current rectification by pauli exclusion in a weakly coupled double quantum dot system. *Science*, 297(5585):1313–1317, Aug 2002.
- [82] C. Barthel, J. Medford, H. Bluhm, A. Yacoby, C. M. Marcus, M. P. Hanson, and A. C. Gossard. Relaxation and readout visibility of a singlet-triplet qubit in an overhauser field gradient. *Phys. Rev. B*, 85:035306, Jan 2012.
- [83] G. Burkard, D. Loss, and D. P. DiVincenzo. Coupled quantum dots as quantum gates. *Phys. Rev. B*, 59:2070–2078, Jan 1999.
- [84] D. Loss and D. P. DiVincenzo. Quantum computation with quantum dots. *Phys. Rev. A*, 57:120–126, Jan 1998.
- [85] X. Hu and S. Das Sarma. Hilbert-space structure of a solid-state quantum computer: Two-electron states of a double-quantum-dot artificial molecule. *Phys. Rev. A*, 61:062301, May 2000.
- [86] C. Zener. Non-adiabatic crossing of energy levels. *Proceedings of the Royal Society of London A: Mathematical, Physical and Engineering Sciences*, 137(833):696–702, Sep 1932.
- [87] A. Grodecka, P. Machnikowski, and J. Förstner. Phonon-assisted tunneling between singlet states in two-electron quantum dot molecules. *Phys. Rev. B*, 78:085302, Aug 2008.
- [88] H. Bluhm, S. Foletti, D. Mahalu, V. Umansky, and A. Yacoby. Enhancing the coherence of a spin qubit by operating it as a feedback loop that controls its nuclear spin bath. *Phys. Rev. Lett.*, 105:216803, Nov 2010.
- [89] H.Flenje, P-A.Mortemousque, R.Thalineau, A.Ludwig, A.D.Wieck, C. Bäuerle, and T.Meunier. Coherent long-distance displacement of individual electron spins. *arXiv:1701.01279*, 2017.
- [90] R. Thalinea, S. R. Valentin, A. D. Wieck, C. Bäuerle, and T. Meunier. Interplay between exchange interaction and magnetic field gradient in a double quantum dot with two individual electron spin qubits. *Phys. Rev. B*, 90:075436, Aug 2014.
- [91] M. D. Shulman, O. E. Dial, S. P. Harvey, H. Bluhm, V. Umansky, and A. Yacoby. Demonstration of entanglement of electrostatically coupled singlet-triplet qubits. *Science*, 336(6078):202–205, Apr 2012.
-

- 
- [92] I. van Weperen, B. D. Armstrong, E. A. Laird, J. Medford, C. M. Marcus, M. P. Hanson, and A. C. Gossard. Charge-state conditional operation of a spin qubit. *Phys. Rev. Lett.*, 107:030506, Jul 2011.
- [93] R. C. Ashoori, H. L. Stormer, L. N. Pfeiffer, K. W. Baldwin, and K. West. Edge magnetoplasmons in the time domain. *Phys. Rev. B*, 45:3894–3897, Feb 1992.
- [94] N. B. Zhitenev, R. J. Haug, K. v. Klitzing, and K. Eberl. Experimental determination of the dispersion of edge magnetoplasmons confined in edge channels. *Phys. Rev. B*, 49:7809–7812, Mar 1994.
- [95] N. Kumada, H. Kamata, and T. Fujisawa. Edge magnetoplasmon transport in gated and ungated quantum hall systems. *Phys. Rev. B*, 84:045314, Jul 2011.
- [96] M. Büttiker. Four-terminal phase-coherent conductance. *Phys. Rev. Lett.*, 57:1761–1764, Oct 1986.
- [97] R. Landauer. Spatial variation of currents and fields due to localized scatterers in metallic conduction. *IBM Journal of Research and Development*, 1(3):223–231, July 1957.
- [98] R.J. Haug. Edge-state transport and its experimental consequences in high magnetic fields. *Semicond. Sci. Technol.*, 8(2):131, 1993.
- [99] T. Fujisawa and Y. Hirayama. Charge noise analysis of an algaas/gaas quantum dot using transmission-type radio-frequency single-electron transistor technique. *Applied Physics Letters*, 77(4):543–545, Jul 2000.
- [100] S. Komiyama, H. Hirai, M. Ohsawa, Y. Matsuda, S. Sasa, and T. Fujii. Inter-edge-state scattering and nonlinear effects in a two-dimensional electron gas at high magnetic fields. *Phys. Rev. B*, 45:11085–11107, May 1992.
- [101] G. Müller, D. Weiss, A. V. Khaetskii, K. von Klitzing, S. Koch, H. Nickel, W. Schlapp, and R. Lösch. Equilibration length of electrons in spin-polarized edge channels. *Phys. Rev. B*, 45:3932–3935, Feb 1992.
- [102] H. Hirai, S. Komiyama, S. Fukatsu, T. Osada, Y. Shiraki, and H. Toyoshima. Dependence of inter-edge-channel scattering on temperature and magnetic field: Insight into the edge-confining potential. *Phys. Rev. B*, 52:11159–11164, Oct 1995.
- [103] T. Otsuka, Y. Sugihara, J. Yoneda, T. Nakajima, and S. Tarucha. Measurement of energy relaxation in quantum hall edge states utilizing quantum point contacts. *Journal of the Physical Society of Japan*, 83(1):014710, Dec 2014.
- [104] N. B. Zhitenev, R. J. Haug, K. v. Klitzing, and K. Eberl. Time-resolved measurements of transport in edge channels. *Phys. Rev. Lett.*, 71:2292–2295, Oct 1993.
-

- [105] G. Ernst, R. J. Haug, J. Kuhl, K. von Klitzing, and K. Eberl. Acoustic edge modes of the degenerate two-dimensional electron gas studied by time-resolved magnetotransport measurements. *Phys. Rev. Lett.*, 77:4245–4248, Nov 1996.
-